Structural and Functional Investigations of Transmembrane Signaling Histidine Kinase Using NMR

A dissertation submitted in partial fulfillment
of the requirements for the degree of
”Doctor rerum naturalium” (Dr. rer. nat.)

Division of Mathematics and Natural Sciences
of the Georg-August-Universität-Göttingen

within the doctoral program *Molecular Biology*
of the Georg-August University School of Science (GAUSS)

Göttingen, 2021

submitted by

Xizhou Zhang

From

Suzhou, China

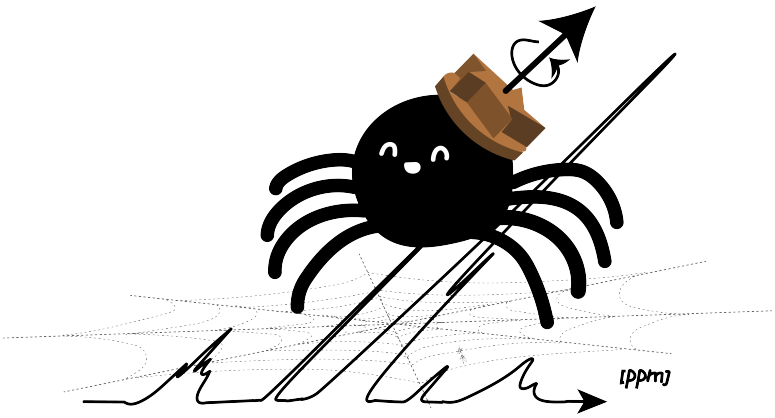
[ppm]

Thesis Committee:

Prof. Dr. Christian Griesinger, NMR-based Structural Biology, Max Planck Institute for Biophysical Chemistry, Göttingen, Germany

Prof. Dr. Blanche Schwappach, Department of Molecular Biology, Universitätsmedizin Göttingen, Göttingen, Germany

Prof. Dr. Bert de Groot, Computational Biomolecular Dynamics, Max Planck Institute for Biophysical Chemistry, Göttingen, Germany

Dr. Loren Andreas, Solid-State NMR Spectroscopy, Max Planck Institute for Biophysical Chemistry, Göttingen, Germany

Members of the Examination Board

Referee: Prof. Dr. Christian Griesinger, NMR-based Structural Biology, Max Planck Institute for Biophysical Chemistry, Göttingen, Germany

2nd Referee: Prof. Dr. Kai Tittmann, Department of Molecular Enzymology, Georg-August-Universität Göttingen, Göttingen, Germany

Further members of the Examination Board

Prof. Dr. Blanche Schwappach, Department of Molecular Biology, Universitätsmedizin Göttingen, Göttingen, Germany

Prof. Dr. Bert de Groot, Computational Biomolecular Dynamics, Max Planck Institute for Biophysical Chemistry, Göttingen, Germany

Dr. Loren Andreas, Solid-State NMR Spectroscopy, Max Planck Institute for Biophysical Chemistry, Göttingen, Germany

Prof. Dr. Marina Bennati, EPR Spectroscopy, Max Planck Institute for Biophysical Chemistry, Göttingen, Germany

Date of oral examination: 15/02/2022

Seldom, very seldom, does complete truth belong to any human disclosure; seldom can it happen that something is not a little disguised or a little mistaken.

—-Jane Austen, *Emma*

ACKNOWLEDGMENTS

I owe it to many people for both my professional and my personal growth in the duration of my doctorate study. The following list contains only the small portion of them that are most directly related to the works presented in this thesis.

First and foremost, I would like to thank Dr. Loren Andreas and Prof. Dr. Christian Griesinger as great academic supervisors. Without their insights into NMR, constant support and encouragement, none of my doctorate work would take place. Their shared passion for food and music has made my time in the department all the more colorful. Better mentors than them I could not have hoped for.

For the CitA project, my heart-felt gratitude towards Karin Giller and Dr. Stefan Becker for supplying exclusively the excellent CitA protein samples used in this thesis and inspiring discussions regarding the sample preparations. I would like to thank Dr. Michele Salvi for the excellent tutelage in the start of my study and continuous scientific contributions throughout. I would like to thank my student Jonas Mehrens for his contributions in the assignment process and the ^{31}P activity assay. The collaborations with Prof. Dr. Gottfried Unden and his group have been crucial in the biological groundings of the project. Special thank also goes to Dr. Marius Stopp for the PASc-kin data and Dr. Mookyoung Han for the DLS data. I would also like to thank Dr. Kai Xue for starting the ^{19}F CODEX measurement with me on the DNP two years ago. Without his insightful opinions, tempering with the DNP machines would have been a lot harder than it already is.

I would not trade anything for the wonderful time I had with all of the solid-state group members. Dr. Marcel Forster is the best co-author for the TREDOR project I could hope for, and has been great as both an office-mate in the ”girl’s office”, a co-summer school attendee in Mallorca and an involuntary German email proof-reader. The other member of the ”girl’s office”, Dr. Eszter Éva Najbauer, deserves special thanks for her patience in proof-reading my numerous texts in English and our wonderful time playing flute and piano duets. I also enjoyed the many, often on weekends, scientific discussions with Dr. Kumar Tekwani Movellen. I would like to thank Vrinda Sant as a great colleague, a co-residence of the ”Sant-Zhang” apartment and a co-mama of our cat Bubbles. Dr. Supriya Pratihar has been a great co-responsible for the 950 MHz magnet and it was a great pleasure for me to do magnet service work with him over the years.

I want to thank my cohort from the IMPRS MolBio for their stimulating discussions. I would like thank my program coordinators Dr. Steffen Burkhardt and Kerstin Grüniger for bringing me to Göttingen and their amazing organization and administrative support. I would

also like to thank my TAC committee members Prof. Dr. Blanche Schwappach and Prof. Dr. Bert de Groot for their continuous mentoring. In addition, I would like to thank my examination committee Prof. Dr. Kai Tittmann and Prof. Dr. Marina Bennati for taking their time in reviewing this thesis.

My time in Göttingen would have been dull without my friends. My university roommate Sophie Ochmann and her family have been the people who first introduced the city of Göttingen to me back in my first year in Germany. I do not regret coming to their hometown for my doctorate study and thank them for their friendship. I want to thank my good friend and my ”sister”, Ruoshi Zhang, for proof-reading parts of this thesis and all the good times we had together throughout the years.

Lastly, my greatest gratitude to my parents for showing me all the love and support in the world.

RELATED PUBLICATIONS

The work presented in this thesis led to the following publications:

Evgeny Nimerovsky, Kumar Tekwani Movellan, Xizhou Cecily Zhang, Marcel C Forster, Eszter Najbauer, Kai Xue, Rıza Dervişoğlu, Karin Giller, Christian Griesinger, Stefan Becker, and Loren B Andreas. Proton detected solid-state nmr of membrane proteins at 28 tesla (1.2 GHz) and 100 kHz magic-angle spinning. *Biomolecules*, 11(5):752, 2021.

Kai Xue, Kumar Tekwani Movellan, Xizhou Zhang, Eszter E Najbauer, Marcel C Forster, Stefan Becker, and Loren B Andreas. Towards a native environment: Structure and function of membrane proteins in lipid bilayers by nmr. *Chemical Science*, 2021.

Xizhou Cecily Zhang, Marcel C Forster, Evgeny Nimerovsky, Kumar Tekwani Movellan, and Loren B Andreas. Transferred-rotational-echo double resonance. The Journal of *Physical Chemistry A*, 125(3):754–769, 2021.

TABLE OF CONTENTS

LIST OF FIGURES

FIGURE

LIST OF TABLES

TABLE

LIST OF APPENDICES

LIST OF ACRONYMS

GPCR G-protein coupled receptor

PDB protein data bank

NMR nuclear magnetic resonance

cryo-EM cryo-electron microscopy

TCST two-component signal transduction

RR response regulator

HK histidine kinase

TM transmembrane helix

DHp dimerisation and histidine phosphorylation

CA ATP-binding kinase domain

CitA citrate receptor A

PAS Per-ARNT-Sim

PASp periplasmic PAS

PASc cytoplasmic PAS

PASpc periplasmic and cytoplasmic PAS

MAS magic angle spinning

RF radio frequency

CSA chemical shift anisotropy

REDOR rotational echo double resonance

TEDOR transferred-echo double resonance

AHT average Hamiltonian theory

CODEX centerband-only detection of exchange

CP cross-polarization

P-helix periplasmic helix

DMPC 1,2-dimyristoyl-sn-glycero-3-phosphocholine

DMPA 1,2-dimyristoyl-sn-glycero-3-phosphatic acid

DMPC 1,2-dimyristoyl-sn-glycero-3-phosphocholine

DMPA 1,2-dimyristoyl-sn-glycero-3-phosphatic acid

CEST chemical exchange saturation transfer

sPRE solvent paramagnetic relaxation enhancement

GT *G.thermodenitrificans*

WT wild type

COLD cryogenic optical localization

SPA scintillation proximity assay

IMAC immobilized metal affinity chromatography

DLS dynamic light scattering

DM decylmaltoside

TCEP Tris-(2-carboxyethyl)-phosphine hydrochloride

MTSL Methanethiosulfonate

DNP dynamic nuclear polarization

HFA hexafluoroacetone

IPTG isopropyl-β-D-thiogalactopyranoside

DTT dithiothreitol

LDAO n-dodecyl-N,N-dimethylamine-N-oxide

DEER double electron-electron resonance

TREDOR Transferred-Rotational-Echo DOuble Resonance

CS chemical shift

DSS sodium trimethylsilylpropanesulfonate

ATP adenosine triphosphate

ABSTRACT

Membrane proteins play a central role in biology as the gatekeepers of all cellular compartments. And transmembrane signaling through membrane bound kinases is a particularly important process for cellular adaptation to a changing environment. In prokaryotes, the membrane bound HK, which is part of the ubiquitous two-component system, is the most common type of signal transduction employing a protein phosphorylation mechanism. Due to their lipid-bound native environment, structural studies of membrane bound HKs have remained challenging for a spectrum of techniques. The first five chapters of this thesis will be dedicated to the functional and structural studies of a membrane HK CitA, which is activated for cross-phosphorylation upon citrate binding by hydrolysis of ATP molecules, employing NMR spectroscopy. The new regime of ultra-fast MAS NMR has allowed the application of ^{1}H-detected experiments to more challenging system. We employed this method for the residue specific assignment of the PASpc construct of CitA and gained chemical shift information of the previously unavailable TM helices, along with their linker regions (Chapter 2). This new piece of information confirms the formation of a P-helix at the end of the PASp domain to further residues downstream, as well as reveals the loosening of a conserved KK linker upon citrate binding between the TM2 helix and the PASc domain.

The role of cytosolic PAS domain in HK activation has remain unsolved since the discovery of HKs over 30 years ago. Based on the functional mutants in the PASc domain of CitA, sPRE profile and NMR visibility, an anti-parallel to parallel dimer rearrangement model for CitA activation in its PASc domain was proposed. However, direct structural evidence and functional data confirming the validity of this structural model is still lacking. We investigated the functional impact of this model on the CitA phosphorylation rate by tracking the ATP hydrolysis using ^{31}P NMR (Chapter 3). An attenuation of CitA's kinase activity when the anti-parallel N288D mutant PASc domain, instead of the parallel WT PASc domain, was attached to the DHp domain is observed by us. This confirms the functional relevance of this dimer transition in the activity of CitA. The same ^{31}P NMR method provides a convenient way to test the functionality of CitA with different chemical tags, which is a pre-requisite for site-specific inter-dimer distance measurement. We found that tagging CitA with a small CF_3 group of a cysteine mutation site,

N308C, at the end of the PASc domain retains its functionality and responsiveness to citrate binding, while tagging of the same site with MTSL does not. This paves the way for gaining site specific evidence to prove the anti-parallel to parallel transition upon citrate binding using DNP enhanced ^{19}F NMR (Chapter 4). From this, we found a large change in inter-N308C distance between the citrate free (more than 20 Å apart) and the citrate bound state (11 Å). This supports the drastic anti-parallel to parallel dimer transition directly. Although our data are collected using a fragment of CitA lacking the DHp domain, they provide key information regarding the structural rearrangement of PASc that lead to HK activation in the context of the TM helices. Combined with the ^{1}H-detected MAS NMR assignment, the works presented here suggest that the P-helix formation at the end of PASp, the piston-like upward motion of the TM2 helix, the KK domain loosening at the linker between the TM2 helix and the PASc domain, and the anti-parallel to parallel dimer transition are key events in the activation of CitA with citrate binding.

Internuclear distance determination is the foundation for NMR-based structure calculation. However, high-precision distance measurement is a laborious process requiring lengthy data acquisitions due to the large set of multidimensional spectra needed at different mixing times. This prevents application to large or challenging molecular systems. The last chapter of this thesis will present a new approach, transferred-rotational-echo double resonance (TREDOR), a heteronuclear transfer method in which we simultaneously detect both starting and transferred signals in a single spectrum. This co-acquisition is used to compensate for coherence decay, resulting in accurate and precise distance determination by a single parameter fit using a single spectrum recorded at an ideal mixing time. We showcase TREDOR with the microcrystalline SH3 protein using 3D spectra to resolve resonances. By combining the measured N–C and H–C distances, we calculate the structure of SH3, which converges to the correct fold, with a root-mean-square deviation of 2.1 Å compared to a reference X-ray structure. This demonstrates TREDOR as a fast and straightforward method for determining structures via magic-angle spinning NMR.

CHAPTER 1

Introduction

1.1 Transmembrane signal transduction through receptor kinases

Membrane proteins, as the gatekeepers of all cellular compartments, play a central role in biology. For cells to perceive and respond to a changing environment, both chemical and physical stimuli need to get transmitted through the membrane in order to initiate the appropriate cellular adaptations. This process, called the transmembrane signal transduction, is most commonly conducted through protein phosphorylation catalyzed by receptor kinases. Receptor kinases are employed in all domains of life and are characterised by a kinase domain that phosphorylates specific amino acid residues (primarily serine/threonine, tyrosine or histidine) either of an effector protein or within the receptor itself [87]. Using protein phosphorylation for signal processing is thermodynamically favorable, as phosphorylation is achieved using a trinucleotide-phosphate molecule, most commonly adenosine triphosphate (ATP), as a high energy phosphate donor. The reverse reaction of dephosphorylation, which restores the system to its original state, can either be done by auto-hydrolysis with the bulk water or by phosphatases, which selectively dephosphorylate the phosphoprotein. The signal network constructed through protein phosphorylation is thus highly tunable, as kinases often act in concert with phosphatases to integrate a multitude of signal inputs. This ensures the intra-cellular crosstalk between different signaling pathways and enables an analog cellular output. Due to their biological importance, these membrane bound receptor kinases represent a major class of drug targets, with G-protein coupled receptors (GPCRs) alone accounting for 11 % of them [144].

Structural determination of the membrane bound receptor kinases has been notoriously challenging. Despite comprising a good 30% of all proteins, only 4517 membrane protein structures, *i.e.,* 2.5 %, are deposited in the protein data bank (PDB) among a total of 182418 entries up till 2021. On top of the usually poor yield upon recombinant production, membrane proteins lose their native structures outside the lipid environment. Solutions to tackle this problem exist across the spectrum of structural biology techniques. Short chain detergents that form micelles are used both in X-ray crystallography and solution state nuclear magnetic resonance (NMR), but are not ideal as they are prone to denature the protein of interest. Recent advances using nanodiscs (discoidal lipid bilayers made soluble by encircling protein belts) in combination with cryo-electron microscopy (cryo-EM) [53] are also proven successful in several cases. But structural techniques in near native lipid environment like liposomes are still desired, due to their resemblance to the protein's natural environment and the relative ease of the sample preparation protocol. For studying transmembrane signaling specifically, the amount of already difficult work is at least doubled, as the signaling proteins usually come in both activated and deactivated states. One gains biological insights into the signaling event from the changes between the two, not from a single state. This is even more crucial in the rational design of drugs, where one state over the other needs to be specifically selected in order to achieve the desired physiological effect.

1.2 Membrane bound histidine kinase in the two-component signal transduction mechanism

The two-component signal transduction mechanism (TCST) is the most prevalent mechanism for sensing and responding to environmental changes in prokaryotes [36]. Five percentage of all TCST systems are found in fungi, amoebae and plants [209] but they are absent in animals [39]. Considering the magnitude of their habitats, microbes receive a large variety of environmental signals and must be equipped to respond to a collection of inputs including nutrients, chemo-attractants, cell density, osmotic pressure *etc*. There are tens of thousands of TCST systems present in the currently sequenced genomes and the large repertoire of their input signals makes

them important tools in synthetic biology [109].

TCSTs are named after their two protein signaling components: an often membrane bound dimeric histidine kinase (HK) and a response regulator (RR) (Figure 1.1 [30]). The signal transduction usually starts with a ligand binding event at the sensing domain at the HK N-terminus, and the signal is transmitted through the membrane via a transmembrane helix (TM) bundle and often, cytoplasmic transmitter domains. In the cytoplasm, the signal triggers phosphorylation of the conserved histidine site of the enzymatic transmitter domain at the C-terminus of the HK, catalyzed with the hydrolysis of ATP molecules. A phosphotransfer event then follows, during which the phosphate group on the HK is carried to an aspartate residue in the receiver domain of RR. The phosphorylated RR undergoes extensive structural rearrangement to activate its output domain, which often changes the expression levels of genes relevant for the processing of the diverse input signals received by the HK. This thesis will focus on the investigation of one HK but not RRs, as RRs are often not membrane bound. Extensive review articles are available regarding RRs' structures [225, 63]. To further fine-tune the respective cellular responses and coordinate the various input signals, TCST systems can also be aided by auxiliary proteins, which range from transporters on the membrane to cytosolic binding partners which change the phosphorylation states of HK and RR. They have been summarized by various literature [36, 213, 208].

The first evidence of prokaryote HKs came 30 years ago from the *in vitro* studies of the HKs NtrB [154] and CheA [90] after the initial findings of protein phosphorylation [32] in the 1960s. Since then, they have emerged as the most common type of signal transduction employing a protein phosphorylation mechanism in microbes, including pathogens. Due to their absence in animals, interfering with the HK signaling important for pathogenicity has been proposed as a potential anti-microbial strategy with the added benefits of fewer side effects and lower likelihood of resistance compared with classical antibiotics [227]. HKs are a diverse group of proteins that do not share domain architecture but are rather characterized by a conserved kinase core consisting of a dimerisation and histidine phosphorylation domain (DHp) and a catalytic, ATP-binding kinase domain (CA). Three classes of HKs are known: **Class I HKs** are independent sensor proteins that can be either soluble or membrane bound; **Class II HKs** are soluble kinases that

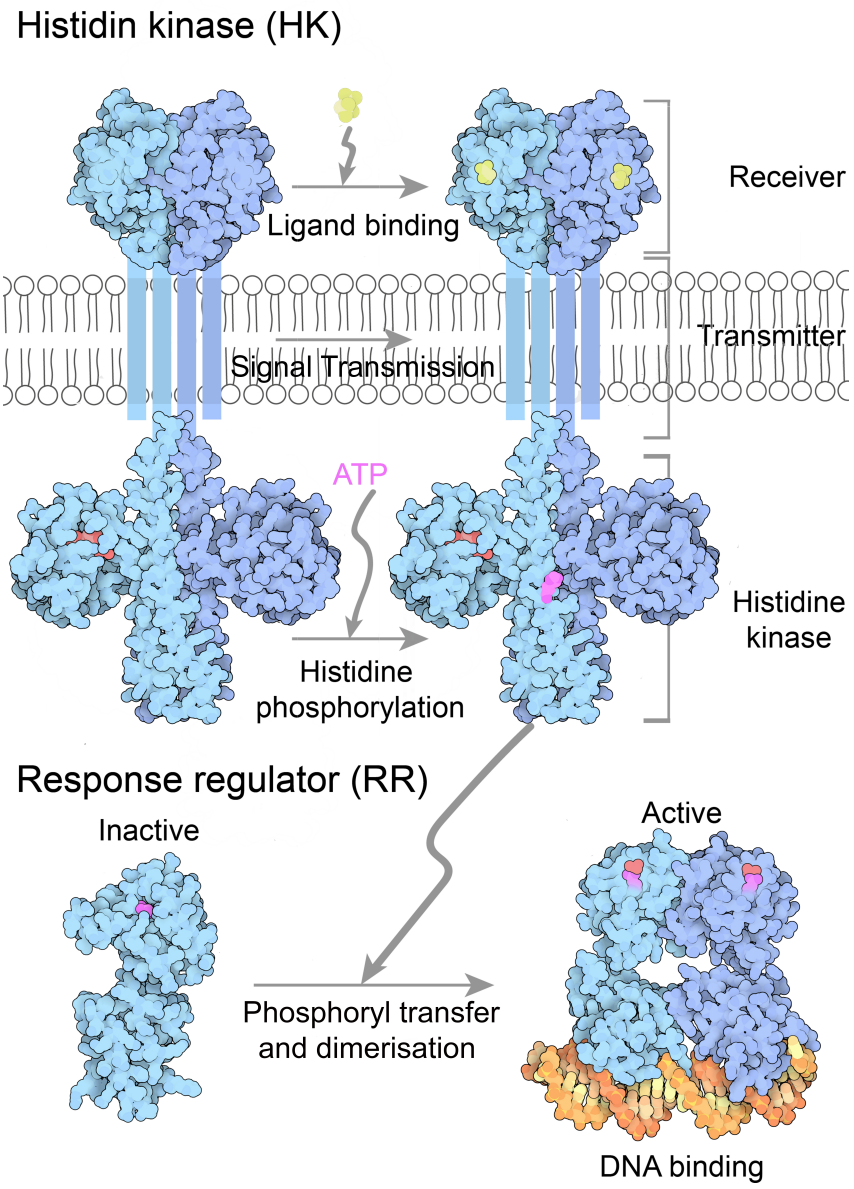

Figure 1.1: Common signaling mechanism of a TCST system that consists of a Class I histidine kinase (HK) and a response regulator (RR). The HK usually has three domains: the sensor domain (modeled after PDB entry of a citrate binding PAS domain: 3by8 [43]) which responds to the incoming signal (yellow), the transmitter domain(s) which usually spans the bacterial inner membrane and relays the signal to the DHp domain (modeled after PDB entry: 2c2a [139]), which can cross-phosphorylate in between the dimer at a conserved histidine site (upper red). The cross-phosphorylation reaction happens due to the binding and hydrolysis of ATP molecules (upper magenta). A phosphotransfer event then follows so that an aspartate residue (lower magenta) in the response regulator (RR) is phosphorylated (inactive state modeled after PDB entry: 1kgs [35]). This activates the RR and causes it to dimerize and bind to DNA (yellow, lower) for transcription activation of relevant downstream genes (active states modeled after PDB entries: 1gxp [27] and 1zes [14]). The drawings of individual domains are taken from works of the group of D. Goodsell [30]

lack the sensor domain, and need to function with other receptor proteins [88, 159]; **Class III HKs** are hybrids between Class I and Class II kinases and are characterized by the presence of the sensory domains and the lack of a DHp domain [2]. From here on, HKs will refer solely to Class I HKs. In Class I HKs, the CA domain can phosphorylate the conserved histidine residue in the DHp domain. They have highly modular constructions and often borrow from the same set of signal recognition and signal transduction modules but arrange them in different orders to achieve their diverse functions [81]. Class I HKs can be further divided into subgroups according to their putative sequences and structural motifs [227, 140, 205]. Importantly, almost all HKs characterized structurally function as homo-dimers [39], with the only exceptions being the *Pseudomonas aeruginosa* GacS-RetS HK hetero-dimers [70] and the monomeric soluble blue light-activated HK from *Erythrobacter litoralis* HTCC2594, EL346 [170]. Recently, evidence of tetramer organization in the *in vivo* studies of the CitA/DcuS type of HKs [185] has also been presented. 83 % of all HKs contain transmembrane segments [81], and most of these HKs contain two transmembrane helices. Structural evidence of the transmembrane signal transduction mechanism in these two-pass membrane bound HKs from the periplasmic receiver domain to the cytoplasmic domain is only available from the crystallography data of the TM domain-containing fragment of the nitrate/nitrite sensor NarQ [82]. In it, a piston type upward motion is observed in the TM domains. However, due to the diversity of the domain architecture of HKs, the structural insight from one HK is not nearly enough to cover the canonical signaling mechanism in the TM domains. Studying other types of HKs is therefore necessary.

In the cytoplasm, between the TM domain and the DHp domain, two types of cytoplasmic connector domains can be found: PAS and HAMP. Both domains are often connected to the TM helix by extended α-helical stretches such as the signaling helix [6] and other short and long connector α-helices [220, 83, 3]. Signaling through the cytoplasmic HAMP domain has been substantially studied, and it is proposed that the HAMP domains serve as converters of the piston-like input in the TM region signal into a helical rotation signal in the DHp domain [82, 81]. The signaling in the cytoplasm through the Per-ARNT-Sim domain (PAS), which can alternatively be found in the periplasm as a ligand receiver domain, is less well studied. The Per-ARNT-Sim domains that form the acronym "PAS" refer to the names of the first three proteins in which

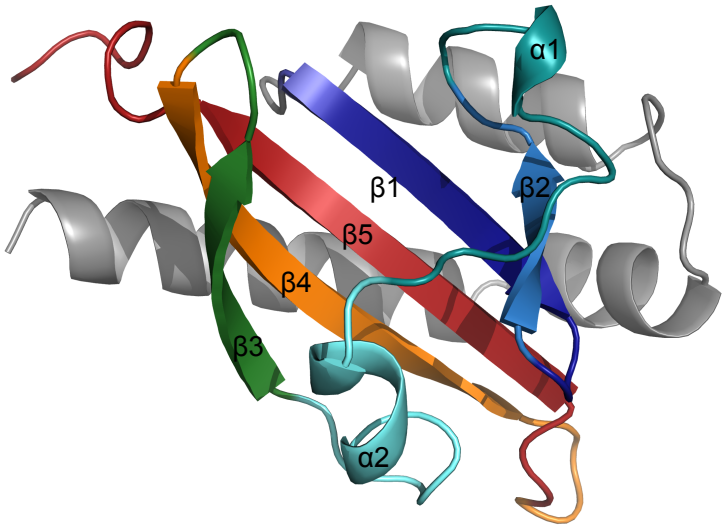

Figure 1.2: The PASp domain from the bacteria *G. thermodenitrificans* CitA in the citrate free state is shown as the typical PAS fold. The N-terminal helix (grey) is the connector between the core PAS domain and the TM1 helix and does not belong to the core PAS fold. The central β-scaffold consists of five anti-parallel β-strand. A major loop between the β2 and β3 strands hovers over the core β-scaffold and has a varying number of short α-helices. The crystal structure was solved in the group of S.Becker.

its structural motif was recognized: the *Drosophila* period clock protein (PER), vertebrate aryl hydrocarbon receptor nuclear translocator (ARNT), and *Drosophila* single-minded protein (SIM). The structure of a typical PAS fold has both β-strand and α-helical components (Figure 1.2). It consists of an N-terminal helix and a core β-scaffold with five anti-parallel β-strands facing a large major loop with a varying number of small α-helices. Crystal structures have suggested great versatility of the relative position between the N-terminal helix and the PAS domain fold [55, 111]. A dynamic bundle model has been proposed for the PAS domain-mediated cytoplasmic signaling, in which the active, ligand-bound state has an overall higher mobility in the cytoplasmic connector PAS domain [178]. But structural insights of the cytoplasmic connector PAS domain are needed, since there is no evidence that the HAMP domain and PAS domain are interchangeable in their cytoplasmic signal transduction mechanisms. Mutagenesis studies only provided evidence for the existence of dimer rearrangement [55] upon the signaling event, but its interpretation remains ambiguous as to what the structural rearrangements are.

1.3 Citrate receptor A (CitA) in the thermophilic bacterium *Geobacillus thermodenitrificans*

The CitA/DcuS sensor kinase family [72] is a subfamily of Class I HKs, which can bind to citrate (in the case of CitA) and other C_4-dicarboxylates (in the case of DcuS). These are key nutrient sources to be degraded in bacterial aerobic growth. The activation of this family of HKs induces the expression of enzymes responsible for catabolizing these C_4-dicarboxylates (fumarate reductase, PEP carboxykinase *etc*.), as well as their respective membrane transporters [213]. CitA is the ideal model protein for studying PAS domain containing HKs, since it is not known so far to require any auxiliary proteins to function, unlike DcuS, which requires the presence of the proteins DctA or DcuB. Otherwise, DcuS remains by itself in a constantly active state [201].

CitA belongs to the class of HKs that contain two PAS domains: the periplasmic PAS domain (PASp) for citrate binding and the cytosolic PAS domain (PASc) as an adaptor between transmembrane helix two (TM2) and the DHp domain. The domain architecture of CitA is shown in Figure 1.3. The ligand binding of CitA is highly selective to citrate. Closely related molecules like isocitrate and tricarballylate does not trigger CitA activation [104]. Depending on whether citrate is bound to the PASp domain, CitA has two functional states: i) the "bound" state in which the kinase is activated and can cross-phosphorylate each monomer by ATP hydrolysis and ii) the "free" state when the PASp domain is in its *apo* form without citrate, in which the kinase is inactive. The PASp can be studied in isolation without the need for membrane reconstitution, so its structure has been characterized in both signaling states. Structures of the *Klebsiella pneumoniae* CitA PASp in citrate-free and citrate-bound forms are available both with X-ray crystallography [168, 189] and by solution state NMR [178, 158, 157]. Upon citrate binding, the β-sheets of PASp tighten to form the binding pocket of CitA; this is accompanied by a rearrangement of the major loop too. The tightening of the β-sheet core of PASp with ligand binding is compatible with a piston motion of the TM2 first hypothesized based on a cysteine accessibility assay [145]. This was also confirmed with ^{13}C-detected solid-state NMR, albeit in only one residue, L154 [178].

The transmembrane signaling mechanism from the TM helices to the PASc domain remains

elusive, mainly because the signaling states cannot be solved in isolation without the sensor domain, PASp. Technical challenges inherent to studying membrane bound kinases cannot be avoided. Crystallography and NMR studies of *K. pneumoniae* and *E. coli* CitA PASc domains have thus far remained inconclusive, due to the high mobility of their PASc domains which prevents crystallization and reduces NMR visibility. Fortuitously, a CitA homolog found in the thermophilic bacterium *Geobacillus thermodenitrificans* (GT CitA) was shown to give NMR spectra of excellent quality both in the PASp and the PASc domains [186] likely owing to reduced PASc dynamics in proteins in thermophilic organisms [166]. GT CitA can be divided into different fragments depending on the purpose of the study. The constructs used in this thesis are presented in Figure 1.3. They are either soluble samples or solid samples embedded in liposomes. The soluble constructs are the isolated periplasmic PAS domain (PASp), the isolated cytoplasmic PAS domain (PASc), and the DHp domain attached with the PASc domain (PASc-kin). The liposome-embedded constructs contain the PASp and PASc domains with the two TM helices (PASpc) alone or including DHp domain as the full length CitA. The dynamic bundle model of cytoplasmic PAS domain [178] mentioned in the previous section was proposed using the GT CitA PASpc construct. In this model, the PASc domain increases its mobility when the citrate is bound to allow CitA activation.

The effects of different point mutations in the PASc domain were tested in *E. coli* DcuS [145]. A functional mutant N288D in the GT CitA PASc domain can be generated from the constitutively active N304D mutant in *E. coli* DcuS based on protein sequence alignment results [177] between GT CitA and *E. coli* DcuS. Another point mutation R289D, also a polar residue, neighbouring the N288D mutation was selected as a second possible mutant to rule out potential errors in the sequence alignment. The functionality of both mutants was verified *in vivo* in the lab of Prof. Unden [177]. A structural model was proposed based on the crystal structures of the N288D mutant and the WT PASc in *G. thermodenitrificans* solved in the group of Stefan Becker (department of NMR-based Structural Biology, Max-Planck-Institute for Biophysical chemistry)(Figure 3.1). The N288D mutant displayed an anti-parallel dimer form in the crystal structure, which is different from the parallel dimer form observed with the WT PASc, even though the N288D mutant does not disturb the functionality of CitA in *G. thermodenitrificans*

[186, 177] (Figure A.1). The two dimers differ from one another in the arrangement of the N-terminal helix, but not the central PAS fold. Another difference between the two dimer forms is the inter-dimer distance at the C-terminus, with the anti-parallel dimer having a much larger C-terminal inter-dimer distance than the parallel dimer. M. Salvi *et al.* proposed that the PASc dimer switches from an anti-parallel to parallel dimer arrangement upon activation by citrate binding, based on chemical exchange saturation transfer (CEST) [214] and solvent paramagnetic relaxation enhancement (sPRE) measurements [236]. The R289D mutant displayed an "open" dimer arrangement, where the two N-terminal helices do not form the dimer interface in the PASc. This dimer form will not be the focus in this thesis, as it is proposed to either be a lowly populated, non-detectable transition state between the anti-parallel and parallel dimers or a dimer form only adopted by isolated PASc domain, since evidence of its existence could not be found through NMR visibility or in the sPRE profile in the membrane bound PASpc construct [177]. More details regarding this structural model of CitA PASc can be found in Chapter 3. However, direct structural and functional evidence in CitA still needs to be found to prove the validity of this model conclusively. This thesis will aim to verify if the anti-parallel dimer form leads to deactivation of the HK activity of GT CitA through a ^{31}P NMR based ATP hydrolysis assay in Chapter 3. In addition, residue specific inter-dimer distance changes that proves this anti-parallel to parallel dimer transition upon CitA activation will be shown in Chapter 4 using a chemically tagged CitA PASpc sample.

1.4 MAS NMR spectroscopy

High-resolution magic angle spinning (MAS) NMR is emerging as a powerful tool in giving structural insights in natural materials [124, 125], and in determining membrane protein structures. It has no theoretical limit to the size of the molecule of interest. Protein dynamics, particularly important in studying conformational plasticity, can also be readily studied in almost all time scales by NMR [229]. Hardware developments including ultra-fast MAS probes and high field magnets have incrementally contributed to better resolution and sensitivity over the years. Most notably are the recent availability of the high magnetic fields up to 1.2 GHz, which have been reported to increase resolution and sensitivity across a spectrum of membrane proteins

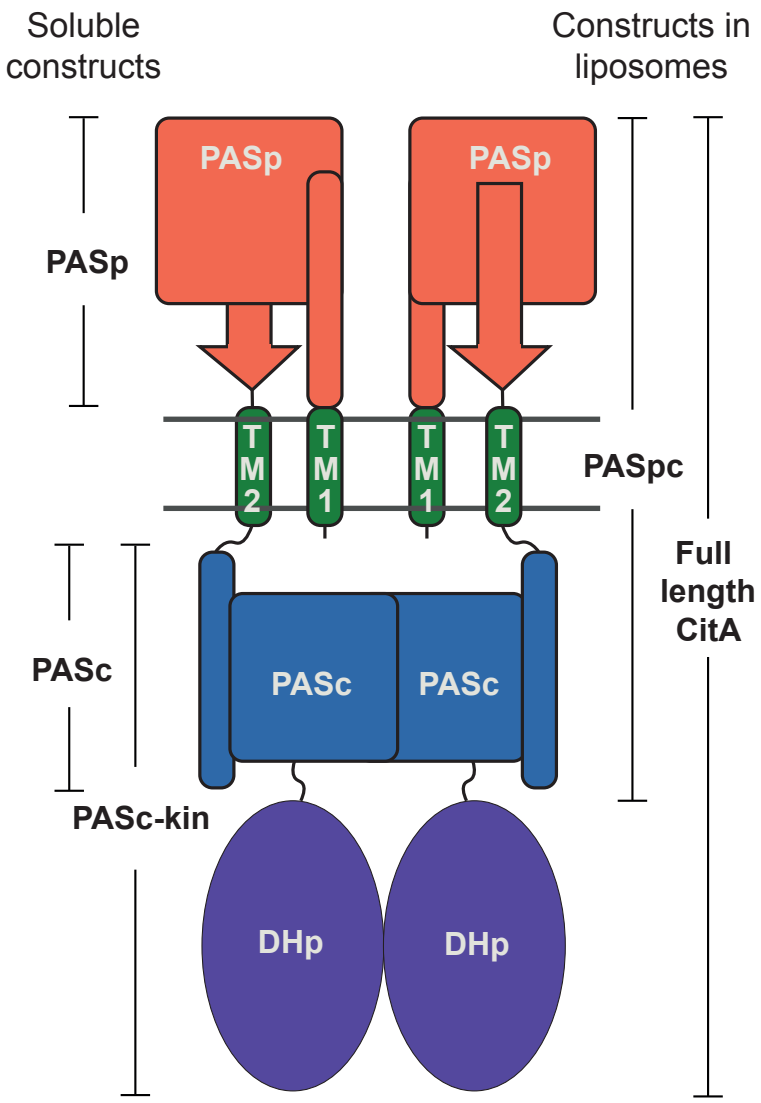

Figure 1.3: Domain architecture of GT CitA and subdivisions of it that form the constructs used in this thesis. The soluble constructs are isolated PASp, isolated PASc and PASc-kin which contains the PASc domain and the DHp domain. The solid constructs are the full length CitA and the PASpc construct which contains the PASp domain, TM1 and TM2 helices, and the PASc domain.

[38, 153]. Application of MAS NMR to biological samples is still in its nascent stage, with earliest membrane protein structures solved only about ten years ago. In the last years, significant contributions of MAS NMR to membrane-associated proteins include [229], i) the transmembrane domain of SARS-CoV-2 envelop protein E from Hong's group [136, 95] ii) the bacterial alkane transporter AlkL [187] from the group of Pintacuda and Andreas, iii) evolution of membrane associated α-Synuclein fibrils from the group of Griesinger and Andreas [12], iv) the atomic resolution structure of the HIV capsid tubes by the group of Gronenborn and Polenova [130]. The new regime of ^{1}H-detection reduces the requirements for sample quantity and measurement time significantly. With faster spinning, the large proton homonuclear dipolar coupling is reduced under the coherent averaging by MAS, making the ^{1}H linewidth small enough to extract site-specific chemical shift (CS) information in proteins. This additional dimension on top of the four-fold sensitivity gain compared with that of the ^{13}C-detection, makes ^{1}H-detection suitable for more challenging proteins.

Sequence specific chemical shift assignment is the first step in the investigation of proteins using NMR. Only from this, residue specific chemical shift information can be obtained. Strategies and recent development of sequence specific assignment using ^{1}H-detected solid state NMR will be reviewed in Chapter 2. Previously, isolated PASp and PASc constructs from GT CitA have been assigned using solution state NMR [178]. The chemical shift information from them are borrowed for assigning the ^{13}C-detected solid state NMR spectra. The drawback is obvious: the TM regions cannot be assigned since they are missing in the isolated domains. All information contained in the chemical shift including the dihedral angles of the peptide bond and local dynamics in the TM domains is missing. This prevents us from detecting any secondary structural or dynamics changes in the regions that connect the PASp and PASc upon citrate binding, which is crucial in understanding the transmembrane signaling mechanism in CitA. With the advantage offered by ^{1}H-detection, we performed residue specific assignment experiment in GT CitA PASpc construct including the TM1 and TM2. The dynamic and structural implications from these data in the context of CitA transmembrane signal transduction form the PASp to the PASc domain are discussed in Chapter 2.

The following subsections will introduce the basics of spin physics behind the concepts of the NMR experiments done in this thesis.

1.5 Spin Hamiltonians relevant to MAS NMR

The concept of spin was first inferred from the Stern-Gerlach experiment, where the unpaired electron silver atom is observed to interact with an inhomogeneous magnetic field. For NMR experiments, nuclear spin is relevant, which is an intrinsic property of the atom nuclei themselves, rather than originating from rotation in physical space. Its effect is first described by Purcell, Torrey, and Pound [164] in solids. Simultaneously, Bloch, Hansen, and Packard [28] measured the same effect in what they called the "nuclear induction experiment." Its quantum mechanics treatment is analogous to that of angular momentum in classical mechanics and has been formulated extensively in literature [46, 73, 176, 198]. The descriptions presented here will follow those from the book Spin Dynamics by M. Levitt [114] and Solid-State NMR Spectroscopy by M. Duer [54]. Without going deeper into spin physics, the spin angular momentum (μ) and the magnetic moment (S) are proportional to each other (the $\hat{}$ sign denotes operators), by:

$$\hat{\mu} = \gamma \hat{S} \tag{1.1}$$

where γ is called the gyromagnetic ratio, whose magnitude is an indication of the strength of interaction between the nuclear angular momentum and the magnetic field. It is dependent on the nucleus type. For biological systems, the nuclei of interest are ^{1}H, ^{19}F, ^{13}C, ^{31}P and ^{15}N, with the size of gyromagnetic ratio in descending order. For this reason, ^{1}H-detected NMR experiments have the added advantage of being more sensitive than their ^{13}C detected counterparts. The entire quantum state of a system can be described by the wave function $|\Psi_{full}(t) >$ which obeys the time dependent Schrödinger equation. For our purpose, we will only be concerned with the part, $|\Psi(t) >$, that is involved in the spin state:

$$\frac{d}{dt}|\Psi(t) > \approx -i\hat{\mathcal{H}}|\Psi(t) > \tag{1.2}$$

The Hamiltonian operator $\hat{\mathcal{H}}$ that appears here is called the nuclear spin Hamiltonian, and describes the direction of nuclear spin polarization. An important assumption here is that any rapid influence from the surrounding electrons of the nucleus is treated as an average and has no time dependence. Components that contribute to the nuclear spin Hamiltonians will be discussed.

External spin Hamiltonians and simple NMR experiments

When a single spin is placed in a large static magnetic field, the interaction of spin angular momentum and a large magnetic field B_0 is dependent on the minus dot product of their respective operator, and when the field is aligned along the z-axis in the laboratory frame, becomes:

$$\hat{\mathcal{H}}^{static} = -\hat{\mu}B_0 = -\gamma\hat{S}_z B_0 \tag{1.3}$$

This part of the spin Hamiltonian (expressed in angular frequency unit) is called the Zeeman interaction. For nuclei with a quantum number $1/2$, which account for the most common types of the spins relevant in biological systems, there are two Zeeman eigenstates, $|\alpha>$ and $|\beta>$:

$$|\alpha>=|\frac{1}{2},+\frac{1}{2}>, |\beta>=|\frac{1}{2},-\frac{1}{2}> \tag{1.4}$$

The matrix representation of the spin angular momentum operator at the z direction $\hat{S}_z$ with the above-mentioned $|\alpha>$ and $|\beta>$ Zeeman eigenbasis is:

$$\hat{S}_z = \frac{1}{2}\begin{pmatrix} 1 & 0 \\ 0 & -1 \end{pmatrix} \tag{1.5}$$

which should also satisfy the cyclic commutation relationship with $\hat{S}_x$ and $\hat{S}_y$. The Zeeman interaction spin Hamiltonian becomes:

$$\hat{\mathcal{H}}^{static} = -\frac{\gamma B_0}{2}\begin{pmatrix} 1 & 0 \\ 0 & -1 \end{pmatrix} \tag{1.6}$$

When plugged into the time dependent Schrödinger equation, one gets the spin precession at the Larmor frequency term γB_0. This means that the frequency at which a specific spin precesses is

dependent on both the external magnetic field and the gyromagnetic ratio of the spin itself. For a simple NMR experiment, when the sample (essentially a mass of spins) is placed in the coil inside the large magnetic field, an oscillating radio frequency (RF) field B_1 linearly polarized with phase,ϕ, is applied near the Larmor frequency (ω_{rf}) along the transverse plane. For convenience, it can be decomposed into two rotating components, one in the same sense as the spin precession and one opposite. It can be shown that the non-resonant component (the one opposite in the direction of the spin precession) has negligible effects. So only the resonant component should be considered:

$$B_1{}^{res}(t) = \frac{1}{2}B_1[cos(\omega_{rf}t + \phi)\vec{e}_x + sin(\omega_{rf}t + \phi)\vec{e}_y] \tag{1.7}$$

, where $\vec{e}_x$ and $\vec{e}_y$ are unitary vectors in the x and y directions in the laboratory frame, respectively. The effect of this transverse RF field on the spin Hamiltonian can be approximated:

$$\hat{\mathcal{H}}^{RF}(t) \approx -\frac{1}{2}\gamma B_1[cos(\omega_{rf}t + \phi)\hat{S}_x + sin(\omega_{rf}t + \phi)\hat{S}_y] \tag{1.8}$$

This Hamiltonian, became explicitly time independent when expressed in the rotating frame if the spins are in resonance, *i.e.,* $\omega_{rf} = \gamma B_0$.

$$\hat{\mathcal{H}}_r^{RF}(t) = -\frac{1}{2}\gamma B_1[cos(\phi)\hat{S}_x + sin(\phi)\hat{S}_y] \tag{1.9}$$

Effectively, this Hamiltonian is a rotation about the x-axis in the rotating frame. The polarization generated by the Zeeman Hamiltonian is "tipped" into the transverse plane by the application of this RF field. This can then be detected by the current induced in the coil. The combination of the Zeeman Hamiltonian and the RF Hamiltonian constitute the external part of the spin Hamiltonian.

Internal spin Hamiltonians

Influences of the electric and magnetic fields originating from the sample itself constitute the internal spin Hamiltonian. They are important properties of the sample as they encode geometric, distance and dynamic information. In terms of structural biology, the structure and functional dynamics of proteins can be inferred from these parameters. The internal Hamiltonians include the

following terms:

$$\hat{\mathcal{H}}^{internal} = \hat{\mathcal{H}}^{CS,iso} + \hat{\mathcal{H}}^{CSA} + \hat{\mathcal{H}}^{DD} + \hat{\mathcal{H}}^{J} + \hat{\mathcal{H}}^{quadrupole} \tag{1.10}$$

The quadrupole coupling Hamiltonian $\hat{\mathcal{H}}^{quadrupole}$ only concerns larger than spin 1/2 nuclei and will not be discussed here. The J-coupling term $\hat{\mathcal{H}}^{J}$ comes from the direct chemical bond between atoms, including hydrogen bonds. Though very important for solution NMR, in biological solid-state NMR, they are usually too weak to be resolved because of the broad spectral lines. However, with the emergence of ultra-fast high resolution MAS NMR, J-coupling has been used to study key features of proteins, like the study of hydrogen bonding in the influenza A protein M2 [146].

$\hat{\mathcal{H}}^{CS,iso}$ and $\hat{\mathcal{H}}^{CSA}$ are isotropic and anisotropic chemical shift terms, respectively. Physically, they can be described as a "local magnetic field" $\vec{B}^{induced}$ generated by the electronic environment of the nucleus. Typically, they come from the nearby electron density of the nucleus and therefore are mainly influenced by the type of chemical bonds and the bonded nuclei. This induced field is linearly dependent on the applied magnetic field along the z-axis.

$$\vec{B}^{induced} = \boldsymbol{\delta} \cdot \vec{B}_0 \tag{1.11}$$

, where $\boldsymbol{\delta}$ is a 3x3 matrix and is called the chemical shift tensor. And since $\vec{B}_0$ only has the z component, the chemical shift tensor can be reduced to:

$$\vec{B}^{induced} = \begin{pmatrix} \delta_{xz} B_0 \\ \delta_{yz} B_0 \\ \delta_{zz} B_0 \end{pmatrix} \tag{1.12}$$

And under the secular approximation, the chemical shift Hamiltonian is simplified to:

$$\hat{\mathcal{H}}^{CS} = -\hat{\mu} \cdot \vec{B}^{induced} \approx -\gamma \delta_{zz} B_0 \hat{S}_z \tag{1.13}$$

The size of the δ_{zz} is dependent on the orientation of the molecule with regard to the magnetic field. In an isotropic liquid, the δ^{iso} is the average over all possible configurations, and is called the isotropic chemical shift. It is convenient to combine the isotropic chemical shift Hamiltonian with the Zeeman interaction Hamiltonian:

$$\hat{\mathcal{H}}^0 = \hat{\mathcal{H}}^{CS,iso} + \hat{\mathcal{H}}^{static} = -\gamma(1+\delta^{iso})B_0\hat{S}_z \tag{1.14}$$

This term will determine the isotropic peak position in an NMR spectrum for a molecule and its prefactor ,$-\gamma(1+\delta^{iso})B_0$, is called the chemically shifted Larmor frequency. The major influences of its value and dynamic range are the type of nuclei, the electronegativity of the directly bonded chemical group, and other nearby molecular units in space. For proteins, the isotropic chemical shifts of the C_α and C_β atoms are identifying parameters for residue typing during assignment. In solids, where there is no intrinsic motional averaging, the chemical shift is dependent on the relative orientation of the molecule with the external field. This orientation dependent chemical shift Hamiltonian is called the chemical shift anisotropy (CSA) $\hat{\mathcal{H}}^{CSA}$. Without MAS, a solid sample containing a random ensemble of orientations will give the so called powder spectrum, a very broad pattern with some sharp corners. With sufficient MAS frequency, one gets back the isotropic spectrum as spinning about the magic angle averages the chemical shift anisotropy. Note that the chemical shift anisotropy in Hz scale also increases with the external magnetic field.

The dipolar coupling Hamiltonian is maybe the most important interaction in biological solid-state NMR due to its direct dependence on the distance between two spins. The direct dipole-dipole coupling between two spins i and j originates from the interaction of the magnetic fields generated by the spins themselves. It will depend on the relative orientation between the two spins and their internuclear distance. Expressed in angular frequency unit, it is :

$$\hat{\mathcal{H}}^{DD} = -\frac{\mu_0}{4\pi}\frac{\gamma_i\gamma_j\hbar}{r_{ij}^3}[3(\hat{S}_i\cdot\vec{e_{ij}})(\hat{S}_j\cdot\vec{e_{ij}}) - \hat{S}_i\cdot\hat{S}_j] \tag{1.15}$$

, where $\vec{e_{ij}}$ is a unit vector parallel to the line joining the center of the two nuclei (the internuclear vector), and μ_0 the magnetic constant. In spherical coordinates using raising ($\hat{S_+}$) and lowering

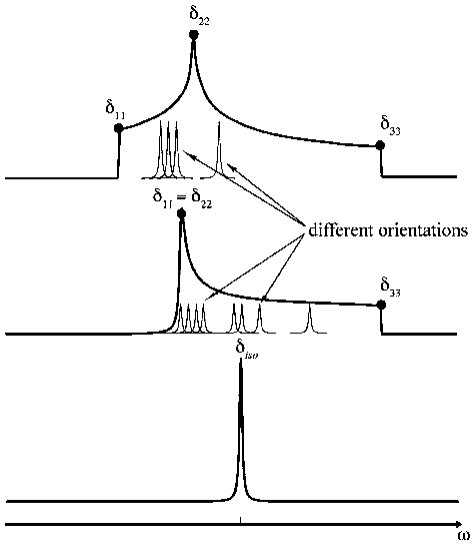

Figure 1.4: Powder pattern of CSA which consists of a very broad spectrum with sharp corners. The broadening is caused by the different chemical shifts with different molecular orientations. Different chemical shift tensors give different powder pattern. The powder patterns of a rhombic (upper) and an axially symmetric (middle) CSA tensor are shown. The most probable orientation in the powder arises from the situation when the principal axis is perpendicular to the magnetic field. Under sufficient coherent averaging by MAS, this inhomogeneous interaction is eliminated, leaving a sharp peak at the isotropic chemical shift, which is the numerical average of the three tensor components (lower) described in equation 1.12 [31].

($\hat{S_-}$) operators, the dipolar coupling Hamiltonian is:

$$\hat{\mathcal{H}}^{DD} = -\frac{\mu_0}{4\pi}\frac{\gamma_i\gamma_j\hbar}{r_{ij}^3}(A+B+C+D+E+F) \tag{1.16}$$

where,

$$\begin{aligned}
A &= \hat{S_z^i}\hat{S_z^j}(3cos^2\theta - 1) \\
B &= -\frac{1}{4}[\hat{S_+^i}\hat{S_-^j} + \hat{S_-^i}\hat{S_+^j}](3cos^2\theta - 1) \\
C &= \frac{3}{2}[\hat{S_z^i}\hat{S_+^j} + \hat{S_+^i}\hat{S_z^j}]sin\theta cos\theta e^{-i\phi} \\
D &= \frac{3}{2}[\hat{S_z^i}\hat{S_-^j} + \hat{S_-^i}\hat{S_z^j}]sin\theta cos\theta e^{+i\phi} \\
E &= \frac{3}{4}[\hat{S_+^i}\hat{S_+^j}]sin^2\theta e^{-2i\phi} \\
F &= \frac{3}{4}[\hat{S_-^i}\hat{S_-^j}]sin^2\theta e^{+2i\phi}
\end{aligned}$$

, and the raising ($\hat{S_+}$) and the lowering ($\hat{S_-}$) operators satisfy the relations:

$$\hat{S_\pm} = \hat{S_x} \pm i\hat{S_y} \tag{1.17}$$

The spherical coordinates here are defined such that θ is the tilt angle from the z-axis (the direction of the B_0 field) and ϕ as the tilt angle at the transverse plane. In the case of homonuclear dipolar coupling, where spin i and spin j are the same nuclei type, after zero order (or high field) approximation, we get:

$$\hat{\mathcal{H}}^{DD}_{homo} = -\frac{\mu_0}{4\pi}\frac{\gamma_i\gamma_j\hbar}{r_{ij}^3}(3cos^2\theta - 1)[\hat{S_z^i}\hat{S_z^j} - \frac{1}{2}(\hat{S_x^i}\hat{S_x^j} + \hat{S_y^i}\hat{S_y^j})] \tag{1.18}$$

The first part of the spin operator terms (the ones inside the square bracket) acts as the J-coupling and leads to peak splitting in an NMR spectrum. The second part, however, splits previously degenerate Zeeman levels, and leads to peak splitting in a similar way as in the strong coupling regime, where the coupling constant is not much smaller than the chemical shift separation. This

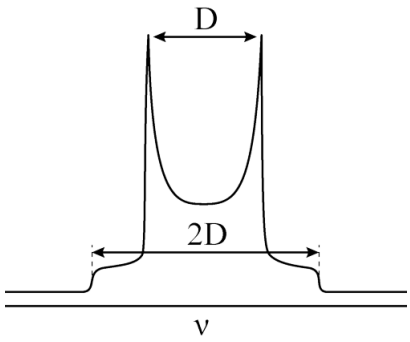

Figure 1.5: A typical Pake pattern in solid-state NMR [65]. It has the characteristic double corners as the two possible transitions are of the opposite sign, which comes from the dipolar coupling that behaves as two axially symmetric CSA tensors that are mirror images of themselves at the isotropic chemical shift. The separation of the two corners is the strength of the interaction. And just like the CSA powder pattern, the most probable orientation (the sharp corner) corresponds to the situation when the principal axis of the interactions are perpendicular to the magnetic field.

is not the case for heteronuclear dipolar coupling, where the situation is simpler:

$$\hat{\mathcal{H}}^{DD}_{hetero} = -\frac{\mu_0}{4\pi}\frac{\gamma_i\gamma_j\hbar}{r^3_{ij}}(3cos^2\theta - 1)\hat{S}^i_z\hat{S}^j_z \tag{1.19}$$

The effect of heteronuclear dipolar coupling on the NMR spectrum is only splitting of Zeeman energies, so much like the J-coupling, it splits the spectrum, but one transition will be the mirror image of the other with respect to the isotropic chemical shift. And adding the spatial dependencies of the dipolar coupling, one would get something like two mirror image powder spectra (Figure.1.4) added together, this is called a Pake pattern (Figure.1.5). It is worth noting that the quadrupole transitions in nuclei like deuterium results in similar patterns. Just like the chemical shift Hamiltonian, the spatial dependence of the dipolar coupling can be averaged out with spinning the sample sufficiently quickly at an tilt angle from the B_0 field θ_R, if it satisfies the relation:

$$3cos^2\theta_R - 1 = 0 \tag{1.20}$$

and one gets $\theta_R \approx 54.74^\circ$, which is the magic angle.

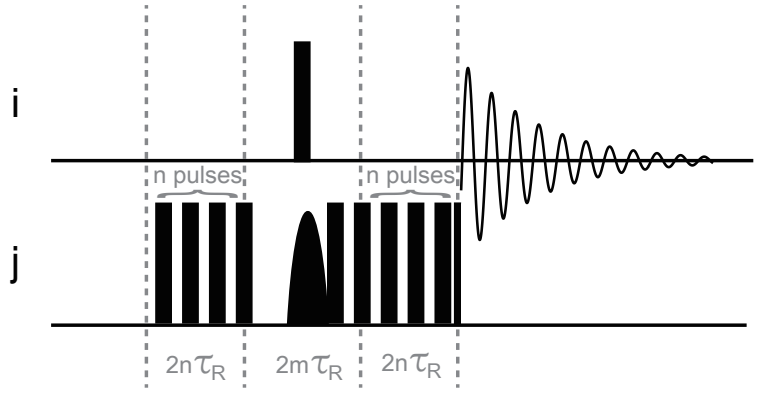

Figure 1.6: The REDOR pulse sequence for dipolar recoupling under MAS. Two blocks of π-pulse (filled rectangle) trains applied exactly every half rotor cycle on the j spin is used to recouple the coherently averaged dipolar coupling Hamiltonian under MAS. In between, π-pulses are applied on the both spins to refocus the isotropic chemical shift. In this version shown, a soft π-pulse (filled hyperbola) followed by a hard pulse is applied on the j spin to selectively refocus the j spins with isotropic chemical shift of interest.

1.6 Heteronuclear dipolar recoupling

Due to the importance of measuring dipolar coupling in structure characterization in an NMR sample, it is of interest to recouple the averaged dipolar coupling Hamiltonian during MAS. Recoupling of heteronuclear dipole interactions in MAS NMR is a well-established method to measure distances [151, 150]. Due to a favorable scaling factor and relatively low RF power requirement, one of the earlier recoupling sequences, rotational echo double resonance (REDOR) [80, 183] remains widely applied to both materials and biological samples. Since the spin part of the recoupled Hamiltonian is identical to the J-coupling Hamiltonian, a transferred sequence analogous to the solution HSQC sequence was developed soon after, and is referred to as transferred-echo double resonance (TEDOR) [92]. Here we will look at the recoupling block of the REDOR sequence, where a spin I, dipole coupled to another nuclei S, is getting dephased.

The recoupling block is such that there is an π pulse applied exactly every half rotor period. Another π pulse is applied in the middle of the recoupling block on the spin to refocus the dephased chemical shift. In addition, the sequence shown here has a selective π pulse on the i spin, followed by a hard π pulse, this serves the additional function of selecting only those spins that fall in a

certain chemical shift range. The effect of spinning the sample at the magic angle can be better understood after a frame transformation from the laboratory frame (B_0 field as the z-axis) into the rotor frame (axis of spinning as the z-axis), in which the heteronuclear dipolar Hamiltonian is written as:

$$\hat{\mathcal{H}}^{DD}_{hetero}(t) = -\frac{\mu_0}{2\pi}\frac{\gamma_i\gamma_j\hbar}{r^3_{ij}}(-\frac{1}{\sqrt{2}}sin2\beta cos(\omega_R t+\gamma)+\frac{1}{2}sin^2\beta cos(2\omega_R t+2\gamma))\hat{S}^i_z\hat{S}^j_z \tag{1.21}$$

In the rotor frame, the angle γ is the initial orientation of the internuclear vector with in the rotor transverse plane, β is the angle between the MAS axis and the internuclear vector and ω_R is the spinning speed. As this Hamiltonian has characteristic frequency of ω_R and $2\omega_R$, the spatial part (the terms in brackets from equation1.21) changes sign every half rotor cycle. And integration over one rotor cycle can be shown to result in a zero Hamiltonian. During the REDOR recoupling, the two π-pulses within a rotor period manipulate the spin part of the dipolar Hamiltonian $\hat{S}^i_z\hat{S}^j_z$, changing its signs every half rotor period. This results in a non-zero Hamiltonian at the end, effectively recoupling the dipolar coupling Hamiltonian. A quantitative analysis can be shown using the average Hamiltonian theory (AHT). Such analysis is applicable when several conditions are satisfied by the pulse sequence: i) the total duration for which the sequence is applied τ_c is a multiple of the rotor period τ_R ii) The net rotation produced by each block of RF pulses is zero iii) τ_c is short enough, so that the internal Hamiltonians do not produce a large enough effect to change the state of the system. All are exactly true for REDOR. Importantly for AHT analysis, the Hamiltonian needs to be transformed into the interaction frame, where the RF pulses do not appear directly but rather as the time dependence of the Hamiltonian. This allows a direct observation of the effect of the pulses by integration of the toggling frame Hamiltonian over time. For REDOR, the toggling frame Hamiltonian (the effective Hamiltonian) integrated over one rotor period is:

$$\overline{\hat{\mathcal{H}}^{eff}_{REDOR}} = -\frac{\mu_0}{4\pi^2}\frac{\gamma_i\gamma_j\hbar}{r^3_{ij}}(\sqrt{2}sin2\beta sin\gamma)2\hat{S}^i_z\hat{S}^j_z \tag{1.22}$$

which is non-zero and results in the loss of magnetization on i spin due to the incomplete refocusing of the dipolar coupling. The amount of dephased i magnetization corresponds to the transverse magnetization that does not lie on the original axis after rotor period. This can be calculated as the phase angle Φ acquired over one rotor period. For a certain crystalline orientation described by

Euler angles (β, γ), this phase angle is:

$$\Phi(\beta, \gamma, \tau_R) = \pm \frac{\mu_0}{4\pi^2} \frac{\gamma_i \gamma_j \hbar}{r_{ij}^3} \frac{2\sqrt{2}}{\omega_R} sin2\beta sin\gamma \tag{1.23}$$

The phase angle acquired after N rotor periods is then simply $N\Phi$. This term is dependent on $\frac{1}{r_{ij}^3}$, thus the dephasing rate is an accurate reporter of the internuclear distance and used frequently in structure calculation. In a powder sample, the dephased i spin magnetization I_f is found by summing over all possible crystalline orientation. A good approximation based on the expansion of Bessel functions was derived previously [147] to describe the powder averaged dipolar recoupling signal under MAS, and will be discussed more in details in Chapter 5. It is important to note that the equation 1.23 does not take into account the effect of relaxation, while during the actual REDOR experiment, there is significant longitudinal relaxation. Therefore, a separate reference experiment recording the non-dephased magnetization with relaxation is required. The final REDOR parameter is the ratio of the dephased magnetization and reference magnetization. When there is multiple dephasing spins j, the related experiment TEDOR [92] is needed to extract the distance information in each individual dipolar coupled spin pair, by recording the chemical shift of not only the dephased i spin but also the dephasing j spins. The detailed analysis of the two experiments, along with an improved, more time saving pulse sequence for measuring dipolar coupling TREDOR [231] will be discussed in Chapter 5.

1.7 Chemical shift anisotropy recoupling in the CODEX experiment

Just like dipolar recoupling, RF pulses applied at the correct internals of the rotor period can also recouple the CSA Hamiltonian averaged out by MAS. The one to be introduced in this section is used as CSA encoding in the centerband-only detection of exchange (CODEX) experiment [97]. It is made in the spirit of REDOR, in that the dephasing of the magnetization resulted from the recoupled CSA Hamiltonian is measured. Similarly, a π-pulse train is applied every half a rotor period (Figure 1.7). At the end of the block (after the pulse train is applied for a duration of N rotor

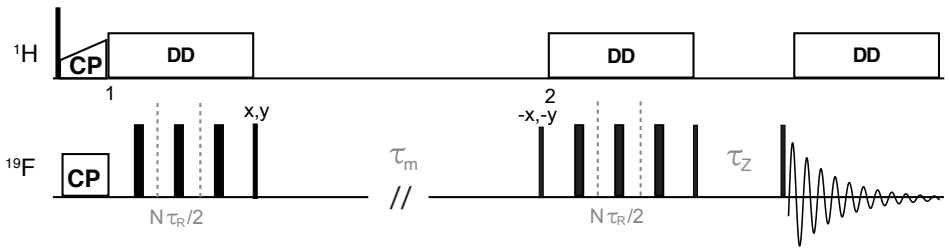

Figure 1.7: The CODEX pulse sequence for determination of oligomeric state and internuclear distance. The sequence is shown specifically for ^{19}F CODEX following a ^{1}H to ^{19}F cross polarization (CP). Decoupling on the proton channel is applied throughout both the CSA recoupling blocks and the acquisition. π-pulse trains spaced by exactly half a rotor period is applied on the ^{19}F channel for CSA encoding (1) and decoding (2). Spin diffusion based exchanged is allowed to happen during the long rotor synchronized mixing period τ_m. The two $\pi/2$ pulses before an after the mixing period has opposite phases so that an incomplete CSA refocusing will lead to loss of the magnetization. To ensure there is no dephasing caused by incomplete rotor cycle, both first and second parts are triggered from the same phase in MAS rotation.

periods), the phase angle acquired is

$$\Phi = N \int_0^{t_R/2} \omega(t) dt \tag{1.24}$$

with $\omega(t)$ being the dephasing frequency that depends on the strength of the CSA. For CODEX specifically, two such CSA recoupling blocks [61, 52, 97] (1 and 2 in Figure 1.7) are applied before and after a rotor synchronized long mixing time τ_m. The $\pi/2$ pulse sandwiching the τ_m has a 180 degree phase inversion. If exchange between those spins with different segmental reorientation could happen (mainly by spin diffusion), meaning that the dephasing frequencies are different between the two CSA recoupling blocks, the magnetization at the end of the pulse sequence cannot be completely refocused and leads to a net loss. The strength of the dephasing will depend on the dipolar coupling (which will affect the spin diffusion rate) during the mixing period. Effectively, this means it is possible to determine distance between spins with even the same isotropic chemical shift, making it useful in measuring inter-oligomer distance. The implication and application of this will be discussed in Chapter 4. Also similar to the analysis of REDOR, a reference spectrum is required to eliminate the effect of the longitudinal relaxation during the mixing period and the dephasing is measured as a ratio S/S_0 between the leftover magnetization S and the reference magnetization S_0.

1.8 Thesis outline

Chapter 2 of this thesis will demonstrate the application of ^{1}H-detected NMR methods in the CitA PASpc construct in both the citrate bound and citrate free state, along with functionally important structural changes upon citrate binding observed in the TM2 helix and its accompanying linker regions. Chapter 3 will introduce the ^{31}P activity assay applied to the soluble PASc-kin constructs to gain insights of the PASc dimer rearrangements on the kinase activity, and the same assay applied to a N308C mutant full length CitA with two different chemical tags for preparation of site-specific distance measurements. Chapter 4 will introduce the application of site-specific inter-dimer distance measurement using ^{19}F CODEX and provide direct structural evidence for the dimer rearrangement mechanism of PASc upon citrate binding using the PASpc construct. A structural and dynamics model based on these changes observed by us in the context of CitA transmembrane signal transduction mechanism will be discussed together in Chapter6. Chapter 5 will present a new method to measure the dipolar coupling strength with MAS solid-state NMR, TREDOR.

CHAPTER 2

Sequence Specific Resonance Assignment of CitA Reveals a Loosening of a KK Linker with a Piston-like Pulling Motion

2.1 Introduction

Sequence specific assignment is the first step in the investigation of proteins with NMR. Previously[186], isolated domains available in solution from CitA (namely the PASp and PASc) have been assigned. The analysis of the chemical shifts, which are sensitive to the dihedral angles of the peptide bonds, shows that the C-terminus of PASp switches from random coil to alpha helical conformation [178] upon citrate binding. This helix is called the periplasmic helix (P-helix) [25]. It is a consensus structural feature in the stimulus transmission of HKs, and its formation is compatible with a piston motion proposed for CitA activation. This process, derived for GT CitA from the structural data of the isolated PASp domain (crystal structure and solution state NMR) and the membrane bound PASpc construct (^{13}C-detected MAS NMR), is illustrated in Figure 2.1: as the citrate binds to the PASp domain, the β-strand scaffold "hugs" the citrate molecule and thus leads to a contraction of the C-terminus of PASp. This piston motion is also confirmed in CitA's homologous protein DcuS [145] by cysteine accessibility assay, in which the TM2 helix experiences a rigid body upward motion upon activation by fumarate binding. In addition to revealing functionally relevant structural changes in the PASp domain, the resonances of the isolated domains (both PASp and PASc) have been used solely for the chemical shift assignment of the ^{13}C detected MAS NMR spectra of the PASpc (CitA without the DHp domain)

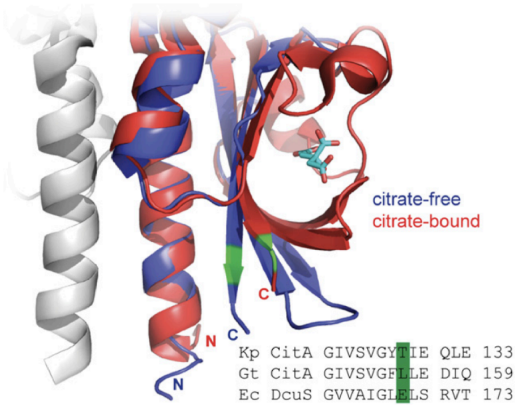

Figure 2.1: P-helix formation at the C-terminus of PASp with citrate binding, confirmed by secondary chemical shift analysis from ^{13}C-detected MAS NMR of the membrane bound PASpc construct, the secondary chemical shift analysis from solution NMR of the isolated PASp domain, and the crystal structure of the PASp domain in both the citrate bound and the citrate free state [178].

construct in liposomes. However, the drawback of "borrowing" the assignments of isolated domains is obvious: whatever is not available in the isolated domains, including the TM helices, cannot be assigned even if it is visible in the solid-state experiments. More importantly, the parts of CitA that interact with lipids might not have the same chemical shifts in the isolated constructs versus the PASpc construct, making us blind to the mechanistic insights only available from the PASpc construct. This includes the structural and dynamic features in the TM helices and their accompanying linker regions, even when these linkers can bear important functions according to mutational analysis and structural studies of PASc in the kinase BvgS [55]. In the crystal structure of the PASc domain monomer from BvgS, the overall arrangement of the N-terminal helix and the β-scaffold is similar to that observed in the WT PASc domain in CitA (Figure 3.1 B), indicating the similarity between the PASc domain of BvgS and CitA. Moreover, relevant structural changes involving the PASc domain cannot be predicted directly using the isolated PASc construct, as it does not bear an "on" or "off" state by itself. Sequence specific assignment, through which chemical shift information can be acquired *ab initio*, becomes the prerequisite to studying the transmembrane signaling of CitA in its entirety.

Assignment of protein backbone resonances using NMR is done by a series of experiments with well defined transfers in relation to the primary sequence [10]. Specifically, assignment

strategies using ^{1}H detected MAS NMR have been developed based on the already available experiments in solution NMR [179], which employ magnetization transfers between atoms that are related in a predictable manner according to the primary sequence. The available assignment experiments available have been summarized in various literature [18, 161, 10, 91]. In MAS NMR, short dipolar coupling based transfer, typically cross polarization (CP) transfer, between hetero-nuclei is preferred instead of J-coupling based transfer due to the short T_2 time with moderate MAS speed. For homo-nuclear transfers at the MAS frequency of 60 kHz or above, at which the carbon T_2 becomes long enough, J-based transfers [18] are more straightforward as the RF power for carbon-carbon dipolar recoupling becomes demanding. With knowledge of the characteristic chemical shifts of Cα and Cβ of different amino acid and the connectivity pattern of the individual experiment, one could perform a "walk" along the sequence and place stretches of residues in the correct positions in the sequence. This is usually the most time consuming but also an indispensable step in getting atomic resolution information. The recent development in fast MAS probes (up to 100 kHz) and high magnetic field (up to 1.2 GHz) have increased the sensitivity and resolution of the spectra to make the assignment process less sample and time demanding. The increase in magnetic field (from 950 MHz to 1.2 GHz) has been shown to significantly improve the spectral quality of fully protonated CitA PASpc [153] (Figure2.2). At moderate spinning (about 60 kHz), the dilution of the proton network with sample deuteration can significantly narrow the proton linewidth by reducing the proton coupling network [232, 167]. The backbone resonance assignment presented in this chapter will be solely based on experiments with perdeuterated CitA PASpc samples at 55 kHz MAS.

Despite the technical advances, assignment of the 310 residue CitA PASpc monomer is still challenging. Though there is no theoretical size limit in using MAS NMR, the difficulty of resonance assignment increases with the size of the protein due to increased spectral complexity. In the case of CitA's TM helices, the situation is made worse as α-helix and coils have smaller chemical shift dispersion [230], resulting in more severe spectral overlap for individual peaks to be separated. To tackle these issues, both the sequence and the topology of CitA PASpc construct are exploited. In addition to conventional sets of assignment experiments, we measure 3D correlation experiments that link sequential amide nitrogens [11], whose chemical shift dispersion is large even in coils.

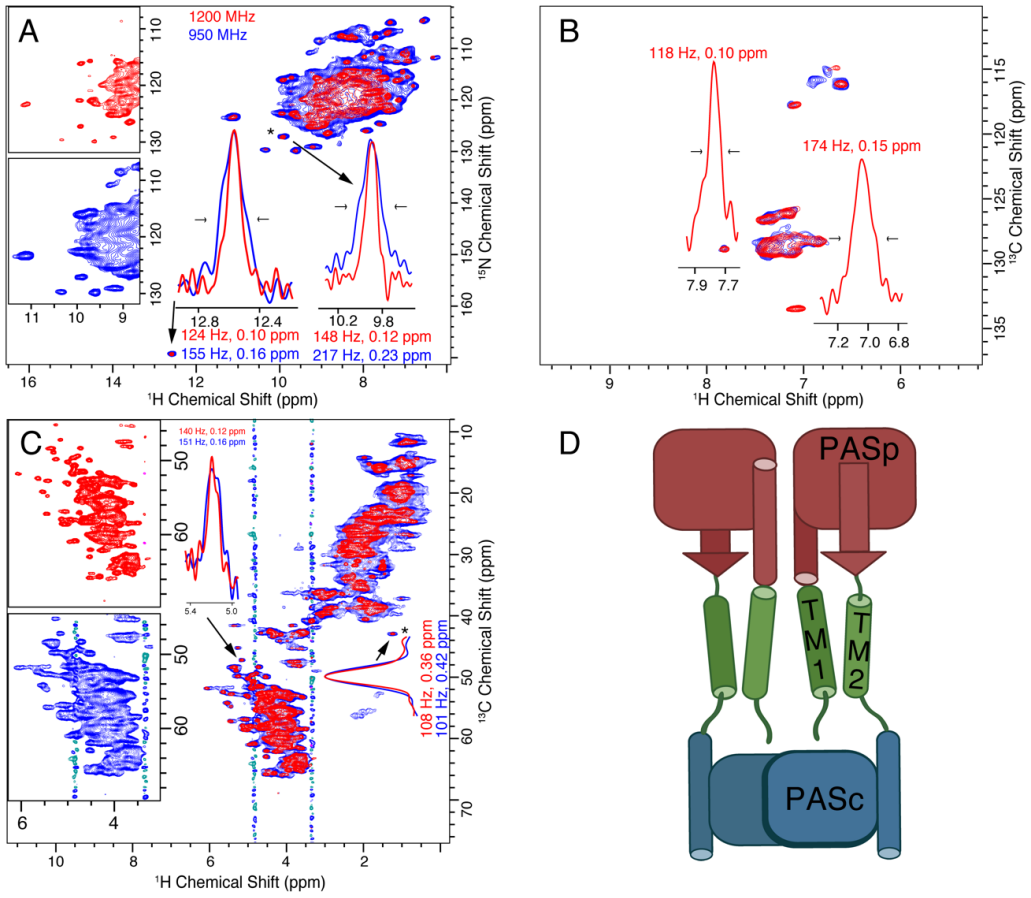

Figure 2.2: Resolution and sensitivity of CitA PASpc (H)NH and (H)CH spectra are improved using the 1200 MHz instrument (red) as compared with the 950 MHz (blue). The resulting improvement in peak separation is evident in both the (H)NH (A) and (H)CH (B, C) spectra. The expansion of the alpha region is shown side-by-side. This is especially obvious in the glycine region of the (H)NH spectra below 110 ppm. 1D proton traces (inset in A-C) reveal the resolution improvement of various isolated peaks. The aromatic carbon region of the (H)CH spectrum (B) has a sensitivity at the 950 MHz magnet, that was too low for reliable linewidth measurement. The insets show the linewidths of selected peaks that are resolved in the 2D spectrum. The peak indicated with a (*) was used to set the base contour level to a consistent fraction of the peak intensity for each set of overlaid spectra. The topology of the protein is shown in (D) with the sensor PASp domain in red, the TM helices (TM1 and TM2) shown in green, and the PASc domain shown in blue. The T_1 noise at about 3.3 and 4.7 ppm are from choline and water protons, respectively [153].

For amino acid typing, instead of relying solely on the characteristic carbon chemical shifts, we can reverse lable the amino acids isoleucine (I), value (V), phenylalanine (F) and leucine (L) (IVFL reversed labeled PASpc). To distinguish chemical shifts from the transmembrane regions (*i.e* TM helices) versus those from water contacting domains (PASp, PASc and water-contacting regions), solvent magnetization transfer experiments can be performed [149]. This combinatorial strategy is used to enable assignment of both the citrate bound and the citrate free state. From the chemical shifts functionally relevant conformational changes accompanying citrate binding can be tracked.

2.2 Materials and methods

2.2.1 Protein sample preparation

For producing approximately 100% deuterated, ^{15}N, ^{13}C-labeled C12A/R93A CitA PASpc, the plasmid coding for C12A/R93A CitA PASpc (Figure 2.6) was transformed into the strain C43 (DE3) (Imaxio, France). The R93A mutant was previously used in the isolated PASp domain to investigate its structure in both the citrate bound and citrate free form [178]. Without the R93A mutation, the PASp domain in GT CitA binds the citrate molecule too tightly for a citrate free state to be produced. A single colony was transferred into a 2 ml minimal medium shaking culture and step-wise adapted to 100 % D_2O, followed by expression in minimal medium with 100 % D_2O, ^{15}N-NH_4Cl as nitrogen source and $^{13}C_6$-D-glucose as carbon source. For additional reverse labeling with isoleucine, valine, phenylalanine and leucine, 150 mg/L D_10-L-isoleucine, 100 mg/L D_8-L-valine, 50 mg/L D_8-L-phenylalanine and 150 mg/L D_10-L-leucine (CORTECNET) were added to the expression culture shortly before induction. After purification with the established protocol [178] for C12A/R93A CitA PASpc and reconstitution into 1,2-dimyristoyl-sn-glycero-3-phosphocholine (DMPC) and 1,2-dimyristoyl-sn-glycero-3-phosphatic acid (DMPA) liposomes (with DMPC to DMPA molar ratio of 9:1) at a lipid:protein ratio of 75:1 (mol/mol), the liposomes were taken up in 20 mM sodium phosphate, pH 6.5, 5 mM sodium citrate. The samples were packed in a Bruker 1.3 mm rotor by ultracentrifugation.

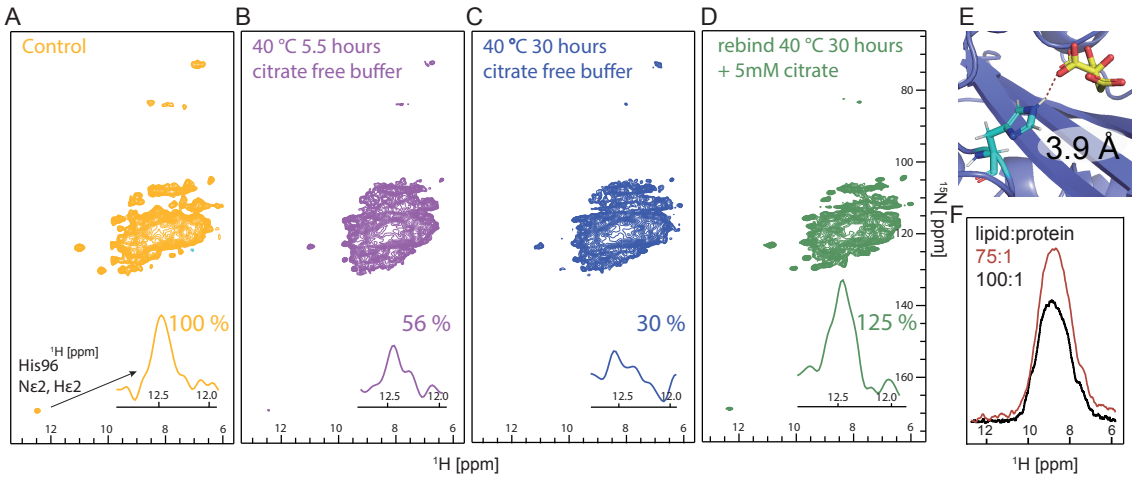

Figure 2.3: Citrate unbinds from the CitA PASpc through incubation in citrate free buffer tracked by intensity of H96 side chain, which hydrogen bonds with citrate at the bound state (E). The loss of this hydrogen bond causes H96 side chain to become unstructured and thus too dynamic to be detected by CP based (H)NH experiment. The intensity drops to 30 % after 30 hours of incubation (B to C). The protein remains functional, as adding citrate to the buffer immediately restores the spectra to the bound state (D). This unbinding protocol is necessary for the residue specific assignment in the citrate free state, as it (F, red) increases the sensitivity by 30 % compared with the original protocol (F, black), using which the signals become too weak for residue-specific assignment.

The citrate free sample is made by simply incubating the citrate bound CitA PASpc sample with the citrate free buffer (20 mM sodium phosphate pH 6.5) at 40 °C for a week. This process is monitored by tracking the intensity of the H96 side chain with 2D (H)NH spectra.

2.2.2 NMR spectroscopy

The NMR settings including CP powers, hard pulse powers, sweep width, inter-scan delays *etc.* of the assignment experiments acquired are summarized in Table 2.1 (triple labeled, perdeuterated PASpc sample in the citrate free state), Table 2.2 (triple labeled, perdeuterated PASpc sample in the citrate bound state), Table 2.3 (IVFL reverse labeled, perdeuterated PASpc sample in the citrate free state) and Table 2.4 (IVFL reverse labeled, perdeuterated PASpc sample in the citrate bound state). The powers for soft pulses are taken at the maximum value. All experiments at the field of 850 MHz were measured with a Bruker 1.3 mm H/C/D/N four channel probe. The experiment (H)N(CA)(CO)NH in the bound fully labeled CitA PASpc was acquired at the field of 800 MHz with a Bruker 1.3 mm H/X/Y three channel probe. The sample temperature was set to 293 K adjusted with the chemical shift of water, using a cooling gas flow of 1350 L/h. Chemical shifts of ^{13}C are referenced relative to sodium trimethylsilylpropanesulfonate (DSS).

Table 2.1: NMR experiment parameters used in sequence specific assignments in the free state CitA PASpc sample.

Spectrum	**(H)NH**	**(H)CANH**	**(H)(CO)CA(CO)NH**	**(H)CONH**	**(H)CO(CA)NH**
Scans per point	8	24	96	8	96
Experimental time / h	0.9	112	205.3	17.2	206.4
Signal/noise	85.99	28.22	10.29	20.85	15.06
Field	850	850	850	850	850
Spinning frequency/Hz	55000	55000	55000	55000	55000
interscan delay /s	1	1	1	1	1
Sweep width (t1) / ppm	160 (N)	32 (N)	40 (N)	40 (N)	40 (N)
Max indirect evolution (t1) / ms	14.5 (N)	21.8 (N)	10.1 (N)	12.5 (N)	12.5 (N)
Sweep width (t2) / ppm	40.3 (H)	32 (C)	30 (C)	18.0 (C)	18.0 (C)
Max indirect evolution (t2) / ms	30.0 (H)	10.2 (C)	8.6 (C)	11.7 (C)	11.7 (C)
Sweep width (t3) / ppm	N/A	58.8 (H)	40.3 (H)	40.3 (H)	40.3 (H)
Max indirect evolution (t3) / ms	N/A	20.5 (H)	30.0 (H)	30.0 (H)	30.0 (H)
Transfer I	**HN (dipolar)**	**HCA (dipolar)**	**HCO (dipolar)**	**HCO (dipolar)**	**HCO (dipolar)**
^{1}H field / kHz	99.4	95.1	96.3	100	100
X field / kHz	38.1	40.4	40.1	40.1	40.1
Shape	100 - 80 % ramp (H)	85 - 100 % ramp (H)	85 - 100 % ramp (H)	85 - 100 % ramp (H)	85 - 100 % ramp (H)
Carrier ^{13}C	N/A	53.7	173.3	173.8	173.8
Time / ms	1.15	6	3.5	3.5	3.5
Transfer II	**HN (dipolar)**	**CAN (dipolar)**	**COCA (scalar)**	**CON (dipolar)**	**COCA (scalar, SCT)**
^{1}H field / kHz	95.5	N/A	N/A	N/A	N/A
^{13}C field / kHz	N/A	35.5	N/A	27.4	N/A
^{15}N field / kHz	38.1	29.2	N/A	31.6	N/A

Spectrum	(H)NH	(H)CANH	(H)(CO)CA(CO)NH	(H)CONH	(H)CO(CA)NH
Carrier ^{13}C	N/A	N/A	173.3 and 53.3	173.8	173.8 and 53.3
Shape	100 - 80 % ramp (H)	Tan_ampmod_63_94.land (N)		Tan_ampmod_63_94.land (N)	
Time / ms	0.85	11	13.2	9	6.6 (1st step) 4.6 (2nd step)
Transfer III		**NH (dipolar)**	**CON (dipolar)**	**NH (dipolar)**	**CAN (dipolar)**
^{1}H field / kHz	N/A	98.1	N/A	98.1	N/A
^{13}C field / kHz	N/A	N/A	27.4	N/A	27.4
^{15}N field / kHz	N/A	38.6	30.3	38.1	30.3
Carrier ^{13}C	N/A	N/A	173.3	N/A	53.3
Shape	N/A	100 - 80 % ramp (H)	Tan_ampmod_63_94.land (N)	100 - 80 % ramp (H)	Tan_ampmod_63_94.land (N)
Time / ms	N/A	0.85	9	0.85	9
Transfer IV			**NH (dipolar)**		**NH (dipolar)**
^{1}H field / kHz	N/A	N/A	93.7	N/A	98.1
^{13}C field / kHz	N/A	N/A	N/A	N/A	N/A
^{15}N field / kHz	N/A	N/A	38.1	N/A	38.1
Carrier ^{13}C	N/A	N/A	N/A	N/A	N/A
Shape	N/A	N/A	100 - 80 % ramp (H)	N/A	100 - 80 % ramp (H)
Time / ms	N/A	N/A	0.85	N/A	0.85
interscan delay /s	1	1	1	1	1

Spectrum	(H)(CA)CB(CA)NH	(H)(CA)CB(CA)(CO)NH	(H)N(CA)(CO)NH
Scans per point	12	88	96
Experimental time / h	102	322.7	116
Signal/noise	N/A	N/A	6.91
Field	850	850	850
Spinning frequency/Hz	55000	55000	55000
interscan delay /s	1	1	1
Sweep width (t1) / ppm	32(N)	40(N)	40.0 (N)
Max indirect evolution (t1) / ms	16.3 (N)	9.6 (N)	9.6 (N)
Sweep width (t2) / ppm	90.0 (C)	84 (C)	40.0 (N)

Spectrum	(H)(CA)CB(CA)NH	(H)(CA)CB(CA)(CO)NH	(H)N(CA)(CO)NH
Max indirect evolution (t2) / ms	8.8 (C)	5.6 (C)	9.6 (N)
Sweep width (t3) / ppm	58.8 (H)	40.3 (H)	40.3 (H)
Max indirect evolution (t3) / ms	20.5 (H)	30.0 (H)	30.0 (H)
Transfer I	**HCA (dipolar)**	**HCA (dipolar)**	**HN (dipolar)**
^{1}H field / kHz	95.1	98.1	100
X field / kHz	40.4	40.1	38.7
Shape	85 - 100 % ramp (H)	85 - 100 % ramp (H)	100 - 80 % ramp (H)
Carrier ^{13}C	53.7	53.7	N/A
Time / ms	7	3.5	1.15
Transfer II	**CACBCA(scalar)**	**CACBCA(scalar)**	**NCA (dipolar)**
^{1}H field / kHz	N/A	N/A	N/A
^{13}C field / kHz	N/A	N/A	27.4
^{15}N field / kHz	N/A	N/A	29.4
Carrier ^{13}C	53.7 and 48	53.7 and 48	53.3
Shape	N/A	N/A	Tan_ampmod_63_94.land (N)
Time / ms	12	12	9
Transfer III	**CAN (dipolar)**	**COCA (scalar)**	**CACO (scalar)**
^{1}H field / kHz	N/A	N/A	N/A
^{13}C field / kHz	35.5	N/A	N/A
^{15}N field / kHz	29.2	N/A	N/A
Carrier ^{13}C	53.3	173.3 and 53.3	53.3 and 173.3
Shape	Tan_ampmod_63_94.land (N)		N/A
Time / ms	11	6.6 (1st step) 4.6 (2nd step)	4.6 (1st step) 6.6 (2nd step)
Transfer IV	**NH (dipolar)**	**CON (dipolar)**	**CON (dipolar)**
^{1}H field / kHz	98.1	N/A	N/A
^{13}C field / kHz	N/A	27.4	27.4
^{15}N field / kHz	38.6	28.9	30.1
Carrier ^{13}C	N/A	173.3	173.3

Spectrum	(H)(CA)CB(CA)NH	(H)(CA)CB(CA)(CO)NH	(H)N(CA)(CO)NH
Shape	100 - 80 % ramp (H)	Tan_ampmod_63_94.l and (N)	Tan_ampmod_63_94.land (N)
Time / ms	0.85	9	9
Transfer V		**NH (dipolar)**	**NH (dipolar)**
^{1}H field / kHz	N/A	100	95.1
^{13}C field / kHz	N/A	N/A	N/A
^{15}N field / kHz	N/A	38.1	38.7
Carrier ^{13}C	N/A	N/A	N/A
Shape	N/A	100 - 80 % ramp (H)	100 - 80 % ramp (H)
Time / ms	N/A	0.85	0.85
Spectrum	**(H)N(CO)(CA)NH**	**(H)COCA(N)H**	**H(H)NH**
Scans per point	128	72	8
Experimental time / h	154.9	158.1	22
Signal/noise	7.85	11.9	104.84
Field	850	850	850
Spinning frequency/Hz	55000	55000	55000
interscan delay /s	1	1	1
Sweep width (t1) / ppm	40.0 (N)	18.0 (CO)	50.0 (N)
Max indirect evolution (t1) / ms	9.6 (N)	9.9 (CO)	12.3 (N)
Sweep width (t2) / ppm	40.0 (N)	30 (CA)	15.0 (H)
Max indirect evolution (t2) / ms	9.6 (N)	8.1 (CA)	3.5 (H)
Sweep width (t3) / ppm	40.3 (H)	40.3 (H)	40.3 (H)
Max indirect evolution (t3) / ms	30.0 (H)	30.0 (H)	30.0 (H)
Transfer I	**HN (dipolar)**	**HCO (dipolar)**	**HH (NOE)**
^{1}H field / kHz	100	96.1	N/A
X field / kHz	38.7	40.1	N/A
Shape	100 - 80 % ramp (H)	85 - 100 % ramp (H)	N/A
Carrier ^{13}C	N/A	173.3	N/A
Time / ms	1.15	3.5	100

Spectrum	(H)N(CO)(CA)NH	(H)COCA(N)H	H(H)NH
Transfer II	**NCO(dipolar)**	**COCA (scalar, SCT)**	**HN (dipolar)**
^{1}H field / kHz	N/A	N/A	98.4
^{13}C field / kHz	27.4	N/A	N/A
^{15}N field / kHz	30.1	N/A	40.5
Carrier ^{13}C	173.3	173.3 then 53.3	N/A
Shape	Tan_ampmod_63_94.land (N)		80 - 100 % ramp (H)
Time / ms	9	6.6 (1st step) 4.6 (2nd step)	**1.15**
Transfer III	**COCA (scalar)**	**CAN (dipolar)**	**HN (dipolar)**
^{1}H field / kHz	N/A	N/A	95
^{13}C field / kHz	N/A	27.4	N/A
^{15}N field / kHz	N/A	27.8	40.5
Carrier ^{13}C	173.3 and 53.3	53.3	N/A
Shape	N/A	Tan_ampmod_63_94.land (N)	100 - 80 % ramp (H)
Time / ms	6.6 (1st step) 4.6 (2nd step)	9	0.85
Transfer IV	**CAN (dipolar)**	**NH (dipolar)**	
^{1}H field / kHz	N/A	101.9	N/A
^{13}C field / kHz	27.4	N/A	N/A
^{15}N field / kHz	29.4	38.1	N/A
Carrier ^{13}C	53.3	N/A	N/A
Shape	Tan_ampmod_63_94.land (N)	100 - 80 % ramp (H)	N/A
Time / ms	9	0.85	N/A
Transfer V	**NH (dipolar)**		
^{1}H field / kHz	95.1	N/A	N/A
^{13}C field / kHz	N/A	N/A	N/A
^{15}N field / kHz	38.7	N/A	N/A
Carrier ^{13}C	N/A	N/A	N/A
Shape	100 - 80 % ramp (H)	N/A	N/A
Time / ms	0.85	N/A	N/A

Table 2.2: NMR experiment parameters used in sequence specific assignments in the bound state CitA PASpc sample.

Spectrum	**(H)NH**	**(H)CANH**	**(H)(CO)CA(CO)NH**	**(H)CONH**	**(H)CO(CA)NH**
Scans per point	64	8	56	24	64
Experimental time / h	15.9	57.6	131.4	61.9	144.9
Signal/noise	232	20.64	12.65	22.99	8.57
Field	850	850	850	850	850
Spinning frequency/Hz	55000	55000	55000	55000	55000
interscan delay /s	3.5	2.5	1	1	0.74
Sweep width (t1) / ppm	120.0 (N)	36 (N)	36 (N)	34(N)	34(N)
Max indirect evolution (t1) / ms	24.8 (N)	17.4 (N)	15.5 (N)	18.4 (N)	18.4 (N)
Sweep width (t2) / ppm	40.8 (H)	32 (C)	32 (C)	16.0 (C)	16.0 (C)
Max indirect evolution (t2) / ms	29.5 (H)	7.0 (C)	6.4 (C)	12.6 (C)	12.6 (C)
Sweep width (t3) / ppm	N/A	58.8 (H)	58.8 (H)	58.8 (H)	58.8 (H)
Max indirect evolution (t3) / ms	N/A	20.5 (H)	20.5 (H)	20.5 (H)	20.5 (H)
Transfer I	**HN (dipolar)**	**HCA (dipolar)**	**HCO (dipolar)**	**HCO (dipolar)**	**HCO (dipolar)**
^{1}H field / kHz	96.4	94.35	93.1	91.8	94.1
X field / kHz	70.7	40	40	39.8	40.1
Shape	85 - 100 % ramp (H)	85 - 100 % ramp (H)	85 - 100 % ramp (H)	85 - 100 % ramp (H)	85 - 100 % ramp (H)
Carrier ^{13}C		53.7	173.3	173.8	173.8
Time / ms	1.2	4	5	4	4.2
Transfer II	**HN (dipolar)**	**CAN (dipolar)**	**COCA (scalar)**	**CON (dipolar)**	**COCA (scalar)**
^{1}H field / kHz	96.4	N/A	N/A	N/A	N/A
^{13}C field / kHz	N/A	34.35	N/A	34.4	N/A
^{15}N field / kHz	70.7	30.61	N/A	31.5	N/A
Carrier ^{13}C	N/A	53.7	173.3 and 53.3	173.8	173.8 and 53.3

Spectrum	(H)NH	(H)CANH	(H)(CO)CA(CO)NH	(H)CONH	(H)CO(CA)NH
Shape	80 - 100 % ramp (H)	Tan_ampmod_63_94.land (N)	N/A	Tan_ampmod_63_94.land (N)	N/A
Time / ms	1.2	13	15	13	7.46
Transfer III		**NH (dipolar)**	**CON (dipolar)**	**NH (dipolar)**	**CAN (dipolar)**
^{1}H field / kHz	N/A	96.45	N/A	95.1	N/A
^{13}C field / kHz	N/A	N/A	34.6	N/A	34.9
^{15}N field / kHz	N/A	39.41	32	38.7	30.1
Carrier ^{13}C	N/A	N/A	173.3	N/A	53.3
Shape	N/A	100 - 80 % ramp (H)	Tan_ampmod_63_94.land (N)	100 - 80 % ramp (H)	Tan_ampmod_63_94.land (N)
Time / ms	N/A	1.2	11.5	0.85	13
Transfer IV			**NH (dipolar)**		**NH (dipolar)**
^{1}H field / kHz	N/A	N/A	96.45	N/A	99.2
^{13}C field / kHz	N/A	N/A	N/A	N/A	N/A
^{15}N field / kHz	N/A	N/A	39.41	N/A	38.7
Carrier ^{13}C	N/A	N/A	N/A	N/A	N/A
Shape	N/A	N/A	100 - 80 % ramp (H)	N/A	100 - 80 % ramp (H)
Time / ms	N/A	N/A	1.15	N/A	0.7

Spectrum	(H)(CA)CB(CA)NH	(H)(CA)CB(CA)(CO)NH	(H)N(CA)(CO)NH
Scans per point	48	48	88
Experimental time / h	296.3	269.3	262.9
Signal/noise	N/A	N/A	14.81
Field	850	850	800
Spinning frequency/Hz	55000	55000	55000
interscan delay /s	1	1	1
Sweep width (t1) / ppm	34(N)	34(N)	36.0 (N)
Max indirect evolution (t1) / ms	18.4 (N)	17.4 (N)	16.5 (N)
Sweep width (t2) / ppm	70.0 (C)	70.0 (C)	36.0 (N)
Max indirect evolution (t2) / ms	6.7 (C)	6.6 (C)	16.1 (N)

Spectrum	(H)(CA)CB(CA)NH	(H)(CA)CB(CA)(CO)NH	(H)N(CA)(CO)NH
Sweep width (t3) / ppm	58.8 (H)	58.8 (H)	30.1 (H)
Max indirect evolution (t3) / ms	20.5 (H)	20.5 (H)	21.3 (H)
Transfer I	**HCA (dipolar)**	**HCA (dipolar)**	**HN (dipolar)**
^{1}H field / kHz	94.7	94.4	104.2
X field / kHz	40	38.7	39.1
Shape	85 - 100 % ramp (H)	85 - 100 % ramp (H)	80 - 100 % ramp (H)
Carrier ^{13}C	53.7	53.7	N/A
Time / ms	4	4	1
Transfer II	**CACBCA(scalar)**	**CACBCA(scalar)**	**NCA (dipolar)**
^{1}H field / kHz	N/A	N/A	N/A
^{13}C field / kHz	N/A	N/A	20.9
^{15}N field / kHz	N/A	N/A	43.7
Carrier ^{13}C	53.7 and 48	53.7 and 48	53.3
Shape	N/A	N/A	Tan_ampmod_63_94.land (N)
Time / ms	18.56	18.56	13
Transfer III	**CAN (dipolar)**	**COCA (scalar)**	**CACO (scalar)**
^{1}H field / kHz	N/A	N/A	N/A
^{13}C field / kHz	34.8	N/A	N/A
^{15}N field / kHz	30.6	N/A	N/A
Carrier ^{13}C	53.7	173.3 and 53.3	53.3 and 173.3
Shape	Tan_ampmod_63_94.land (N)		N/A
Time / ms	13	7.2 (1st step) 6.4 (2nd step)	6.4 (1st step) 7.2 (2nd step)
Transfer IV	**NH (dipolar)**	**CON (dipolar)**	**CON (dipolar)**
^{1}H field / kHz	95.4	N/A	N/A
^{13}C field / kHz	N/A	34.4	18.4
^{15}N field / kHz	39.4	30.6	46.5
Carrier ^{13}C	N/A	173.3	173.3
Shape	100 - 80 % ramp (H)	Tan_ampmod_63_94.land (N)	Tan_ampmod_63_94.land (N)

Spectrum	(H)(CA)CB(CA)NH	(H)(CA)CB(CA)(CO)NH	(H)N(CA)(CO)NH
Time / ms	1.15	13	13
Transfer V		**NH (dipolar)**	**NH (dipolar)**
^{1}H field / kHz	N/A	96.4	95.6
^{13}C field / kHz	N/A	N/A	N/A
^{15}N field / kHz	N/A	39.4	39.1
Carrier ^{13}C	N/A	N/A	N/A
Shape	N/A	100 - 80 % ramp (H)	100 - 80 % ramp (H)
Time / ms	N/A	1.15	0.6
Spectrum	**(H)N(CO)(CA)NH**	**(H)COCA(N)H**	**H(H)NH**
Scans per point	144	64	16
Experimental time / h	338.6	159	102.4
Signal/noise	11.19	13.53	66.4
Field	850	850	850
Spinning frequency/Hz	55000	55000	55000
interscan delay /s	1	1	1
Sweep width (t1) / ppm	36.0 (N)	16.0 (CO)	60.0 (N)
Max indirect evolution (t1) / ms	14.8 (N)	12.3 (CO)	24.8 (N)
Sweep width (t2) / ppm	36.0 (N)	32 (CA)	15.0 (H)
Max indirect evolution (t2) / ms	14.8 (N)	7.6 (CA)	3.5 (H)
Sweep width (t3) / ppm	58.8 (H)	58.8 (H)	40.8 (H)
Max indirect evolution (t3) / ms	20.5 (H)	20.5 (H)	29.5 (H)
Transfer I	**HN (dipolar)**	**HCO (dipolar)**	**HH (NOE)**
^{1}H field / kHz	96	91.5	N/A
X field / kHz	38.7	39.8	N/A
Shape	100 - 80 % ramp (H)	85 - 100 % ramp (H)	N/A
Carrier ^{13}C	N/A	173.3	N/A
Time / ms	1.15	4	100
Transfer II	**NCO(dipolar)**	**COCA (scalar, SCT)**	**HN (dipolar)**

Spectrum	(H)N(CO)(CA)NH	(H)COCA(N)H	H(H)NH
^{1}H field / kHz	N/A	N/A	93.6
^{13}C field / kHz	27.1	N/A	N/A
^{15}N field / kHz	37.7	N/A	38.7
Carrier ^{13}C	173.3	173.3 then 53.3	N/A
Shape	Tan_ampmod_63_94.land (N)		100 - 80 % ramp (H)
Time / ms	13	7.2 (1st step) 6.4 (2nd step)	0.7
Transfer III	**COCA (scalar)**	**CAN (dipolar)**	**HN (dipolar)**
^{1}H field / kHz	N/A	N/A	94.2
^{13}C field / kHz	N/A	35	N/A
^{15}N field / kHz	N/A	29.7	38.7
Carrier ^{13}C	173.3 and 53.3	N/A	N/A
Shape	N/A	Tan_ampmod_63_94.land (N)	100 - 80 % ramp (H)
Time / ms	7.2 (1st step) 6.4 (2nd step)	12.5	0.6
Transfer IV	**CAN (dipolar)**	**NH (dipolar)**	
^{1}H field / kHz	N/A	95.1	N/A
^{13}C field / kHz	35.1	N/A	N/A
^{15}N field / kHz	30.1	38.7	N/A
Carrier ^{13}C	53.3	N/A	N/A
Shape	Tan_ampmod_63_94.land (N)	100 - 80 % ramp (H)	N/A
Time / ms	12.5	0.85	N/A
Transfer V	**NH (dipolar)**		
^{1}H field / kHz	95.1	N/A	N/A
^{13}C field / kHz	N/A	N/A	N/A
^{15}N field / kHz	38.7	N/A	N/A
Carrier ^{13}C	N/A	N/A	N/A
Shape	100 - 80 % ramp (H)	N/A	N/A
Time / ms	0.85	N/A	N/A

Table 2.3: NMR experiment parameters used in sequence specific assignments in the free state CitA PASpc sample with IVFL reverse labeling.

Spectrum	(H)NH	(H)CANH	(H)(CO)CA(CO)NH
Scans per point	136	24	32
Experimental time / h	15.1	58.8	117.3
Signal/noise	226.17	21.43	N/A
Field	850	850	850
Spinning frequency/Hz	55000	55000	55000
interscan delay /s	1	1	1
Sweep width (t1) / ppm	160 (N)	40 (N)	40(N)
Max indirect evolution (t1) / ms	14.5 (N)	11.0 (N)	9.6 (N)
Sweep width (t2) / ppm	40.3 (H)	30 (C)	84 (C)
Max indirect evolution (t2) / ms	30.0 (H)	9.0 (C)	5.6 (C)
Sweep width (t3) / ppm	N/A	40.3 (H)	40.3 (H)
Max indirect evolution (t3) / ms	N/A	30.0 (H)	30.0 (H)
Transfer I	**HN (dipolar)**	**HCA (dipolar)**	**HCA (dipolar)**
^{1}H field / kHz	98.2	100.9	103.6
X field / kHz	38.1	40.1	40.1
Shape	100 - 80 % ramp (H)	85 - 100 % ramp (H)	85 - 100 % ramp (H)
Carrier ^{13}C	N/A	53.7	53.7
Time / ms	1.15	3.5	3.5
Transfer II	**HN (dipolar)**	**CAN (dipolar)**	**CACBCA(scalar)**
^{1}H field / kHz	94.5	N/A	N/A
^{13}C field / kHz	N/A	27.4	N/A
^{15}N field / kHz	38.1	26.6	N/A
Carrier ^{13}C	N/A	53.7	53.7 and 48
Shape	100 - 80 % ramp (H)	Tan_ampmod_63_94.land (N)	
Time / ms	0.8	9	6
Transfer III		**NH (dipolar)**	**CAN (dipolar)**
^{1}H field / kHz	N/A	98.1	N/A

Spectrum	(H)NH	(H)CANH	(H)(CO)CA(CO)NH
^{13}C field / kHz	N/A	N/A	27.4
^{15}N field / kHz	N/A	38.1	26.6
Carrier ^{13}C	N/A	N/A	53.3
Shape	N/A	100 - 80 % ramp (H)	Tan_ampmod_63_94.land (N)
Time / ms	N/A	0.85	9
Transfer IV			**NH (dipolar)**
^{1}H field / kHz	N/A	N/A	97.2
^{13}C field / kHz		N/A	N/A
^{15}N field / kHz	N/A	N/A	38.1
Carrier ^{13}C	N/A	N/A	N/A
Shape	N/A	N/A	100 - 80 % ramp (H)
Time / ms	N/A	N/A	0.85

Table 2.4: NMR experiment parameters used in sequence specific assignments in the bound state CitA PASpc sample with IVFL reverse labeling.

Spectrum	(H)NH	(H)CANH	(H)(CO)CA(CO)NH	(H)(CA)CB(CA)NH	(H)(CA)CB(CA)(CO)NH
Scans per point	80	16	64	32	72
Experimental time / h	6.2	85.3	153.5	158.4	337.9
Signal/noise	181.46	21.65	10.86	N/A	N/A
Field	850	850	850	850	850
Spinning frequency/Hz	55000	55000	55000	55000	55000
interscan delay /s	1	2	1	1	1
Sweep width (t1) / ppm	120 (N)	36 (N)	36 (N)	36(N)	34(N)
Max indirect evolution (t1) / ms	13.5 (N)	16.1 (N)	14.5 (N)	14.5 (N)	15.0 (N)
Sweep width (t2) / ppm	40.8 (H)	32 (C)	32 (C)	70.0 (C)	70 (C)
Max indirect evolution (t2) / ms	29.5 (H)	7.0 (C)	7.0 (C)	6.6 (C)	6.4 (C)
Sweep width (t3) / ppm	N/A	58.8 (H)	58.8 (H)	58.8 (H)	58.8 (H)
Max indirect evolution (t3) / ms	N/A	20.5 (H)	20.5 (H)	20.5 (H)	20.5 (H)
Transfer I	**HN (dipolar)**	**HCA (dipolar)**	**HCO (dipolar)**	**HCA (dipolar)**	**HCA (dipolar)**
^{1}H field / kHz	96	92.9	82.6	90.7	87.3
X field / kHz	38.1	41	41	41	37.7
Shape	100 - 80 % ramp (H)	85 - 100 % ramp (H)	85 - 100 % ramp (H)	85 - 100 % ramp (H)	85 - 100 % ramp (H)
Carrier ^{13}C		53.7	173.3	53.7	53.7
Time / ms	1	6	6	5.5	4
Transfer II	**HN (dipolar)**	**CAN (dipolar)**	**COCA (scalar)**	**CACBCA(scalar)**	**CACBCA(scalar)**
^{1}H field / kHz	95.4	N/A	N/A	N/A	N/A
^{13}C field / kHz	N/A	36	N/A	N/A	N/A

Spectrum	(H)NH	(H)CANH	(H)(CO)CA(CO)NH	(H)(CA)CB(CA)NH	(H)(CA)CB(CA)(CO)NH
^{15}N field / kHz	38.1	28.4	N/A	N/A	N/A
Carrier ^{13}C	N/A	53.7	173.3 and 53.3	53.7 and 48	53.7 and 48
Shape	100 - 80 % ramp (H)	Tan_ampmod_63_94.land (N)		N/A	N/A
Time / ms	0.8	11	15.6	18.4	18.4
Transfer III		**NH (dipolar)**	**CON (dipolar)**	**CAN (dipolar)**	**COCA (scalar)**
^{1}H field / kHz	N/A	95.4	N/A	N/A	N/A
^{13}C field / kHz	N/A	N/A	35.4	36	N/A
^{15}N field / kHz	N/A	38.1	31	28.9	N/A
Carrier ^{13}C	N/A	N/A	173.3	53.3	173.3 and 53.3
Shape	N/A	100 - 80 % ramp (H)	Tan_ampmod_63_94.land (N)	Tan_ampmod_63_94.land (N)	
Time / ms	N/A	1.15	11	11	15.6
Transfer IV			**NH (dipolar)**	**NH (dipolar)**	**CON (dipolar)**
^{1}H field / kHz	N/A	N/A	92.2	89.6	N/A
^{13}C field / kHz	N/A	N/A	N/A	N/A	33.5
^{15}N field / kHz	N/A	N/A	38.1	38.1	30.3
Carrier ^{13}C	N/A	N/A	N/A	N/A	173.3
Shape	N/A	N/A	100 - 80 % ramp (H)	100 - 80 % ramp (H)	Tan_ampmod_63_94.land (N)
Time / ms	N/A	N/A	1.15	0.8	13
Transfer V					**NH (dipolar)**
^{1}H field / kHz	N/A	N/A	N/A	N/A	88.7
^{13}C field / kHz	N/A	N/A	N/A	N/A	N/A
^{15}N field / kHz	N/A	N/A	N/A	N/A	38.1
Carrier ^{13}C	N/A	N/A	N/A	N/A	N/A
Shape	N/A	N/A	N/A	N/A	100 - 80 % ramp (H)
Time / ms	N/A	N/A	0.85	N/A	0.85

2.2.3 Automated assignment with FLYA

The peak lists extracted from the assignment experiments except for the lipid transfer H(H)NH spectrum from the deuterated triple labeled CitA PASpc and deuterated IVFL reverse labeled CitA

PASpc samples can be used in automated assignment by FLYA [126], which is an evolution algorithm based program. The addition of peak lists from IVFL reverse labeled spectra did not improve the results of the automated assignment, but aided in confirming the assignments, especially those in the transmembrane regions during the later step of the manual assignment (an example of manual assignment based on Cα, Cβ, and linking amide nitrogen is shown in Figure 2.10).

2.2.4 Secondary chemical shift calculation and torsion angle prediction with TALOS-N

The secondary chemical shift of a particular residue based on Cα and Cβ shifts are calculated with the following equation, after deuterium shift correction [135].

$$\Delta\delta_i = (\delta^i_{C\alpha} - \delta^{coil}_{C\alpha}) - (\delta^i_{C\beta} - \delta^{coil}_{C\beta}), \tag{2.1}$$

where δ is the chemical shift. The random coil chemical shifts were taken from literature [188]. The chemical shifts from the sequence specific assignment can be put into TALOS-N [193] for residue specific torsion angle prediction. Only TALOS-N "strong" predictions (Table B.4 and B.3) were included for structural model calculation with CYANA [84].

2.3 Results and Discussion

2.3.1 ^{1}H-detected-experiment based sequence specific assignments increase the completeness of the chemical shift assignment in CitA PASpc

The sensitivity gain, the additional proton dimension and the short experimental time of ^{1}H-detected sequence specific assignment together improve the completeness of the assignment in CitA PASpc. The production of the citrate free sample from the citrate bound sample is crucial to get high enough sensitivity (increase in the sensitivity of the (H)NH spectra by 130 %)(Figure 2.3, F) in the citrate free state to perform residue specific assignment. When citrate dissociates from the PASp domain, the hydrogen bond between H96 and the citrate is broken (Figure 2.3, E), and H96 becomes unstructured, thus losing its visibility in the solid-state spectrum. This allows

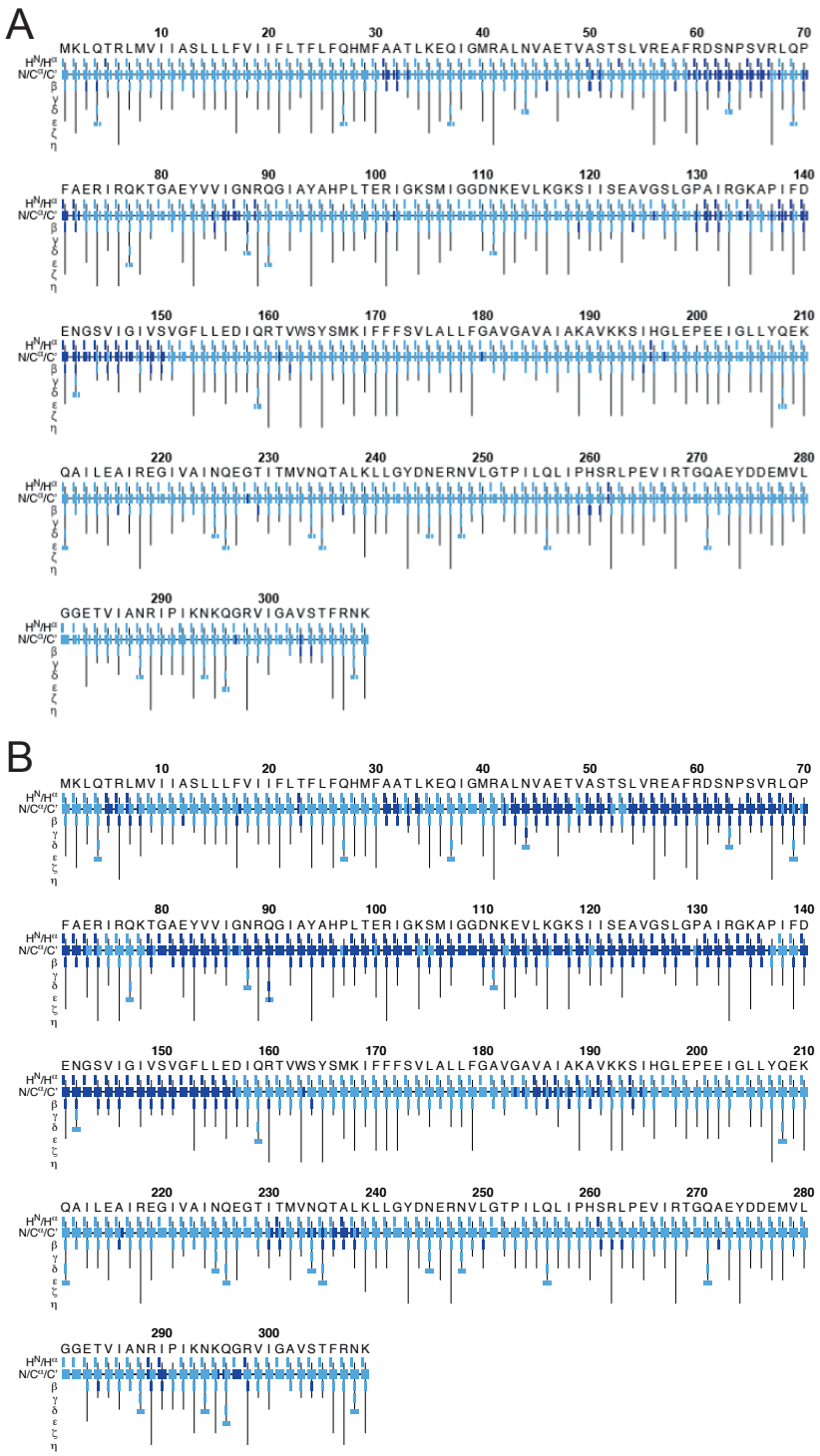

Figure 2.4: Automated assignment using FLYA with ^{1}H-detected experiments based sequence specific assignments in the free (A) and bound (B) state of CitA PASpc. The dark blue shows assignment that is the same in 90% of the runs. FLYA could assign most of PASp in the bound state with certainty but only a small fraction of the residues in the free state.

monitoring of the unbinding process. The intensity of the H96 side chain resonance in the (H)NH spectra decays to 30% after just 30 hours of incubation (Figure 2.3A to C). It should be noted that the protein did not denature during the whole process, as the unbound PASpc can be reversed to the bound state by simply supplementing the buffer with 5 mM sodium citrate (Figure 2.3D). 76% of the residues in the free state and 65% of residues in the bound state can be manually assigned and, this corresponds roughly to 61.1% and 64% of the assignable peaks from all peaks (H)CANH spectra of the citrate free and citrate bound state of the PASpc construct, respectively. Using ^{1}H-detection, the total percentage of assigned resonances increased by 26% in the free state and 14% in the bound state (Table 2.5) compared with ^{13}C-detection. This gain mainly comes from the resonance assignment of the TM helices, which was not available before using assignment transfer from the isolated domains. There is no major difference between the chemical shifts assigned with ^{1}H detection and that with ^{13}C detection. The PASc domain in the citrate bound state, however, has fewer assignments with ^{1}H-detection than ^{13}C-detection. This might be caused by a more rigorous process with ^{1}H-detection versus the simple chemical shift transfer with ^{13}C-detection, as all resonances assigned need to satisfy the magnetization transfer pathway of the assignment experiments. Upon citrate binding, the overall NMR visibility of the PASp domain increased from 78% to 93%, while that of the PASc domain dropped from 80% to 38% (Table 2.5). The same trend was observed with ^{13}C-detection between the citrate free and the citrate bound state (in PASp, the assignment increased from 70% to 86%; in PASc, it decreased from 59 % to 45 %). The visibility of resonances in dipolar coupling transfer based experiments is highly dependent on the dynamics of the protein, because fast regime (in ns scale) and large amplitude motions reduce the magnitude of anisotropic interaction, which is crucial for CP transfer [222]. The direct interpretation of a lower NMR visibility is protein dynamics. So the citrate produces a "see-saw" type of dynamics change in PASp and PASc: it stabilizes the PASp and makes the PASc more flexible.

Citrate binding causes large chemical shift perturbation in the (H)CANH spectrum (Figure 2.5), as it induces large local and global structural differences and changes in the hydrogen bond network [186]. This can be observed in the large chemical shift changes between the two states. The chemical shift perturbation in the isolated PASp domain produced by citrate binding is mainly observed [178] in the β-scaffold of PASp. The major loop of PASp between residue L98 and I120 has in-

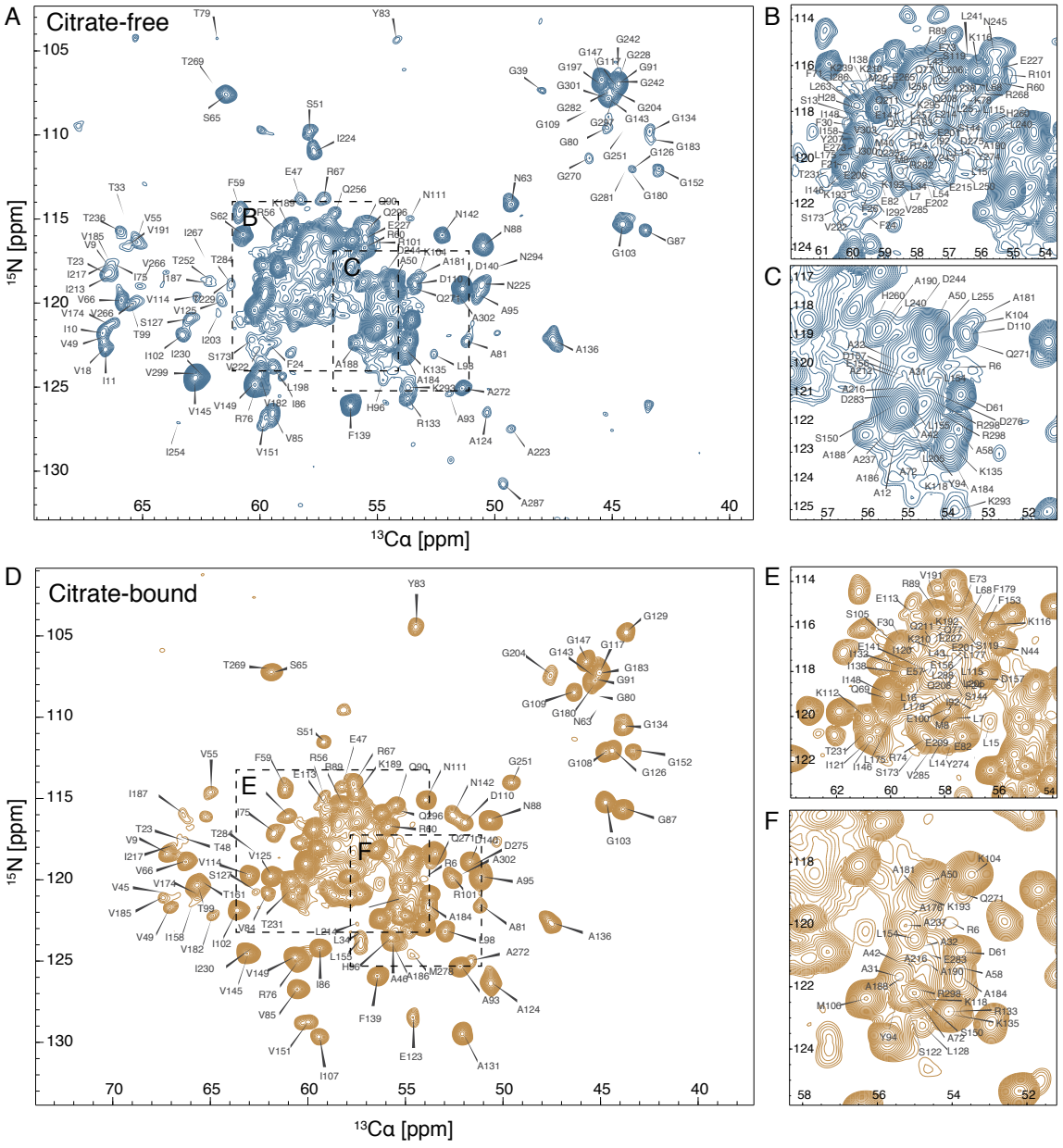

Figure 2.5: N-Cα projection from 3D (H)CANH spectrum of the citrate free (A-C) and citrate bound state (D-E). The assignment is mapped onto the spectra. The citrate bound state has more isolated peaks than the citrate free state. All resonances from the assignment of the two state are included in Table B.1 and Table B.2.

Table 2.5: Fraction of assigned residues in the PASp, TM and PASc domains in the CitA PASpc free and bound state with ^{1}H-detected and ^{13}C-detected MAS NMR experiments. Other than in the PASc domain in the bound state, ^{1}H-detection increases the percentage of assigned residues in both free and bound state compared with ^{13}C-detection.

	Free		Bound	
Domain	^{1}H-detected	^{13}C-detected	^{1}H-detected	^{13}C-detected
PASp (31 - 160)	78%	70%	93%	86%
TM I (1 - 30) & TM II (161 - 199)	65%	0%	55%	0%
PASc (200 - 309)	80%	59%	38%	45%
Total	76%	50%	65%	51%

creased visibility in the citrate bound state, as it forms the cradle for the citrate after binding. The opposite trend is observed in PASc. The NMR visibility of both the major loop between V233 and A272 and the β-scaffold decreased after citrate binding.

2.3.2 Reverse labeling and H(H)NH solvent transfer experiment confirm assignment in the TM helices

The biochemical properties and environment of the TM helices can be used to confirm their resonance assignments. The CitA TM helices have an over-representation of bulky amino acids compared with the cytosolic domains, namely the amino acids isoleucine, valine, phenylalanine and leucine. The range of Cα and Cβ chemical shifts in these residues is similar to that of aspartate and glutamate which are abundant in the PASp and PASc domains. To untangle this ambiguity, we reverse labeled I, V, F, L to confirm the residue typing of the assignment from the TM domains. Instead of relying solely on the combination of signature chemical shift alone, we could use the disappearing signal intensities in the reverse labeled residues during residue typing. This increases the confidence of the assignment, especially in the TM helices. An example is shown in Figure 2.7. All reverse labeled residue types like L175, L177, L178, F179 lose their intensity in the reverse labeled sample. It is worth noting, however, that the reverse labeling of valine is not complete by our protocol, as we observe residual intensities in some valine residues. Surprisingly, reverse label-

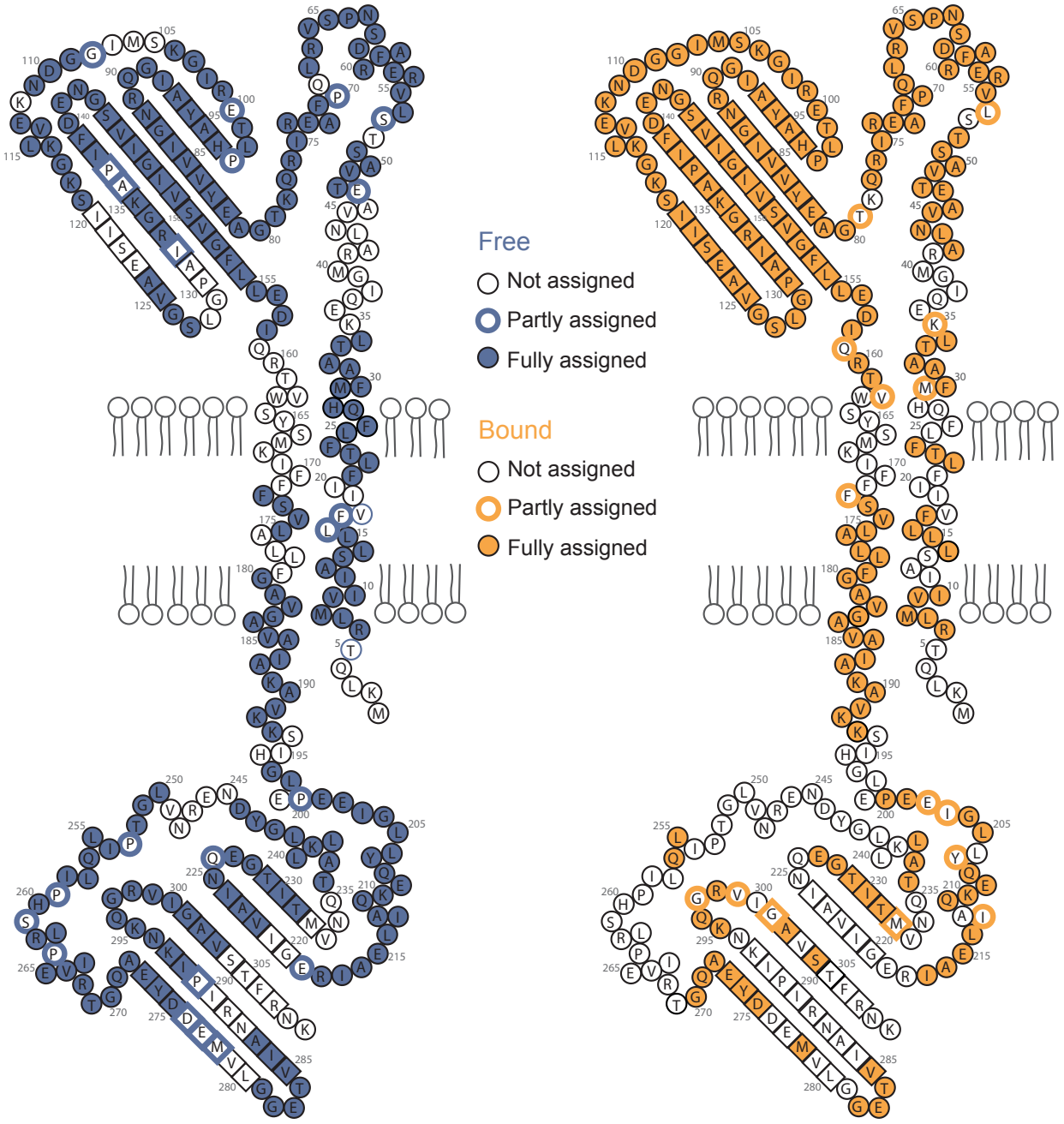

Figure 2.6: Availability of chemical shift assignment using ^{1}H-detection MAS NMR mapped onto the CitA PASpc topology map in both the citrate free (blue) and citrate bound (yellow) states. The unassigned residues are shown in hollow shapes, the partially assigned residues are marked in shapes with colored frames and fully assigned residues in filled shapes. The fully assigned residues have resonance information on the H_N, N, Cα, Cβ and C'.

ing did not contribute significantly to the automated assignment process by FLYA, despite adding exclusive information which is not available in the set of 3D assignment experiments. FLYA might perform poorly in assigning the TM helices because they typically result in weak peaks, indicating dynamics and may have too many missing resonances to be assigned reliably by FLYA. The partially retained valine signal also makes it hard to integrate the information from reverse labeled sample without manual supervision.

The TM region is, by definition, contacting the lipids instead of water in the sample. Since the proton NMR signals from water and from lipids are separated by chemical shift, a "solvent dimension" can be added to distinguish the signals from water contacting (both PAS domains) and those from lipid contacting (transmembrane domains). Such experiment is proposed [149] by adding a proton to proton NOE mixing before the start of the initial CP transfer. The mixing time is chosen to maximize sensitivity in the lipid contacting region. The signals are separated based on their solvent environment as shown in figure 2.8 A and D. The lipid tail contacting region in the free state is more intense and has larger chemical shift dispersion in both the N and H_N dimension (figure 2.8 B and E). A version of the solvent accessibility experiment that additionally acquires the C_α dimension is available as a 4D spectrum, but in CitA PASpc, the sensitivity of such experiments is too low to be used, even using non-uniform sampling (NUS). There are additional resonances in the lipid contacting planes in both the free and bound state. They most likely belong to those unassigned residues in the TM helices. On the other hand, not all assigned residues in the TM helices show lipid contact. This is expected, as the linker regions (or at least part of it) are not predicted to be embedded in the lipid bilayer [202].

In the linker regions between the PASp and TM2 helix, a cysteine accessibility assay showed that the binding of citrate causes a long range, piston-like shift in the membrane embedded portion of TM2 in *E. coli* DcuS [145]. A similar trend is seen by NMR at the C-terminus of TM2: A184 and V185 show lipid contact in the citrate bound state but not in the citrate free state (Figure 2.9). This supports the upward movement of the TM2 helix into the periplasmic space upon citrate binding. Changes on the N-terminus of the TM1 helix are not as drastic, with L7 being the most upstream lipid contacting residue in both states (Figure 2.9). This indicates that the TM1 likely acts as a

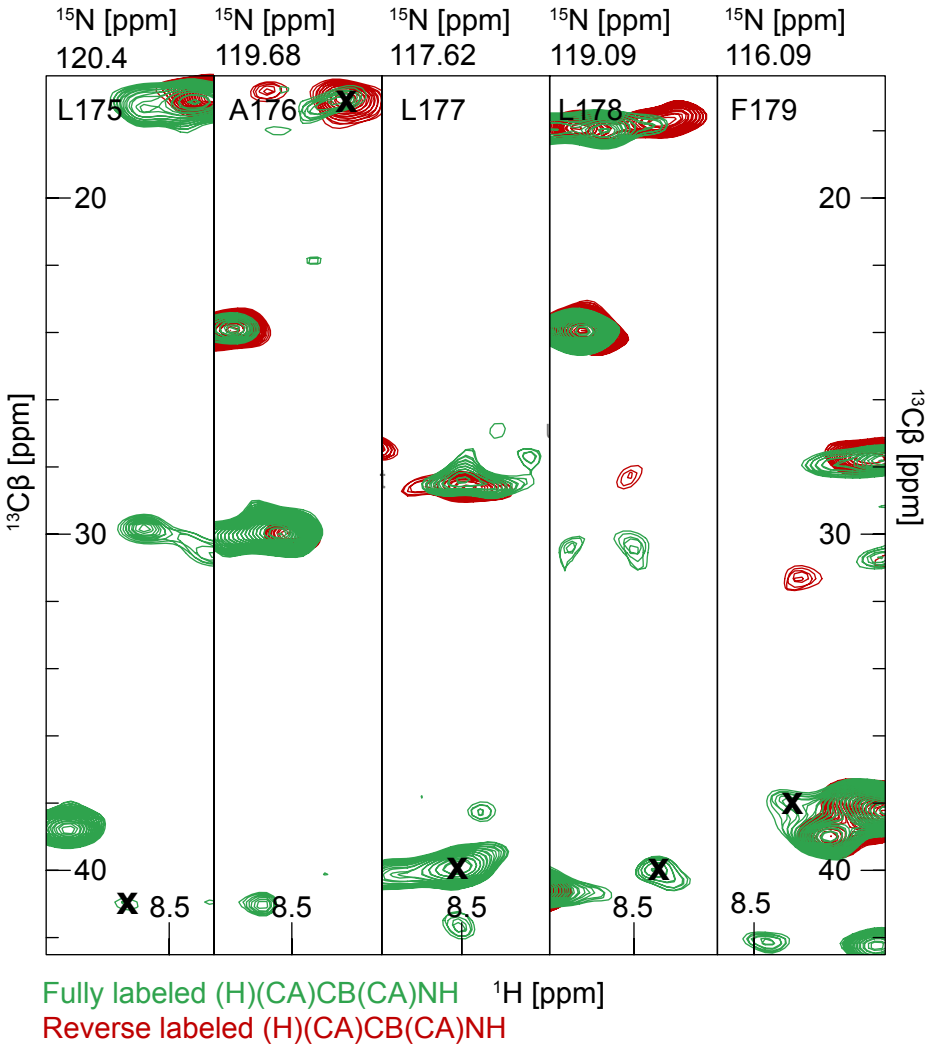

Figure 2.7: IVFL reverse labeled PASpc CitA sample helps with residue typing in the manual assignment process of the TM helices. An example is shown for the comparison of H(CA)CB(CA)NH spectra in both fully labeled (green) and reverse labeled (red) of residue L175 to F179 in the citrate bound state. The visibility along with the characteristic chemical shifts untangles the ambiguity of the assignment as the signal intensity for L175, L177, F179 disappeared, while the non-reverse labeled residue A176 remains the same.

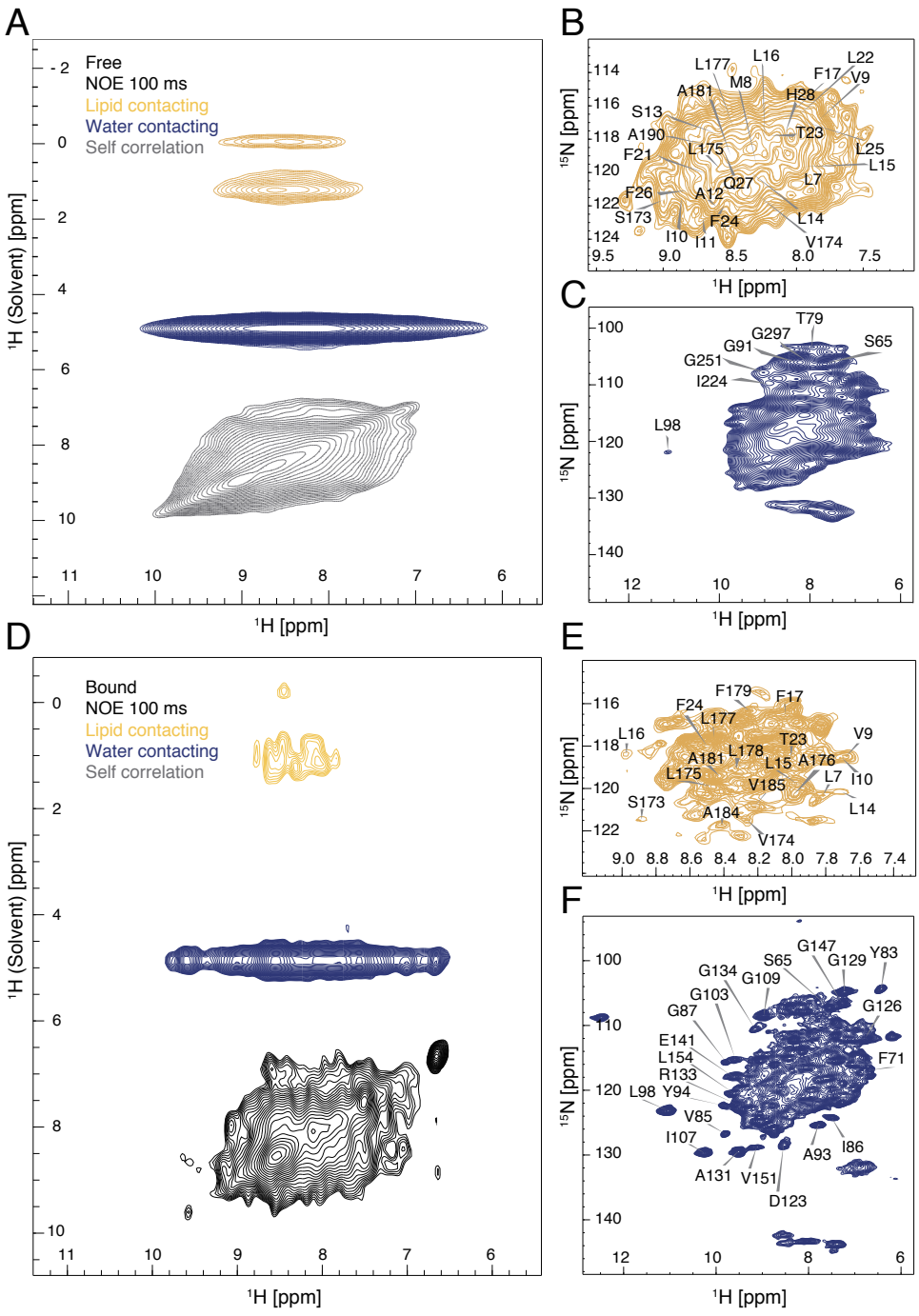

Figure 2.8: (H)HNH lipid contacting spectra of CitA PASpc confirming chemical shift assignment of the TM helices in the citrate free (A, B, C) and citrate bound (D, E, F) state. The additional proton dimension separates the signal from the proton and amide nitrogen dimension into water contacting (blue) and lipid contacting (yellow) parts (A, D). The diagonal self correlation signals are shown in grey. The tail group (0.7 ppm) contacting region in the free state has more intensity than in the bound state. The assigned TM helical resonances can be checked if they are contacting lipid on the H-N planes (B, E). The water (4.7 ppm) contacting regions in both states is the same as the normal (H)NH spectra as isolated peaks mostly come from either PASp or PASc (C, F).

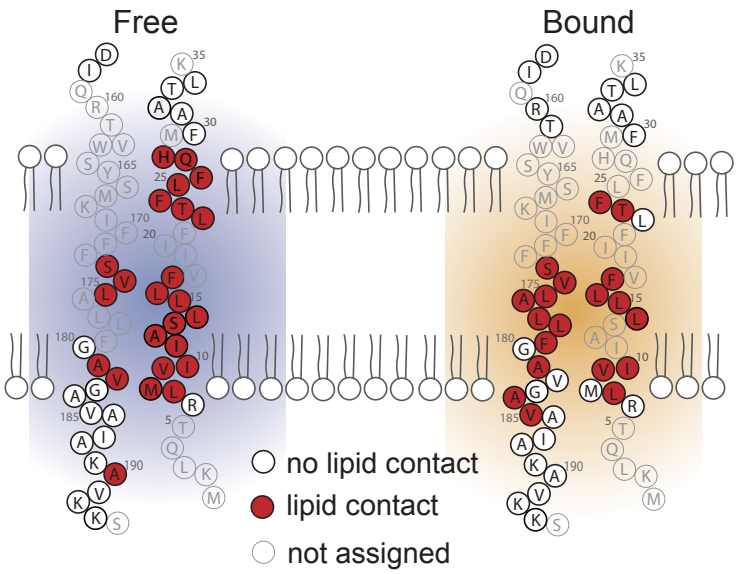

Figure 2.9: Lipid contacting residues in the TM helices mapped onto the CitA topology map in the free (left, blue) and bound (right, yellow) state of CitA. Residues A184 to V185 show lipid contacts in the bound state but not in the free state. Residue A190 loses its lipid contact upon citrate binding. The border of lipid contact in the TM1 helix does not change while the border of lipid contact in the TM2 helix is shifted towards to the cytosol in the TM2 helix.

rigid membrane anchor so that the TM2 can perform rearrangements in its membrane topology. The residue A190 also shows lipid contact even though it is far away from the other membrane contacting residues in the sequence, possibly due to the signal overlap in the H-N dimension with residue S13. As signals separated only by the chemical shifts of H_N and N introduce too much ambiguity in a 309 residue large construct, the lipid contact experiment is used as a rough confirmation for the assignment of the TM region.

2.3.3 Citrate binding induces P-helix formation at PASp C-terminus and 192KK193 motif loosening at the linker between TM2 and PASc

The secondary chemical shift is sensitive to the torsion angles [226] in the peptide bond and is, therefore, a powerful reporter of the local secondary structure. For a short stretch of residues, a structural model can also be predicted based solely on chemical shifts. This has been done for the C-terminus of PASp, where there is an obvious switch from negative (β-strand conformation) to positive (α-helical) secondary chemical shift values upon citrate binding. With the assignment

available for the TM helices, we observed changes in the secondary chemical shift between the free and bound state in the cytosol proximal part of TM2 helix between residue A181 to K193 (Figure 2.10). The same negative to positive secondary chemical shift change upon citrate binding as in the PASp C-terminus is observed from residue F179 to G183, while the opposite trend is seen from residue V191 to K193 (Figure 2.11C). This indicates that the citrate binding in the periplasm causes the TM2 helix upstream of the conserved 192KK193 motif the TM2 to be pulled up in a piston like motion forming a long α-helix. This upward motion loosens the 192KK193 motif and allows the dynamic changes in the cytosolic domain. The torsion angles in the peptide bonds can be predicted using TALOS-N and are used to model the TM2 helix in both the free and bound states (Figure 2.11D). A "see-saw" type of conformational changes are seen on the two sides of the region between F179 to K193: with the helix forming at the N-terminus, the C-terminal 192KK193 motif is loosened into a random coil. The residue A184 and V185 showed lipid contact in the citrate bound state but not in the free state from the lipid contact experiment (Figure 2.9). Both residues also sit at the border of the inner membrane and the cytosol. This change in the solvent environment of this part of TM2 could cause the shift in secondary structure of 180GAVG183 from β-sheet to α-helix upon citrate binding, since both glycine and alanine have a higher tendency to form an α-helix in hydrophobic environment [117].

2.4 Conclusions

^{1}H-detected MAS NMR improved the quality of assignment in the CitA PASpc construct. In combination with I, V, F, L reverse labeled CitA PASpc samples and lipid transfer (H)HNH experiments, sequence specific assignment in the TM helices is available in both the free and bound state. A structural model based on the chemical shift values of the C-terminus of PASp confirmed the P-helix formation upon citrate binding, which was previously proven only with the secondary chemical shift changes of the residue L154 (Figure 2.11). The solvent transfer experiment shows that citrate binding causes a piston-like upward shift of the TM2 helix into the periplasm, moving the residues A184 and V185 into the membrane. Accompanying the changes in solvent environment, this upward motion causes the 180GAVG183 to form a helix while loosening the 192KK193 motif into a random coil. With the *de-novo* sequence specific assignment available using ^{1}H-

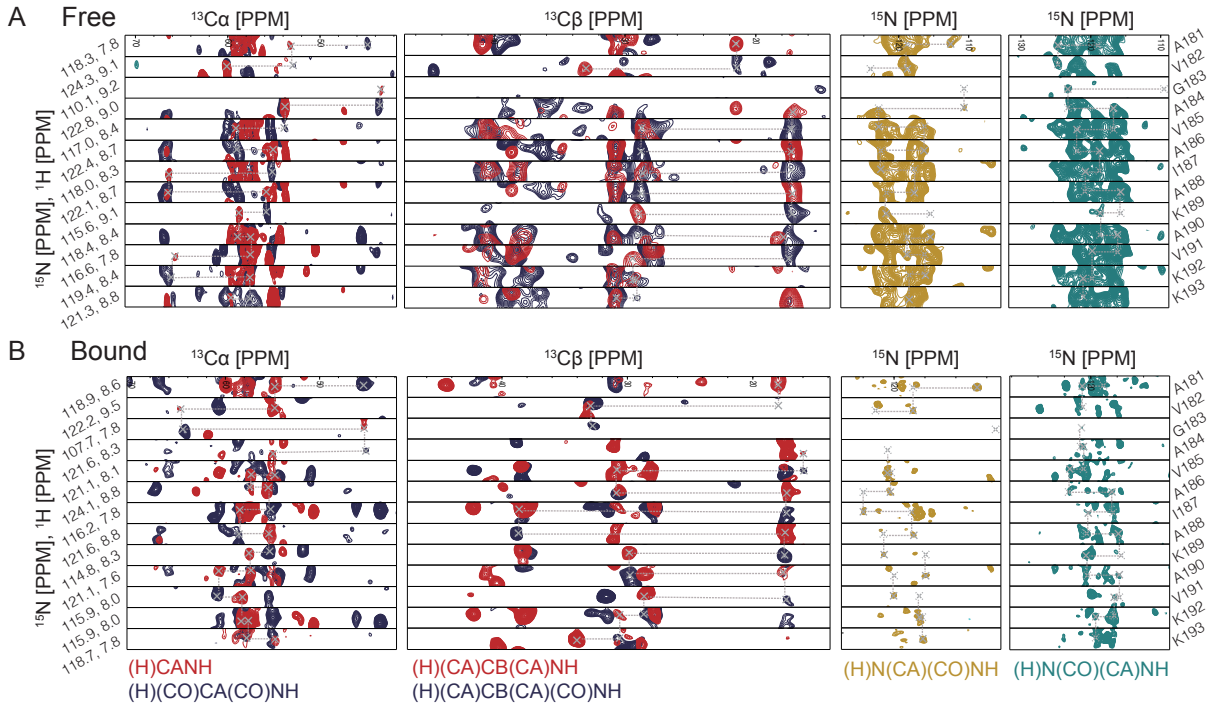

Figure 2.10: Sequence specific assignment of residue A181 to K193 in citrate free(A) and citrate bound(B) state of CitA PASpc. The assignment process using (H)CANH, (H)(CO)CA(C))NH, (H)(CA)CB(CA)NH, (H)(CA)CB(CA)(CO)NH, (H)N(CA)(CO)NH and (H)N(CO)(CA)NH is shown. The same manual assignment process is done throughout CitA PASpc in both states. The Cβ chemical shifts of K192 and K193 in the (H)(CA)CB(CA)NH spectra change to higher values with citrate binding. This indicates that the K192 and K193 residues have higher helix forming propensity in the citrate free state.

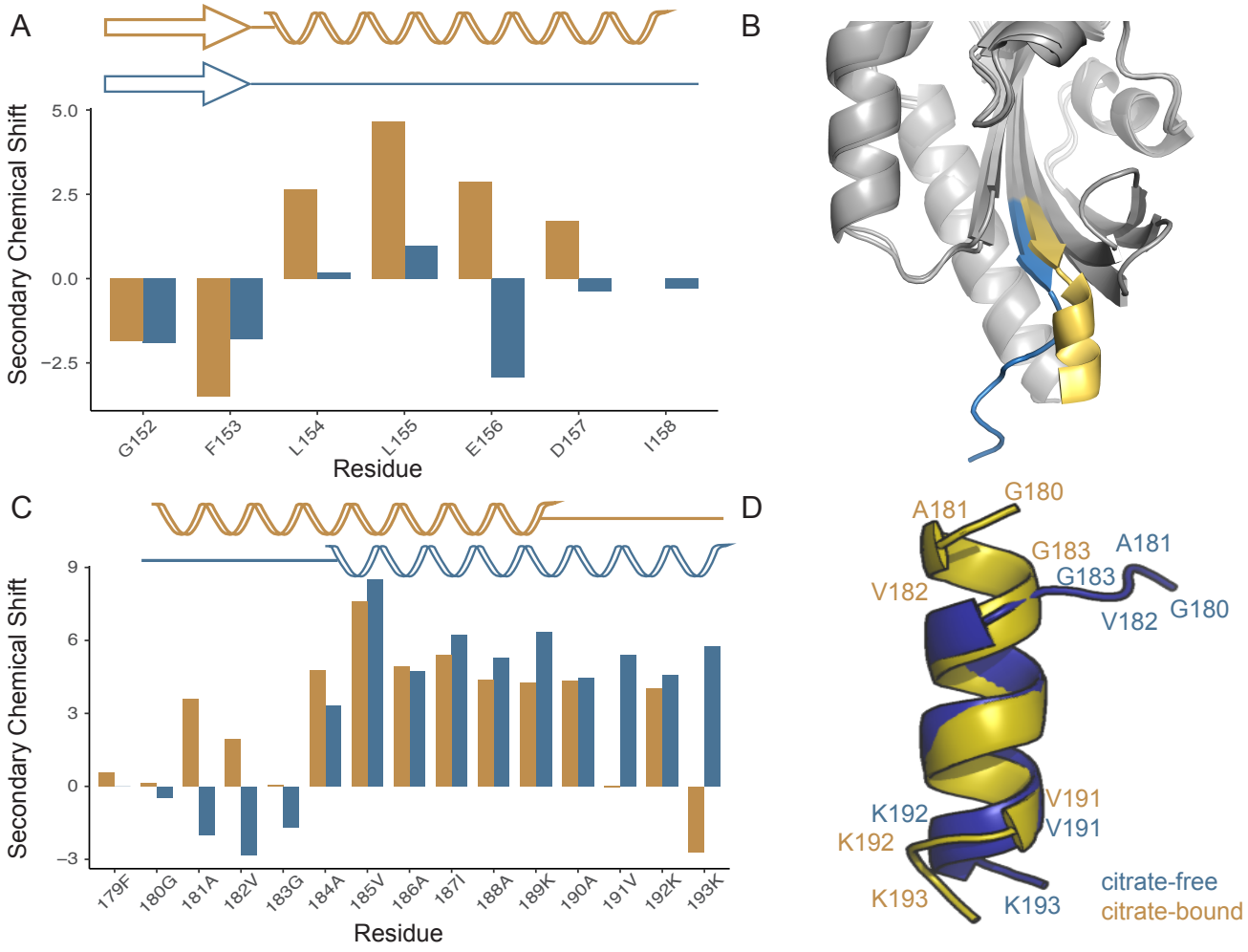

Figure 2.11: Secondary chemical shift changes upon citrate binding in the PASp domain and the TM2 helix. The C-terminus of PASp is pulled up to form the P-helix (orange in B) as indicated by the negative to positive secondary chemical shift changes from residue L154 to I158 (A) after citrate binding. This motion is propagated to the TM2 helix as residue F179 to G183 undergoes the same trend in secondary chemical shift. In contrary, the 192KK193 motif is loosened into a random coil conformation (interchanging negative and positive secondary chemical shift values in residue V191, K192 and K193) after citrate binding (D). This loosening allows elevated dynamics in the downstream PASc domain.

detected MAS NMR, structural changes in the TM helices and their accompanying linker regions with citrate binding could be clarified. The P-helix formation at the end of the PASp domain extending to further residues downstream could be confirmed. The higher mobility in the PASc domain in the citrate bound state observed with both ^{1}H-detected and ^{13}C-detected experiments can be explained with the structural model calculated from the chemical shift of the linker between the TM2 helix and the PASc domain. The loosened 192KK193 motif in the citrate bound state allows more flexibility for structural rearrangement in the PASc domain. In addition, it provides structural explanation why there is higher mobility in the PASc domain upon citrate binding. However, as CitA is a homo-dimer, the two monomer sub-units do not display chemical shift differences between each other. This hinders the direct structural characterization of the CitA dimer interface using NMR even when the monomer can be assigned to relative completeness. To study the dimer rearrangements in CitA and their effects on the kinase function, we designed a functional assay detecting the ATP hydrolysis rate (Chapter 3) and distance measurement using residue-specific CF_3 tagging (Chapter 4).

CHAPTER 3

Functional analysis of CitA with phosphorous NMR

3.1 Introduction

Defining the functionality is as important as structural characterization in studies of proteins, especially in kinases, whose ATP hydrolysis catalyzing activity is tightly connected to their biological roles. M. Salvi has previously reported a potential PASc domain kinase control mechanism [177], based on chemical exchange saturation transfer (CEST) [214] and solvent paramagnetic relaxation enhancement (sPRE) measurements [236]. In the CEST studies, the N-terminal helix of the PASc domain undergoes conformational exchange in solution. The sPRE profile of the PASc in the citrate bound state resembles the model predicted for the parallel dimer and the profile in the citrate free form resembles that of an anti-parallel mutant that was solved by S. Becker in the department of NMR-based structural biology. Based on this evidence, we explored the hypothesis that the PASc dimer switches from an anti-parallel to parallel dimer arrangement upon activation by citrate binding (Figure3.1). The anti-parallel dimer was originally observed in the crystal structure of the N288D mutant in PASc from *G. thermodenitrificans* CitA (GT CitA). Structurally, the differences between the anti-parallel and parallel dimer are mainly in the PASc N-terminal inter-helix orientations (the anti-parallel dimer's N-terminal helices run in the same direction, while the parallel dimer's N-terminal helices run in opposite directions) and in the C-terminal inter-dimer distances. To confirm both functionally and structurally that the anti-parallel to parallel dimer rearrangement occurs upon citrate binding, an activity assay suitable for CitA needs to be designed. Functionally, if the anti-parallel dimer is the inactive form, attaching the mutant PASc domain that forms this dimer directly onto the kinase should lead to a lower activity. Structurally,

measuring the inter-N308C distance, which is located at the C-terminal end of the PASc domain, is crucial to distinguish the two dimer forms, as the inter-dimer distance in the parallel dimer is significantly shorter than that in the anti-parallel dimer. Available techniques for site-specfic distance measurement will be reviewed in Chapter 4, but it is important to note that a chemical modification on the target residue is required. Previously, the N308C residue has been tagged with the fluorophore Atto647N to prove that the solution dimer form of wild type (WT) PASc has the parallel arrangement by the cryogenic optical localization (COLD) measurement [224]. Since COLD measurement is not successful using liposome samples, another site-specific inter-dimer distance measurement had to be designed. The prerequisite to study a chemically tagged protein is the confirmation of its functionality. For CitA, these modifications must not disrupt its kinase activity nor its responsiveness to citrate binding. So an elevated ATP hydrolysis rate in the target construct after citrate binding should be observed before structural studies can be undertaken in CitA.

Biochemical methods for tracking the kinase activity typically fall into two categories depending on the readout: direct detection of phosphorylated kinase or indirect measurement of ATP hydrolysis [203]. The scintillation proximity assay (SPA) measures protein phosphorylation by the incorporation of ^{33}P-labeled ATP into a kinase substrate [24]. The safety and cost of SPA are of concern to the users, and alternative nonradioactive methods are desired. Fluorescent or luminescent kinase assays have been designed using phosphopeptide binding reagents such as antibodies [156, 171, 69, 175], but they have varied binding specificity. Samples with low yield do not have high enough sensitivity for methods with direct readout to be used. The protein samples are also often exhausted after such measurement. Indeed, the SPA assay (provided by M. Stopp in the group of Prof. Unden from the University of Mainz), though indicating a lower kinase activity with the N288D mutant (Figure C.1), did not provide statistically significant results. ATP consumption can also be monitored by the amount of remaining ATP in the solution by generation of light in a Luciferase reaction. But the procedure itself is cumbersome and reports only ATP in a narrow dynamic range (smaller than 15 μM) outside of the useful range of many kinases [106]. This assay does not report ADP or free phosphate production either. In comparison, the detection of ATP in solution with NMR is very straightforward, owing to the

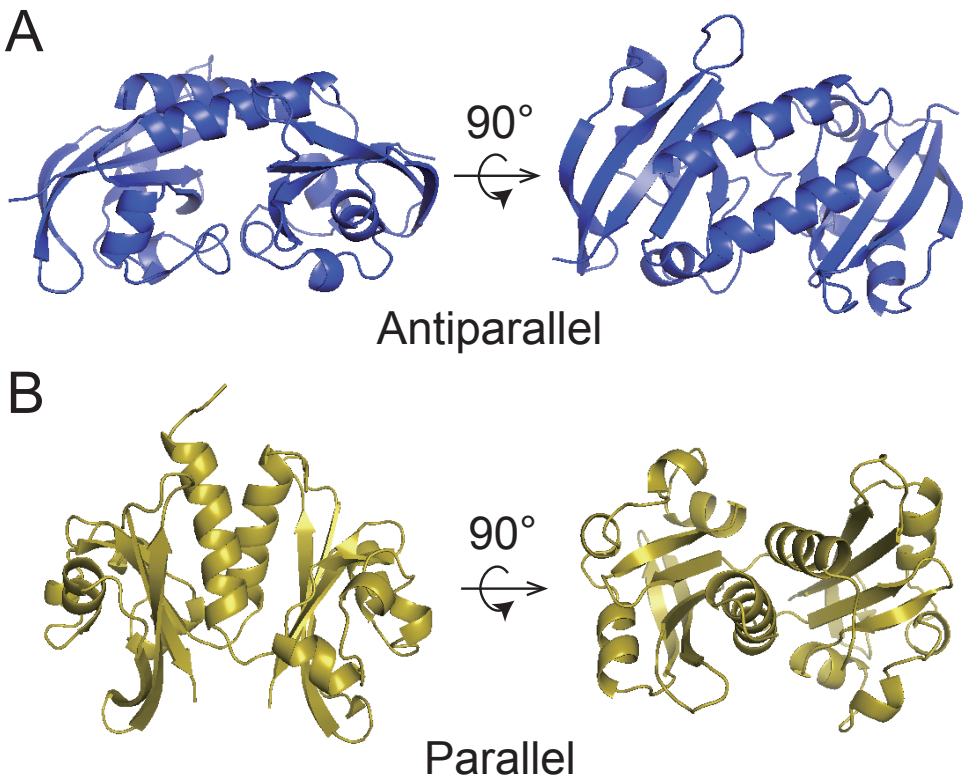

Figure 3.1: Crystal structure of the WT PASc parallel dimer (B) and the N288D anti-parallel dimer (A). In the parallel dimer, the N-terminal helices in WT PASc are parallel to each other and the β-scaffold are organized so that the C-termini are pointing to the same direction and close in space. The anti-parallel dimer's N-terminal helices runs in the opposite directions and β-scaffolds are organized so that the C-termini are far away from each other. The crystal structures are solved in the group of S. Becker.

100% natural abundance of the NMR-active nucleus ^{31}P and its large chemical shift dispersion. It has been successfully used in several systems for measurement of kinase activity [212, 235, 26], dating back to the 1980s for studying the *in vivo* activity of creatine kinase in living mouse tissues. During the measurement, one can also detect the production of ADP and free phosphate in a one pot reaction, as they are separated from the ATP signal in chemical shift (Figure 3.4).

In this chapter, the ^{31}P NMR kinase activity assay will be used to test the activity in two constructs: the soluble PASc-kin construct with only the PASc and kinase domains and the full length CitA. With the PASc-kin constructs, the activities of the WT PASc-kin and the N288D anti-parallel

mutant PASc-kin were compared to test if the suspected kinase inactivation in the citrate free state by the anti-parallel dimer indeed leads to an attenuated activity. The activities of three full length CitA constructs were measured in both the citrate bound and citrate free state for the preparation of site-specific distance measurement in the N308C mutant: the unlabeled CitA N308C mutant, the N3083C mutant tagged with Methanethiosulfonate (MTSL) and with the CF_3 group.

3.2 Materials and methods

3.2.1 Sample preparation

To produce soluble kinase samples with WT and N288D mutant PASc domains (PASc-kin construct), a pET16bTEV-construct coding for a C-terminal fragment of GT CitA starting from amino acid 200, comprising the PASc and the histidine kinase domains, was expressed at 30 °C in strain BL21(DE3) in Luria-Bertani medium supplemented with 50 mg/L ampicillin by induction with 0.5 mM IPTG at OD600 = 0.7. The culture was harvested 7 hours after induction. The cells were lysed by ultrasonication and purified by immobilized metal affinity chromatography (IMAC) on 3 ml Ni^{2+}-NTA resin (Qiagen). The N-terminal Histidine-tag was cleaved off by digestion with Tobacco etch virus (IMAC) protease, removed with Ni^{2+}-NTA resin and further purified by ion exchange chromatography on a Hi Trap Q XL column (GE Healthcare) and by gel-filtration on a SD75 16/60 column (GE Healthcare). The fractions containing the protein were combined and finally dialyzed against 20 mM Tris/HCl, pH 6.5, 50 mM KCl, 10 mM $MgCl_2$, 0.5 mM EGTA. After dialysis 0.5 mM Pefabloc (Roth) and 0.02 % NaN_3 (w/v) were added. The final protein concentration was adjusted to 0.17 mM using a 10 kDa MWCO Vivascience concentrator (Sartorius). The same protocol was applied for producing and purifying the N288D mutant of this GT CitA fragment. This mutant fragment eluted from the gel-filtration as a single peak (Figure 3.2 D). All PASc-kinase mutants were diluted for measurement to a final concentration of 0.16 mM. ATP was added right before measurement to a final concentration of 6 mM. Critically, to prevent sedimentation, the appropriate amount of ATP should be pre-diluted in the Tris buffer at pH 6.5 with the addition of 10% D_20 before adding both components to the protein solution, as D_2O precipitated the protein when added as an isolated component. All PASc-kinase samples can be stored under

room temperature.

Full length C12A/R93A/N308C GT CitA was expressed and purified using a pET16bTEV-vector based construct following the established protocol for the C12A/R93A/N308C GT PASpc construct (see section 2.2.1) with modifications. After purification by gel-filtration, the protein was loaded onto 4 ml Ni^{2+}-NTA resin and eluted with 20 mM Tris/HCl, pH 7.4, 150 mM NaCl, 500 mM Imidazole, 0.694 % (w/v) decylmaltoside (DM) and 0.5 mM Tris-(2-carboxyethyl)-phosphine hydrochloride (TCEP). After adding 6 mM ATP, the protein was reconstituted into DMPC liposomes at a lipid to protein ratio of 20/1 (w/w), removing the detergent with BioBeads (RioRad). The final concentration of the liposome-reconstituted protein in the buffer was adjusted to 100 µM. For tagging with (1-Oxyl-2,2,5,5-tetramethyl-Δ3-pyrroline-3-methyl) Methanethiosulfonate (paramagnetic MTSL), the protein was transferred into 20mM Tris pH 7.4, 150mM NaCl, 0,3% (w/v) LDAO in the gel-filtration step to remove reducing agent. MTSL was added in 20 fold excess (mol/mol) and the solution was incubated for 3 days on ice. The protein was again loaded onto 4 ml Ni^{2+}-NTA resin to switch to 0.694 % DM and after adding 6 mM ATP reconstituted into DMPC liposomes at a lipid to protein ratio of 20/1 (w/w), adjusting the protein concentration to 100 µM.

Tagging of the C12A/R93A/N308C-GT CitA protein with 3-bromo-1,1,1-trifluoroacetone (BTFA) was performed similar to the protocol for MTSL tagging, using 50 mM sodium phosphate, pH 7.0, 200 mM NaCl, 0.3% (w/v) LDAO in the gel-filtration step. Subsequently BTFA was added drop-wise to the protein solution as described for the BTFA-tagged PASpc (section 4.2.1), from a 100 mM stock solution in 50 mM sodium phosphate, pH 7.0, 200 mM NaCl. After incubation overnight on ice, the protein was loaded according to the protocol for MTSL onto 4 ml Ni^{2+}-NTA resin to switch to 0.694 % DM and reconstituted in DMPC liposomes at a lipid to protein ratio of 20/1 (w/w), with 6 mM ATP added to the buffer. The final protein concentration was adjusted to 100 µM. To obtain the citrate bound state, buffer containing 5 mM sodium citrate was added to the sample and equilibrated overnight at 4 °C.

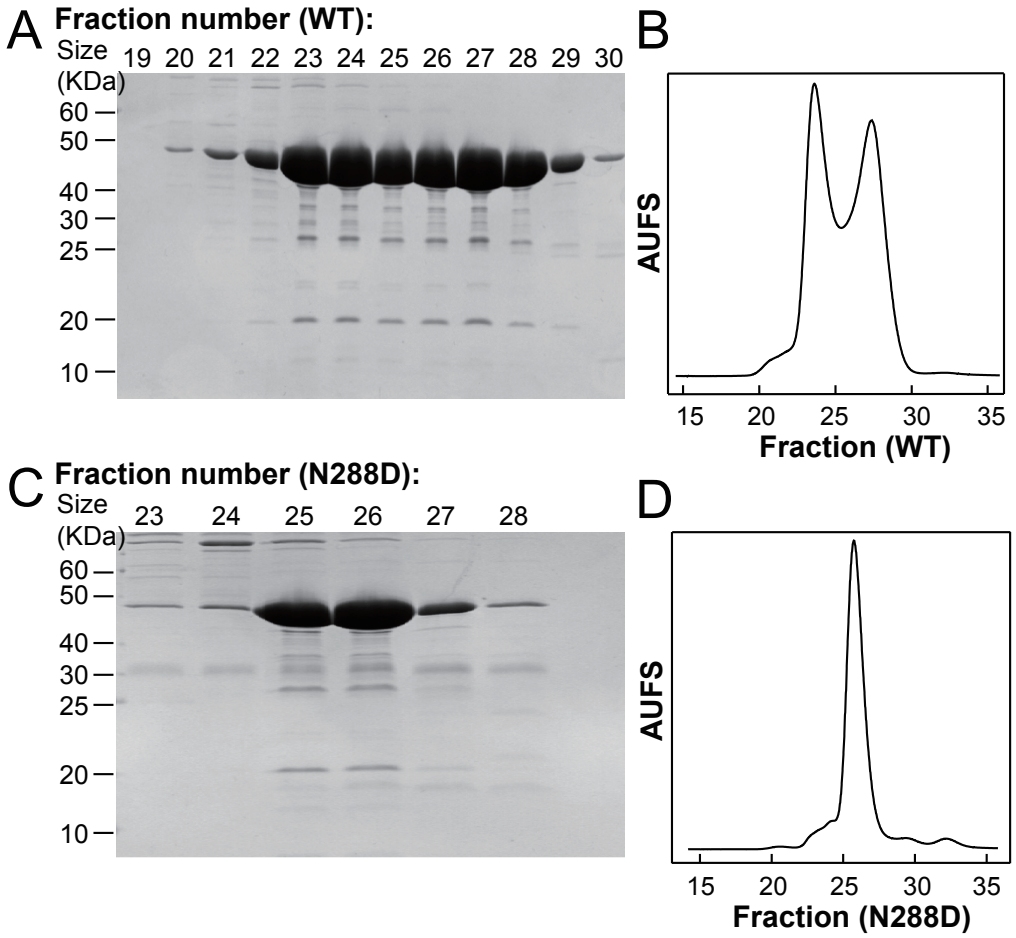

Figure 3.2: Purification of CitA PASc-kin WT (A and B) and N288D mutant (C and D) constructs by gel filtration. SDS-polyacrylamide gel (A) shows fractions 19 to 30 of the chromatography run (B) of the WT construct, which showed two peak representing different oligomer state. Particle size measurement with dynamic light scattering (DLS) (Figure C.3) confirmed the two peaks originate from a potential dimer to tetramer exchange. SDS-polyacrylamide gel (C) of the N288D mutant PASc-kin construct shows fractions 23 to 28 of the chromatography run (D) showed only a single peak. The data are provided by Karin Giller and Dr. Stefan Becker.

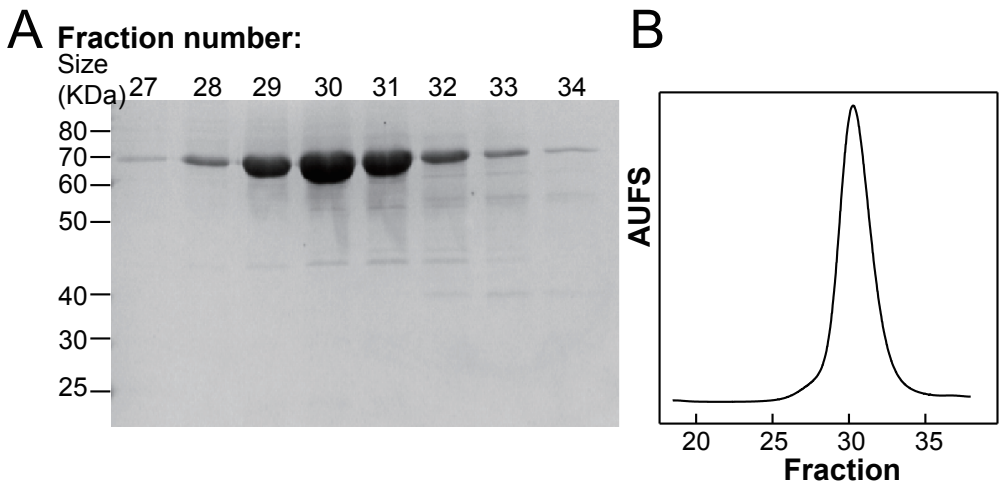

Figure 3.3: Purification of full length CitA R93A/C12A/N308C constructs by gel filtration. SDS-polyacrylamide gel (A) shows fractions 27 to 34 of the chromatography run (B). The data are provided by Karin Giller and Dr. Stefan Becker.

3.2.1.1 NMR spectroscopy and data analysis

1D phosphorus spectra were measured with a Bruker 400 MHz magnet. The spectra for PASc-kin WT and N288D, and full length un-tagged R93A/C12A/N308C CitA were measured with a room temperature QXI H/P-C/N/D five channel probe with a B_1 field of 7.5 kHz. The spectra for MTSL and CF_3 tagged R93A/C12AN/308C CitA were measured with a room temperature TBO H/F-C/N/P-D probe. All spectra were measured with an inter-scan delay of 1 s and an offset at -15 ppm. Number of scans was set to 1920. 10% D_2O was used in all samples as lock signal. The temperature of measurement of all CitA full length constructs is 37 °C.

The initial speed of the reaction was used to measure the kinase activity since the only reactant (ATP) is added in large excess to the enzyme. ATP is stable under the experimental condition (Figure 3.4), so its auto-hydrolysis does not need to be taken into account. The error is estimated from the noise level of the spectra. According to first order kinetics, the consumption of the reactant in the complete reaction should follow a single exponential decay. At very short reaction time, the free phosphate (Pi) production approaches a linear equation with the slope corresponding to the exponential decay rate (see section C.1). This can also be observed experimentally. For all PASc-kinase constructs, the reaction was measured to significantly long time to

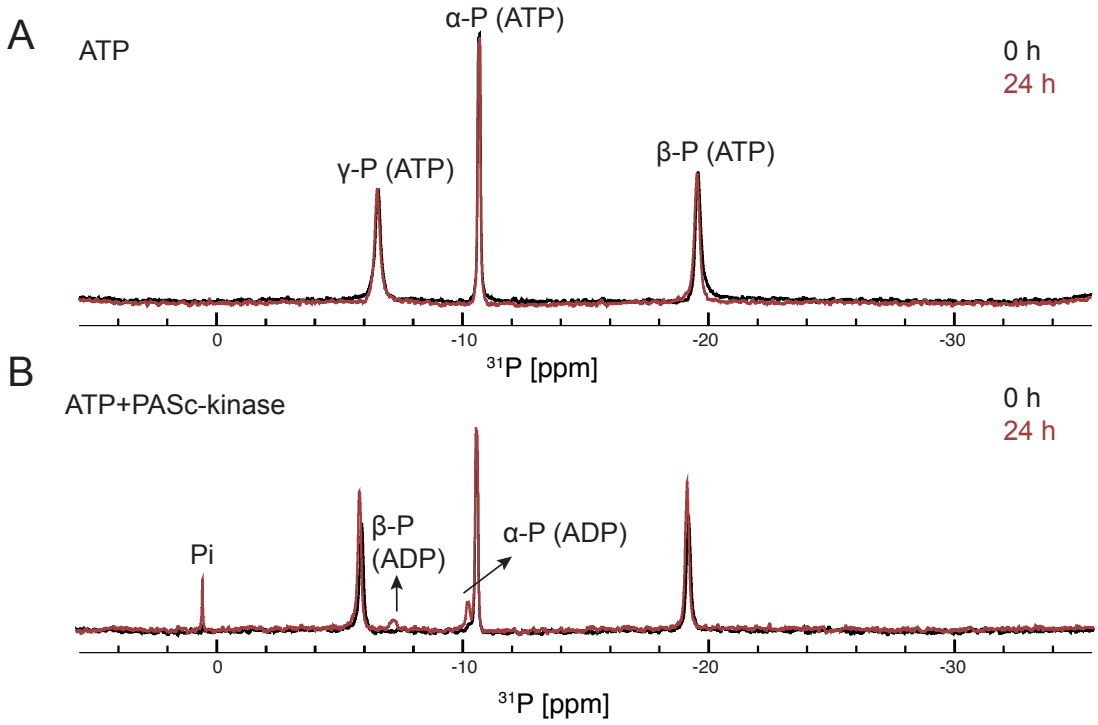

Figure 3.4: The addition of the PASc-kin WT construct hydrolyzes ATP into ADP (B), which is otherwise stable under the experimental conditions (A). The 1D ^{31}P spectrum of ATP does not change after 24 hours, indicating the stability of the ATP under the experimental conditions. The spectrum shows three peaks, corresponding to the signals of β-P, α-P and γ-P. The addition of PASc-kinase leads to the appearance of signals of the degradation products ADP (β-P and α-P in ADP) and free phosphate (Pi)

acquire the full exponential decay. The exponential decay rate of the full reaction is the same as the linear decay rate in the initial phase of the reaction (Figure C.2). There are several advantages in monitoring the free phosphate during the initial reaction. Due to its narrow linewidth, the peak is easily trackable. Measuring only the initial rate also saves experimental time, especially in slow reactions like these. Product inhibition by ADP might become a significant factor later when the ADP concentration is getting higher, although such inhibition has not been observed by us, as the full reaction followed a single exponential decay till the end.

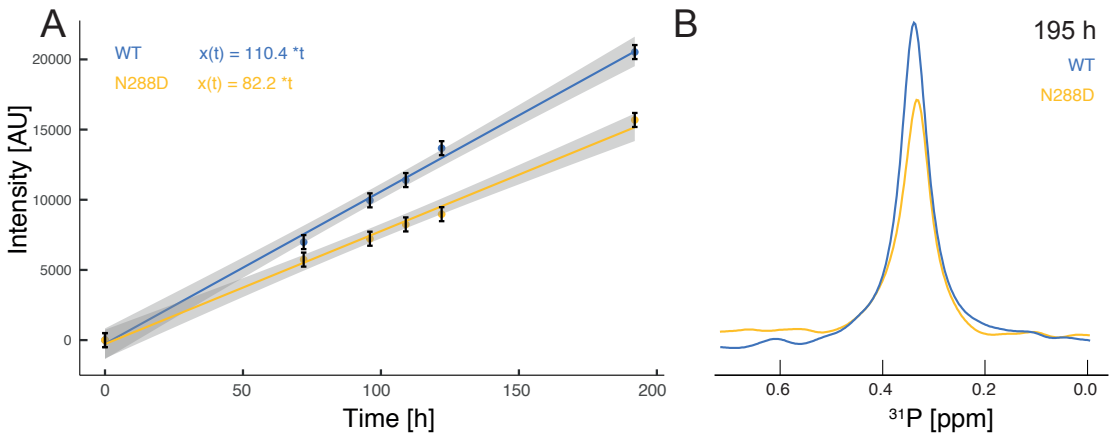

Figure 3.5: The kinase attached to the PASc N288D mutant has 25% lower activity in the ^{31}P assay PASc WT. The initial rate of the kinase activity with the PASc N288D mutant is 82 h^{-1} (yellow), and that of WT is 110 h^{-1} (blue). Both curves measured to 200 hours still satisfy the zero order reaction approximation and are linear (A). At the end of the reaction (195 h), ^{31}P NMR signal of free phosphate, one of the end product of ATP hydrolysis, is 25% lower with the N288D mutant (B) than with the WT PASc.

3.3 Results

3.3.1 Anti-parallel mutant N288D attenuates kinase activity

The addition of WT PASc-kinase leads to an immediate hydrolysis of ATP to ADP and free phosphate, as indicated by the decay of ATP peak intensities along with the appearance of ADP and free phosphate peaks. The N288D mutant of the PASc-kinase (which shows an anti-parallel dimer arrangement in the crystal structure in the isolated PASc domain) attenuates the kinase activity by 25% according to the production of the free phosphate. The same level of ATP consumption reduction was observed in the full reaction measured to 800 h (Figure C.2). This confirms that the initial rate of Pi production corresponds to the rate of ATP consumption. The WT PASc-kin eluted from the SEC column in a double peak, probably representing different aggregation states (Figure 3.2 B). A particle size measurement using dynamic light scattering (DLS) revealed that the two peaks represent an exchange between a dimer and a tetramer (Figure C.3). The possibility that any activity drop should come from a dissociated dimer can be ruled out. The N288D mutant PASc-kin sample eluted as one peak, but a fast exchange between a dimer and a tetramer is still possible. The kinase activity is not fully abolished when it is attached to the PASc N288D mutant, likely

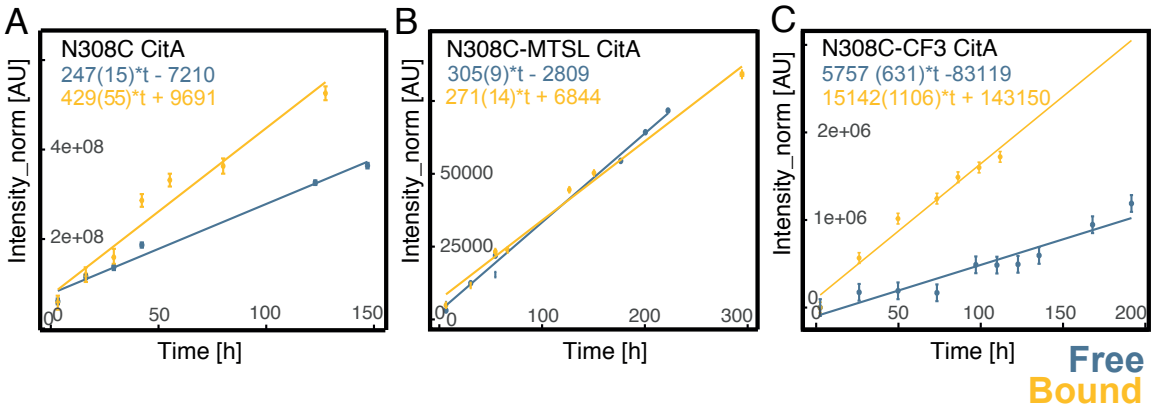

Figure 3.6: Kinase activity of full length C12A/R93A/N308C CitA without tag (A), with MTSL (B) and with CF_3 (C) from ^{31}P NMR assay. The citrate bound state (yellow) in the non-tagged and CF_3-tagged CitA has two to three times higher activity compared with the citrate free state (blue). The MTSL tagged CitA does not respond to the addition of citrate, since the kinase activity is the same between the two states.

due to dimer exchanged in the PASc domain, as seen by CEST experiments done with isolated PASc domains [177]. Similar change in kinase activity was also confirmed by SPA assay with ^{33}P-ATP (Figure C.1), although the rate changes are not statistically significant due to precision of the method. We also raised the temperature of the measurement to 37 °C for the WT PASc-kinase and noticed a very dramatic jump of the kinase activity to four times compared with that at 25 °C. This fits well with the fact that *G. thermodenitrificans* is thermophilic and all proteins derived from there are optimized to function at very high temperature up to 60 °C.

3.3.2 Activity of CitA N308C mutant changes with different tags

The N308C mutant of the isolated WT PASc domain has been previously tagged with the fluorescent dye Atto647N for COLD studies and retains the parallel dimer forms observed in crystal[224]. The functionality of the full length N308C CitA without tag is confirmed again by the ^{31}P NMR activity assay. When citrate is added to the CitA N308C mutant in liposomes, the activity rises by a factor of 1.9 (247 h^{-1} to 429 h^{-1}). In the CF_3 tagged CitA, the activity rises by 2.6 times when citrate is added (15142 h^{-1} to 575 h^{-1}). The *in vivo* β-Galactosidase activity assay of GT CitA performed in the group of Prof. Unden found the same factor of 2 to 3 times of activity gain with citrate binding [177]. This factor of increase in ATP hydrolysis rate might be subject to further

downstream signal amplification in the bacteria [88]. The MTSL labeled CitA, however, did not respond to the addition of citrate, with the free state having a slightly higher activity (305 h^{-1} without citrate compared with 275 h^{-1} with citrate). MTSL tagged CitA could be locked in either the inactive or the active state.

3.4 Discussion

Kinase activity can be measured to high precision by tracking the ATP hydrolysis and free phosphate production with ^{31}P NMR. Due to the 100% natural abundance and large chemical shift dispersion of ^{31}P, the amount of individual components of the reaction can be easily determined. This method confirms the attenuating effect of the anti-parallel N288D mutant of PASc on the kinase activity, as it decreases the ATP consumption rate by 30 % compared with the WT PASc. Interestingly, this is in rough agreement with the results from the more conventional radioactive ^{33}P SPA assay. However, it is important to note that these two methods measure essentially different parameters. While the ^{31}P NMR activity assay measures reaction kinetics by production of reaction products, the ^{33}P radioactivity SPA assay reports the speed of protein phosphorylation. These two parameters both reflect the the activity of the kinase, and should be comparable with each other if the dissociation of the phosphate from the kinase is not the rate limiting step of the reaction. The stability of the phosphorylated kinase is in the range of minutes [107], much shorter than the measured rate in the range of hours. It cannot be ruled out that the attenuated kinase activity of the N288D mutant PASc is caused by the lack of dimer to tetramer exchange observed in the WT PASc-kin construct (Figure 3.2). But there is no current evidence that such exchange promotes kinase activity. The propensity to form an anti-parallel dimer in the N288D instead of the parallel arrangement in the WT PASc is still considered to be the major cause of the lower activity in the PASc-kinase construct. So, the anti-parallel dimer indeed resembles the off state of CitA in its effect on the kinase activity.

The high precision and high sensitivity of the ^{31}P activity assay made it possible to determine the activity of the low-yield full length CitA construct. The functionality of CitA with site-specific tags can be tested, a prerequisite for inter-dimer distance determination. The CF_3

tagged CitA has a slightly more elevated response to citrate than the untagged CitA. The reason is either the uncertainty in the protein quantity estimation as the efficiency of protein incorporation into liposome might be different between the samples, or the CF_3 tag still slightly disturbed the protein structure, causing gain of function in the activity. For an even more precise rate measurement, all other phosphorous peaks can be calibrated to the ATP signal intensity at time zero since it is titrated to the same concentration. The MTSL tag, however, completely abolished CitA's response to citrate binding. MTSL is much larger than the CF_3 group and is thus more likely to disrupt the PASc structure. Altogether, tagging with the small CF_3 group has not impeded the kinase activity of CitA, opposite to tagging with MTSL. With CF_3-tagged CitA at hand, functionally relevant distance changes in CitA should now be measurable. The measurement of site-specific distances using a CF_3-tagged CitA PASpc construct will be described in Chapter 4.

CHAPTER 4

Distance Measurement between CitA Dimer with 19F CODEX

4.1 Introduction

Understanding the dimer interface is crucial for membrane bound HKs like CitA which needs to be cross-phosphorylated for their functionality. This is not trivial for conventional NMR experiments. In uniformly labeled samples, if measured NMR contacts are inter- or intra-dimeric needs to be discerned. This is not straightforward for proteins in the size range of CitA. Alternatively, differential isotope labeling between dimer units has been used successfully in providing site-specific distance information in the isolated PASc dimer through the $^{13}C/^{15}N$ double-edited NOESY experiment [105, 177]. But in the liposome sample, this would require dimer mixing during reconstitution, which does not happen during CitA sample preparation. The double electron-electron resonance (DEER) [143, 142] experiment is designed to measure distance between electron spin pairs, usually in the form of MTSL labeled cysteine residues in proteins and is sensitive to a distance range of 1.8 to 6 nm in fully protonated membrane proteins [103]. However, MTSL labeled N308C CitA does not respond to citrate binding (Chapter 3), so could not provide functionally relevant distance information. The Cryogenic Optical Localization in 3D (COLD) has successfully reproduced the inter-dimer distance at N308 in the PASc WT crystal structure [224], but the technique itself is incompatible with liposome samples as it requires isotropic behavior of the molecule.

The centerband-only detection of exchange (CODEX) experiment has proven to be a unique solution to solving the oligomeric state in proteins and, after fitting to a rate equation, measuring

inter-oligomer distances. CODEX has been successful in elucidating functionally important side chain conformation in the influenza virus membrane proton channel M2 [132, 133] in addition to other membrane associated systems such as antimicrobial peptides (AMPs) [137, 37]. The CODEX pulse program consists of two CSA recoupling blocks sandwiching a long mixing period τ_m that lasts an integer number of rotor periods, between which the magnetization is stored at z-direction and spin diffusion can happen [97]. If there is dipolar exchange between spins with different instantaneous CSA during the mixing period, the orientation dependent frequency is changed and leads to incomplete refocusing of the CSA. This dephasing is observed as an decrease in intensity compared with a reference spectrum that eliminates the effect of T_1 relaxation during spin diffusion. A detailed description is available in section 1.6. The choice of nucleus is also critical. As the dephasing process is dipolar coupling driven, the dipolar coupling strength between spins will determine the dynamic range of the observed distance. ^{19}F has the second highest gyromagnetic ratio after the proton. This confers high sensitivity in ^{19}F-detected NMR experiments and allows ^{19}F to ^{19}F spin diffusion to be sensitive to a relatively large distance range of 5 to 20 Å. For the CODEX experiment specifically, ^{19}F detection does not need natural abundance correction either, like in its ^{13}C-detected [228] counterpart, making precise distance determination easier.

^{19}F has been used as a popular probe for biological NMR, because ^{19}F is almost absent in proteins. Selective labeling with ^{19}F can therefore be easily done without background. In both solution and solid-state NMR, ^{19}F based experiments have yielded important functional results in systems like GPCRs [123] and HIV-1 Capsid protein [221]. A variety of ^{19}F containing labels have been designed. In solution NMR, CF_3 groups are preferred due to their smaller CSA, small size and neutral chemical properties compared with ^{19}F-containing aromatic groups [123]. The CF_3 group also undergoes very fast axial rotation, making all three ^{19}F atoms magnetically equivalent. This CF_3 hopping motion gives a three fold signal enhancement and narrow line width in the NMR signal, making it an ideal tag in proteins when sensitivity is of concern. However, even with the sensitive ^{19}F labeling, detecting a single tag to complex biological systems remains challenging due to low sensitivity. Recent advances in dynamic nuclear polarization (DNP) techniques have further increased the sensitivity of ^{19}F detected NMR experiments [131]. Currently, in solid-state,

^{19}F CODEX experiments are done using ^{19}F labeled aromatic amino acids like phenylalanine and tryptophan, because ^{19}F on aromatic rings have large CSA that is beneficial for the CSA encoding. However, for large membrane proteins like CitA, this labeling strategy will not be applicable due to inevitable chemical shift overlap. Here, we propose a solution by selectively tagging a single cysteine residue with a CF_3 group to measure site-specific inter-dimer distances in CitA. This is combined with dynamic nuclear polarization (DNP) and proton to ^{19}F CP for signal enhancement.

4.2 Material and Methods

4.2.1 Hexafluoroacetone(HFA) and protein sample preparation

The 8M and 8 mM hexafluoroacetone (HFA) DNP sample was prepared by mixing pure HFA and 1000x dilution of HFA in water, respectively, with the "DNP juice" (10 mM TEMTriPol, 60% glycerol, 30% H_2O and 10% D_2O) in a ratio of 1:3.

For incorporating ^{19}F-tryptophan into mutant C12A/R93A GT CitA PASpc protein (^{19}F-W163 CitA PASpc) in the citrate bound state, we basically followed a published protocol [49]. One hour before induction, 60 mg/L of 5-fluoroindole (TCI) were added to M9 minimal medium supplemented with ^{15}N-NH_4Cl. Expression was performed at 20 °C by induction at OD600 of 0.65 with 0.5 mM isopropyl-β-D-thiogalactopyranoside (IPTG, AppliChem). The cells were harvested 16 hours after induction. Protein purification and reconstitution were performed as described in section 2.2.1.

The introduction of fluorine labels using cysteine alkylation by BTFA is done according to the protocols published by the group of Schofield [1, 34, 173]. For tagging with BTFA (Aldrich) of ^{15}N-labelled, sodium citrate loaded C12A/R93A/N308C mutant of GT CitA PASpc, the initial purification step on the Ni^{2+}-column was performed with 5 mM dithiothreitol (DTT, GERBU) added to all buffers. After elution from the Ni^{2+}-column the GT CitA PASpc mutant protein solution was supplemented with 5 mM Tris(2-carboxyethyl)phosphine-hydrochloride (TCEP, Sigma-Aldrich) and incubated for 1 hour on ice to secure complete reduction of cysteine 308.

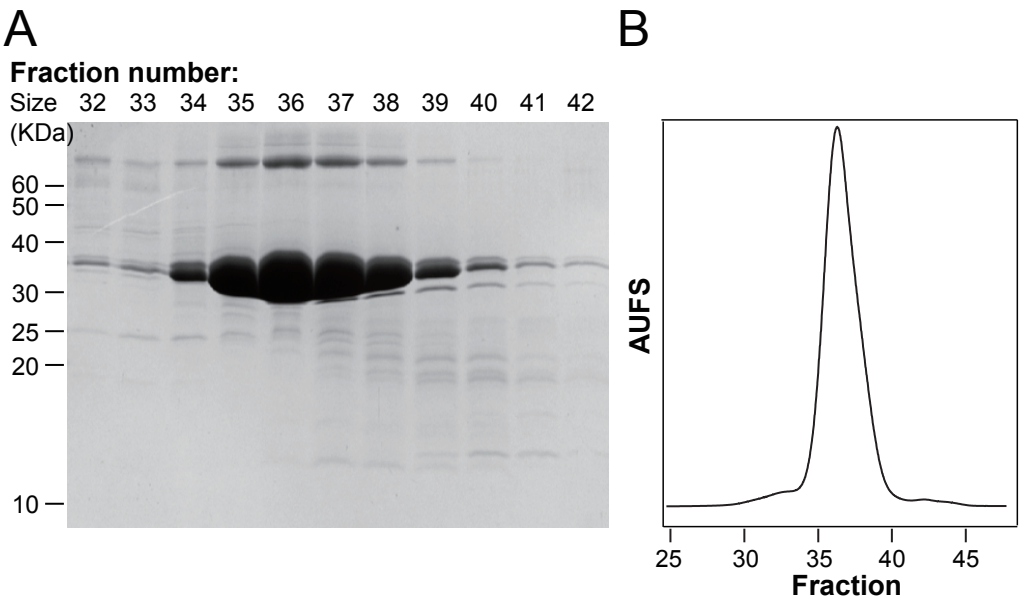

Figure 4.1: Purification of CitA PASpc construct by after Ni^{2+} column. SDS-polyacrylamide gel (A) shows fractions 32 to 42 of the chromatography run (B). Data are provided by Karin Giller and Dr. Stefan Becker

Exchange against BTFA-tagging buffer (50 mM sodium phosphate pH 7.0, 200 mM NaCl, 5 mM sodium citrate, 0.3 % (w/v) n-dodecyl-N, N-dimethylamine-N-oxide (LDAO, Anatrace)), was achieved by gel filtration on a SD200 16/60 column (GE Healthcare). BTFA was added drop-wise with intermediate vortexing in 35 fold excess (mol/mol) to the protein solution, from a 100 mM stock solution in 50 mM sodium phosphate, pH 7.0, 200 mM NaCl, 5 mM sodium citrate. After incubation overnight on ice the volume of the protein solution was reduced with a 30,000 MWCO Amicon Ultra concentrator (Millipore) and excess BTFA agent was removed by another gel-filtration step on a SD200 16/60 column equilibrated with 20 mM sodium phosphate, pH 6.5, 150 mM NaCl, 0.3% (w/v) LDAO, 5 mM sodium citrate. For final reconstitution into liposomes a lipid film of 1,2-dimyristoyl-sn-glycero-3-phosphocholine (DMPC)/ 1,2-dimyristoyl-sn-glycero-3-phosphate (DMPA) (9/1, mol/mol, Avanti Polar Lipids) was dissolved at 5 mg/ml in the gel-filtration buffer, sonicated to obtain a homogeneous suspension and added to the protein solution at a final lipid to protein ratio of 75/1 (mol/mol). After incubation for two hours, the detergent was removed by adding BioBeads (BioRad, 2 g BioBeads/66 mg LDAO) followed by further incubation overnight at 42 °C on an orbital shaker. To separate the liposomes from

the beads the mixture was loaded onto a gravity-flow column and the liposomes containing the reconstituted, BTFA-tagged C12A/R93A/N308C mutant GT CitA PASpc protein were washed from the column with 20 mM sodium phosphate pH 6.5, 5mM sodium citrate, 0.5 mM Pefabloc (Roth, Germany), 0.02% (w/v) NaN_3. The CitA PASpc liposome samples are produced in the bound form initially, and the free state sample is prepared by stripping the citrate bound proteins off of citrate using the protocol introduced in section 2.2.1 under incubation at 40 °C.

The liposome samples are prepared for DNP experiments according to matrix free preparation protocol by adding TEMTriPol powder to the liposome sample until the solubility is saturated. All samples are packed into 2.5 mm phoenix MAS rotors and shock frozen by plunging into liquid nitrogen.

4.2.2 CODEX measurement

All CODEX experiments are measured with a previously published pulse program [97, 132, 228] on a Bruker 600 MHz magnet, with a 2.5 mm Phoenix DNP probe equipped with H/F double channel tuning at 20 kHz MAS and a set temperature of 90 K. We measured a DNP enhancement, ϵ, of 8 from both proton one pulse and ^{1}H to ^{19}F CP experiment (Figure D.1). ^{1}H to ^{19}F CP retains the enhancement factor from that of the proton. Measurement of DNP enhancement on ^{19}F is not possible as for dilute samples ^{19}F direct irradiation does not yield enough signal with or without DNP. The initial ^{1}H to ^{19}F CP contact time is 1500 μs with 41.6 kHz ^{19}F irradiation and 51 kHz ^{1}H irradiation. The ^{19}F and ^{1}H hard pulse power is 65.8 kHz and 53.2 kHz, respectively. The ^{1}H TPPM decoupling power is set to 50 kHz. The inter-scan delays are optimized for each sample individually. The offset of ^{19}F and ^{1}H is -74 ppm and 3 ppm respectively. The sweep width for all ^{19}F-detected experiments is set to 400 ppm.

4.2.3 Fitting of CODEX curve

The spin diffusion rate can be calculated from the CODEX dephasing curve using models described in literature [132, 204, 57], by the following equations:

$$M(t) = e^{-Kt}M(0) \tag{4.1}$$

Equation 4.1 describes the magnetization evolution, $M(t)$, with spin diffusion time. K is the n-dimensional exchange matrix containing the rate constants k_{ij} between exchange of two spins i and j, where n is the total number of orientationally different spins in close enough vicinity to undergo magnetization exchange.

$$k_{ij} = 0.5\pi \cdot F_{ij}(0) \cdot \omega_{ij}^2 \tag{4.2}$$

Balancing of the exchange matrix requires the sum of each column of the exchange matrix, K, to be zero and that the rate constants satisfy $k_{ij} = k_{ji}$ for equal population of magnetization [132, 15]. Note that K should contain not only the rate of direct exchange k_{ij} but also relayed elements, which are magnetization transfer through two or more spins. It can be shown that at large enough t, $M(t)$ approaches the value of $1/n$. This means that CODEX decay will plateau at the value of one over the oligomer number. Distance determination using CODEX relies on the dependence of spin diffusion rate. The spectral overlap function $F_{ij}(0)$ is the overlap integral describing the probability that single-quantum transition occurs at the same frequency for two spins. The exact value of it is usually extracted by fitting rates to known crystal structures. Here, we took the previously published value of 30 to 60 μs [172]. Least square fitting of the exchange rate is done using home written MATLAB code [228].

4.3 Results

4.3.1 CF_3 hopping exits at 90 K under DNP condition

The CF_3 group undergoes fast rotational motional averaging under room temperature, making all three fluorines chemically and magnetically equivalent. This behavior is favorable due to the

additional sensitivity enhancement offered by the three fluorines. However, it has not been reported if this is still true under the DNP experimental temperature of 90 K. Since CODEX is sensitive to magnetically nonequivalent spins, the CODEX decay in the CF_3 group can be used as a simple test for the existence of the CF_3 group hopping. We performed the CODEX experiment on the small molecule hexafluoroacetone (HFA). In the 8M HFA sample, the CODEX curves decays slowly and plateaus at 0.5, meaning the three fluorine spins are orientationally equivalent also at 90 K. This makes tagging protein with CF_3 groups optimal as this offers a three-fold signal enhancement just like under room temperature. We mimicked the concentration in the range expected for a membrane protein sample by diluting the HFA sample to 8 mM. With both the DNP and ^{1}H to ^{19}F CP applied, there is decent signal to noise ratio with 16 scans (Figure 4.2D). ^{19}F one pulse experiment , on the other hand, did not yield any signal from HFA even with DNP enhancement, instead, we were only able to see a sharp background after 1024 scans. This sharp background potentially originates from the fluorinated materials used in the probe design. It is clear that for a membrane protein, enhancement offered by ^{1}H to ^{19}F CP will be indispensable to make the experiment feasible. Since CODEX experiments involve two CSA recoupling blocks, the small CSA of the CF_3 group might be concerning. However, with the observation of spinning side bands of HFA at 20 kHz MAS frequency, we can assume that the CSA of the CF_3 group is larger than 20 kHz and thus not averaged out completely under the MAS frequency used here. It agrees with the CSA magnitude of 63 ppm (corresponding to 36 kHz for ^{19}F in a 600 MHz magnet) in the CF_3 group of 3-F-alanine reported in literature [56]. We observed an unstable buildup of the HFA CODEX curve under 2 ms of mixing time. As the magnetization is stored at the z-direction after the first CSA recoupling block, the mixing period functions additionally as a z-filter to eliminate unwanted transverse terms. A mixing period shorter than 2 ms might be inefficient as a z-filter and thus cause unreliable readouts. So for CODEX experiments, a true zero mixing time has not been recorded, and previous CODEX experiments also started with the measurement at roughly 2 to 5 ms of mixing time [132].// // We then proceeded with the ^{19}F-W163 CitA PASpc sample in the citrate bound state to test our experimental conditions. This sample was tested prior to the CF_3 group tagged CitA PASpc sample due to the high efficiency of incorporating fluorine labeled amino acids into proteins. So the ^{19}F-W163 CitA PASpc is used as to gauge the sensitivity of the CODEX experiment in membrane proteins. Indeed, with the experiment setup established for the

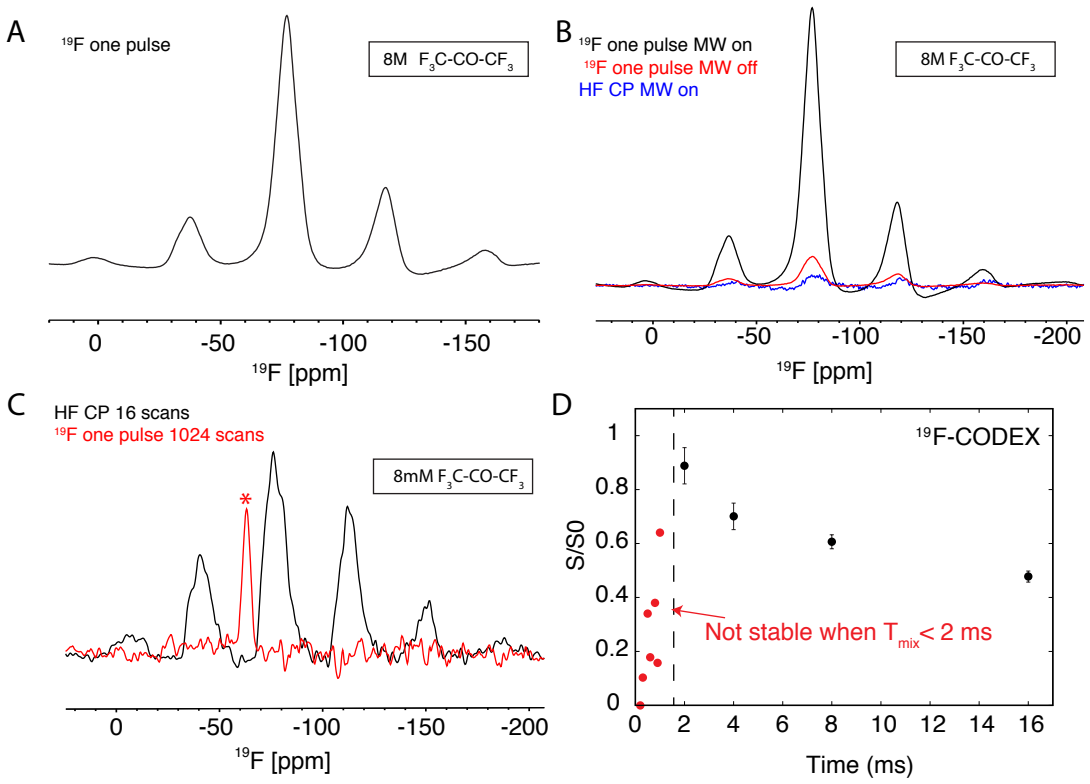

Figure 4.2: CODEX decay curve for HFA plateaus at 0.5 proving the existence of fast CF_3 hopping at 90K. With 8M HFA, the one pulse experiment has strong signal with a DNP enhancement factor of 10 (B), the ^{1}H to ^{19}F CP gives only very weak signal due to the low proton content in the sample. in diluted HFA of 8 mM, the H to F CP experiment has significantly better signal with 16 scans (C, black), while the one pulse experiment gives only a background signal after 1024 scans (C, red). The plateau of the CODEX dephasing curve is 0.5 (D) instead of 0.167 supporting orientationally averaged fluorines on the CF_3 groups, after 2 ms of mixing time (D, red). All spectra are measured with an inter-scan delay of 10s, an acquisition time of 1.5 ms.

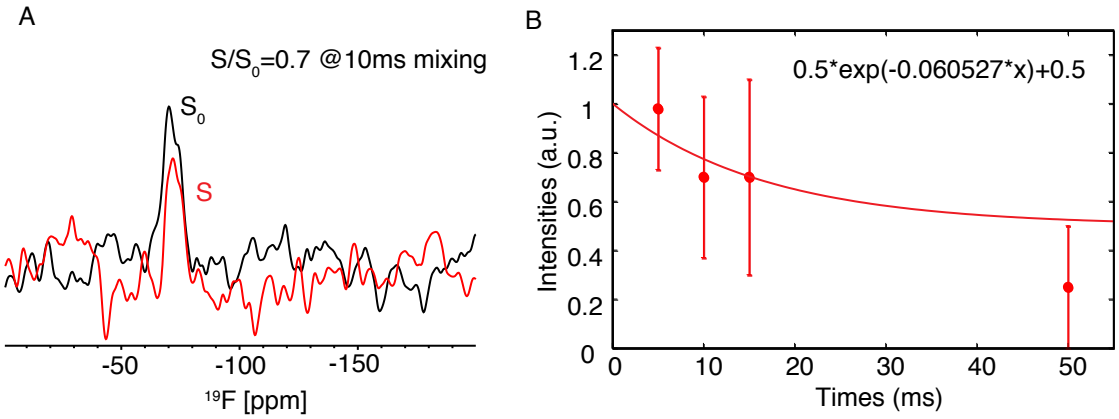

Figure 4.3: CODEX experiment of ^{19}F-W163 CitA PASpc plateaus at 0.5 (B), indicating a dimeric TM2 interface. The DNP enhancement combined with ^{1}H to ^{19}F yields decent sensitivity to monitor CODEX decay (A). A mono-exponential decay can be fitted to the CODEX rate equation, the extracted rates infer a inter-helical distance of 6 Å at W163.

8 mM HFA sample, we could acquire a CODEX decay curve. We observed a plateau of around 0.5 at 50 ms of mixing, which is compatible with a dimeric arrangment of the TM2. The fitted rate revealed a inter-dimer distance of 6 Å at W163 for CitA. Such distances suggest that the residues W163 from the monomers are facing each other at the dimer interface when the citrate is bound, which is compatible with the TM2 dimer modeled with cysteine crosslinking data [202].

4.3.2 Site-specific distance measurement supports an anti-parallel to parallel dimer rearrangement in PASc upon citrate binding

The tagging of a specific location in a protein with the CF_3 group relies on a single site cysteine at this position that does not interfere with the functionality and structure of the protein. Fortuitously, for CitA, the N308C mutation at the C-terminus of the PASc domain has been previously shown by COLD to conserve the structure observed by X-ray crystallography [177]. We further validated the functionality of this mutant along with its CF_3 tagged counterpart using ^{31}P ATP assay in Chapter 3. The inter-dimer distance at this position can help to discern the parallel (11 Å) and the anti-parallel (45 Å) dimer arrangement (Figure 4.4A and B), as N308 is at the very end of the PASc domain. Now, with the availability of CODEX and the favorable conditions offered by using a CF_3 pair as a distance ruler, we can distinguish between the parallel and anti-parallel dimers in the membrane bound PASpc sample in its functional states, *i.e.,* citrate bound and citrate free states.

The readout is straightforward for anti-parallel dimer, as the inter-C308 distance in it is larger than 45 Å (Figure 4.4A, right panel), which is beyond the limit for inter-fluorine spin diffusion to happen. This is what we observed in the free state of CitA PASpc, where there is no decay in the CODEX signal compared with the reference experiment beyond 500 ms (Figure 4.4C, blue). In the case of the parallel dimer, for whom the inter-C308 distance is 11 Å, we should be able to observe a CODEX decay rate corresponding to this distance. We extracted a single exponential decay of $0.5 * e^{(-0.0006*t)-0.5}$ for the CODEX decay curve in the CitA PASpc bound sample and found a distance of 14.5 $\pm$ 3 Å, fitting exactly to the parallel dimer (where the inter-N308C thiol group distance measures 11 Å). A single exponential fit suffices here because the CODEX decays curve plateaued at a value of 0.5. The short ^{19}F T_1 of 321 ms (Figure 4.4D) prevented the acquisition of mixing time beyond 500 ms. However, as we already observed the plateau in the bound state at 250 ms (Figure 4.4A and B), it is sufficient to acquire the data at a mixing time of around 300 ms. We observed some fluctuating, minor decay also for the free state, especially at 250 ms and 300 ms mixing, but not at 500 ms mixing time (when the S/S_0 value equals ones exactly). From the NMR settings, this might be caused by minor incomplete CSA refocusing from spinning speed deviation or imperfect pulse power calibrations. But more likely, this can also be attributed to fractions of bound PASpc population in the sample as there is still very minor intensity of the H96 side chain, which is an indicator of the citrate bound state of PASpc, in the measured (H)NH spectrum of the CF_3-tagged PASpc after washing with the citrate free buffer (Figure D.2).

4.4 Discussions

We applied CODEX to measure the inter-oligomer distances in the range of 5 to 20 Å in a membrane protein aided by the sensitivity enhancement offered by DNP, CF_3 hopping and ^{1}H to ^{19}F CP. With this approach, we observed dramatic inter-dimer distance changes at the C-terminus of the PASc domain in CitA. Upon citrate binding, the C-terminus of PASc switches from being more than 20 Å apart to 11 Å apart, providing site-specific distance evidence for previously hypothesized [177] anti-parallel to parallel dimer rearrangement. For a more precise determination, an experimentally fitted F(0) can be done with bis-CF_3-phenyl with a known inter CF_3 distance of 5.9 Å [56]. Tagging of CitA with a chemically neutral, and small CF_3

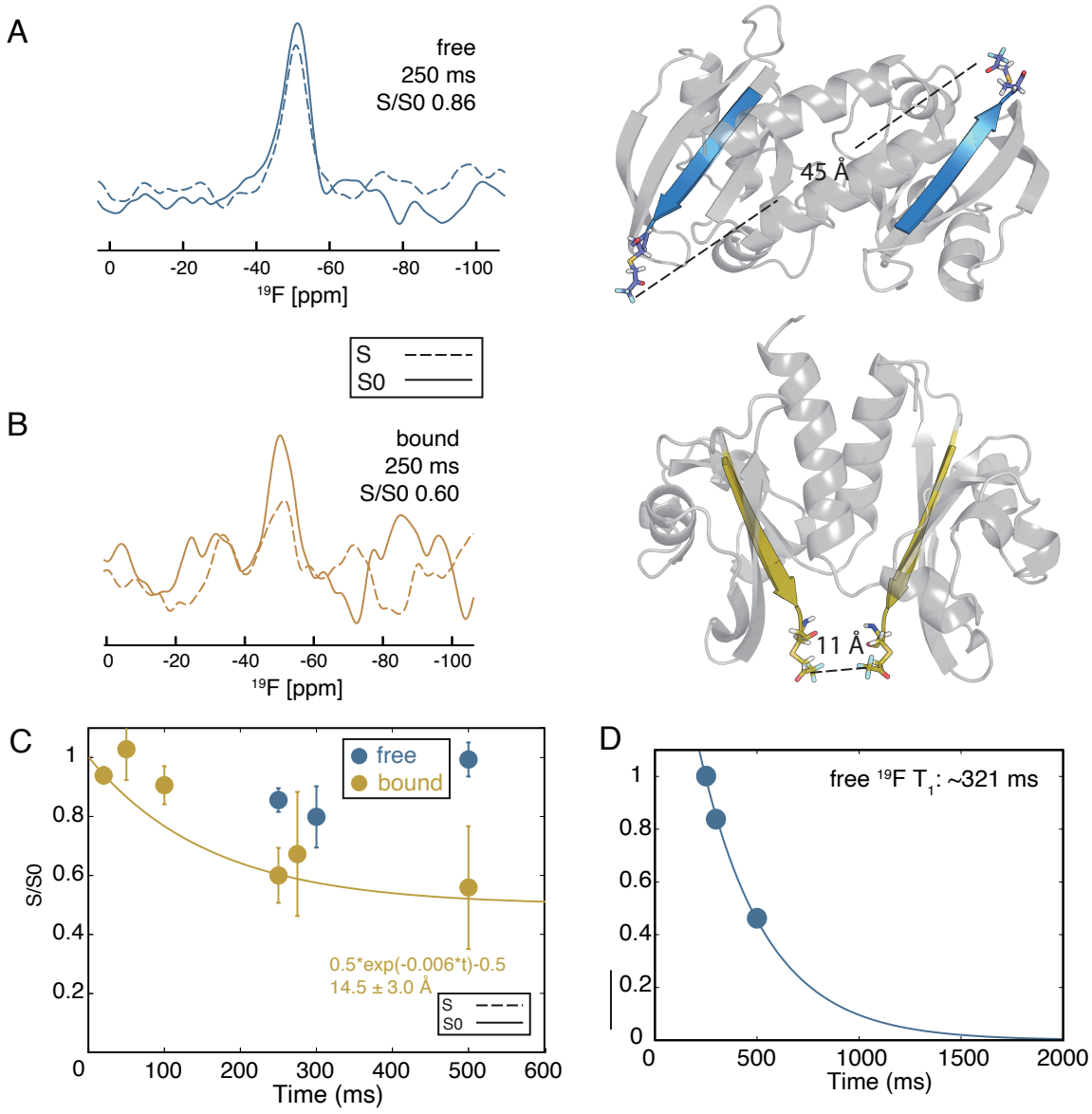

Figure 4.4: Large inter-dimer distance at C-terminus of PASc changes observed by CODEX dephasing between bound and free state of CitA PASpc. At mixing time of 250 ms, the bound state CODEX signal decays to 0.60(Table D.2) of the reference experiment (B, left); the decay rate can be fitted to a inter CF_3 distance of 14.5 $\pm$ 3 Å(C, yellow), corresponding exactly the the inter-dimer distance at the C-terminus of the parallel dimer (B, right). At the same mixing time, the free state CODEX signal is almost the same (Table D.1) as the reference experiment (A, left) through all mixing times, corresponding to a large inter dimer distance at the C-terminus of more than 20 Å, agreeing with the anti-parallel dimer (A, right). The CODEX decay curve cannot be acquired to more than 500 ms due to ^{19}F T_1 of 321ms (D), but is sufficient for observation of the plateau.

group does not disturb its functionality, making site-specific distance measurement possible. In addition, dilution of the sample with either lipids or untagged proteins is not necessary because the measurement is sensitive only to a short range of distances and given the large dimer size is thus not expected to be influenced by inter-dimer contacts. This is beneficial, especially if the protein of interest tends to cluster in the membrane. In our CitA liposome sample, the DNP enhancement is only 8 times, which is significantly lower than what had been achieved by other groups of at least 50 times [131]. The DNP conditions including the type of biradical, the mixing strategy *etc.* can be optimized to further improve the sensitivity of the method. This will allow site-specific distance measurements in even larger, more challenging constructs like full length CitA, where not only the spin density is halved due to the size of the construct, but also the yield of the protein is much poorer. But already with the current setup, measurement is possible even in membrane protein samples with a CF_3 label density in the μM range. This provides an alternative solution to measure site-specific inter-oligomer distances when the system is too large for conventional NMR contact determination or when homodimers cannot be prepared with orthogonal labeling.

With the combination of determination of the inter-N308C distance in both the citrate bound and citrate free state, functionality test of the different dimer-forming mutants using the ^{31}P activity assay (Chapter 3) and the residue-specific assignment using ^{1}H-detected MAS NMR (Chapter 2), key events underlying the activation of the kinase activity of CitA can be defined. A model for the transmembrane signal transduction mechanism from the end of the PASp domain, through the TM2 and its accompanying linker regions to the PASc domain can be developed and is summarized in Chapter 6.

CHAPTER 5

Transferred-Rotational-Echo DOuble Resonance (TREDOR)

This chapter is based entirely on the following publication, and contains identical text passages: Xizhou Cecily Zhang, Marcel C Forster, Evgeny Nimerovsky, Kumar Tekwani Movellan,and Loren B Andreas. Transferred-rotational-echo double resonance. *The Journal of Physical Chemistry A*,125(3):754–769, 2021. The author of this thesis, Xizhou Cecily Zhang, contributed to the writing of the manuscript, the development and analysis of the pulse program, the processing of the data and the structure calculation.

5.1 Introduction

Distance determination is the foundation for determination of 3D molecular structure via NMR, both in solution and in solid samples. Multidimensional spectra, in combination with homonuclear recoupling or spin diffusion methods have been developed for structure determination with applications to biological molecules [162, 211, 47, 219, 190, 74] and materials.[199, 62, 23] Typically, a large set of internuclear distances, often categorized as imprecise distance ranges, are used as input to simulated annealing protocols that converge to the correct protein fold. These structural representations are improved with more precise distance information.[217, 216, 74] However determination of precise distances is still extremely challenging for proteins, particularly for large proteins in the solid state where multiple dimensions are required to resolve resonances.

Improved distance precision typically requires many such multidimensional data sets, each acquired with a different mixing time such that distance-dependent buildup of magnetization can be recorded precisely. This dramatically increases the required measurement time.

Commonly, homonuclear recoupling or spin diffusion methods [4, 17, 120, 108] such as RFDR [21], DARR [207, 206] and DREAM [215] are employed for distance determination and subsequent 3D structure calculation. These have the drawback of yielding only rough distance bounds [121, 234, 122], while for solution NMR, experiments for the precise determination of these have been developed.[217, 216] Only recently, attempts at determining precise distances in the solid state using RFDR have been made.[74]

Recoupling of heteronuclear dipole interactions in magic-angle spinning (MAS) NMR is a well-established method to measure distances [151, 150] and order parameters.[13, 98, 60, 127, 129, 128, 174] Due to a favorable scaling factor and relatively low RF power requirement, one of the earlier recoupling sequences, rotational echo double resonance (REDOR) [80, 183] remains widely applied to both materials and biological samples. Since the spin part of the recoupled Hamiltonian is identical to the J-coupling Hamiltonian, a transferred sequence analogous to the solution HSQC sequence was developed soon after, and is referred to as transferred-echo double resonance (TEDOR).[92] The REDOR and TEDOR sequences were originally devised for isolated spin pairs. Application to uniformly labeled samples by addition of z-filters [101] or insertion of selective pulses [99] has extended the applicability of the method. The REDOR and TEDOR pulse sequences have also been combined sequentially with other recoupling sequences to construct multidimensional pulse sequences for assignment and distance determination.[9, 50, 180]

A key advantage of the REDOR pulse sequence is that a reference spectrum is interleaved with the dephased spectrum in order to remove the effects of transverse coherence decay. On the other hand, a key advantage of TEDOR is that the dephasing nucleus is frequency encoded, and it is possible to separate the effects of multiple dephasing spins. This has been used for the simultaneous determination of multiple distances.[101, 7] A major disadvantage in the use of

TEDOR for precise distance determination is that unlike REDOR, there is no reference spectrum to account for transverse coherence decay. To make matters worse, there is a second parameter needed to fit TEDOR data, which is an overall amplitude scaling factor. The amplitude scale is not evident from TEDOR alone, but can often be approximately determined based on TEDOR peaks arising from strong couplings or from a separate reference spectrum.[93, 94, 101] In practice, this means that when precise distances are needed, typical TEDOR data are recorded to sufficient time so as to observe a dipolar oscillation, and when only a partial oscillation can be recorded, or when the signal is over-damped due to coherence decay, free variation of the two fit parameters (amplitude scaling and coherence decay) results in fits to the data for a wide range of dipolar couplings.[7] The case of over-damping (transverse coherence decay rates of comparable magnitude to the couplings) occurs for weak couplings that encode useful structural information in protein samples, particularly for non-crystalline samples like membrane proteins, which are of great biological interest. The ^{15}N T_2 time, relevant during REDOR periods, is reported to be around 10 ms for non-exchanging backbone amide nitrogens in M2 protein from the influenza virus [96], and around 31 ms in perdeuterated SH3 microcrystals (100% back exchanged) without decoupling.[115] In the case of deuterated proteins or ultrafast MAS, proton T_2 can also reach ~5 ms or more, long enough to acquire REDOR data [67] and suggesting that complementary H-C distances could be recorded.

In addition to T_2 decay, the effects of multiple spin interactions, as well as pulse imperfections can lead to faster signal loss during REDOR periods.[101, 196] This results in lower signal-to-noise and less precise distance determination, particularly for uniform labeled samples. Ideally, we would like to apply a sequence that can precisely determine distances using short mixing times (less than a dipolar oscillation) where the signal is still strong. At the same time, the sequence should identify both the dephased and the dephasing spins such that it can be applied to uniformly labeled samples.

We took inspiration from transfer sequences used for the measurement of homonuclear J-couplings [116, 19, 146] and for protein assignment [76] in order to design a heteronuclear sequence that retains both the starting signal (REDOR) as well as the transferred signal (TEDOR).

The resulting transferred-rotational-echo double resonance pulse sequence (TREDOR) co-acquires the chemical shifts of both dipolar coupled nuclei (here ^{13}C and ^{15}N or ^{13}C and ^{1}H) in one indirect dimension. Pulse sequences for two implementations of TREDOR are shown in Figure 5.1. By tracking both the original and transferred signal, it is possible to account for coherence decay at each mixing time, and in so doing to remove two fit parameters of amplitude scaling and transverse coherence decay. The result is a single parameter fit to determine the dipolar coupling.

5.2 Material and Methods

5.2.1 SH3 sample preparation

Perdeuterated chicken brain α-spectrin SH3 was expressed, purified and crystallized based on previous publications. [160, 44] Transformed *Escherichia coli* BL21(DE3) cells were grown in 250 ml D_2O-based M9 minimal medium with 3 g/l ^{13}C-d_7-glucose and 1 g/l ^{15}N-NH_4Cl, at 37°C with shaking at 120 rpm. At OD_{600nm} 0.7, the temperature was switched to 30°C until the OD_{600nm} reached ~0.8 before induction with 1 mM isopropyl β-D-1-thiogalactopyranoside (IPTG). After overnight expression, SH3 was purified by anion exchange chromatography (HiTrap Q XL, GE Healthcare, 20 mM Tris, pH 8.0, 1 mM EDTA, gradient 0-1 M NaCl), gel filtration (Superdex 75, GE Healthcare, 20 mM citric acid, pH 3.5, 200 mM NaCl, 1 mM EDTA) followed by dialysis against H_2O-HCl (pH 3.5). Lyophilized protein was resuspended in H_2O-HCl (pH 3.5) at ~20mg/ml, and the same volume of 200 mM $(NH_4)_2SO_4$ (pH 3.5, 0.04% NaN_3) was added. Crystallization was induced by shifting the pH to ~7.0 with gaseous NH_3. Samples were subsequently kept for 3 days at 4°C before packing into a Bruker zirconia 1.3 mm NMR rotor using centrifugation protocol introduced previously.

5.2.2 NMR spectroscopy

All TREDOR SH3 spectra were recorded on a Bruker AVIIIHD 600 UltraShield spectrometer with a field strength of 14.1 Tesla, with a MASDVT600W2 BL1.3 HXY probe. The MAS frequency was set 55.555 kHz and the temperature was set to 240K (1000 L/h cooling gas). Proton and ^{13}C hard pulse powers were both 100 kHz, and ^{15}N hard pulse power was 83.3

kHz. REDOR pulses were applied on the carbon channel, employing the xy-8 scheme [79]. TPPM heteronuclear proton decoupling [22] was 12 kHz, MISSISSIPPI water suppression [233] was applied for 100 ms with 13.9 kHz, and WALTZ-16 heteronuclear decoupling [191] was 10kHz.

Pseudo-4D TREDOR N-Cx spectra were recorded with 8 scans and a recycle delay of 1 s, with a total acquisition time of ~2 days and 1 hour for each mixing time (4, 6, 10 ms). For ^{1}H, the carrier frequency was set to 4.5 ppm, acquisition time was 20.5 ms, and spectral width was 41.7 ppm. For ^{13}C (the combined dimension), the carrier frequency was 40 ppm, the acquisition time 8 ms (making the ^{15}N acquisition time in this dimension 19.9 ms), and the spectral width was 130.7 ppm. For ^{15}N, the carrier was 90 ppm, the acquisition time 16.5 ms, and the spectral width was 30 ppm. ^{1}H to ^{15}N cross polarization was 700 μs long, with ^{15}N power of 45 kHz and a linear power ramp on proton from 89.6 Hz to 112 Hz. ^{15}N to ^{1}H cross polarization was 500 μs long, with ^{15}N power of 45 kHz and a linear power ramp on proton from 112 Hz to 89.6 Hz. The selective Reburp [119] pulse during the REDOR period was adjusted to have a bandwidth of 48 ppm, with an offset placing the center at 28 ppm.

Pseudo-4D TREDOR H-CO spectra were recorded with 4 scans and a recycle delay of 1.5 s, with a total acquisition time of ~1 day and 20 hours for each mixing time (0.6 and 1.2 ms). For ^{1}H, the carrier frequency was set to 4.5 ppm, acquisition time was 20.5 ms, and spectral width was 41.7 ppm. For ^{13}C (the combined dimension), the carrier frequency was 203.7 ppm to place the double quantum artifacts away from the signal of interest (supporting information Figure S2). The acquisition time is 7.2 ms for both ^{13}C and ^{1}H, such that only ^{13}C has the correct ppm scale. The spectral width was 184.4 ppm. For ^{15}N, the carrier was 118 ppm, the acquisition time 16.5 ms, and the spectral width was 30 ppm. ^{1}H to ^{15}N cross polarization was 1700 μs long with ^{15}N power of 41 kHz and a linear power ramp on proton from 85.6 Hz to 107 Hz. ^{15}N to ^{1}H cross polarization was 600 μs long with ^{15}N power of 45 kHz and a linear power ramp on proton from 110 Hz to 88 Hz was applied. The selective Reburp [119] pulse during the REDOR period was adjusted to have a bandwidth of 100 ppm, with an offset placing the center at 203.7 ppm.

Pseudo-4D Opa60 H-CO spectrum was recorded on a BRUKER ASCEND 1.2 GHz mag-

net equipped with a MASDVT1200S6 BL0.7 NCH probe. The MAS frequency was set to 100 kHz and the temperature to 265 K (425 l/h cooling gas). Proton hard pulse power was set to 147 kHz, ^{13}C to 114 kHz and ^{15}N to 78 kHz. TPPM heteronuclear [22] proton decoupling was 23 kHz and MISSISSIPPI [233] water suppression was 25 kHz applied for 80 ms. The spectrum was recorded with 4 scans at two mixing times (0.64 ms and 0.96 ms), and the measurement time totaled 1 day and 7 hours for each mixing time. The interscan delay was set to 0.9 s. The ^{1}H dimension had a carrier frequency at 4.72 ppm, an acquisition time of 21 ms and spectral width of 40.4 ppm. The ^{13}C dimension (the combined TREDOR dimension) has a spectral width of 331.3 ppm and an acquisition time of 3 ms with a carrier frequency at 203.7 ppm. The ^{15}N dimension's carrier frequency was set to 120 ppm, with a spectral width of 30 ppm and an acquisition time of 6.3 ms. ^{1}H to ^{15}N cross polarization was 1400 μs long with ^{15}N power of 65.6 kHz and a linear power ramp on proton from 158 Hz to 197 Hz. ^{15}N to ^{1}H cross polarization was 350 μs long with ^{15}N power of 65.6 kHz and a linear power ramp on proton from 197 Hz to 158 Hz was applied. Additionally, due to the large field drift of the newly charged magnet, we applied linear drift correction [148] to the spectra before analysis. All other parameters were the same the H-CO TREDOR acquired for SH3.

5.2.3 SH3 data analysis and structure calculation

SH3 TREDOR spectra were processed with Bruker TopSpin 3.5 and analysed with CcpNmr.[197, 218] Side-chain carbon and backbone carbonyl resonances were assigned using the pseudo-4D N-Cx and H-CO TREDOR at short mixing time and verified against published chemical shifts.[115] Extracted peak intensities were fit with equation E.6 using MATLAB R2016b [141] to determine internuclear distances. The rms noise level was used to estimate the error in the fits. Since the random error always corresponded to less than 10%, and 10% deviation can occur due to geometrical considerations [101], the imposed error for the calculation was always 10%. The SH3 structure was calculated using CYANA 3.98.13.[84] Specifically, 100 structures were calculated to satisfy the TREDOR distance restraints, entered as upper and lower distance boundaries, as well as TALOS-N torsion angle restraints (generated from all assigned residues which include Cα, Cβ chemical shifts).[193] Only TALOS-N "strong" predictions were included (see supporting infor-

mation Table S3). The final restraint list can be found in the supporting information. After an initial structure calculation, two TALOS-N torsion angle restraints (psi of residue 38 and phi of residue 39) were observed to violate by more than 50 degrees on average. These were removed from the restraint list. For RMSD calculations, all heteroatoms of residues 11-58 were compared. Images of protein structures were prepared using UCSF Chimera 1.11.2.[163]

5.2.4 Simulations

TREDOR simulations were performed with in-house MATLAB scripts by numerical solutions of the von Neumann equations of motion.[223] The numerical solution was obtained using a previously described method [152] where each of the Dyson-dependent propagators was divided on a series of N Dyson-independent propagators with the first order Hamiltonian approximation.[138, 85] For each of N propagators the analytical integration of the time dependent functions of the first order Hamiltonian was applied and N propagators in the matrix form were multiplied on each other, keeping the order. This converges to the exact solution for large enough N. The simulated signals represent the powder integration of the product of the trigonometric functions with power 2. 1154 angles were used in the powder integrations according to ZCW1. The Bessel function simulation was also performed with in-house MATLAB scripts according to the previously published Bessel approximation.

5.2.5 TREDOR fitting

TREDOR curves were fit in a MATLAB script (available upon request) based on the Bessel function approximation of TREDOR described in this paper. The best fit dipolar coupling was found by minimization of the reduced χ^2 (Equation5.1).

$$\chi^2 = \sum (\zeta_{fitted} - \zeta_{experimental})^2 \tag{5.1}$$

The fit curves were plotted with the ggplot package in R.[165] Experimental error is estimated by propagating spectral noise (taken at one standard deviation). Fitting error was generated by Monte Carlo error analysis with 100 Monte Carlo runs assuming a Gaussian noise distribution.

5.3 Results and discussion

5.3.1 Pulse program and sequence analysis

Shown in Figure 5.1 are the pulse programs for pseudo-4D TREDOR. The pulse sequence analysis for the TREDOR period will exclusively focus on the pseudo-4D (H)(N)CNH, as the pseudo-4D (H)N(H)COH experiment requires only replacing N with H.

The TREDOR pulse sequence resembles that of the 3D zf-TEDOR introduced previously [101, 99] and modified later for proton detection [112] except for four major distinctions. First, during acquisition of the indirect (carbon) dimension, TREDOR co-acquires the untransferred (nitrogen) signal. These spectral regions can be placed in the spectrum relative to one another by appropriate placement of the offset, and need not have the same sampling rate. Additional phases and appropriate processing of sum and differences could also be used to separate the two pathways.[192] We used a dwell time ratio of ~2.48, such that both carbon and nitrogen peaks display correctly in ppm after Fourier transformation. Second, TREDOR removes the first z-filter, since it is incompatible with storing both transferred and dephased signals that lie along x and y after the first REDOR period. The second z-filter can be retained, and doubles as water suppression. Third, our implementation of TREDOR begins with cross polarization (CP) to nitrogen, since ^{15}N-^{15}N J couplings are negligible, and therefore antiphase terms associated with homonuclear J-couplings do not build up during the first REDOR period. This allows the removal of the z-filter without significant spectral artifacts even at long mixing times. Fourth, rather than detecting a heteronucleus, the TREDOR sequence is implemented here with a final CP to proton for detection, in order to improve sensitivity and to resolve the resonances in an additional dimension.

For the case of two spins, the pulse program can be understood with a product operator analysis as follows, where we start with transverse nitrogen magnetization generated by CP from

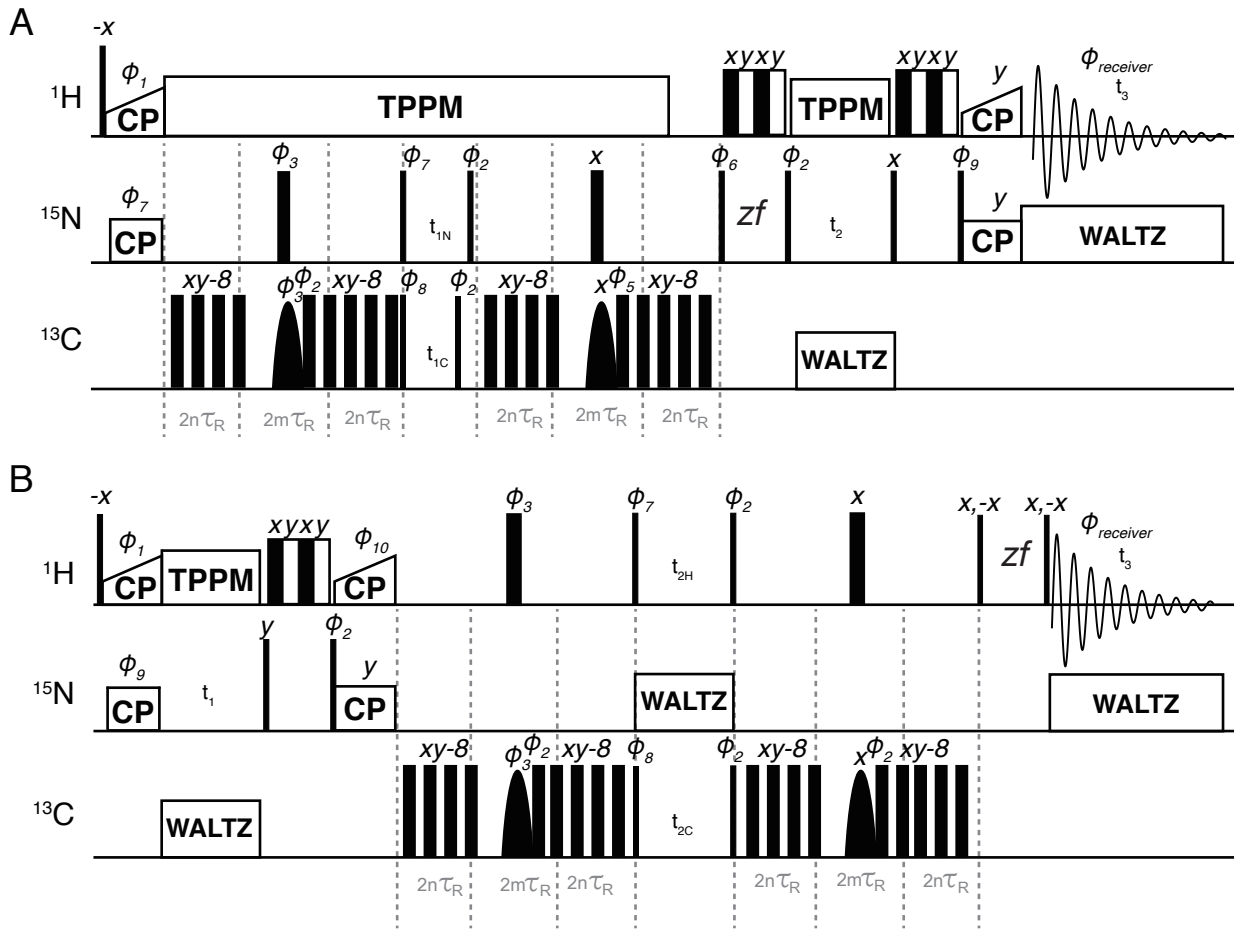

Figure 5.1: Pseudo-4D TREDOR (H)(N)CNH and (H)N(H)CH pulse sequences shown in (A) and (B), respectively. Narrow and wide filled rectangles represent hard $\pi/2$ and π pulses respectively, while soft selective pulses on the carbon channel are shown as parabolas. The REDOR periods are implemented with the usual two hard π pulses [80, 183] per rotor period applied to the carbon channel. REDOR pulses were cycled according to to the xy-8 scheme.[79] In the middle of each REDOR period, a REBURP [119] shaped pulse is used to select the ^{13}C chemical shifts of interest. For ^{15}N-^{13}C$_\alpha$ TREDOR, the bandwidth of this pulse is set to 40 to 70 ppm; for ^{15}N-^{13}Cx TREDOR, to 5 to 53 ppm, which should refocus all side-chain ^{13}C shifts except for that of the C$_\beta$ of serine and threonine; for H-CO TREDOR, to 154 ppm to 254 ppm. In (A) water suppression [233] is split before and after acquisition of the second dimension (t_2). This doubles as two z-filter elements, allowing a reduced phase cycle. Pulses were phase cycled as $\Phi_1 = 11333311, \Phi_2 = 00222200, \Phi_3 = 01, \Phi_5 = 0022, \Phi_6 = 1133, \Phi_7 = 0022, \Phi_8 = 2200, \Phi_9 = 0022, \Phi_{10} = 2, \Phi_{rec'r} = 02202002$, where 0 = x , 1= y, 2= -x, 3 = -y. Unless indicated, other pulses have phase 0. To conveniently encode a correct ppm scale during acquisition of the first indirect dimension in (A) for both ^{15}N and ^{13}C, the increment of the ^{13}C shifts t_{1C} is set to t_{1N}*(γ^{15}N/γ^{13}C), where γ is the gyromagnetic ratio, so that ^{15}N and ^{13}C will share the same ppm scale. Hypercomplex data were acquired by shifting $\Phi_7, \Phi_8, \Phi_{10}$ by -90 degrees, and Φ_9 by +90 in a separate acquisition to acquire pure phases, according to the procedure of Ruben and co-workers.[200]

the protons:

$$\begin{aligned}
\mathrm{N}_x &\xrightarrow{REDOR} \mathrm{N}_x\mathrm{c}_{12} + 2\mathrm{N}_y\mathrm{C}_z\mathrm{s}_{12} \xrightarrow{90_x(\mathrm{N}),90_{-x}(\mathrm{C})} \mathrm{N}_x\mathrm{c}_{12} + 2\mathrm{N}_z\mathrm{C}_y\mathrm{s}_{12} \\
&\xrightarrow{t_{1N},t_{1C}} \mathrm{N}_x\mathrm{c}_{12}cos(\Omega_N t_{1N}) + 2\mathrm{N}_z\mathrm{C}_y\mathrm{s}_{12}cos(\Omega_C t_{1C}) \\
&\xrightarrow{90_x(\mathrm{N}),90_x(\mathrm{C})} \mathrm{N}_x\mathrm{c}_{12}cos(\Omega_N t_{1N}) - 2\mathrm{N}_y\mathrm{C}_z\mathrm{s}_{12}cos(\Omega_C t_{1C}) \\
&\xrightarrow{REDOR} \mathrm{N}_x[\mathrm{c}_{12}^2 cos(\Omega_N t_{1N}) + \mathrm{s}_{12}^2 cos(\Omega_C t_{1C})] \qquad (5.2)
\end{aligned}$$

with

$$\begin{aligned}
\mathrm{s}_{12} &= sin(\omega\frac{t_{mix}}{2}) \\
\mathrm{c}_{12} &= cos(\omega\frac{t_{mix}}{2})
\end{aligned}$$

All terms not converted to observable magnetization are ignored. The analysis presented here follows the real part of the signal in t_1; that is, the cosine-modulated part of the signal. Since the spin part of the Hamiltonian is identical to a J-coupling, the analysis is essentially identical to the 'in-phase COSY' [19] with the only difference being the orientation dependence of the coupling frequency ω, as in REDOR and TEDOR. The first REDOR period creates antiphase carbon coherence with respect to nitrogen ($\mathrm{N}_y\mathrm{C}_z$), which is frequency labeled in t_{1C} with the ^{13}C chemical shift after coherence transfer ($\mathrm{N}_z\mathrm{C}_y$) with two π/2 pulses. The second REDOR period then converts it back to in-phase nitrogen magnetization, which is subsequently frequency labeled in t_2 with the ^{15}N chemical shift. The remaining untransferred nitrogen magnetization (N_x) stays the same during both REDOR periods; it is frequency labeled in both t_{1N} and t_2 with the ^{15}N chemical shift and will thus appear as diagonal peaks in the t_1 and t_2 dimensions. Fortunately, there are relatively few untransferred nitrogen signals, one for each residue, while there are potentially many transferred signals that are resolved in an additional dimension. It should also be noted that during acquisition of the first indirect dimension, the carbon spins ($-2\mathrm{N}_z\mathrm{C}_y$) have a 180 degree phase shift with respect to the untransferred ^{15}N shifts (N_x). They will thus appear with opposite sign in the spectrum and are easily distinguishable.

In proteins, spin systems typically contain multiple couplings, which has the potential to

generate multiple quantum terms. For such cases, the product operator analysis for a NC_2 spin system with the nitrogen coupled to two carbon spins can be considered explicitly, as follows, again starting from nitrogen transverse magnetization:

$$
\begin{aligned}
\mathrm{N}_x &\overset{\omega_{12}2N_zC_{2z},\omega_{13}2N_zC_{3z}}{\longrightarrow} \mathrm{N}_x\mathrm{c}_{12}\mathrm{c}_{13} + 2\mathrm{N}_yC_{2z}\mathrm{s}_{12}\mathrm{c}_{13} + 2\mathrm{N}_yC_{3z}\mathrm{c}_{12}\mathrm{s}_{13} - 4\mathrm{N}_xC_{2z}C_{3z}\mathrm{s}_{12}\mathrm{s}_{13} \\
&\overset{90_x(\mathrm{N}),90_{-x}(\mathrm{C})}{\longrightarrow} \mathrm{N}_x\mathrm{c}_{12}\mathrm{c}_{13} + 2\mathrm{N}_zC_{2y}\mathrm{s}_{12}\mathrm{c}_{13} + 2\mathrm{N}_zC_{3y}\mathrm{c}_{12}\mathrm{s}_{13} - 4\mathrm{N}_xC_{2y}C_{3y}\mathrm{s}_{12}\mathrm{s}_{13} \\
&\overset{t_{1N},t_{1C}}{\longrightarrow} \mathrm{N}_x\mathrm{c}_{12}\mathrm{c}_{13}cos(\Omega_Nt_{1N}) + 2\mathrm{N}_zC_{2y}\mathrm{s}_{12}\mathrm{c}_{13}cos(\Omega_{2C}t_{1C}) + 2\mathrm{N}_zC_{3y}\mathrm{c}_{12}\mathrm{s}_{13}cos(\Omega_{3C}t_{1C}) \\
&- 4\mathrm{N}_xC_{2y}C_{3y}\mathrm{s}_{12}\mathrm{s}_{13}cos(\Omega_Nt_{1N})cos(\Omega_{2C}t_{1C})cos(\Omega_{3C}t_{1C}) \\
&\overset{90_x(\mathrm{N}),90_x(\mathrm{C})}{\longrightarrow} \mathrm{N}_x\mathrm{c}_{12}\mathrm{c}_{13}cos(\Omega_Nt_{1N}) - 2\mathrm{N}_yC_{2z}\mathrm{s}_{12}\mathrm{c}_{13}cos(\Omega_{2C}t_{1C}) - 2\mathrm{N}_yC_{3z}\mathrm{c}_{12}\mathrm{s}_{13}cos(\Omega_{3C}t_{1C}) \\
&- 4\mathrm{N}_xC_{2z}C_{3z}\mathrm{s}_{12}\mathrm{s}_{13}cos(\Omega_Nt_{1N})cos(\Omega_{2C}t_{1C})cos(\Omega_{3C}t_{1C}) \\
&\overset{\omega_{12}2N_zC_{2z},\omega_{13}2N_zC_{3z}}{\longrightarrow} \mathrm{N}_x\mathrm{c}_{12}^2\mathrm{c}_{13}^2cos(\Omega_Nt_{1N}) + \mathrm{N}_x\mathrm{s}_{12}^2\mathrm{c}_{13}^2cos(\Omega_{2C}t_{1C}) + \mathrm{N}_x\mathrm{c}_{12}^2\mathrm{s}_{13}^2cos(\Omega_{3C}t_{1C}) \\
&+ \mathrm{N}_x\mathrm{s}_{12}^2\mathrm{s}_{13}^2cos(\Omega_Nt_{1N})cos(\Omega_{2C}t_{1C})cos(\Omega_{3C}t_{1C}) \qquad (5.3)
\end{aligned}
$$

with

$$
\begin{aligned}
\mathrm{s}_{12} &= sin(\omega_{12}\frac{t_{mix}}{2}) \\
\mathrm{c}_{12} &= cos(\omega_{12}\frac{t_{mix}}{2}) \\
\mathrm{s}_{13} &= sin(\omega_{13}\frac{t_{mix}}{2}) \\
\mathrm{c}_{13} &= cos(\omega_{13}\frac{t_{mix}}{2})
\end{aligned}
$$

All multiple quantum terms not converted to detectable signal are ignored in the analysis, however, one multiple quantum term survives. There is a 3-spin term, $4N_xC_{2y}C_{3y}$ during t_1 evolution, that could appear in the first dimension with a frequency that is dependent on the chemical shifts of all spins. The term is modulated by a sine squared function of both active coupling strengths, such that it builds up more slowly. We identified such multiple quantum signals for H-C TREDOR, as weak peaks placed at the sum of the 3 chemical shifts, and at the proton shift minus the sum of the carbon offsets (see Figure S2). These produce artifacts in the spectrum, similar to those detailed

previously [101] but the position of the artifacts can be placed away from the peaks of interest such that they do not degrade the spectrum.

For a $N_1 - C_i$ spin pair with an active dipolar coupling of ω_{1i}, its crosspeak intensity $V_{1i}(t_{mix})$ in a TEDOR-type spectrum with mixing time t_{mix}, is given as:

$$V_{1i}(t_{mix}) = V_1(0)exp(-\Gamma_1 t_{mix})\langle sin^2(\omega_{1i}t_{mix}/2) \prod_{k=1\neq i}^{n_i} cos^2(\omega_{1k}t_{mix}/2)\rangle \tag{5.4}$$

We follow the notation previously introduced [101] in which $V_1(0)$ is the intensity of the N_1 spin at 0 ms mixing time, n_i is the number of ^{13}C nuclei that are simultaneously coupled to N_1 within the same spin system with a passive coupling of ω_{1k}. The $\langle\rangle$ symbols indicate a powder average. The parameter Γ_1 gives the coherence decay rate of the spin coherence, which can be modeled as a single exponential. The corresponding REDOR-type nitrogen signal, dephased by all multiple couplings inside the system, is:

$$V_1(t_{mix}) = V_1(0)exp(-\Gamma_1 t_{mix})\langle \prod_{k=1}^{n_i} cos^2(\omega_{1k}t_{mix}/2)\rangle \tag{5.5}$$

$$= V_1(0)exp(-\Gamma_1 t_{mix})\langle cos^2(\omega_{1i}t_{mix}/2) \prod_{k=1\neq i}^{n_i} cos^2(\omega_{1k}t_{mix}/2)\rangle \tag{5.6}$$

In the pseudo-4D TREDOR spectrum, since the intensity of the untransferred part of the magnetization is also recorded, the following ratio $\zeta_{ij}(t_{mix})$ of REDOR and TREDOR terms approximately removes the influence of coherence decay and passive couplings:

$$\zeta_{1i}(t_{mix}) = \frac{V_{1i}(t_{mix})}{V_1(t_{mix}) + V_{1i}(t_{mix})} \tag{5.7}$$

$$= \frac{\langle sin^2(\omega_{1i}t_{mix}/2)\prod_{k=1\neq i}^{n_i} cos^2(\omega_{1k}t_{mix}/2)\rangle}{\langle sin^2(\omega_{1i}t_{mix}/2)\prod_{k=1\neq i}^{n_i} cos^2(\omega_{1k}t_{mix}/2) + cos^2(\omega_{1i}t_{mix}/2)\prod_{k=1\neq i}^{n_i} cos^2(\omega_{1k}t_{mix}/2)\rangle} \tag{5.8}$$

$$= \frac{\langle sin^2(\omega_{1i}t_{mix}/2)\prod_{k=1\neq i}^{n_i} cos^2(\omega_{1k}t_{mix}/2)\rangle}{\langle \prod_{k=1\neq i}^{n_i} cos^2(\omega_{1k}t_{mix}/2)\rangle} \tag{5.9}$$

$$\approx \langle sin^2(\omega_{1i}t_{mix}/2)\rangle \tag{5.10}$$

The TREDOR parameter $\zeta_{1i}(t_{mix})$ is free of the impact of coherence decay, if both the transferred and the total magnetization follow the same decay properties during the REDOR periods. This is found to be true for SH3 spectra, even though ^{15}N T_2 is not the dominant source of signal loss, as discussed later. The ratio $\zeta_{1i}(t_{mix})$ does not depend on the starting signal or need correction for experimental imperfections as both signals are acquired simultaneously. Similar to REDOR, the buildup of $\zeta_{1i}(t_{mix})$ is sensitive to the strength of the dipolar coupling and follows an absolute amplitude scale such that dipolar coupling measurements can be performed with short mixing times before the first dipolar oscillation. A good approximation based on the expansion of Bessel functions was derived previously [147] to describe the powder averaged dipolar recoupling signal under MAS. Only the zeroth order Bessel function expansion $J_0(x)$ is needed to describe the observed signal buildup, and the error introduced by ignoring the relative orientations of the active and passive dipolar couplings was shown to be less than 5 to 10 percent.[101] The ratio $\zeta_{1i}(t_{mix})$ can then be approximated as:

$$\zeta_{1i}(t_{mix}) = \frac{1}{2}(1 - [J_0(\sqrt{2}D_{1i}t_{mix})]^2) \tag{5.11}$$

where J_0 is the 0^{th} order Bessel function. This applies for any spin pair 1i in which the spin 1 is coupled to an arbitrary number of heteronuclei i. Formally, this means that the TREDOR curve will build up to a maximum value of 0.5 in a fully labeled sample. Partial labeling of the dephasing nucleus would result in a predictable down-scaling of the TREDOR curve. In a standard TEDOR fit [101], to extract the dipolar couplings, one needs to additionally fit the overall coherence decay rate and an arbitrary amplitude scaling factor since the starting signal is typically not recorded. This consequently puts a high demand on the data density, i.e. many mixing times recorded. In comparison to TEDOR, TREDOR reduces the number of fit parameters by two, which as shown in the later sections allows determination of the dipolar couplings, and therefore C-N distances, with a single mixing time. The two fit parameters that are removed by TREDOR are an amplitude scaling factor and a relaxation parameter, namely $V_1(0)$ and Γ_1 in equation 5.4)

5.3.2 Buildup of the multiple quantum terms

For a multiple spin system with an I spin coupled to more than one spin, the product operator analysis showed that there exists a multiple quantum term that is modulated by two couplings (Equation 5.3). This term is eliminated in zf-TEDOR by the first z-filter, but not removed in TREDOR. It could be detected by an appropriate phase cycle to select double or zero quantum coherences, however, the term builds up slower than the antiphase TEDOR terms (Figure 5.2), and will therefore be more difficult to detect. In TREDOR, it represents a mechanism for total signal loss, and we observe artifacts from this term in the H-CO TREDOR spectrum at the expected offsets for the component that is double quantum in carbon (see Figure S2). The artifacts are similar in appearance to those seen before for carbon detected TEDOR.[101] We simulated the buildup of this term for an NC_2 spin system with similar couplings (Figure 5.2A), and found that it is negligible when the mixing time is smaller than 8 ms. However, when the two couplings are different, the buildup of this term can be as fast as the desired TEDOR term (Figure 5.2B)[48], which explains the observation of artifacts in the H-CO spectra. (The artifacts can be placed such that they do not obscure the desired peaks, see the experimental section and supporting information). However, for mixing times smaller than 4 ms, the contribution of this term is in all cases negligible for N-C TREDOR. Multiple quantum terms with even higher coherence orders coming from systems with more than three spins are not considered, as they will build up even more slowly than the double quantum terms. The influence of passive couplings in a multi-spin system is also revealed by the exact simulation (Figure 5.2C). For the coupling of interest, the modulation by passive couplings in the system leads to a slight damping of the buildup compared with simulation of an isolated spin pair which could bias the fitting towards a slightly larger distance (4.1 Å instead of 4 Å). This bias could be reconciled by fitting TREDOR curves in a system-wide way, taking into account the modulation by other couplings (supporting information). However, for us, the analysis with the single curve fit method (Equation 5.11) produced the same results within experimental error.

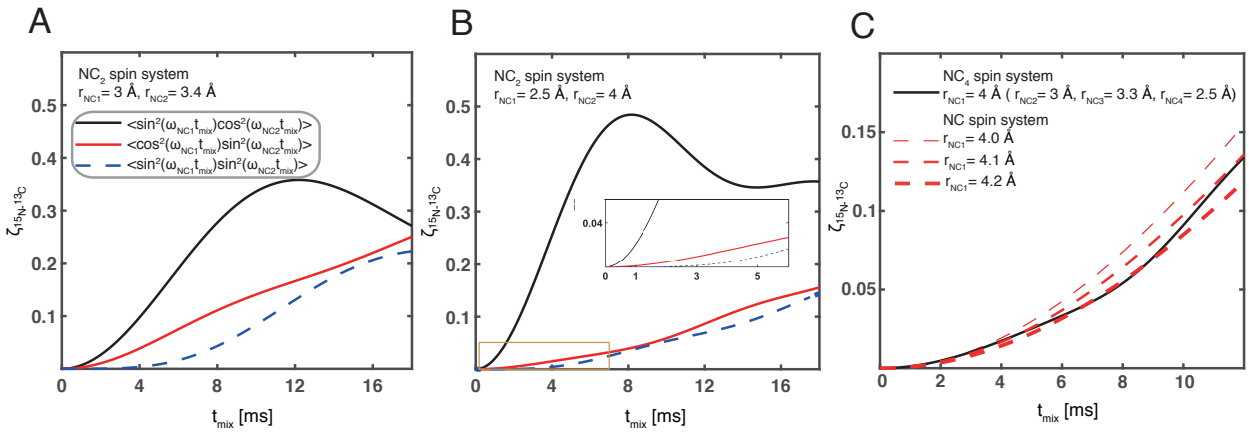

Figure 5.2: Build up of multiple quantum terms in pseudo-4D TREDOR as a function of mixing time. In (A) and (B) an NC_2 system was simulated by an exact numerical method, with distances of r_{NC_1} = 3 Å and r_{NC_2} = 3.5 Å, and of r_{NC_1} = 2.5 Å and r_{NC_2} = 4 Å, respectively. The black line shows buildup of transferred signal via the $2N_yC_{z_1}$ operator, the thick red line shows the buildup of the $2N_yC_{z_2}$ term, and the blue dotted line shows the buildup of the $4N_xC_{z_1}C_{z_2}$ term. The area indicated with a yellow rectangle is expanded in the inset to show the difference in initial buildup rates. In (C), exact simulation of TREDOR signal for a nitrogen-carbon spin pair with distance of 4 Å in a NC_4 system (black line), for isolated nitrogen-carbon spin pairs with distances of 4 Å (thin red dashed line), 4.1 Å (red dashed line) and 4.2 Å (thick red dashed line) is shown.

5.4 TREDOR fitting

To test the performance of TREDOR in measuring accurate distance information in a protein, spectra were acquired at different mixing times for the microcrystalline protein SH3. Since pulse imperfections and RF inhomogeneity impact the apparent dipolar oscillation, we used the one bond N_H-C_α distance of Glycine 51 to calibrate the fit dipolar coupling (Figure 5.3). Since in our spectrum, both dimensions are undersampled, both ^{13}C and ^{15}N have approximately the same lineshape such that the use of peak amplitude was a good measure of the intensity. In other cases, it may be necessary to integrate peaks, or scale amplitudes according to the linewidths. The theoretical dipolar coupling for a rigid one-bond distance of 1.45 Å [58] between ^{15}N and ^{13}C is 1005 Hz when delta pulses are assumed, compared with the coupling value of 810 or 798 Hz measured using TREDOR, giving us an overall scaling factor of 0.8. One contribution to scaling is the result of non-perfect coherence transfer caused by non-ideal pulses. These imperfections include RF inhomogeneity [155, 196], pulse miscalibration and finite pulse effects [102], all of which can be simulated. Under our experimental conditions, the finite pulse effect accounts for a scaling of the dipolar coupling by 0.93. The remaining scaling comes from inhomogeneity, as well as a true scaling, which is a result of fast molecular motions at ambient temperature [64, 210, 89], compared with a low temperature crystal. This factor can be approximated by the order parameter which is reported to be about 0.9 at the protein backbone.[86, 182, 184, 13] Combining the two factors, finite pulses and order parameter, already comes close to the measured scaling factor of 0.8. This value was used to calibrate all other measured distances.

Since TREDOR extracts dipolar couplings by fitting a single parameter, in principle, only one data point is needed for fitting each curve. Figure 5.4 shows TREDOR distance determination for structurally important distances using 1, 2, or 3 mixing points (Figure 5.4A). The full set of distances (above 3-bonds separated) are shown in panel A. All two point fits correctly reported the same distance as the three point fits. However, in some cases, single points with very short (4 ms) or very long mixing time (10 ms) lead to deviation from the fitting with the full set, while the 6 ms mixing time provided faithful fitting. To some degree this is expected, in particular for stronger couplings, due to the non-monotonous nature of the dipolar oscillation curve; without

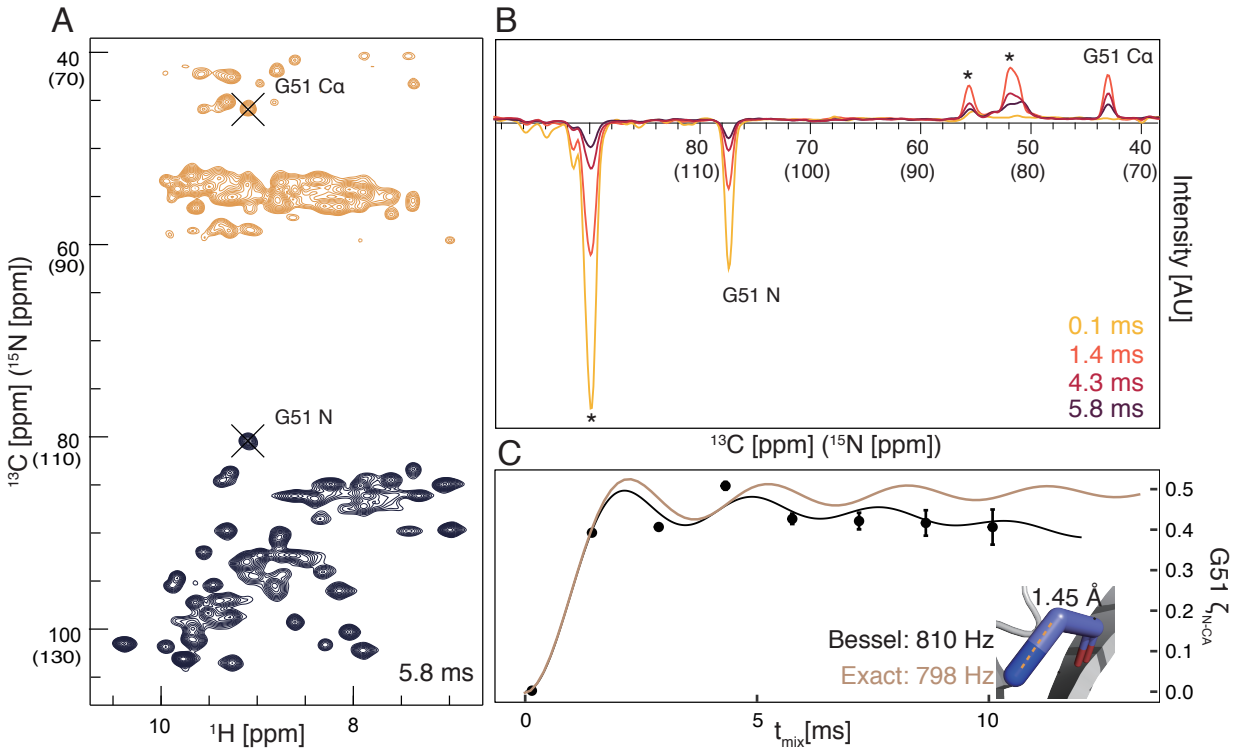

Figure 5.3: Pseudo 4D N-C_α TREDOR and determination of scaling factor. The 2D carbon(nitrogen)-proton plane of pseudo 4D N–C_α TREDOR at 5.8 ms TREDOR mixing is shown in (A). Positive signals from ^{13}C resonances are contoured in orange while the negative ^{15}N signals are shown in black. The peaks of Glycine 51 of the untransferred ^{15}N and transferred carbon resonances are indicated with black crosses. (B) Signal modulation of dephased and transferred magnetization of Glycine 51 N-C_α, shown as 1D carbon (nitrogen) dimension traces at different mixing times. The relevant peaks are as labeled. (C) Fitting of the experimental TREDOR signal to two spin simulations $\zeta_{N-C\alpha}$ with Bessel approximation (black) and exact numerical simulation (red). The dipolar coupling is fit to 810 Hz with the Bessel approximation and to 798 Hz with the exact numerical simulation, which corresponds to a N-C_α distance of 1.45 Å [58] in the crystal structure (inset), revealing a scaling factor of 0.8 (details in text). Asterisks indicates overlapped signals from residues K18, K59, I30 and E45, which are separated in the pseudo-4D spectrum.

prior knowledge of the range of reasonable coupling values, a single point might result in an unstable fit. However, such a case can be easily recognized, since it will only occur when the measured point reaches close to the maximum value of 0.5. Importantly, site-specific distance information was readily determined with short mixing times of 4 and 6 ms, which suggests that the method will be applicable to samples with a wide range of relaxation properties. In Figure 5.4B-E, both intra-residue (Val9N to Val9C_β and C_γ) and inter-residue (Trp42N_ϵ to Ala55C_β) distances are highlighted. Since these distances are well isolated in pseudo-4D TREDOR spectra and have known dipole couplings, we chose them to show in detail how TREDOR faithfully reproduces their N to C distance even with sparse data. The Trp42N_ϵ to Ala55C_β distance is of particular interest for three-dimensional protein structure determination, and was investigated previously using REDOR in a specifically labeled sample.[134] We found the same dipolar coupling using TREDOR, but in a uniformly labeled sample. The TREDOR measured value after scaling of 55.3 $\pm$ 1.4 Hz is equivalent to the previously reported 53 $\pm$ 8 Hz within experimental error. Figure 5.4F shows resolved cross-peaks in the pseudo-4D HCO TREDOR spectrum.

5.4.1 Coherence decay under TREDOR and Choice of Mixing Time

As TREDOR fitting with a single point is possible (Figure 5.4A), it makes sense to choose the optimal mixing time that will provide the most precise fitting. Two opposing factors must be taken into consideration. First, the mixing time needs to be sufficiently long so that the signal can build up, and second, the overall intensity should not relax beyond detection. Since TREDOR measures multiple couplings simultaneously, there will not be a single optimum. Nevertheless, a single mixing point is near optimal for the range of structurally relevant couplings below about 100 Hz, as detailed below. The trade-off between the two factors can be modeled by scaling the TREDOR curve by an exponential decay as in Equation 5.12, taking again the Bessel approximation of powder averaged dipolar recoupling. Additionally, the uncertainty in the TREDOR curve is not constant, but is reduced for later mixing times due to the additional information detected in the

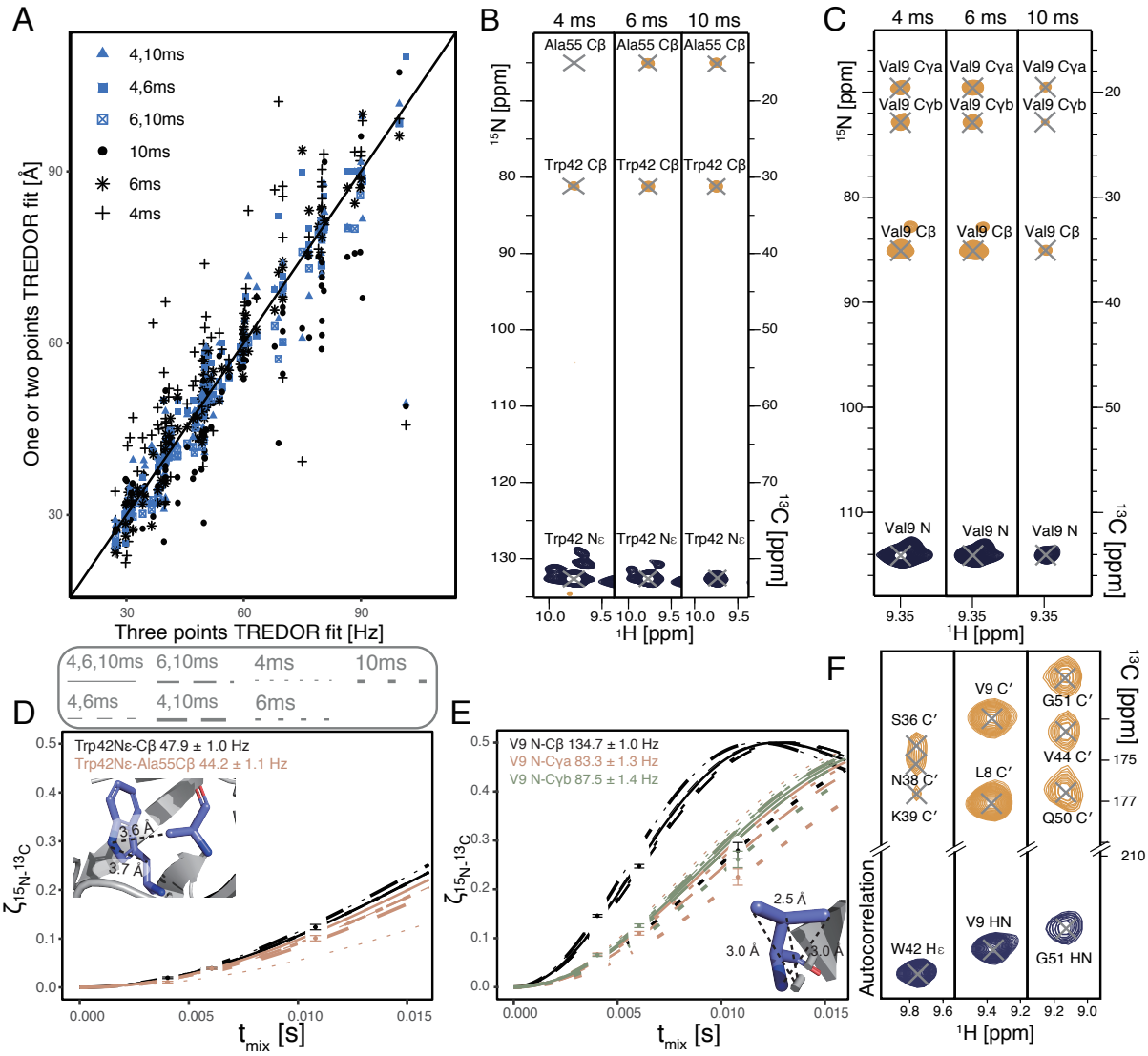

Figure 5.4: Dipolar couplings extracted from pseudo-4D N-Cx and H-CO TREDOR with different sets of mixing times. (A) shows all contacts found in SH3, with dipole coupling measured by fitting subsets of one mixing time (black) and two mixing times (blue) plotted against the fit with the complete set. Site-specific TREDOR fitting for (B,D) Val9 N (C,E) Trp42N$_\epsilon$, with distances from crystal structure as inset. Bessel function fits are shown with three mixing times (solid line), sets of two mixing times (dashed lines), and single mixing time (dotted lines). (F) shows exemplary TREDOR H-CO strips for Trp42N$_\epsilon$, Val9 N, and Gly51 N with a mixing time of 1.2 ms.

REDOR part of the signal. Combining both factors,

$$S/N_{1i}(t_{mix}) = exp(-\Gamma_i t_{mix}) \frac{V_{1i}(t_{mix})}{V_1(t_{mix}) + V_{1i}(t_{mix})} \left[\frac{V_{1i}(t_{mix})^2 + V_{1i}(t_{mix})^2}{(V_1(t_{mix}) + V_{1i}(t_{mix}))^2} \sigma^2 \right]^{-0.5} \quad (5.12)$$

The optimal mixing time is found when $S/N_{1i}(t_{mix})$ is at its maximum. This represents a 'transfer efficiency' that takes into consideration the signal available from both the REDOR and TEDOR components. We simulated several combinations of active and passive couplings that are representative of typical spin systems relevant for protein structure determination (Figure 5.5). We found that for a microcrystalline sample like SH3, this optimal mixing time is around 8 ms for a typical N_H-C_β coupling of 132 Hz, when the coherence decay time is 10 ms (Figure 5.5A). For coupling strengths relevant for structure calculation, which are around 30 to 60 Hz for measuring torsion angles or long range distances in proteins, the optimal mixing time is below 8 ms when the transverse decay time is smaller than 10 ms. However, in practice, it is advisable to use mixing times slightly smaller than that. This is not only to observe spins with short site-specific transverse coherence lifetime, but also to more accurately fit those that have a larger N_H-C_β coupling. This explains our observation that a mixing time of 6 ms leads to the most stable fitting. The effect of other passive couplings in the system is seen by comparing the buildup of similar couplings with varying number and strength of passive couplings. When a relatively weak dipolar coupling (30 or 60 Hz) is modulated by two passive couplings (150 Hz, 65 Hz), the absolute intensity is only slightly smaller than when there is only one passive coupling (150 Hz). In the extreme case, when a weak coupling (60 Hz) is modulated by a very large passive coupling (800 Hz) (Figure 5.5D), the overall profile of the buildup is similar to a smaller passive coupling (Figure 5.5D) but with slightly reduced intensity. This shows that the optimal mixing time is mostly determined by the coherence decay rate and the active coupling. Equation 5.7 assumes the decay of both the REDOR and TEDOR part of the magnetization is dominated by a single exponential decay, which would follow if it is dominated by ^{15}N T_2. This can be checked experimentally by comparing the decay of total signal in TREDOR for each residue in SH3. Indeed, one single exponential decay rate results in a good fit to the total signal decay (Figure 5.6). Surprisingly though, the coherence decay under TREDOR is much faster than the ^{15}N T_2 measured site-specifically via the dephased signals in the (H)NH spectrum. This potentially originates from relaxation of the multiple quantum terms generated during

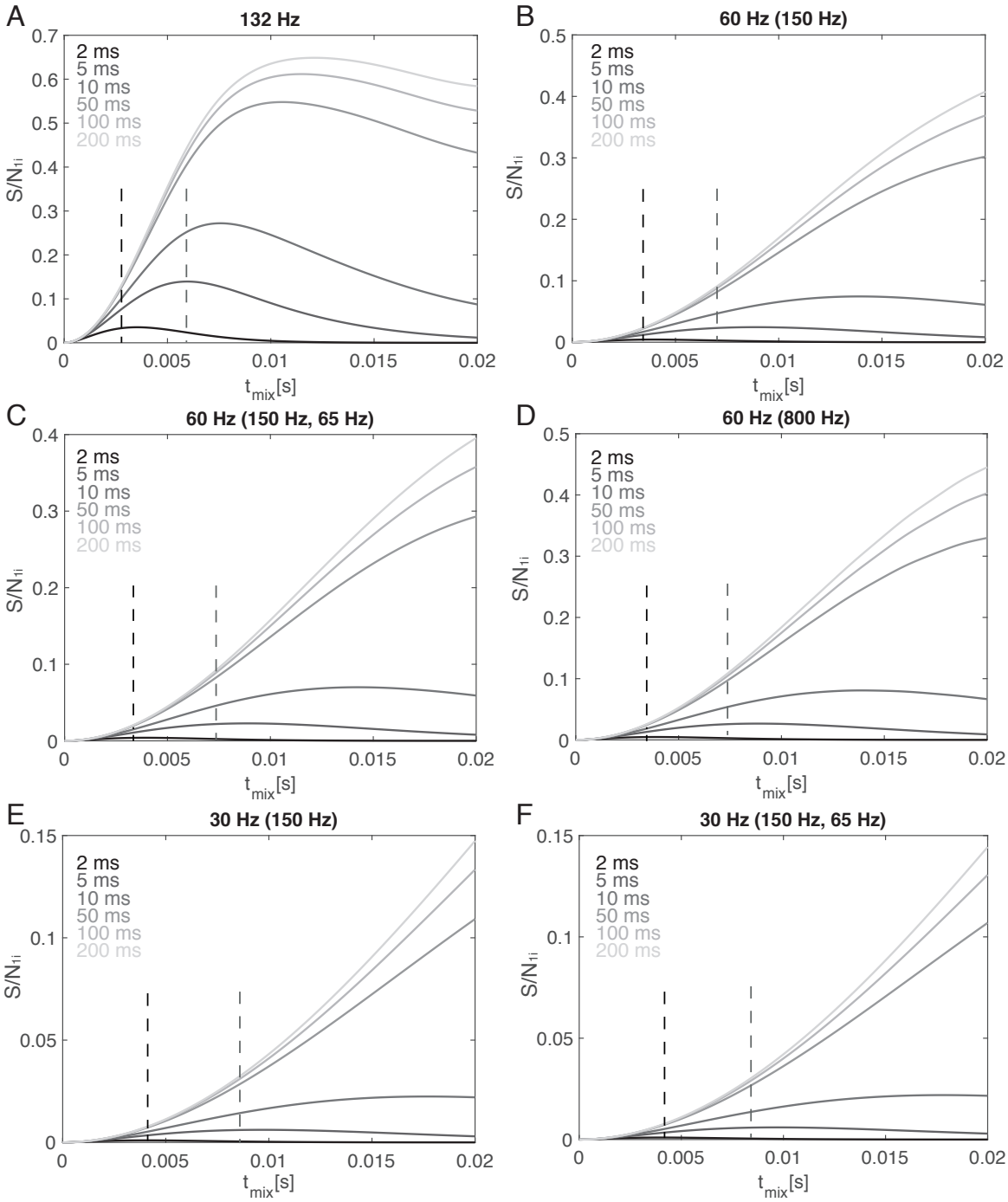

Figure 5.5: Bessel approximation of the TREDOR 'transfer efficiency', shown as signal to noise S/N_{1i} in spin systems with different combinations of active and passive dipolar coupling. Typical active C-N dipole coupling strengths for proteins are indicated, with passive coupling(s) in brackets. Different site-specific coherence decay rates are also included; the system with one spin (A), two (B, D, E) and three (C, F) coupled spins all have an optimal mixing time between 4 to 16 ms when T_2 is smaller than 10 ms. The maximum TREDOR signal to noise when decay time is short ($<$10 ms) is around 5 percent of the starting signal for a 60 Hz coupling and around 2 percent for 30 Hz coupling. Optimal mixing times when the decay time is 5 ms (grey dashed lines) and 2 ms (black dashed lines) are indicated.

the REDOR periods from non ideal pulses. One potential origin is the RF inhomogeneity of the hard pulses during REDOR which will cause incomplete inversion of anti-phase terms $2N_yC_z$. In that case, the additional undesired operators $-2N_yC_x$ and $2N_yC_y$ are created. The effects are minimized with xy phase cycling [79], but not removed. The quantitative description of the influence of the RF inhomogeneity on the TREDOR signal is complicated with the additional influences of the carbon offset, the external field inhomogeneity, the carbon chemical shift anisotropy interaction, the carbon spin-spin relaxation, and non-ideal long selective pulses. All these effects can be approximately replaced with the influence of the apparent spin-spin coherence decay, i.e the measured decay of the combined REDOR and TEDOR parts of the signal. The REDOR pulses on the carbon channel could also result in decoherence through a $T_{2\rho}$ process. We measured the bulk $T_{2\rho}$ of Cα and C' with various spin lock offsets and power (supporting information Table S4 and Table S5). However, $T_{2\rho}$ values of interest are significantly longer than the apparent relaxation rate in TREDOR, eliminating $T_{2\rho}$ as the major contributor to signal losses. The dramatic increase in decay rates further justifies the need for a dipolar recoupling measurement that only requires a short mixing time. Figure 5.6 indicates coherence decay times of about 5 to 10 ms. Note that several residues deviate from the average, but this is likely the result of fitting only 3 time points. A typical TREDOR decay time of 5 to 10 ms indicates an ideal TREDOR mixing time of around 6 ms (Figure 5.5), and the stable fits for 4 and 6 ms suggest that TREDOR will also be useful in the case of faster decay.

5.4.2 Structure calculation

We recorded site-specific TREDOR data on a microcrystalline SH3 sample and performed a structure calculation. The structure of SH3 has previously been calculated [40] using ^{13}C-detected solid-state NMR, based largely on restraints derived from a set of PDSD spectra with a range of mixing times. The distances determined from pseudo-4D TREDOR (full fitting information available in supporting information) are in good agreement with a previously published crystal structure of the SH3 domain (PDB-code 2NUZ). Discrepancies are mostly due to spectral overlap or ambiguous assignments. The fit dipolar couplings were multiplied with the previously determined scaling factor of 1.25 and converted to distances. Unambiguous pseudo-4D N-Cx TREDOR re-

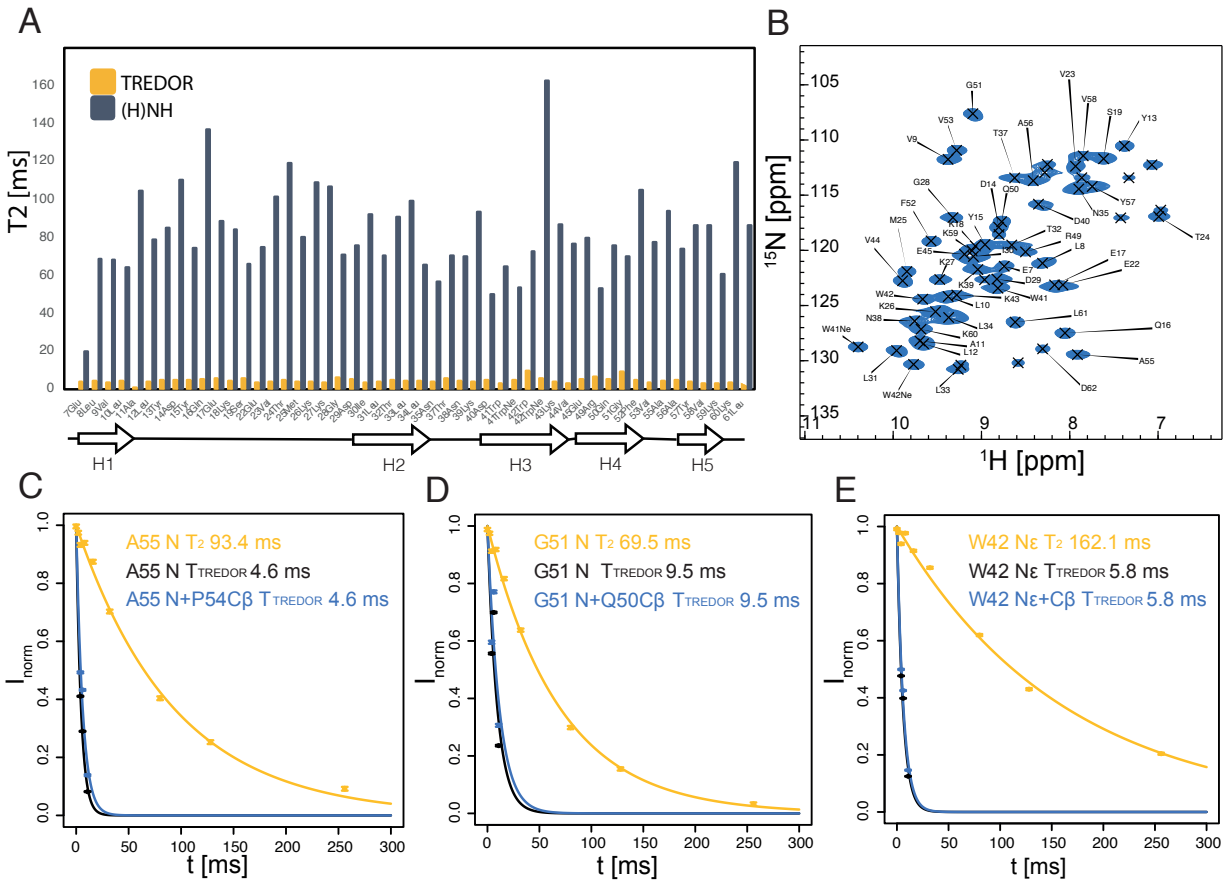

Figure 5.6: Site-specific ^{15}N T_2 rate during TREDOR (A yellow) and (H)NH (A dark blue) and (H)NH spectrum at 0 ms delay (B). The topology of SH3 is plotted under (A); there is no obvious correlation of the size of the ^{15}N T_2 with the secondary structure of the residue. The coherence decay rate under TREDOR is significantly higher than that under (H)NH (supporting information table S1); but for all residues, a single exponential decay well predicts the total signal decay (examples of decay of residues A55, G51 and W42 are shown in (C), (D) and (E)).

straints relevant for torsion angle determination can be compared with distances in the crystal structure (Figure 5.7). Compared with TEDOR data alone, TREDOR determines the $\chi 1$ and ψ angle more accurately as indicated by comparison of the corresponding distances with the crystal structure (correlation coefficient of 0.82 for TREDOR compared with 0.30 for TEDOR using 3 data points). For the comparison, only isolated peaks were considered. Where peak overlap occurs, the TREDOR distance tends to be too large, since the overlap mainly increases the intensity of the REDOR signal. Avoiding this problem would require a more sophisticated peak deconvolution, or extension to higher dimensional spectra. This is also seen from the fit curves: most cases where fit curves deviate from the experimental data significantly are due to spectral overlap (supporting in-

formation Figure S1). However, TREDOR still performed better in predicting the precise distance when overlapped peaks in the 2D (H)NH spectra (Figure 5.6B) are included for the analysis (correlation coefficient of 0.57 for TREDOR compared with 0.21 for TEDOR). All distances extracted from the pseudo-4D N-C TREDOR and the pseudo-4D H-CO TREDOR were subsequently used as restraints for a CYANA [84] structure calculation (see Material and Methods). The pseudo-4D H-CO TREDOR spectra provide orthogonal contacts to define the beta-fold of SH3 better and are particularly suitable for determination of inter-strand contacts in anti-parallel beta sheet structures.

As input, we used 5 (N-Cx) + 12 (H-CO) medium (contacts 2 to 4 residues apart) and 18 (N-Cx)

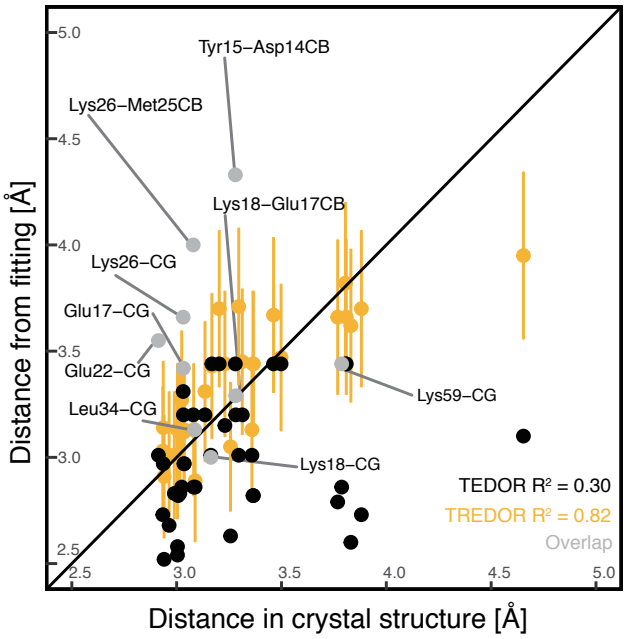

Figure 5.7: Comparison of NMR derived distances that define $\chi 1$ and ψ torsion angles for residues with a single conformer in the crystal structure. Distances are compared with those of the crystal structure 2NUZ either fitting with pseudo-4D TREDOR data (yellow and grey) or only the N-C TEDOR component (black). Long range contacts or ambiguous torsion angle restraints are not included in the analysis to exclude potential assignment errors. Contacts with overlapped nitrogen signals are shown in grey and were not included in the determination of R^2. Pseudo-4D TREDOR predicts distances (R^2 0.82) more accurately than TEDOR (R^2 0.30) with data from 3 mixing times. Yellow error bars are indicated at $\pm$ 10% to indicate the expected error from ignoring relative orientations.[101]

+ 16 (H-CO) long range restraints (contacts greater than 4 residues apart) from the N-Cx and H-CO spectra (details in the supporting information). In addition we input 83 (N-Cx) + 26 (H-CO) intra-residue or sequential restraints that help define torsion angles. These include the ψ angle that

is already defined by the chemical shifts for most residues, but also the $\chi 1$ angle that is not. The 10 percent distance error estimates used here results in large errors in angles, and further improvement would be needed for true angle determination. Nevertheless, the information excludes part of the Ramachandran space, which is helpful particularly for glycine residues where TALOS does not always provide confident predictions. Considering that the short mixing time TREDOR was used primarily for assignments, four days of experiments are enough to determine the distances used in the structure calculation. Additionally, we enforced backbone torsion angles predicted by TALOS-N.[193] The resulting structured ensemble (20 lowest energy structures, residues 11-58) is shown in Figure 5.8, alongside an overlay of the average structure with the reference crystal structure (PDB-code 2NUZ). Distance information from the TREDOR method faithfully reproduced the overall fold of the SH3 domain with an backbone ensemble RMSD of 1.8 Å in the structured part (residues 11 to 58). This covers nearly the range of assigned resicues (7-62), which coincides with the range of residues determined by x-ray diffraction. The TREDOR calculated structure differs from the crystal structure by 2.1 Å (again comparing residues 11-58) mainly on the ends of the sequence due to lack of contacts, and the very dynamic loop region. Additionally, we measured N-CA, N-CO and H-CA distances with TREDOR. However, we found very few structurally interesting long-range distances, which is likely due to the presence very strong 1-bond dipole couplings for the N-CA and N-CO cases, and to somewhat longer distances for the H-CA case as compared with H-CO distances. Mostly we observed intra-residue or sequential contacts. We therefore used only the N-Cx and H-CO data during structure calculation. Figure 5.8C shows the per-residue RMSD as compared to the crystal structure. In the loop regions, TREDOR side-chain to side-chain contacts (see supporting information Table S2, last 7 contacts, for details) improve the RMSD and thus aid in accurately determining structure. Since the N-Cx TREDOR data contains a multitude of backbone to side-chain contacts, it is surprisingly valuable in defining the structure of the RT-loop, which is particularly challenging using backbone data alone.[121, 122] This is obvious, as in the loop region, the all atom RMSD is improved by 2 to 4 Å (Figure 5.8C)

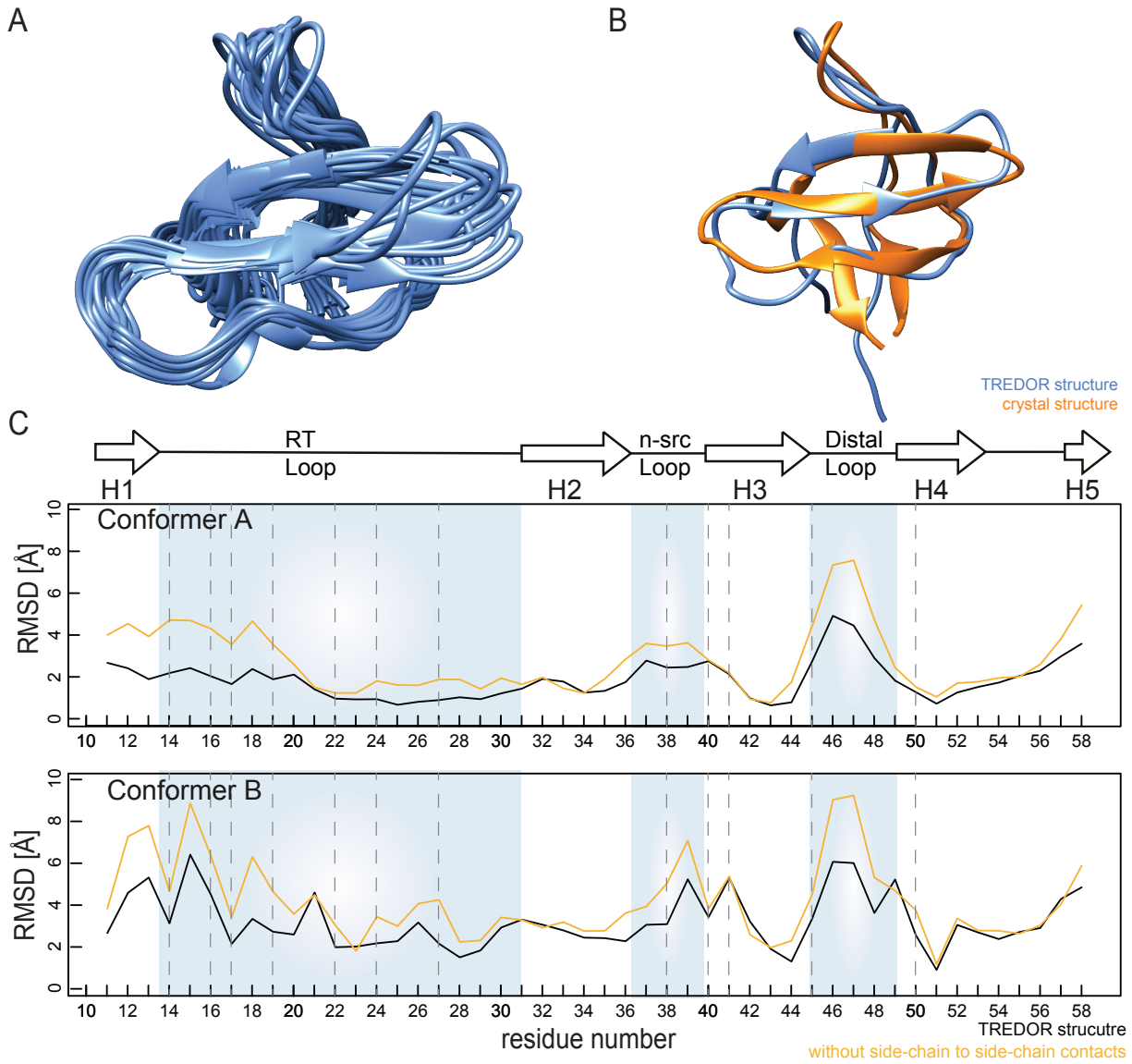

Figure 5.8: Structure of SH3 obtained from TREDOR distances and TALOS-N backbone dihedral angle-restraints. (A) shows the 20 lowest energy structures of 100 calculated structures from a CYANA calculation. The structurally defined region from residues 11-58 is shown. The backbone ensemble RMSD of 20 structures is 1.8 Å for these residues. (B) compares the lowest-energy TREDOR structure with the reference crystal structure (PDB-code 2NUZ, orange), revealing the correct overall fold of SH3. The RMSD of the TREDOR calculated structure vs the crystal structure A (upper panel) is 2.1 Å. (C) TREDOR derived restraints faithfully reproduced the crystal SH3 structure, as shown by the low residue specific all atom RMSD values across the sequence to both conformations in the crystal structure (conformers A and B). Including side-chain to side-chain contacts (black line), which are a unique feature of TREDOR, increases the accuracy in the loop region (blue shading) compared with the structure calculated without (yellow line). Dashed lines indicate residues with side-chain proton to side-chain carbon contacts.

5.5 Conclusion

In conclusion, we demonstrate TREDOR as a fast and robust method to precisely measure site-specific internuclear distances using MAS NMR. We show that the 2-fold increased information in TREDOR leads to accurate distance determination by stabilizing the dipolar oscillation fitting even for the extreme limit of a single point fit. This allows acquisition at the optimal mixing time where signal is maximized, which together with the simultaneous acquisition inherent to the TREDOR method leads to an order of magnitude improvement. We demonstrate TREDOR in two variants, pseudo-4D N-Cx and H-CO. The data results in efficient protein structure determination. We expect that adaptations of TREDOR, including extension to other spin 1/2 nuclei, will be useful for a variety of applications in materials science, chemistry and biology. While we demonstrate TREDOR with deuterated protein and fast spinning of 55 kHz, or with fully protonated protein and 100 kHz spinning, the relatively low RF requirement of REDOR will allow extension to even faster spinning, so long as the hardware allows the Rabi frequency of the REDOR pulses to exceed the magic-angle spinning frequency.

CHAPTER 6

Conclusion

The transmembrane signaling mechanism of the histidine kinase CitA can be solved piece-wise by a combination of NMR techniques (Figure 6.1). The possibility to do sequence specific assignment offered by the high sensitivity and additional proton dimension of ^{1}H-detected MAS NMR made the resonances of TM helices available (Chapter 2). The analysis of chemical shift revealed in secondary structure changes involved in the kinase activation. The monomer unit could be assigned to up to 70% completeness despite CitA having the largest monomer size of a membrane protein to be assigned in such a way up till today. The P-helix formation at the end of PASp from a coil, which was only shown in one residue, L154, previously [178], could be extended to further residues from L155 to I158 into the TM2 helix. The coil to helix transition is also seen at 180GAVG183 motif, which sits at the interface between the inner membrane and the cytosol according to the solvent transfer experiments. This allows the upward, piston-like motion of TM2 into the periplasm. The conserved 192KK193 linker acts like an anchor between TM2 and PASc and loosens the PASc dynamics with the TM2 pulling by transitioning into a coil conformation. As a result, the PASc domain has higher mobility and necessary for conformational changes.

The cytosolic signaling mechanism of the PAS domain, found in more than 2000 sensor kinases [113] is not known. The N-terminal helix of PASc, which directly follows the TM2 helix, undergoes functionally important exchange in solution as seen by CEST measurement [177]. Following this, M. Salvi postulated that the PASc domain undergoes dramatic changes from an anti-parallel to a parallel dimer arrangement in the PASc N-terminal helix upon CitA activation [177]. From the crystal structure, the N-terminal helix rearrangement is accompanied by the

drastic movement of the β-sheets of the PASc domain, which can be observed at the PASc domain C-terminal as the large difference in the inter-dimer distance. This model is confirmed in this thesis both by the ^{19}F CODEX based site-specific distance measurement (Chapter 4) and the validated functionally ^{31}P-detected NMR based assay (Chapter C). The N288D anti-parallel dimer mutation in the PASc domain of the PASc-kin construct results in a drop of the ATP hydrolysis rate compared to the WT PASc, as revealed by the ^{31}P activity assay. The inter-dimer distance between residue N308 at the C-terminus of the PASc domain in the PASpc construct decreased to 11 Å, leading to an observable ^{19}F CODEX decay.

We were able to paint a holistic picture of CitA activation by citrate binding in the periplasm to the DHp domain in the cytosol through eclectic NMR approaches. However, the signal transduction mechanism from the cytosolic PAS domain to the DHp domain cannot be studied with the current constructs used in this thesis. The common themes involved in the signal transduction to DHp domains is the symmetry-asymmetry transitions (where the DHp dimer transition from a symmetric dimer to an asymmetric dimer) and stabilization-destabilization of the α-helical linkers at the DHp domain N-terminus [88, 159]. The faster dynamics and the parallel dimer arrangement observed by the experiments presented here can contribute to the destabilization of the α-helical linkers and the symmetry-assymetry transition, respectively. But, how exactly theses changes upon citrate binding in the PASc domain would cause the DHp domain activation requires further studies using the full length CitA [81]. For more detailed structural insights into the PASpc construct, side chain resonance assignment will also be a must. To achieve this, either experimental conditions compatible with non-deuterated sample or contact measurements using carbon or nitrogen nuclei are needed. In addition, enough contacts should be available to resolve the ambiguity between inter- versus intra-monomer contacts. For this, more time-saving contacts determination methods applicable to membrane proteins like TREDOR (Chapter 5) will be preferred. With the availability of the high magnetic field up to 1.2 GHz, ultra-fast MAS up to 100 kHz and better pulse sequences, solving the full structure of the CitA PASpc construct might indeed be on the horizon.

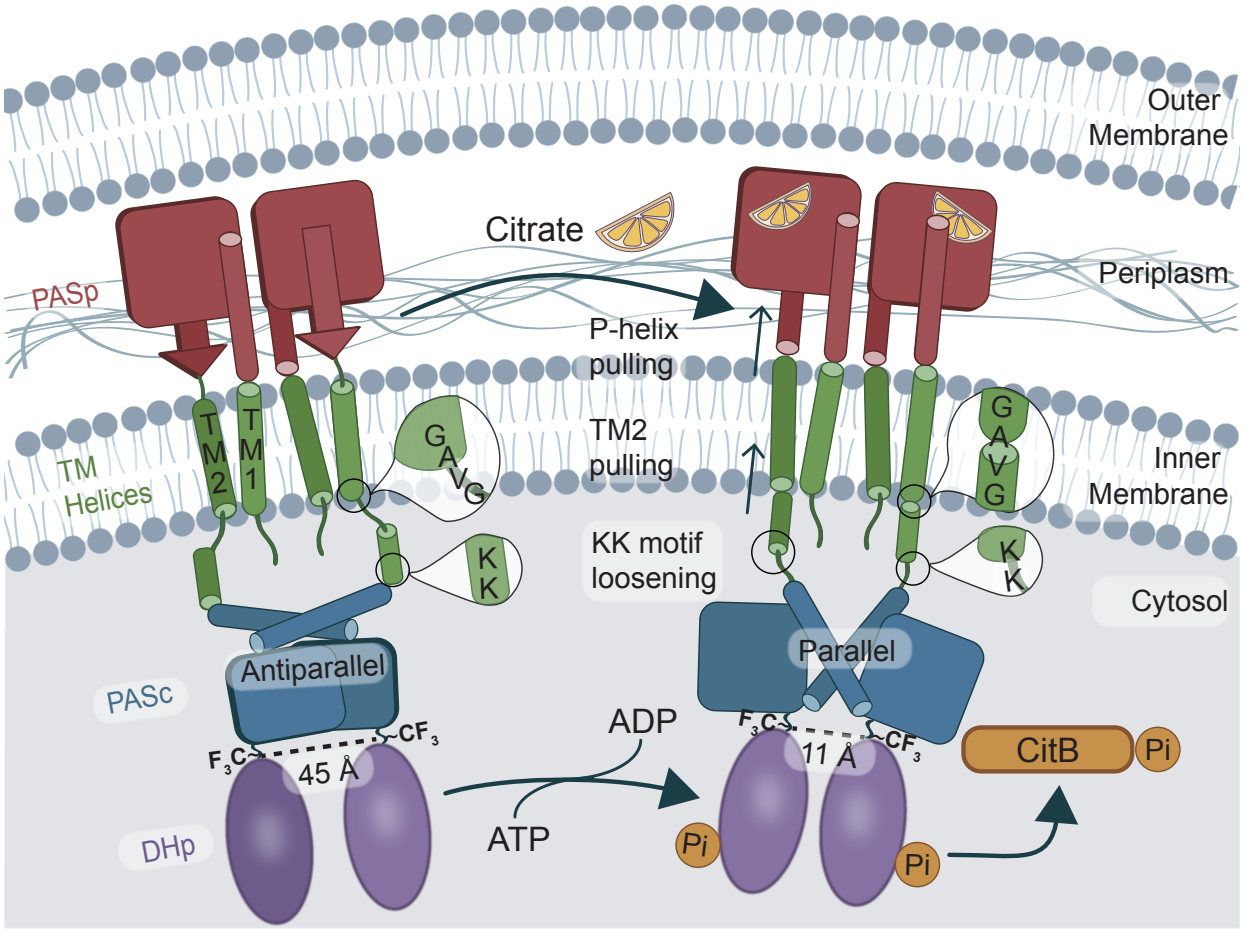

Figure 6.1: Mechanism of CitA activation by citrate binding. The binding of citrate in the PASp citrate binding site causes a change in the hydrogen bond network and a contraction of the β-scaffold. This stabilizes the PASp and forms a P-helix at the PASp C-terminus. Such change in the secondary structure propagates through the membrane, shifting the TM2 helix upwards in a piston-like motion into the periplasm. The 180GAVG183 motif at the end of TM2 undergoes the same random coil to α-helix transition as the P-helix after citrate binding. Effectively, the 192KK193 motif upstream of PASc gets loosened due to the upward pulling of TM2 and increases the PASc dynamics downstream. These sequential structural and dynamics changes allows the PASc dimer to switch from an anti-parallel to parallel arrangement. The parallel arrangement in the PASc has a smaller inter-dimer distance compared with the anti-parallel arrangement, which potentially causes DHp domain symmetry-asymmetry transition and consequently, CitA cross-phosphorylation.

BIBLIOGRAPHY

[1] Martine I Abboud, Philip Hinchliffe, Jürgen Brem, Robert Macsics, Inga Pfeffer, Anne Makena, Klaus-Daniel Umland, Anna M Rydzik, Guo-Bo Li, James Spencer, et al. 19f-nmr reveals the role of mobile loops in product and inhibitor binding by the são paulo metallo-β-lactamase. *Angewandte Chemie International Edition*, 56(14):3862–3866, 2017.

[2] Ogun Adebali, Marharyta G Petukh, Alexander O Reznik, Artem V Tishkov, Amit A Upadhyay, and Igor B Zhulin. Class iii histidine kinases: a recently accessorized kinase domain in putative modulators of type iv pilus-based motility. *Journal of bacteriology*, 199(18):e00218–17, 2017.

[3] Michael V Airola, Kylie J Watts, Alexandrine M Bilwes, and Brian R Crane. Structure of concatenated hamp domains provides a mechanism for signal transduction. *Structure*, 18(4):436–448, 2010.

[4] Umit Akbey, Hartmut Oschkinat, and Barth-Jan van Rossum. Double-nucleus enhanced recoupling for efficient 13c mas nmr correlation spectroscopy of perdeuterated proteins. *J. Am. Chem. Soc.*, 131(47):17054–17055, 2009.

[5] Bruce Alberts, Alexander Johnson, Julian Lewis, David Morgan, Martin Raff, Keith Roberts, Peter Walter, John Wilson, and Tim Hunt. *Molecular biology of the cell*. WW Norton & Company, 2017.

[6] Vivek Anantharaman, S Balaji, and L Aravind. The signaling helix: a common functional theme in diverse signaling proteins. *Biology direct*, 1(1):1–16, 2006.

[7] Loren B. Andreas, Alexander B. Barnes, Bjoern Corzilius, James J. Chou, Eric A. Miller, Marc Caporini, Melanie Rosay, and Robert G. Griffin. Dynamic nuclear polarization study of inhibitor binding to the m2 18-60 proton transporter from influenza a. *Biochemistry*, 52(16):2774–2782, 2013.

[8] Loren B Andreas, Alexander B Barnes, Björn Corzilius, James J Chou, Eric A Miller, Marc Caporini, Melanie Rosay, and Robert G Griffin. Dynamic nuclear polarization study

of inhibitor binding to the m218–60 proton transporter from influenza a. *Biochemistry*, 52(16):2774–2782, 2013.

[9] Loren B Andreas, Matthew T Eddy, James J Chou, and Robert G Griffin. Magic-angle-spinning nmr of the drug resistant s31n m2 proton transporter from influenza a. *J. Am. Chem. Soc.*, 134(17):7215–7218, 2012.

[10] Loren B Andreas, Tanguy Le Marchand, Kristaps Jaudzems, and Guido Pintacuda. High-resolution proton-detected nmr of proteins at very fast mas. *Journal of magnetic resonance*, 253:36–49, 2015.

[11] Loren B Andreas, Jan Stanek, Tanguy Le Marchand, Andrea Bertarello, Diane Cala-De Paepe, Daniela Lalli, Magdaléna Krejčíková, Camille Doyen, Carl Öster, Benno Knott, et al. Protein residue linking in a single spectrum for magic-angle spinning nmr assignment. *Journal of biomolecular NMR*, 62(3):253–261, 2015.

[12] Leif Antonschmidt, Rıza Dervişoğlu, Vrinda Sant, Kumar Tekwani Movellan, Ingo Mey, Dietmar Riedel, Claudia Steinem, Stefan Becker, Loren B Andreas, and Christian Griesinger. Insights into the molecular mechanism of amyloid filament formation: Segmental folding of α-synuclein on lipid membranes. *Science Advances*, 7(20):eabg2174, 2021.

[13] Sam Asami and Bernd Reif. Comparative study of redor and cppi derived order parameters by 1h-detected mas nmr and md simulations. *J. Phys. Chem. B*, 121(37):8719–8730, 2017.

[14] Priti Bachhawat, GVT Swapna, Gaetano T Montelione, and Ann M Stock. Mechanism of activation for transcription factor phob suggested by different modes of dimerization in the inactive and active states. *Structure*, 13(9):1353–1363, 2005.

[15] Alex D Bain. Chemical exchange in nmr. *Prog. Nucl. Magn. Reson. Spectrosc.*, 43:63–103, 2003.

[16] Vikram S. Bajaj, Melody L. Mak-Jurkauskas, Marina Belenky, Judith Herzfeld, and Robert G. Griffin. DNP enhanced frequency-selective TEDOR experiments in bacteriorhodopsin. *J. Magn. Reson.*, 202(1):9–13, jan 2010.

[17] M Baldus and B H Meier. Broadband polarization transfer under magic-angle spinning: application to total through-space-correlation nmr spectroscopy. *J. Magn. Reson.*, 128(2):172–193, 1997.

[18] Emeline Barbet-Massin, Andrew J Pell, Joren S Retel, Loren B Andreas, Kristaps Jaudzems, W Trent Franks, Andrew J Nieuwkoop, Matthias Hiller, Victoria Higman, Paul Guerry, et al. Rapid proton-detected nmr assignment for proteins with fast magic angle spinning. *Journal of the American Chemical Society*, 136(35):12489–12497, 2014.

[19] Ad Bax, David Max, and David Zax. Measurement of long-range 13c-13c j couplings in a 20-kda protein-peptide complex. *J. Am. Chem. Soc.*, 114(17):6923–6925, 1992.

[20] Marvin J. Bayro, Matthias Huber, Ramesh Ramachandran, Timothy C. Davenport, Beat H. Meier, Matthias Ernst, and Robert G. Griffin. Dipolar truncation in magic-angle spinning NMR recoupling experiments. *J. Chem. Phys.*, 130(11), 2009.

[21] A E Bennett, R G Griffin, J H Ok, and S Vega. Chemical shift correlation spectroscopy in rotating solids: Radio frequency-driven dipolar recoupling and longitudinal exchange. *J.Chem.Phys.*, 96(11):8624–8627, 1992.

[22] Andrew E. Bennett, Chad M. Rienstra, Michèle Auger, K. V. Lakshmi, and Robert G. Griffin. Heteronuclear decoupling in rotating solids. *J. Chem. Phys.*, 103(16):6951–6958, 1995.

[23] Pierrick Berruyer, Moreno Lelli, Matthew P Conley, Daniel L Silverio, Cory M Widdifield, Georges Siddiqi, David Gajan, Anne Lesage, Christophe Copéret, and Lyndon Emsley. Three-dimensional structure determination of surface sites. *J. Am. Chem. Soc.*, 139(2):849–855, 2017.

[24] Maxine Beveridge, Young-Whan Park, Jeff Hermes, Angela Marenghi, Gerard Brophy, and Albert Santos. Detection of p56lck kinase activity using scintillation proximity assay in 384-well format and imaging proximity assay in 384-and 1536-well format. *Journal of biomolecular screening*, 5(4):205–211, 2000.

[25] Manasi P Bhate, Kathleen S Molnar, Mark Goulian, and William F DeGrado. Signal transduction in histidine kinases: insights from new structures. *Structure*, 23(6):981–994, 2015.

[26] John A Bittl, Jean DeLayre, and Joanne S Ingwall. Rate equation for creatine kinase predicts the in vivo reaction velocity: phosphorus-31 nmr surface coil studies in brain, heart, and skeletal muscle of the living rat. *Biochemistry*, 26(19):6083–6090, 1987.

[27] Alexandre G Blanco, Maria Sola, F Xavier Gomis-Rüth, and Miquel Coll. Tandem dna recognition by phob, a two-component signal transduction transcriptional activator. *Structure*, 10(5):701–713, 2002.

[28] Felix Bloch. Nuclear induction. *Physical review*, 70(7-8):460, 1946.

[29] Anja Böckmann, Carole Gardiennet, René Verel, Andreas Hunkeler, Antoine Loquet, Guido Pintacuda, Lyndon Emsley, Beat H Meier, and Anne Lesage. Characterization of different water pools in solid-state nmr protein samples. *J. Biomol. NMR*, 45(3):319, 2009.

[30] Coloring Books, Education Corner, Irving Geis, and David Goodsell. Two-component systems.

[31] Alexey S Borisov, Paul Hazendonk, and Paul G Hayes. Solid-state nuclear magnetic resonance spectroscopy: a review of modern techniques and applications for inorganic polymers. *Journal of Inorganic and Organometallic Polymers and Materials*, 20(2):183–212, 2010.

[32] PD Boyer, Marlene DeLuca, KE Ebner, DE Hultquist, and JB Peter. Identification of phosphohistidine in digests from a probable intermediate of oxidative phosphorylation. *Journal of Biological Chemistry*, 237(10):PC3306–PC3308, 1962.

[33] Ralph A Bradshaw and Edward A Dennis. Cell signaling: yesterday, today, and tomorrow. In *Handbook of Cell Signaling*, pages 1–4. Elsevier, 2010.

[34] Jürgen Brem, Weston B Struwe, Anna M Rydzik, Hanna Tarhonskaya, Inga Pfeffer, Emily Flashman, Sander S van Berkel, James Spencer, Timothy DW Claridge, Michael A McDonough, et al. Studying the active-site loop movement of the são paolo metallo-β-lactamase-1. *Chemical science*, 6(2):956–963, 2015.

[35] David R Buckler, Yuchen Zhou, and Ann M Stock. Evidence of intradomain and interdomain flexibility in an ompr/phob homolog from thermotoga maritima. *Structure*, 10(2):153–164, 2002.

[36] Daelynn R Buelow and Tracy L Raivio. Three (and more) component regulatory systems–auxiliary regulators of bacterial histidine kinases. *Molecular microbiology*, 75(3):547–566, 2010.

[37] Jarrod J Buffy, Alan J Waring, and Mei Hong. Determination of peptide oligomerization in lipid bilayers using 19f spin diffusion nmr. *Journal of the American Chemical Society*, 127(12):4477–4483, 2005.

[38] Morgane Callon, Alexander A Malär, Sara Pfister, Václav Římal, Marco E Weber, Thomas Wiegand, Johannes Zehnder, Matías Chávez, Riccardo Cadalbert, Rajdeep Deb, et al. Biomolecular solid-state nmr spectroscopy at 1200 mhz: the gain in resolution. *Journal of Biomolecular NMR*, pages 1–18, 2021.

[39] Emily J Capra and Michael T Laub. Evolution of two-component signal transduction systems. *Annual review of microbiology*, 66:325–347, 2012.

[40] Federica Castellani, Barth Van Rossum, Annette Diehl, Mario Schubert, Kristina Rehbein, and Hartmut Oschkinat. Structure of a protein determined by solid-state magic-angle-spinning nmr spectroscopy. *Nature*, 420(6911):99–102, 2002.

[41] Lynette Cegelski. REDOR NMR for drug discovery, nov 2013.

[42] Lynette Cegelski, Dirk Steuber, Anil K. Mehta, Daniel W. Kulp, Paul H. Axelsen, and Jacob Schaefer. Conformational and quantitative characterization of oritavancin- peptidoglycan complexes in whole cells of Staphylococcus aureus by in vivo 13C and 15N labeling. *J. Mol. Biol.*, 357(4):1253–1262, apr 2006.

[43] Jonah Cheung and Wayne A Hendrickson. Crystal structures of c4-dicarboxylate ligand complexes with sensor domains of histidine kinases dcus and dctb. *Journal of Biological Chemistry*, 283(44):30256–30265, 2008.

[44] Veniamin Chevelkov, Katja Faelber, Anna Schrey, Kristina Rehbein, Anne Diehl, and Bernd Reif. Differential line broadening in MAS solid-state NMR due to dynamic interference. *J. Am. Chem. Soc.*, 129(33):10195–10200, aug 2007.

[45] Veniamin Chevelkov, Uwe Fink, and Bernd Reif. Accurate determination of order parameters from 1h, 15n dipolar couplings in mas solid-state nmr experiments. *J. Am. Chem. Soc.*, 131(39):14018–14022, 2009.

[46] Claude Cohen-Tannoudji, Bernard Diu, and Franck Laloë. *Quantum Mechanics, Volume 1: Basic Concepts, Tools, and Applications*. John Wiley & Sons, 2019.

[47] Michael T Colvin, Robert Silvers, Qing Zhe Ni, Thach V Can, Ivan Sergeyev, Melanie Rosay, Kevin J Donovan, Brian Michael, Joseph Wall, Sara Linse, et al. Atomic resolution structure of monomorphic aβ42 amyloid fibrils. *J. Am. Chem. Soc.*, 138(30):9663–9674, 2016.

[48] Harold Conroy. Molecular schrödinger equation. viii. a new method for the evaluation of multidimensional integrals. *J. Chem. Phys.*, 47(12):5307–5318, 1967.

[49] Peter B Crowley, Ciara Kyne, and William B Monteith. Simple and inexpensive incorporation of 19 f-tryptophan for protein nmr spectroscopy. *Chemical communications*, 48(86):10681–10683, 2012.

[50] Eugenio Daviso, Matthew T. Eddy, Loren B. Andreas, Robert G. Griffin, and Judith Herzfeld. Efficient resonance assignment of proteins in MAS NMR by simultaneous intra- and inter-residue 3D correlation spectroscopy. *J. Biomol. NMR*, 55(3):257–265, mar 2013.

[51] Marien I de Jonge, Martine P Bos, Hendrik J Hamstra, Wim Jiskoot, Peter van Ulsen, Jan Tommassen, Loek van Alphen, and Peter van der Ley. Conformational analysis of opacity proteins from neisseria meningitidis. *Eur. J. Biochem.*, 269(21):5215–5223, 2002.

[52] Eduardo R deAzevedo, W-G Hu, Tito J Bonagamba, and Klaus Schmidt-Rohr. Principles of centerband-only detection of exchange in solid-state nuclear magnetic resonance, and extension to four-time centerband-only detection of exchange. *The Journal of Chemical Physics*, 112(20):8988–9001, 2000.

[53] Ilia G Denisov and Stephen G Sligar. Nanodiscs for structural and functional studies of membrane proteins. *Nature structural & molecular biology*, 23(6):481–486, 2016.

[54] Melinda J Duer. *Solid state NMR spectroscopy: principles and applications*. John Wiley & Sons, 2008.

[55] Elian Dupré, Bernard Clantin, Youhua Yuan, Sophie Lecher, Elodie Lesne, Rudy Antoine, Vincent Villeret, and Françoise Jacob-Dubuisson. Structural insight into the role of the pas domain for signal transduction in sensor kinase bvgs. *Journal of Bacteriology*, 203(9):e00614–20, 2021.

[56] Ulrich Heiner Nikolaus Dürr. Solid-state 19f-nmr studies on fluorine-labeled model compounds and biomolecules. 2006.

[57] Lyndon Emsley. Spin diffusion in crystalline solids. In *NMR Crystallography*. John Wiley & Sons Ltd., 2009.

[58] Richard A Engh and Robert Huber. Accurate bond and angle parameters for x-ray protein structure refinement. *Acta Cryst. A*, 47(4):392–400, 1991.

[59] Daniel A Fox, Per Larsson, Ryan H Lo, Brett M Kroncke, Peter M Kasson, and Linda Columbus. Structure of the neisserial outer membrane protein opa60: Loop flexibility essential to receptor recognition and bacterial engulfment. *J. Am. Chem. Soc.*, 136(28):9938–9946, 2014.

[60] W Trent Franks, Donghua H Zhou, Benjamin J Wylie, Brian G Money, Daniel T Graesser, Heather L Frericks, Gurmukh Sahota, and Chad M Rienstra. Magic-angle spinning solid-state nmr spectroscopy of the β1 immunoglobulin binding domain of protein g (gb1): 15n and 13c chemical shift assignments and conformational analysis. *J. Am. Chem. Soc.*, 127(35):12291–12305, 2005.

[61] F Fujara, S Wefing, and HW Spiess. Dynamics of molecular reorientations: Analogies between quasielastic neutron scattering and deuteron nmr spin alignment. *The Journal of chemical physics*, 84(8):4579–4584, 1986.

[62] CA Fyfe, Karl Todd Mueller, H Grondey, and KC Wong-Moon. Dipolar dephasing between quadrupolar and spin-12 nuclei. redor and tedor nmr experiments on vpi-5. *Chem. Phys. Lett.*, 199(1-2):198–204, 1992.

[63] Rong Gao, Sophie Bouillet, and Ann M Stock. Structural basis of response regulator function. *Annual review of microbiology*, 73:175–197, 2019.

[64] Joel R. Garbow and Terry Gullion. Chapter 3 - measurement of internuclear distances in biological solids by magic-angle spinning 13c nmr. In Nicolau Beckmann, editor, *Carbon-13 NMR Spectroscopy of Biological Systems*, pages 65 – 115. Academic Press, San Diego, 1995.

[65] J. R. Garbutt, G. Goward, C. Kirby, and W. Power. Solid-state 2 h nmr study of methyl-d 3 - cobalamin. *Biochemistry and Cell Biology*, 76:423–428, 1998.

[66] Helen Geen and Ray Freeman. Band-Selective Radiofrequency Pulses. Technical report.

[67] Manali Ghosh and Chad M Rienstra. 1h-detected redor with fast magic-angle spinning of a deuterated protein. *J. Phys. Chem. B*, 121(36):8503–8511, 2017.

[68] Rossitza K Gitti, Nathan T Wright, Joyce W Margolis, Kristen M Varney, David J Weber, and Frank L Margolis. Backbone dynamics of the olfactory marker protein as studied by 15n nmr relaxation measurements. *Biochemistry*, 44(28):9673–9679, 2005.

[69] J Fraser Glickman, Xiang Wu, Robert Mercuri, Chantal Illy, Benjamin R Bowen, Yang He, and Matthew Sills. A comparison of alphascreen, tr-fret, and trf as assay methods for fxr nuclear receptors. *Journal of biomolecular screening*, 7(1):3–10, 2002.

[70] Andrew L Goodman, Massimo Merighi, Mamoru Hyodo, Isabelle Ventre, Alain Filloux, and Stephen Lory. Direct interaction between sensor kinase proteins mediates acute and chronic disease phenotypes in a bacterial pathogen. *Genes & development*, 23(2):249–259, 2009.

[71] T. Gopinath, Songlin Wang, John Lee, Hideki Aihara, and Gianluigi Veglia. Hybridization of TEDOR and NCX MAS solid-state NMR experiments for simultaneous acquisition of heteronuclear correlation spectra and distance measurements. *J. Biomol. NMR*, 73(3-4):141–153, apr 2019.

[72] Sabrina Graf, Constanze Broll, Juliane Wissig, Alexander Strecker, Maria Parowatkin, and Gottfried Unden. Cita (citrate) and dcus (c4-dicarboxylate) sensor kinases in thermophilic geobacillus kaustophilus and geobacillus thermodenitrificans. *Microbiology*, 162(1):127–137, 2016.

[73] David J Griffiths and Darrell F Schroeter. *Introduction to quantum mechanics*. Cambridge University Press, 2018.

[74] Kristof Grohe, Evgeny Nimerovsky, Himanshu Singh, Suresh K Vasa, Benedikt Söldner, Beat Vögeli, Chad M Rienstra, and Rasmus Linser. Exact distance measurements for structure and dynamics in solid proteins by fast-magic-angle-spinning nmr. *ChemComm.*, 55(55):7899–7902, 2019.

[75] Stephan Grzesiek and A D Bax. An Efficient Experiment for Sequential Backbone Assignment of Medium-Sized Isotopically Enriched Proteins. Technical report.

[76] Stephan Grzesiek and Ad Bax. An efficient experiment for sequential backbone assignment of medium-sized isotopically enriched proteins. *J. Magn. Reson.*, 99(1):201–207, 1992.

[77] Terry Gullio˜, Robert A Mckay, and Asher Schmidt. Spin-Echo, Double-Resonance NMR. with Flipped Spinning (SEDORFS). Technical report.

[78] Terry Gullion. Rotational-Echo, Double-Resonance NMR. Technical report.

[79] Terry Gullion. New, compensated carr-purcell sequences. *J. Magn. Reson.*, 89:479–484, 1990.

[80] Terry Gullion and Jacob Schaefer. Rotational-echo double-resonance NMR. *J. Magn. Reson.*, 81(1):196–200, 1989.

[81] Ivan Gushchin and Valentin Gordeliy. Transmembrane signal transduction in two-component systems: Piston, scissoring, or helical rotation? *Bioessays*, 40(2):1700197, 2018.

[82] Ivan Gushchin, Igor Melnikov, Vitaly Polovinkin, Andrii Ishchenko, Anastasia Yuzhakova, Pavel Buslaev, Gleb Bourenkov, Sergei Grudinin, Ekaterina Round, Taras Balandin, et al.

Mechanism of transmembrane signaling by sensor histidine kinases. *Science*, 356(6342), 2017.

[83] Ivan Yu Gushchin, Valentin I Gordeliy, and Sergei Grudinin. Role of the hamp domain region of sensory rhodopsin transducers in signal transduction. *Biochemistry*, 50(4):574–580, 2011.

[84] P. Güntert, C. Mumenthaler, and K. Wüthrich. Torsion angle dynamics for nmr structure calculation with the new program dyana. *J. Mol. Biol.*, 273:283–298, 1997.

[85] U. Haeberlen and J. S. Waugh. Coherent averaging effects in magnetic resonance. *Phys. Rev.*, 175:453–467, Nov 1968.

[86] Jens D Haller and Paul Schanda. Amplitudes and time scales of picosecond-to-microsecond motion in proteins studied by solid-state nmr: a critical evaluation of experimental approaches and application to crystalline ubiquitin. *J. Biomol. NMR*, 57(3):263–280, 2013.

[87] Phyllis I Hanson and Howard Schulman. Neuronal ca2+/calmodulin-dependent protein kinases. *Annual review of biochemistry*, 61(1):559–601, 1992.

[88] Gerald L Hazelbauer, Joseph J Falke, and John S Parkinson. Bacterial chemoreceptors: high-performance signaling in networked arrays. *Trends in biochemical sciences*, 33(1):9–19, 2008.

[89] Eric R. Henry and Attila Szabo. Influence of vibrational motion on solid state line shapes and nmr relaxation. *J.Chem. Phys.*, 82(11):4753–4761, 1985.

[90] J Fred Hess, Kenji Oosawa, Nachum Kaplan, and Melvin I Simon. Phosphorylation of three proteins in the signaling pathway of bacterial chemotaxis. *Cell*, 53(1):79–87, 1988.

[91] Victoria A Higman. Solid-state mas nmr resonance assignment methods for proteins. *Progress in nuclear magnetic resonance spectroscopy*, 106:37–65, 2018.

[92] Andrew W Hing and Shimon Vega. Transferred-echo double-resonance nmr. *J. Magn. Reson.*, 96:205–209, 1992.

[93] Andrew W Hing, Shimon Vega, and Jacob Schaefer. Transferred-echo double-resonance nmr. *J. Magn. Reson.*, 96(1):205–209, 1992.

[94] Andrew W Hing, Shimon Vega, and Jacob Schaefer. Measurement of heteronuclear dipolar coupling by transferred-echo double-resonance nmr. *J. Magn. Reson. Ser. A*, 103(2):151–162, 1993.

[95] Mei Hong, Venkata Mandala, Matthew McKay, Alexander Shcherbakov, Aurelio Dregni, and Antonios Kolocouris. Structure and drug binding of the sars-cov-2 envelope protein in phospholipid bilayers. *Research Square*, 2020.

[96] Fanghao Hu, Klaus Schmidt-Rohr, and Mei Hong. Nmr detection of ph-dependent histidine–water proton exchange reveals the conduction mechanism of a transmembrane proton channel. *J. Am. Chem. Soc.*, 134(8):3703–3713, 2012.

[97] WG Hu, TJ Bonagamba, K Schmidt-Rohr, et al. Centerband-only detection of exchange: efficient analysis of dynamics in solids by nmr. *Journal of the American Chemical Society*, 121(36):8411–8412, 1999.

[98] Daniel Huster, Linshi Xiao, and Mei Hong. Solid-state nmr investigation of the dynamics of the soluble and membrane-bound colicin ia channel-forming domain. *Biochemistry*, 40(25):7662–7674, 2001.

[99] C. P. Jaroniec, B. A. Tounge, J. Herzfeld, and R. G. Griffin. Frequency selective heteronuclear dipolar recoupling in rotating solids: Accurate 13C-15N distance measurements in uniformly 13C, 15N-labeled peptides. *J. Am. Chem. Soc.*, 123(15):3507–3519, 2001.

[100] C. P. Jaroniec, B. A. Tounge, C. M. Rienstra, J. Herzfeld, and R. G. Griffin. Measurement of 13C-15N distances in uniformly 13C labeled biomolecules: J-decoupled REDOR [14], nov 1999.

[101] Christopher P. Jaroniec, Claudiu Filip, and Robert G. Griffin. 3D TEDOR NMR experiments for the simultaneous measurement of multiple carbon-nitrogen distances in uniformly 13C,15N-labeled solids. *J. Am. Chem. Soc.*, 124(36):10728–10742, sep 2002.

[102] Christopher P. Jaroniec, Brett A. Tounge, Chad M. Rienstra, Judith Herzfeld, and Robert G. Griffin. Recoupling of Heteronuclear Dipolar Interactions with Rotational-Echo Double-Resonance at High Magic-Angle Spinning Frequencies. *J. Magn. Reson.*, 146(1):132–139, 2000.

[103] Gunnar Jeschke. Deer distance measurements on proteins. *Annual review of physical chemistry*, 63:419–446, 2012.

[104] Sibylle Kaspar and Michael Bott. The sensor kinase cita (dpib) of escherichia coli functions as a high-affinity citrate receptor. *Archives of microbiology*, 177(4):313–321, 2002.

[105] Jason Key, Marco Hefti, Erin B Purcell, and Keith Moffat. Structure of the redox sensor domain of azotobacter vinelandii nifl at atomic resolution: signaling, dimerization, and mechanism. *Biochemistry*, 46(12):3614–3623, 2007.

[106] Mitsunori Koresawa and Takayoshi Okabe. High-throughput screening with quantitation of atp consumption: a universal non-radioisotope, homogeneous assay for protein kinase. *Assay and drug development technologies*, 2(2):153–160, 2004.

[107] Tino Krell, Jesús Lacal, Andreas Busch, Hortencia Silva-Jiménez, María-Eugenia Guazzaroni, and Juan Luis Ramos. Bacterial sensor kinases: diversity in the recognition of environmental signals. *Annual review of microbiology*, 64:539–559, 2010.

[108] Natalia Kulminskaya, Suresh Kumar Vasa, Karin Giller, Stefan Becker, Ann Kwan, Margaret Sunde, and Rasmus Linser. Access to side-chain carbon information in deuterated solids under fast mas through non-rotor-synchronized mixing. *ChemComm.*, 52(2):268–271, 2016.

[109] Brian P Landry, Rohan Palanki, Nikola Dyulgyarov, Lucas A Hartsough, and Jeffrey J Tabor. Phosphatase activity tunes two-component system sensor detection threshold. *Nature communications*, 9(1):1–10, 2018.

[110] Naomi R Latorraca, Jason K Wang, Brian Bauer, Raphael JL Townshend, Scott A Hollingsworth, Julia E Olivieri, H Eric Xu, Martha E Sommer, and Ron O Dror. Molecular mechanism of gpcr-mediated arrestin activation. *Nature*, 557(7705):452–456, 2018.

[111] James Lee, Diana R Tomchick, Chad A Brautigam, Mischa Machius, Remco Kort, Klaas J Hellingwerf, and Kevin H Gardner. Changes at the kina pas-a dimerization interface influence histidine kinase function. *Biochemistry*, 47(13):4051–4064, 2008.

[112] Alons Lends, Francesco Ravotti, Giorgia Zandomeneghi, Anja Böckmann, Matthias Ernst, and Beat H. Meier. Direct amide 15 N to 13 C transfers for solid-state assignment experiments in deuterated proteins. *J. Biomol. NMR*, 72(1-2):69–78, oct 2018.

[113] Ivica Letunic, Richard R Copley, Birgit Pils, Stefan Pinkert, Jörg Schultz, and Peer Bork. Smart 5: domains in the context of genomes and networks. *Nucleic acids research*, 34(suppl_1):D257–D260, 2006.

[114] Malcolm H Levitt. *Spin dynamics: basics of nuclear magnetic resonance*. John Wiley & Sons, 2013.

[115] Jozef R Lewandowski, Jean-Nicolas Dumez, Ümit Akbey, Sascha Lange, Lyndon Emsley, and Hartmut Oschkinat. Enhanced resolution and coherence lifetimes in the solid-state nmr spectroscopy of perdeuterated proteins under ultrafast magic-angle spinning. *The J. Phys. Chem. Lett.*, 2(17):2205–2211, 2011.

[116] Jingwen Li, Yefei Wang, Liaoyuan An, Jingfei Chen, and Lishan Yao. Direct observation of ch/ch van der waals interactions in proteins by nmr. *J. Am. Chem. Soc.*, 140(9):3194–3197, 2018.

[117] Shun-Cheng Li and Charles M Deber. A measure of helical propensity for amino acids in membrane environments. *Nature structural biology*, 1(6):368–373, 1994.

[118] Yan Li and Jeremy N S Evans. The Importance of XY-8 Phase Cycling in the Rotational-Echo Double-Resonance Experiment with Total Sideband Suppression. Technical report, 1995.

[119] Ying Li, Benjamin J. Wylie, and Chad M. Rienstra. Selective refocusing pulses in magic-angle spinning nmr: Characterization and applications to multi-dimensional protein spectroscopy. *J. Magn. Reson.*, 179(2):206–216, 2006.

[120] Rasmus Linser. Side-chain to backbone correlations from solid-state nmr of perdeuterated proteins through combined excitation and long-range magnetization transfers. *J. Biomol. NMR*, 51(3):221–226, 2011.

[121] Rasmus Linser, Benjamin Bardiaux, Loren B Andreas, Sven G Hyberts, Vanessa K Morris, Guido Pintacuda, Margaret Sunde, Ann H Kwan, and Gerhard Wagner. Solid-state nmr structure determination from diagonal-compensated, sparsely nonuniform-sampled 4d proton–proton restraints. *J. Am. Chem. Soc.*, 136(31):11002–11010, 2014.

[122] Rasmus Linser, Benjamin Bardiaux, Victoria Higman, Uwe Fink, and Bernd Reif. Structure calculation from unambiguous long-range amide and methyl 1h- 1h distance restraints for a microcrystalline protein with mas solid-state nmr spectroscopy. *J. Am. Chem. Soc.*, 133(15):5905–5912, 2011.

[123] Jeffrey J Liu, Reto Horst, Vsevolod Katritch, Raymond C Stevens, and Kurt Wüthrich. Biased signaling pathways in β2-adrenergic receptor characterized by 19f-nmr. *Science*, 335(6072):1106–1110, 2012.

[124] Peiwen Liu, Huan Liu, Timmy Schäfer, Torsten Gutmann, Holger Gibhardt, Houjuan Qi, Lin Tian, Xizhou Cecily Zhang, Gerd Buntkowsky, and Kai Zhang. Unexpected selective alkaline periodate oxidation of chitin for the isolation of chitin nanocrystals. *Green Chemistry*, 23(2):745–751, 2021.

[125] Peiwen Liu, Bo Pang, Sebastian Dechert, Xizhou Cecily Zhang, Loren B Andreas, Steffen Fischer, Franc Meyer, and Kai Zhang. Structure selectivity of alkaline periodate oxidation on lignocellulose for facile isolation of cellulose nanocrystals. *Angewandte Chemie International Edition*, 59(8):3218–3225, 2020.

[126] Blanca López-Méndez and Peter Güntert. Automated protein structure determination from nmr spectra. *Journal of the American Chemical Society*, 128(40):13112–13122, 2006.

[127] Justin Lorieau and Ann E McDermott. Order parameters based on 13c1h, 13c1h2 and 13c1h3 heteronuclear dipolar powder patterns: a comparison of mas-based solid-state nmr sequences. *Magn. Reson. Chem.*, 44(3):334–347, 2006.

[128] Justin L Lorieau, Loren A Day, and Ann E McDermott. Conformational dynamics of an intact virus: order parameters for the coat protein of pf1 bacteriophage. *Proc. Natl. Acad. Sci. U.S.A*, 105(30):10366–10371, 2008.

[129] Justin L Lorieau and Ann E McDermott. Conformational flexibility of a microcrystalline globular protein: order parameters by solid-state nmr spectroscopy. *J. Am. Chem. Soc.*, 128(35):11505–11512, 2006.

[130] Manman Lu, Ryan W Russell, Alexander J Bryer, Caitlin M Quinn, Guangjin Hou, Huilan Zhang, Charles D Schwieters, Juan R Perilla, Angela M Gronenborn, and Tatyana Polenova. Atomic-resolution structure of hiv-1 capsid tubes by magic-angle spinning nmr. *Nature structural & molecular biology*, 27(9):863–869, 2020.

[131] Manman Lu, Mingzhang Wang, Ivan V Sergeyev, Caitlin M Quinn, Jochem Struppe, Melanie Rosay, Werner Maas, Angela M Gronenborn, and Tatyana Polenova. 19f dynamic nuclear polarization at fast magic angle spinning for nmr of hiv-1 capsid protein assemblies. *Journal of the American Chemical Society*, 141(14):5681–5691, 2019.

[132] Wenbin Luo and Mei Hong. Determination of the oligomeric number and intermolecular distances of membrane protein assemblies by anisotropic 1h-driven spin diffusion nmr spectroscopy. *Journal of the American Chemical Society*, 128(22):7242–7251, 2006.

[133] Wenbin Luo, Rajeswari Mani, and Mei Hong. Side-chain conformation of the m2 transmembrane peptide proton channel of influenza a virus from 19f solid-state nmr. *The Journal of Physical Chemistry B*, 111(36):10825–10832, 2007.

[134] Sven Macholl, Ingolf Sack, Hans-Heinrich Limbach, Jutta Pauli, Mark Kelly, and Gerd Buntkowsky. Solid-state nmr study of the sh3 domain of α-spectrin: application of 13c–15n tedor and redor. *Magn. Reson. Chem.*, 38(7):596–603, 2000.

[135] Alexander S Maltsev, Jinfa Ying, and Ad Bax. Deuterium isotope shifts for backbone 1 h, 15 n and 13 c nuclei in intrinsically disordered protein α-synuclein. *Journal of biomolecular NMR*, 54(2):181–191, 2012.

[136] Venkata S Mandala, Alexander R Loftis, Alexander A Shcherbakov, Bradley L Pentelute, and Mei Hong. Atomic structures of closed and open influenza b m2 proton channel reveal the conduction mechanism. *Nature structural & molecular biology*, 27(2):160–167, 2020.

[137] Rajeswari Mani, Sarah D Cady, Ming Tang, Alan J Waring, Robert I Lehrer, and Mei Hong. Membrane-dependent oligomeric structure and pore formation of a β-hairpin antimicrobial peptide in lipid bilayers from solid-state nmr. *Proceedings of the National Academy of Sciences*, 103(44):16242–16247, 2006.

[138] M. Matti Maricq. Application of average hamiltonian theory to the nmr of solids. *Phys. Rev. B*, 25:6622–6632, Jun 1982.

[139] Alberto Marina, Carey D Waldburger, and Wayne A Hendrickson. Structure of the entire cytoplasmic portion of a sensor histidine-kinase protein. *The EMBO journal*, 24(24):4247–4259, 2005.

[140] Thorsten Mascher, John D Helmann, and Gottfried Unden. Stimulus perception in bacterial signal-transducing histidine kinases. *Microbiology and molecular biology reviews*, 70(4):910–938, 2006.

[141] MATLAB. *9.1.0.441655 (R2016b)*. The MathWorks Inc., Natick, Massachusetts, 2016.

[142] AD Milov, AB Ponomarev, and Yu D Tsvetkov. Electron-electron double resonance in electron spin echo: Model biradical systems and the sensitized photolysis of decalin. *Chemical physics letters*, 110(1):67–72, 1984.

[143] AD Milov, KM Salikhov, and M Shirov. Use of the double resonance in electron spin echo method for the study of paramagnetic center spatial distribution in solids. *Fizika Tverdogo Tela*, 23(4):975–982, 1981.

[144] Stefania Monteleone, Julian E Fuchs, and Klaus R Liedl. Molecular connectivity predefines polypharmacology: Aliphatic rings, chirality, and sp3 centers enhance target selectivity. *Frontiers in pharmacology*, 8:552, 2017.

[145] Christian Monzel, Pia Degreif-Dünnwald, Christina Gröpper, Christian Griesinger, and Gottfried Unden. The cytoplasmic pasc domain of the sensor kinase dcus of e scherichia coli: role in signal transduction, dimer formation, and dcta interaction. *MicrobiologyOpen*, 2(6):912–927, 2013.

[146] Kumar Tekwani Movellan, Melanie Wegstroth, Kerstin Overkamp, Andrei Leonov, Stefan Becker, and Loren B Andreas. Imidazole–imidazole hydrogen bonding in the ph-sensing histidine side chains of influenza a m2. *Journal of the American Chemical Society*, 142(6):2704–2708, 2020.

[147] Karl Todd Mueller, T P Jarvie, David Jeffrey Aurentz, and B W Roberts. The redor transform: direct calculation of internuclear couplings from dipolar-dephasing nmr data. *Chem. Phys. Lett.*, 242(6):535–542, 1995.

[148] Eszter E Najbauer and Loren B Andreas. Correcting for magnetic field drift in magic-angle spinning nmr datasets. *Journal of Magnetic Resonance*, 305:1–4, 2019.

[149] Eszter E Najbauer, Kumar Tekwani Movellan, Tobias Schubeis, Tom Schwarzer, Kathrin Castiglione, Karin Giller, Guido Pintacuda, Stefan Becker, and Loren B Andreas. Probing membrane protein insertion into lipid bilayers by solid-state nmr. *ChemPhysChem*, (2):302–310, 2019.

[150] Andrew J Nieuwkoop and Chad M Rienstra. Supramolecular protein structure determination by site-specific long-range intermolecular solid state nmr spectroscopy. *J. Am. Chem. Soc.*, 132(22):7570–7571, 2010.

[151] Andrew J Nieuwkoop, Benjamin J Wylie, W Trent Franks, Gautam J Shah, and Chad M Rienstra. Atomic resolution protein structure determination by three-dimensional transferred echo double resonance solid-state nuclear magnetic resonance spectroscopy. *J.Chem.Phys.*, 131(9):09B602, 2009.

[152] Evgeny Nimerovsky and Amir Goldbourt. Insights into the spin dynamics of a large anisotropy spin subjected to long-pulse irradiation under a modified redor experiment. *J. Magn. Reson.*, 225(2):130–141, 2012.

[153] Evgeny Nimerovsky, Kumar Tekwani Movellan, Xizhou Cecily Zhang, Marcel C Forster, Eszter Najbauer, Kai Xue, Rıza Dervişoğlu, Karin Giller, Christian Griesinger, Stefan Becker, et al. Proton detected solid-state nmr of membrane proteins at 28 tesla (1.2 ghz) and 100 khz magic-angle spinning. *Biomolecules*, 11(5):752, 2021.

[154] Alexander J Ninfa, E Gottlin Ninfa, Andrei N Lupas, Ann Stock, Boris Magasanik, and Jeff Stock. Crosstalk between bacterial chemotaxis signal transduction proteins and regulators of transcription of the ntr regulon: evidence that nitrogen assimilation and chemotaxis are controlled by a common phosphotransfer mechanism. *Proceedings of the National Academy of Sciences*, 85(15):5492–5496, 1988.

[155] Katsuyuki Nishimura, Riqiang Fu, and Timothy A Cross. The effect of rf inhomogeneity on heteronuclear dipolar recoupling in solid state nmr: practical performance of sfam and redor. *J. Magn. Reson.*, 152(2):227–233, 2001.

[156] Natsue Ohml, Jonathan M Wingfield, Hidenori Yazawa, and Osamu Inagaki. Development of a homogeneous time-resolved fluorescence assay for high throughput screening to identify lck inhibitors: comparison with scintillation proximity assay and streptavidin-coated plate assay. *Journal of biomolecular screening*, 5(6):463–470, 2000.

[157] Lucia Pappalardo, Ingo G Janausch, Vinesh Vijayan, Eva Zientz, Jochen Junker, Wolfgang Peti, Markus Zweckstetter, Gottfried Unden, and Christian Griesinger. The nmr structure of the sensory domain of the membranous two-component fumarate sensor (histidine protein kinase) dcus of escherichia coli. *Journal of Biological Chemistry*, 278(40):39185–39188, 2003.

[158] Tatjana N Parac, E Zientz, G Unden, B Coligaev, Wolfgang Peti, and Christian Griesinger. Assignment of 1h, 13c and 15n resonances to the sensory domain of the membraneous two-component fumarate sensor (histidine protein kinase) dcus of escherichia coli. *Journal of biomolecular NMR*, 19:91–92, 2001.

[159] John S Parkinson, Gerald L Hazelbauer, and Joseph J Falke. Signaling and sensory adaptation in escherichia coli chemoreceptors: 2015 update. *Trends in microbiology*, 23(5):257–266, 2015.

[160] Jutta Pauli, Barth Van Rossum, Hans Förster, Huub J.M. De Groot, and Hartmut Oschkinat. The redor transform: direct calculation of internuclear couplings from dipolar-dephasing nmr data. *J. Magn. Reson.*, 143(2):411–416, 2000.

[161] Susanne Penzel, Albert A Smith, Vipin Agarwal, Andreas Hunkeler, Mai-Liis Org, Ago Samoson, Anja Böckmann, Matthias Ernst, and Beat H Meier. Protein resonance assignment at mas frequencies approaching 100 khz: a quantitative comparison of j-coupling and dipolar-coupling-based transfer methods. *Journal of biomolecular NMR*, 63(2):165–186, 2015.

[162] Aneta T Petkova, Wai-Ming Yau, and Robert Tycko. Experimental constraints on quaternary structure in alzheimer's β-amyloid fibrils. *Biochemistry*, 45(2):498–512, 2006.

[163] Eric F Pettersen, Thomas D Goddard, Conrad C Huang, Gregory S Couch, Daniel M Greenblatt, Elaine C Meng, and Thomas E Ferrin. Ucsf chimera—a visualization system for exploratory research and analysis. *J. Comput. Chem.*, 25(13):1605–1612, 2004.

[164] Edward M Purcell, Henry Cutler Torrey, and Robert V Pound. Resonance absorption by nuclear magnetic moments in a solid. *Physical review*, 69(1-2):37, 1946.

[165] R Core Team. *R: A Language and Environment for Statistical Computing*. R Foundation for Statistical Computing, Vienna, Austria, 2017.

[166] Abbas Razvi and J Martin Scholtz. Lessons in stability from thermophilic proteins. *Protein Science*, 15(7):1569–1578, 2006.

[167] B Reif, CP Jaroniec, CM Rienstra, M Hohwy, and RG Griffin. 1h–1h mas correlation spectroscopy and distance measurements in a deuterated peptide, 2001.

[168] Stefan Reinelt, Eckhard Hofmann, Tanja Gerharz, Michael Bott, and Dean R Madden. The structure of the periplasmic ligand-binding domain of the sensor kinase cita reveals the first extracellular pas domain. *Journal of Biological Chemistry*, 278(40):39189–39196, 2003.

[169] Ludger Rensing. Periodic geophysical and biological signals as zeitgeber and exogenous inducers in animal organisms. *International journal of biometeorology*, 16:113–125, 1972.

[170] Giomar Rivera-Cancel, Wen-huang Ko, Diana R Tomchick, Fernando Correa, and Kevin H Gardner. Full-length structure of a monomeric histidine kinase reveals basis for sensory regulation. *Proceedings of the National Academy of Sciences*, 111(50):17839–17844, 2014.

[171] Steven M Rodems, Brian D Hamman, Christina Lin, Jane Zhao, Sundeep Shah, David Heidary, Lew Makings, Jeffrey H Stack, and Brian A Pollok. A fret-based assay platform for ultra-high density drug screening of protein kinases and phosphatases. *Assay and drug development technologies*, 1(1):9–19, 2002.

[172] Matthias Roos, Tuo Wang, Alexander A Shcherbakov, and Mei Hong. Fast magic-angle-spinning 19f spin exchange nmr for determining nanometer 19f–19f distances in proteins and pharmaceutical compounds. *The Journal of Physical Chemistry B*, 122(11):2900–2911, 2018.

[173] Anna M Rydzik, Jürgen Brem, Sander S van Berkel, Inga Pfeffer, Anne Makena, Timothy DW Claridge, and Christopher J Schofield. Monitoring conformational changes in the ndm-1 metallo-β-lactamase by 19f nmr spectroscopy. *Angewandte Chemie*, 126(12):3193–3197, 2014.

[174] Mirko Sackewitz, Holger A Scheidt, Grit Lodderstedt, Angelika Schierhorn, Elisabeth Schwarz, and Daniel Huster. Structural and dynamical characterization of fibrils from a disease-associated alanine expansion domain using proteolysis and solid-state nmr spectroscopy. *J. Am. Chem. Soc.*, 130(23):7172–7173, 2008.

[175] Tammy M Sadler, Maria Achilleos, Shoba Ragunathan, Adam Pitkin, James LaRocque, John Morin, Rebecca Annable, Lee M Greenberger, Philip Frost, and Yixian Zhang. Development and comparison of two nonradioactive kinase assays for i kappa b kinase. *Analytical biochemistry*, 326(1):106–113, 2004.

[176] JJ Sakurai and J Napolitano. Modern quantum mechanics. 2-nd edition. *Person New International edition*, 2014.

[177] Michele Salvi. *Structural Studies on Transmembrane Signalling Mechanism of Histidine Kinase CitA*. PhD thesis, Georg-August-Universität Göttingen, 2019.

[178] Michele Salvi, Benjamin Schomburg, Karin Giller, Sabrina Graf, Gottfried Unden, Stefan Becker, Adam Lange, and Christian Griesinger. Sensory domain contraction in histidine kinase cita triggers transmembrane signaling in the membrane-bound sensor. *Proceedings of the National Academy of Sciences*, 114(12):3115–3120, 2017.

[179] Michael Sattler, Jürgen Schleucher, and Christian Griesinger. Heteronuclear multidimensional nmr experiments for the structure determination of proteins in solution. *Progress in nuclear magnetic resonance spectroscopy*, 34:93–158, 1999.

[180] Jacob Schaefer. Redor and tedor. *eMagRes*, pages 1–7, 2007.

[181] Jacob Schaefer. "Development of REDOR rotational-echo double-resonance NMR" by Terry Gullion and Jacob Schaefer [J. Magn. Reson. 81 (1989) 196-200], dec 2011.

[182] Paul Schanda, Matthias Huber, Jérôme Boisbouvier, Beat H Meier, and Matthias Ernst. Solid-state nmr measurements of asymmetric dipolar couplings provide insight into protein side-chain motion. *Angew. Chem. Int. Ed.*, 50(46):11005–11009, 2011.

[183] Paul Schanda, Beat H Meier, and Matthias Ernst. Quantitative analysis of protein backbone dynamics in microcrystalline ubiquitin by solid-state nmr spectroscopy. *J. Am. Chem. Soc.*, 132(45):15957–15967, 2010.

[184] Paul Schanda, Beat H Meier, and Matthias Ernst. Accurate measurement of one-bond h–x heteronuclear dipolar couplings in mas solid-state nmr. *J. Magn. Reson.*, 210(2):246–259, 2011.

[185] Patrick D Scheu, Yun-Feng Liao, Julia Bauer, Holger Kneuper, Thomas Basché, Gottfried Unden, and Wolfgang Erker. Oligomeric sensor kinase dcus in the membrane of escherichia coli and in proteoliposomes: chemical cross-linking and fret spectroscopy. *Journal of bacteriology*, 192(13):3474–3483, 2010.

[186] Benjamin Schomburg. Transmembrane signalling: Structural and functional studies on histidine kinase cita. 2015.

[187] Tobias Schubeis, Tanguy Le Marchand, Csaba Daday, Wojciech Kopec, Kumar Tekwani Movellan, Jan Stanek, Tom S Schwarzer, Kathrin Castiglione, Bert L de Groot, Guido Pintacuda, et al. A β-barrel for oil transport through lipid membranes: Dynamic nmr structures of alkl. *Proceedings of the National Academy of Sciences*, 117(35):21014–21021, 2020.

[188] Stephan Schwarzinger, Gerard JA Kroon, Ted R Foss, John Chung, Peter E Wright, and H Jane Dyson. Sequence-dependent correction of random coil nmr chemical shifts. *Journal of the American Chemical Society*, 123(13):2970–2978, 2001.

[189] Madhumati Sevvana, Vinesh Vijayan, Markus Zweckstetter, Stefan Reinelt, Dean R Madden, Regine Herbst-Irmer, George M Sheldrick, Michael Bott, Christian Griesinger, and Stefan Becker. A ligand-induced switch in the periplasmic domain of sensor histidine kinase cita. *Journal of molecular biology*, 377(2):512–523, 2008.

[190] Shakeel Ahmad Shahid, Benjamin Bardiaux, W Trent Franks, Ludwig Krabben, Michael Habeck, Barth-Jan van Rossum, and Dirk Linke. Membrane-protein structure determination by solid-state nmr spectroscopy of microcrystals. *Nat. Methods*, 9(12):1212–1217, 2012.

[191] A. J. Shaka, James Keeler, Tom Frenkiel, and Ray Freeman. An improved sequence for broadband decoupling: Waltz-16. *J. Magn. Reson.*, 52:335–338, 1983.

[192] K Sharma, P K Madhu, V Agarwal, and K R Mote. Simultaneous recording of intra-and inter-residue linking experiments for backbone assignments in proteins at mas frequencies higher than 60 khz. *J. Biomol. NMR*, 74(4-5):229–237, 2020.

[193] Yang Shen and Ad Bax. Protein backbone and sidechain torsion angles predicted from nmr chemical shifts using artificial neural networks. *J. Biomol. NMR*, 56:227–241.

[194] Yang Shen and Ad Bax. Protein backbone and sidechain torsion angles predicted from nmr chemical shifts using artificial neural networks. *Journal of biomolecular NMR*, 56(3):227–241, 2013.

[195] Chaowei Shi, Carl Öster, Claudia Bohg, Longmei Li, Sascha Lange, Veniamin Chevelkov, and Adam Lange. Structure and dynamics of the rhomboid protease glpg in liposomes studied by solid-state nmr. *J. Am. Chem. Soc.*, 141(43):17314–17321, 2019.

[196] Neeraj Sinha, Klaus Schmidt-Rohr, and Mei Hong. Compensation for pulse imperfections in rotational-echo double-resonance nmr by composite pulses and exorcycle. *J. Magn. Reson.*, 168(2):358–365, 2004.

[197] Simon P. Skinner, Rasmus H. Fogh, Wayne Boucher, Timothy J. Ragan, Luca G. Mureddu, and Geerten W. Vuister. Ccpnmr analysisassign: a flexible platform for integrated nmr analysis. *J. Biomol. NMR*, 66:111–124, 2016.

[198] Charles P Slichter. *Principles of magnetic resonance*, volume 1. Springer Science & Business Media, 2013.

[199] TL Spencer, NW Plagos, DH Brouwer, and GR Goward. The use of 6 li {7 Li}-redor nmr spectroscopy to compare the ionic conductivities of solid-state lithium ion electrolytes. *Phys. Chem. Chem. Phys.*, 16(6):2515–2526, 2014.

[200] D J States, R A Haberkorn, and D J Ruben. A two-dimensional nuclear overhauser experiment with pure absorption phase in four quadrants. *J. Magn. Reson.*, 48(2):286–292, 1982.

[201] Philipp Aloysius Steinmetz, Sebastian Wörner, and Gottfried Unden. Differentiation of dcta and dcus function in the dcta/dcus sensor complex of e scherichia coli: function of dcta as an activity switch and of dcus as the c 4-dicarboxylate sensor. *Molecular microbiology*, 94(1):218–229, 2014.

[202] Marius Stopp, Philipp Aloysius Steinmetz, Christopher Schubert, Christian Griesinger, Dirk Schneider, and Gottfried Unden. Transmembrane signaling and cytoplasmic signal conversion by dimeric transmembrane helix 2 and a linker domain of the dcus sensor kinase. *Journal of Biological Chemistry*, 296, 2021.

[203] Hongye Sun, Karen E Low, Sam Woo, Richard L Noble, Ronald J Graham, Sonia S Connaughton, Melissa A Gee, and Linda G Lee. Real-time protein kinase assay. *Analytical chemistry*, 77(7):2043–2049, 2005.

[204] Dieter Suter and RR Ernst. Spin diffusion in resolved solid-state nmr spectra. *Physical Review B*, 32(9):5608, 1985.

[205] Hendrik Szurmant, Robert A White, and James A Hoch. Sensor complexes regulating two-component signal transduction. *Current opinion in structural biology*, 17(6):706–715, 2007.

[206] K Takegoshi, Shinji Nakamura, and Takehiko Terao. 13c–1h dipolar-assisted rotational resonance in magic-angle spinning nmr. *Chem. Phys. Lett.*, 344(5-6):631–637, 2001.

[207] Ming Tang, Gemma Comellas, Leonard J Mueller, and Chad M Rienstra. High resolution 13 c-detected solid-state nmr spectroscopy of a deuterated protein. *J. Biomol. NMR*, 48(2):103–111, 2010.

[208] Larissa Tetsch and Kirsten Jung. The regulatory interplay between membrane-integrated sensors and transport proteins in bacteria. *Molecular microbiology*, 73(6):982–991, 2009.

[209] Peter Thomason and Rob Kay. Eukaryotic signal transduction via histidine-aspartate phosphorelay. *Journal of cell science*, 113(18):3141–3150, 2000.

[210] D.A Torchia and Attila Szabo. Spin-lattice relaxation in solids. *J. Magn. Reson.*, 49(1):107 – 121, 1982.

[211] Marcus D Tuttle, Gemma Comellas, Andrew J Nieuwkoop, Dustin J Covell, Deborah A Berthold, Kathryn D Kloepper, Joseph M Courtney, Jae K Kim, Alexander M Barclay, Amy Kendall, et al. Solid-state nmr structure of a pathogenic fibril of full-length human α-synuclein. *Nat. Struct. Mol. Biol.*, 23(5):409–415, 2016.

[212] Sandra J Ullrich, Ute A Hellmich, Stefan Ullrich, and Clemens Glaubitz. Interfacial enzyme kinetics of a membrane bound kinase analyzed by real-time mas-nmr. *Nature chemical biology*, 7(5):263–270, 2011.

[213] G Unden, S Wörner, and C Monzel. Cooperation of secondary transporters and sensor kinases in transmembrane signalling: the dcta/dcus and dcub/dcus sensor complexes of escherichia coli. *Advances in microbial physiology*, 68:139–167, 2016.

[214] Pramodh Vallurupalli, Ashok Sekhar, Tairan Yuwen, and Lewis E Kay. Probing conformational dynamics in biomolecules via chemical exchange saturation transfer: a primer. *Journal of biomolecular NMR*, 67(4):243–271, 2017.

[215] René Verel, Matthias Ernst, and Beat H Meier. Adiabatic dipolar recoupling in solid-state nmr: the dream scheme. *J. Magn. Reson.*, 150(1):81–99, 2001.

[216] Beat Vögeli, Simon Olsson, Peter Güntert, and Roland Riek. The exact noe as an alternative in ensemble structure determination. *Biophys. J.*, 110(1):113–126, 2016.

[217] Beat Vögeli, Julien Orts, Dean Strotz, Peter Güntert, and Roland Riek. Discrete three-dimensional representation of macromolecular motion from enoe-based ensemble calculation. *CHIMIA*, 66(10):787–790, 2012.

[218] Wim F. Vranken, Wayne Boucher, Tim J. Stevens, Rasmus H. Fogh, Anne Pajon, Miguel Llinas, Eldon L. Ulrich, John L. Markley, John Ionides, and Ernest D. Laue. The ccpn data model for nmr spectroscopy: Development of a software pipeline. *Proteins*, 59:687–696, 2005.

[219] Marielle Aulikki Wälti, Francesco Ravotti, Hiromi Arai, Charles G Glabe, Joseph S Wall, Anja Böckmann, Peter Güntert, Beat H Meier, and Roland Riek. Atomic-resolution structure of a disease-relevant aβ (1–42) amyloid fibril. *Proc. Natl. Acad. Sci. U.S.A*, 113(34):E4976–E4984, 2016.

[220] Chen Wang, Jiayan Sang, Jiawei Wang, Mingyan Su, Jennifer S Downey, Qinggan Wu, Shida Wang, Yongfei Cai, Xiaozheng Xu, Jun Wu, et al. Mechanistic insights revealed by the crystal structure of a histidine kinase with signal transducer and sensor domains. *PLoS biology*, 11(2):e1001493, 2013.

[221] Mingzhang Wang, Manman Lu, Matthew P Fritz, Caitlin M Quinn, In-Ja L Byeon, Chang-Hyeock Byeon, Jochem Struppe, Werner Maas, Angela M Gronenborn, and Tatyana Polenova. Fast magic-angle spinning 19f nmr spectroscopy of hiv-1 capsid protein assemblies. *Angewandte Chemie*, 130(50):16613–16617, 2018.

[222] Dror E Warschawski and Philippe F Devaux. Polarization transfer in lipid membranes, 2000.

[223] John S. Waugh, R. R. Ernst, G. Bodenhausen, and Wokaun A. Principles of nuclear magnetic resonance in one and two dimensions, 1987.

[224] Siegfried Weisenburger, Daniel Boening, Benjamin Schomburg, Karin Giller, Stefan Becker, Christian Griesinger, and Vahid Sandoghdar. Cryogenic optical localization provides 3d protein structure data with angstrom resolution. *Nature methods*, 14(2):141–144, 2017.

[225] Ann H West and Ann M Stock. Histidine kinases and response regulator proteins in two-component signaling systems. *Trends in biochemical sciences*, 26(6):369–376, 2001.

[226] David S Wishart, Brian D Sykes, and Frederic M Richards. Relationship between nuclear magnetic resonance chemical shift and protein secondary structure. *Journal of molecular biology*, 222(2):311–333, 1991.

[227] Peter M Wolanin, Peter A Thomason, and Jeffry B Stock. Histidine protein kinases: key signal transducers outside the animal kingdom. *Genome biology*, 3(10):1–8, 2002.

[228] Kai Xue, Riza Dervisoglu, Heidrun Sowa, and Loren B Andreas. Centerband-only detection of exchange nmr with natural-abundance correction reveals an expanded unit cell in phenylalanine crystals. *ChemPhysChem*, 21(15):1622, 2020.

[229] Kai Xue, Kumar Tekwani Movellan, Xizhou Zhang, Eszter E Najbauer, Marcel C Forster, Stefan Becker, and Loren B Andreas. Towards a native environment: Structure and function of membrane proteins in lipid bilayers by nmr. *Chemical Science*, 2021.

[230] Jian Yao, H Jane Dyson, and Peter E Wright. Chemical shift dispersion and secondary structure prediction in unfolded and partly folded proteins. *FEBS letters*, 419(2-3):285–289, 1997.

[231] Xizhou Cecily Zhang, Marcel C Forster, Evgeny Nimerovsky, Kumar Tekwani Movellan, and Loren B Andreas. Transferred-rotational-echo double resonance. *The Journal of Physical Chemistry A*, 125(3):754–769, 2021.

[232] Ling Zheng, Kenneth W Fishbein, Robert G Griffin, and Judith Herzfeld. Two-dimensional solid-state proton nmr and proton exchange. *Journal of the American Chemical Society*, 115(14):6254–6261, 1993.

[233] Donghua H. Zhou and Chad M. Rienstra. High-performance solvent suppression for proton-detected solid-state nmr. *J. Magn. Reson.*, 192:167–172, 2008.

[234] Donghua H Zhou, John J Shea, Andrew J Nieuwkoop, W Trent Franks, Benjamin J Wylie, Charles Mullen, Dennis Sandoz, and Chad M Rienstra. Solid-state protein-structure determination with proton-detected triple-resonance 3d magic-angle-spinning nmr spectroscopy. *Angew. Chem. Int. Ed.*, 46(44):8380–8383, 2007.

[235] Yuan Zhou, Liqun Huang, Shixia Ji, Shi Hou, Liang Luo, Conggang Li, Maili Liu, Yixiang Liu, and Ling Jiang. Structural basis for the inhibition of the autophosphorylation activity of hk853 by luteolin. *Molecules*, 24(5):933, 2019.

[236] Carl Öster, Simone Kosol, Christoph Hartmüller, Jonathan M Lamley, Dinu Iuga, Andres Oss, Mai-Liis Org, Kalju Vanatalu, Ago Samoson, Tobias Madl, et al. Characterization of protein–protein interfaces in large complexes by solid-state nmr solvent paramagnetic relaxation enhancements. *Journal of the American Chemical Society*, 139(35):12165–12174, 2017.

APPENDIX A

Appendix: Chapter 1

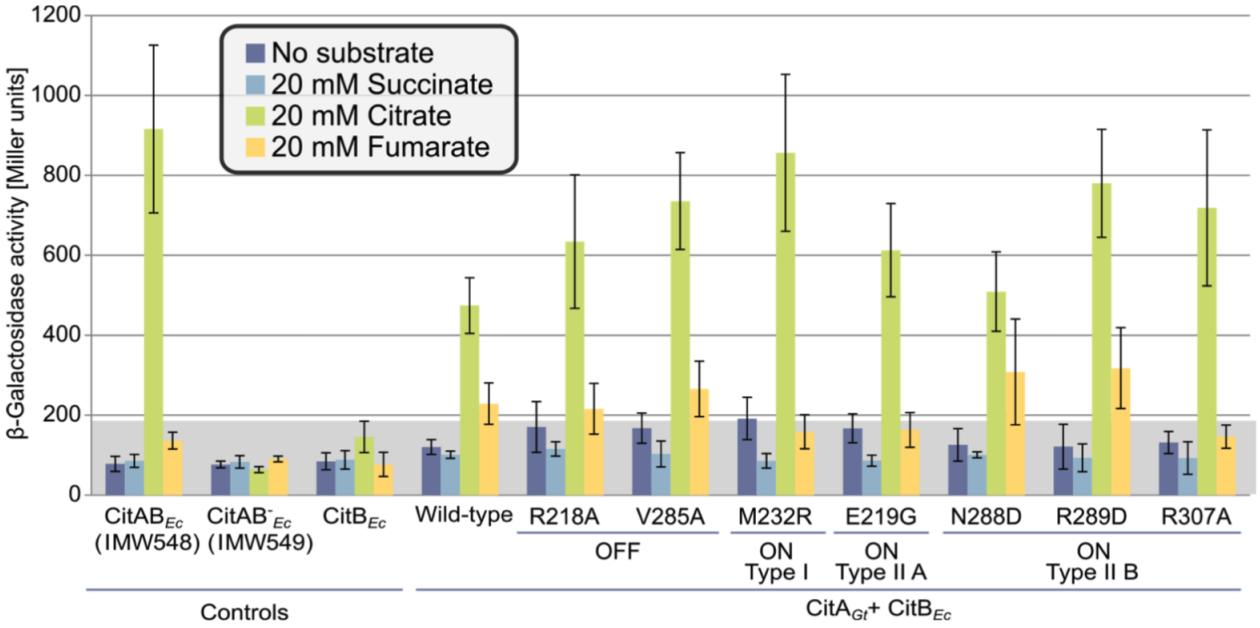

Figure A.1: *In vivo* testing of the proposed *G. thermodenitrificans* CitA PASc functional mutants performed in Prof. Unden lab. In dark blue is shown the value in absence of the substrate; in light blue, green and yellow are shown the activities in presence of succinate, fumarate and citrate, respectively. Figure prepared by M. Salvi [177].

APPENDIX B

Appendix: Chapter 2

Table B.1: Chemical shifts from ^{1}H detected sequence specific assignment of the citrate bound state of CitA PASpc

Residue	H	N	C	Ca	Cb
1Met	None	None	None	None	None
2Lys	None	None	None	None	None
3Leu	None	None	None	None	None
4Gln	None	None	None	None	None
5Thr	None	None	None	None	None
6Arg	9.36	120.09	173.9	54.1	27.89
7Leu	7.92	120.01	177.77	58.13	40.94
8Met	8.43	119.57	177.98	58	29.76
9Val	7.72	118.45	176.88	67.2	29.03
10Ile	7.73	118.42	None	60.01	40.44
11Ile	None	None	None	None	None
12Ala	None	None	None	None	None
13Ser	None	None	None	None	None
14Leu	7.71	120.52	178.6	57.9	40.45
15Leu	7.92	120.17	177.11	56.29	41.24
16Leu	8.95	118.51	178.24	58.76	40.15
17Phe	8.06	117.18	178.44	58.83	38.19
18Val	None	None	None	None	None
19Ile	None	None	None	None	None
20Ile	None	None	None	None	None
21Phe	None	None	None	None	None
22Leu	None	None	178.6	58.33	39.86
23Thr	8.1	118.04	177.68	66.47	67.99
24Phe	8.52	118.01	177.9	57.64	38.19
25Leu	None	None	None	None	None
26Phe	None	None	None	None	None
27Gln	None	None	None	None	None
28His	None	None	None	None	None
29Met	None	None	None	58.32	31.77
30Phe	8.29	116.33	175.92	59.69	38.76
31Ala	8.76	121.72	177.75	55.58	17.4
32Ala	8.09	120.7	178.89	54.83	17.49
33Thr	None	None	179.25	66.68	68.49
34Leu	8.76	123.36	178.94	57.34	39.68
35Lys	8.1	117.81	178.51	58.92	31.38
36Glu	None	None	None	None	None
37Gln	None	None	None	None	None
38Ile	None	None	None	None	None
39Gly	None	None	None	None	None
40Met	None	None	None	None	None
41Arg	None	None	None	None	None
42Ala	8.78	121.34	179.63	55.29	17.4
43Leu	8.74	117.48	178.28	57.33	40.07
44Asn	8.89	116.89	178.77	56.25	38.24
45Val	8.15	121.01	177.3	67.41	30.75
46Ala	8.84	123.99	179.76	55.6	17.33
47Glu	9.13	114.35	179.94	58.23	29.28

Residue	H	N	C	Ca	Cb
48Thr	8	117.58	177.66	66.88	68.17
49Val	8.59	121.74	178.7	67.04	31.1
50Ala	8.77	118.57	178.21	54.59	17.96
51Ser	7.4	111.66	174.35	59.26	64.25
52Thr	7.84	114.99	176	62.6	70.2
53Ser	None	None	None	None	None
54Leu	None	None	177.5	57.96	41.3
55Val	6.91	114.61	175.88	65.07	30.26
56Arg	6.84	115.07	180.15	59.19	29.11
57Glu	8.54	118.2	179.77	58.67	28.57
58Ala	8.41	121.48	179.41	53.81	17.26
59Phe	7.55	114.31	177.08	61.21	38.22
60Arg	7.8	116.85	176.82	55.93	29.47
61Asp	7.44	120.92	176.11	53.74	40.5
62Ser	8.69	116.04	175.53	61.01	61.95
63Asn	8.12	114.06	174.17	49.56	37.99
64Pro	None	None	176.1	64.4	32.68
65Ser	7.55	107.32	175.97	61.89	63.67
66Val	7.25	118.99	178.58	66.29	29.86
67Arg	8.33	113.98	179.3	57.75	31.37
68Leu	8	116.48	177.48	57.61	42.29
69Gln	8.7	119.21	175.02	60.07	23.98
70Pro	None	None	180.11	65.29	29.72
71Phe	6.66	117	176.1	59.94	38.97
72Ala	8.86	122.12	179.68	55.33	17.42
73Glu	8.13	115.66	178.6	57.48	29.5
74Arg	7.63	120.98	178.51	58.64	28.61
75Ile	7.84	117.32	179.68	61.79	33.8
76Arg	8.96	124.99	178.03	60.56	28.31
77Gln	8.05	116.52	179.05	58.47	27.83
78Lys	None	None	None	None	None
79Thr	None	None	176.14	62.86	71.07
80Gly	7.73	108.48	174.09	45.12	None
81Ala	7.13	121.62	175.7	51.11	17.37
82Glu	8.05	120.9	176.6	57.3	28.14
83Tyr	6.41	104.33	172.77	54.45	38.38
84Val	7.88	120.87	174.27	62.11	31.11
85Val	9.79	126.78	175.96	60.58	33.4
86Ile	7.49	124.28	175.4	59.42	39.37
87Gly	9.78	115.73	172.9	43.77	None
88Asn	7.99	116.41	176.54	50.67	38.28
89Arg	7.42	115.49	176.19	58.2	29.03
90Gln	7.35	115.41	176.08	55.49	27.85
91Gly	8.22	107.74	172.72	45.12	None
92Ile	7.5	119.84	175.83	57.89	35.23
93Ala	7.77	125.43	177	52.13	18.11
94Tyr	9.81	122.4	174.82	55.31	39.75
95Ala	7.86	119.92	175.32	51.11	21.47
96His	9.06	123.61	172.61	55.68	33.68

Residue	H	N	C	Ca	Cb
97Pro	None	None	178.11	64.28	30.82
98Leu	10.96	123.13	177.36	52.94	39.94
99Thr	8.47	120.32	177.86	65.71	67.76
100Glu	9.36	119.64	176.6	57.8	27.89
101Arg	7.97	119.87	178.56	52.57	28.32
102Ile	7.26	121.92	177.44	63.67	36.19
103Gly	9.59	115.29	173.66	44.66	None
104Lys	7.8	118.43	176.71	53.42	34.06
105Ser	8.32	116.96	173.66	59.7	63.44
106Met	8.75	122.42	176.49	56.29	34.91
107Ile	10.24	129.59	175.34	59.45	39.08
108Gly	8.27	112.21	176.19	44.67	None
109Gly	8.95	108.53	174.98	46.28	None
110Asp	8.13	116.43	176.62	52.02	37.97
111Asn	8.38	115.1	177.77	53.95	38.46
112Lys	7.9	120.01	179.01	60.81	31.65
113Glu	9	115.4	178.97	58.23	28.47
114Val	7	119.77	180.54	62.96	30.35
115Leu	7.59	118.16	178.09	56.46	40.19
116Lys	7.04	115.96	176.91	56.03	31.79
117Gly	8.35	107.26	173.7	44.99	None
118Lys	7.79	122.41	174.16	54.99	32.88
119Ser	8.09	116.45	175.14	57.18	63.55
120Ile	8.97	116.82	173.59	59.11	42.19
121Ile	8.11	120.95	176.27	60.8	38.51
122Ser	9.54	122.26	173.76	55.06	64.81
123Glu	8.47	128.46	175.29	54.6	30.22
124Ala	8.73	126.35	174.8	50.58	21.51
125Val	8.56	119.8	175.53	61.92	29.94
126Gly	6.75	112.11	176.93	44.29	None
127Ser	7.22	120.8	176.75	62.72	61.94
128Leu	11.08	123.33	176.8	54.75	40.71
129Gly	7.2	104.79	172.21	43.64	None
130Pro	None	None	177.26	63.36	31.3
131Ala	9.49	129.45	175.12	52.02	24.05
132Ile	8.54	117.7	174.07	59.48	39.96
133Arg	9.4	122.87	175.28	53.99	33.01
134Gly	9.15	110.62	171.98	43.73	None
135Lys	9.17	122.8	173.66	54.07	33.22
136Ala	8.91	122.74	173.91	47.51	21.16
137Pro	None	None	174.64	60.64	30.5
138Ile	7.52	118.12	175.38	59.52	38.78
139Phe	8.75	126.04	177.13	56.42	41.53
140Asp	8.93	119.03	178.3	51.65	40.59
141Glu	9.58	117.95	176.78	58.59	27.97
142Asn	8.21	116.08	175.86	52.49	39.02
143Gly	8.04	107.8	174.35	45.48	None
144Ser	8.63	118.73	174.08	57.61	62.98
145Val	8.85	124.59	177.4	63.16	30.6

Residue	H	N	C	Ca	Cb
146Ile	8.91	120.67	175.28	60.49	38.88
147Gly	7.25	106.63	170.13	45.64	None
148Ile	8.63	118.89	174.14	60.13	44.55
149Val	9.14	124.78	174.31	60.67	32.75
150Ser	9.55	122.29	173.9	54.98	65.04
151Val	9.13	128.8	174.96	60.15	31.9
152Gly	7.04	112.16	171.18	43.34	None
153Phe	8.52	116.72	175.17	56.73	42.05
154Leu	9.58	120.47	179.35	54.98	39.41
155Leu	8.82	123.82	179.74	57.34	39.89
156Glu	8.97	117.77	178.26	59.06	28.91
157Asp	8.59	118.28	178.27	57	40.77
158Ile	8.6	121.66	177.72	65.97	37.7
159Gln	None	None	None	None	None
160Arg	None	None	177.45	60.36	28.92
161Thr	8.4	120.11	177.77	65.52	67.75
162Val	7.65	118.22	177.36	66.92	30.89
163Trp	None	None	None	None	None
164Ser	None	None	None	None	None
165Tyr	None	None	None	None	None
166Ser	None	None	None	None	None
167Met	None	None	None	None	None
168Lys	None	None	None	None	None
169Ile	None	None	None	None	None
170Phe	None	None	None	None	None
171Phe	None	None	None	None	None
172Phe	None	122.24	176.11	58.93	38.84
173Ser	8.85	121.35	178.72	59.09	61.72
174Val	8.39	120.86	177.52	65.82	28.35
175Leu	8.66	120.44	177.54	60.18	41.06
176Ala	8.43	119.78	178.31	55.24	17.21
177Leu	8.5	117.59	177.93	57.7	40.3
178Leu	8.33	119.16	178.47	57.8	40.13
179Phe	8.28	116	176.72	57.72	38.22
180Gly	8.36	107.77	174.7	45.21	None
181Ala	8.67	118.85	175.03	54.81	18.02
182Val	9.58	122.23	173.93	64.64	32.86
183Gly	7.63	107.63	172.76	45.31	None
184Ala	8.19	121.62	177.5	54.83	17.37
185Val	8.01	121.1	177.37	67.44	30.86
186Ala	8.83	124.02	177.95	55.38	17.28
187Ile	7.86	116.29	177.66	66.28	38.54
188Ala	8.77	121.79	179.6	55.39	17.55
189Lys	8.34	114.84	179.01	57.53	29.92
190Ala	7.67	121.33	177.55	55.04	17.68
191Val	9.03	115.37	177.76	58.28	28.25
192Lys	8.02	115.87	176.04	58.23	30.73
193Lys	7.77	118.84	178.6	54.77	34.16
194Ser	None	None	None	None	None

Residue	H	N	C	Ca	Cb
195Ile	None	None	None	None	None
196His	None	None	None	None	None
197Gly	None	None	None	None	None
198Leu	None	None	None	None	None
199Glu	None	None	None	None	None
200Pro	None	None	178.45	66.72	29.05
201Glu	8.5	117.56	178.11	57.49	28.47
202Glu	7.98	121.27	177.42	57.39	29.26
203Ile	7.65	121.01	177.72	64.63	41.29
204Gly	8.37	107.02	174.86	47.38	None
205Leu	8.36	119.26	177.72	57.81	40.17
206Leu	None	None	None	None	None
207Tyr	None	None	177.66	58.38	38.79
208Gln	7.89	117.89	179.01	57.47	29.59
209Glu	7.75	120.82	178.55	57.4	28.56
210Lys	7.94	117.23	177.75	58.46	31.34
211Gln	7.84	116.63	178.96	58.65	28.08
212Ala	None	None	None	None	None
213Ile	None	None	179.19	None	None
214Leu	8.55	122.95	None	57.64	40.31
215Glu	7.74	114.79	178.34	57.48	28.46
216Ala	8.08	121.32	179.49	55.12	17.56
217Ile	8.12	118.39	178.65	66.54	36.33
218Arg	None	None	None	None	None
219Glu	None	None	None	None	None
220Gly	None	None	None	None	None
221Ile	None	None	None	None	None
222Val	None	None	None	None	None
223Ala	None	None	None	None	None
224Ile	None	None	None	None	None
225Asn	None	None	None	None	None
226Gln	None	None	None	None	None
227Glu	None	None	None	None	None
228Gly	None	None	None	None	None
229Thr	7.53	114.85	174.53	61.07	68.18
230Ile	8.33	124.24	177.27	62.71	36.12
232Met	None	None	None	None	None
233Val	None	None	None	None	None
234Asn	None	None	None	None	None
235Gln	None	None	None	None	None
236Thr	None	None	178.53	65.85	68.4
237Ala	8.3	120.01	179.67	55.18	17.16
238Leu	8.61	117.5	179.51	57.47	40.06
239Lys	None	None	None	None	None
240Leu	None	None	None	None	None
241Leu	None	None	None	None	None
242Gly	None	None	None	None	None
243Tyr	None	None	None	None	None
244Asp	None	None	None	None	None

Residue	H	N	C	Ca	Cb
245Asn	None	None	None	None	None
246Glu	None	None	None	None	None
247Arg	None	None	None	None	None
248Asn	None	None	None	None	None
249Val	None	None	None	None	None
250Leu	None	None	178.08	None	40.4
251Gly	8.95	109.6	174.17	44.86	None
252Thr	None	None	None	None	None
253Pro	None	None	None	None	None
254Ile	None	None	None	None	None
255Leu	None	None	None	None	None
256Gln	None	None	None	None	None
257Leu	None	None	None	None	None
258Ile	None	None	None	None	None
259Pro	None	None	None	None	None
260His	None	None	None	None	None
261Ser	None	None	None	None	None
262Arg	None	None	None	None	None
263Leu	None	None	None	None	None
264Pro	None	None	None	None	None
265Glu	None	None	None	None	None
266Val	None	None	None	None	None
267Ile	None	None	None	None	None
268Arg	None	None	None	None	None
269Thr	None	None	None	None	None
270Gly	None	None	172.83	47.23	None
271Gln	8.03	119.23	174.35	53.62	29.3
272Ala	8.38	125.14	176.44	51.72	20
273Glu	8.56	118.25	177.78	57.5	28.78
274Tyr	7.64	121.06	177.48	57.74	41.29
275Asp	8.95	119.06	175.43	51.66	40.67
276Asp	None	None	None	None	None
277Glu	None	None	None	None	None
278Met	9.13	124.81	174.97	54.49	30.62
279Val	None	None	None	None	None
280Leu	None	None	None	None	None
281Gly	None	None	None	None	None
282Gly	None	104.25	173.66	44.73	None
283Glu	7.79	121.01	174.31	54.81	30.9
284Thr	8.66	118.52	175.93	62.6	70.69
285Val	9.14	121.46	177.87	58.87	35.63
286Ile	None	None	None	None	None
287Ala	None	None	None	None	None
288Asn	None	None	None	None	None
289Arg	None	None	None	None	None
290Ile	None	None	None	None	None
291Pro	None	None	None	None	None
292Ile	None	None	None	None	None
293Lys	8.57	126.26	176.02	54.06	35.29

Residue	H	N	C	Ca	Cb
294Asn	8.46	117.91	None	50.23	None
295Lys	None	None	177.28	58.32	38.24
296Gln	7.43	115.93	176.25	55.63	28.94
297Gly	8.2	107.55	173.8	45.23	None
298Arg	7.74	121.97	175.95	54.84	32.79
299Val	None	None	None	None	None
300Ile	None	None	None	None	None
301Gly	None	None	171.34	45.25	None
302Ala	8.51	120.02	174.2	52.15	21.87
303Val	None	None	None	None	None
304Ser	None	None	None	None	None
305Thr	None	None	None	None	None
306Phe	None	None	None	None	None
307Arg	None	None	None	None	None
308Asn	None	None	None	None	None
309Lys	None	None	None	None	None

Residue	H	N	C	Ca	Cb
47Glu	9.19	114.54	179.11	58.36	28.83
48Thr	None	None	None	66.85	68.19
49Val	8.66	122.01	178.12	67.02	30.77
50Ala	8.58	118.83	178.06	54.67	18.44
51Ser	7.44	109.79	178.31	58.15	63.75
52Thr	None	None	None	None	None
53Ser	None	None	None	62.51	None
54Leu	7.88	120.17	178.05	58.1	40.78
55Val	6.97	116.5	176.44	65.54	30.24
56Arg	7.03	116	179.93	59.46	29.13
57Glu	8.28	118.07	179.11	58.59	30.77
58Ala	8.51	122.13	179.62	53.97	17.22
59Phe	7.64	114.71	177.15	61.23	38.42
60Arg	7.82	116.83	176.81	55.87	29.49
61Asp	7.46	121.1	176.09	53.87	40.51
62Ser	8.73	116.05	175.57	61.1	61.93
63Asn	8.19	114.12	174.18	49.58	37.93
64Pro	None	None	176.1	64.27	None
65Ser	7.6	107.49	175.97	61.8	63.56
66Val	7.26	119.68	178.56	66.26	29.93
67Arg	8.27	113.92	179.55	57.65	31.52
68Leu	8.07	116.56	177.42	57.36	41.99
69Gln	8.73	119.25	174.19	54.78	30.94
70Pro	None	118.74	179.88	65.06	29.7
71Phe	6.7	117.81	176.17	60.31	39.01
72Ala	8.87	121.71	179.45	55.36	17.45
73Glu	8.13	115.97	177.65	58.03	27.96
74Arg	8.01	120.11	177.99	58.03	29.24
75Ile	8.07	118.8	179.66	62.42	40.82
76Arg	8.85	124.61	178.1	60.42	30.37
77Gln	8.04	116.73	178.9	58.43	27.81
78Lys	8.14	117.28	178.38	57.39	32.23
79Thr	7.89	104.15	176.98	62.07	70.07
80Gly	8.56	109.72	174.13	45.59	None
81Ala	7.32	122.12	176.16	51.46	17.7
82Glu	8.08	120.81	176.2	57.51	29.21
83Tyr	6.46	104.25	172.88	54.39	38.61
84Val	7.87	120.25	173.92	62.04	32.49
85Val	9.5	126.7	175.41	59.88	33.9
86Ile	8.08	123.98	175.44	59.77	40.22
87Gly	9.79	115.65	172.69	43.89	None
88Asn	7.99	116.52	176.66	50.8	38.4
89Arg	7.48	115.73	176.08	58.19	28.87
90Gln	7.48	115.76	176.06	55.97	28.17
91Gly	8.2	107.17	172.76	45.16	None
92Ile	7.5	119.79	175.96	57.88	35.3
93Ala	7.83	125.53	177.04	52.3	18.12
94Tyr	9.82	122.45	174.5	55.18	39.78
95Ala	7.92	119.54	175.46	51.03	21.53

Table B.2: Chemical shifts from ^{1}H detected sequence specific assignment of the citrate free state of CitA PASpc

Residue	H	N	C	Ca	Cb
1Met	None	None	None	None	None
2Lys	None	None	None	None	None
3Leu	None	None	None	None	None
4Gln	None	None	None	None	None
5Thr	None	None	174.49	None	None
6Arg	9.33	119.99	176.4	54.25	30.7
7Leu	8.78	120.72	177.76	58.95	40.89
8Met	8.36	119.98	177.83	58.14	30.85
9Val	7.81	118.1	177.63	66.51	30.73
10Ile	8.85	121.7	177.52	66.97	38.88
11Ile	8.83	122.5	178.09	66.95	36.28
12Ala	8.65	122.23	178.09	55.32	17.38
13Ser	8.58	118.39	178.25	59.76	62.85
14Leu	8.45	119.21	178.02	57.78	40.87
15Leu	7.98	120.37	178.99	55.27	40.75
16Leu	8.25	118.28	178.44	58.46	38.33
17Phe	8.29	118.36	None	None	None
18Val	None	None	None	None	None
19Ile	None	None	None	None	None
20Ile	None	None	175.12	63.04	41.42
21Phe	8.78	120.32	179.17	58.72	38.37
22Leu	8.01	117.1	179.03	57.7	40.29
23Thr	8.05	118.3	179.11	66.88	68.11
24Phe	8.57	122.24	177.87	60.14	38.54
25Leu	7.98	117.65	178.48	57.23	38.39
26Phe	8.78	121.76	178.28	59.81	37.57
27Gln	8.47	118.99	178.98	58.95	28.39
28His	8.25	118.19	178.65	59.67	30.23
29Met	7.53	117.92	178.92	58.98	30.27
30Phe	7.89	118.47	177.88	60.44	40.15
31Ala	8.58	120.5	178.07	54.91	16.58
32Ala	8.54	120.06	178.51	55.39	17.14
33Thr	7.94	115.01	178.89	57.5	68.36
34Leu	7.75	120.78	178.45	57.78	40.67
35Lys	None	None	None	None	None
36Glu	None	None	None	None	None
37Gln	None	None	None	None	None
38Ile	None	None	None	None	None
39Gly	None	None	None	None	None
40Met	None	None	None	None	None
41Arg	None	None	None	None	None
42Ala	None	None	None	None	None
43Leu	None	None	None	None	None
44Asn	None	None	None	None	None
45Val	None	None	None	None	None
46Ala	None	None	179.29	55.92	None

Residue	H	N	C	Ca	Cb
96His	9.24	124.54	173.7	54.25	33.08
97Pro	None	None	None	None	None
98Leu	10.98	123.02	177.36	52.94	None
99Thr	None	None	None	None	None
100Glu	None	None	None	58.5	27.96
101Arg	8.33	116.44	179.03	55.61	28.64
102Ile	7.31	121.6	177.67	63.71	36.14
103Gly	9.56	115.5	172.46	44.75	None
104Lys	7.88	118.61	174.27	53.7	33.72
105Ser	None	None	None	None	None
106Met	None	None	None	None	None
107Ile	None	None	None	None	None
108Gly	9.63	None	173.48	44.85	None
109Gly	9.03	108.75	172.98	46.34	None
110Asp	8	118.91	176.91	53.73	None
111Asn	None	None	None	None	None
112Lys	None	None	None	None	None
113Glu	None	None	178.97	58.69	None
114Val	7.04	119.65	177.94	63.07	30.59
115Leu	7.69	118.15	178.06	56.48	40.27
116Lys	7.1	116.3	176.93	56.42	31.84
117Gly	8.43	106.98	173.51	45.08	None
118Lys	7.73	121.93	174.26	55.14	29.31
119Ser	8.22	116.43	178.08	57.54	None
120Ile	None	None	None	None	None
121Ile	None	None	None	None	None
122Ser	None	None	None	None	None
123Glu	None	None	173.07	59.68	31.58
124Ala	8.81	126.28	177.19	50.53	19.42
125Val	8.85	119.33	178.22	60.25	31.79
126Gly	7.24	112.29	171.5	43.36	None
127Ser	None	None	None	None	None
128Leu	None	None	None	None	None
129Gly	None	None	None	None	None
130Pro	None	None	None	None	None
131Ala	None	None	None	None	None
132Ile	None	None	175.35	60.31	None
133Arg	9.14	125.86	174.72	53.88	32.54
134Gly	9.18	109.99	171.69	43.67	None
135Lys	9.07	122.9	173.85	54.17	36.43
136Ala	9.01	122.27	173.84	47.79	21.88
137Pro	None	None	174.41	60.61	30.9
138Ile	7.52	117.86	175.16	59.66	38.81
139Phe	8.88	126.13	177.14	56.5	41.55
140Asp	8.96	119.13	178.35	51.7	40.6
141Glu	9.56	117.86	176.71	58.6	27.94
142Asn	8.23	116.07	175.83	52.61	38.98
143Gly	8.07	107.87	174.33	45.5	None
144Ser	8.64	118.67	173.95	57.71	63

Residue	H	N	C	Ca	Cb
145Val	8.91	124.54	177.55	63.17	30.54
146Ile	8.95	120.57	175.47	60.59	38.84
147Gly	7.28	106.82	169.96	45.69	None
148Ile	8.59	118.29	174.08	60.07	44.54
149Val	9.15	124.88	174.36	60.54	33.08
150Ser	9.41	121.27	173.68	55.18	64.54
151Val	9.18	126.91	174.24	60.21	33.28
152Gly	7.14	112.07	171.8	43.41	None
153Phe	8.41	117.96	178.54	55.98	40.66
154Leu	8.92	120.34	174.83	54.27	40.98
155Leu	8.91	120.64	174.87	55.22	40.97
156Glu	8.64	120.42	176.56	54.24	30.94
157Asp	7.91	120.42	175.54	55.07	40.74
158Ile	8.63	119.09	175.29	60.01	37.29
159Gln	None	None	None	None	None
160Arg	None	None	None	None	None
161Thr	None	None	None	None	None
162Val	None	None	None	None	None
163Trp	None	None	None	None	None
164Ser	None	None	None	None	None
165Tyr	None	None	None	None	None
166Ser	None	None	None	None	None
167Met	None	None	None	None	None
168Lys	None	None	None	None	None
169Ile	None	None	None	None	None
170Phe	None	None	None	None	None
171Phe	None	None	None	None	None
172Phe	None	None	None	60.28	37.69
173Ser	8.75	121.59	174.43	60.06	None
174Val	8.77	121.26	177.76	66.81	30.84
175Leu	8.69	119.73	178.21	60.09	40.99
176Ala	None	None	None	None	None
177Leu	None	None	None	None	None
178Leu	None	None	None	None	None
179Phe	None	None	175.13	None	None
180Gly	8.27	112.13	176.29	44.65	None
181Ala	8.18	116.72	179.34	52.4	21.6
182Val	9.08	124.39	174.61	60.46	33.14
183Gly	9.14	110.32	171.48	43.67	None
184Ala	8.87	122.78	179.34	54.95	17.18
185Val	8.1	116.76	177.42	66.41	28.76
186Ala	8.71	122.44	179.8	54.67	17.23
187Ile	8.24	117.96	177.4	66.24	38.36
188Ala	8.84	122.2	179.42	55.85	17.29
189Lys	9.12	115.65	180.12	59.13	29.02
190Ala	8.59	118.57	179.29	55.32	17.82
191Val	7.77	116.57	177.46	66.17	31.08
192Lys	8.3	119.45	178.15	58.84	30.93
193Lys	8.44	121.15	178.88	59.97	30.57

Residue	H	N	C	Ca	Cb
194Ser	None	None	174.29	61.63	68.38
195Ile	8.32	124.4	176.88	62.53	37.66
196His	8.64	117.41	177.69	62.33	28.26
197Gly	8.52	107.35	175.15	45.05	None
198Leu	7.96	123.81	175.39	59.75	40.24
199Glu	None	None	None	None	None
200Pro	None	None	177.75	66.62	30.85
201Glu	8.58	118.95	178.95	57.71	30.97
202Glu	7.84	120.65	177.71	57.81	29.45
203Ile	7.76	120.62	179.28	62.06	40.82
204Gly	8.63	107.48	176.31	45.03	None
205Leu	7.66	121.78	178.61	55.18	40.61
206Leu	8.07	116.7	177.52	57.44	38.24
207Tyr	8.98	119.48	178.58	59	38.31
208Gln	8.07	117.51	177.61	57.76	27.99
209Glu	7.99	119.96	178.7	59.48	30.67
210Lys	8.5	117.82	178.45	59.24	30.78
211Gln	7.55	117.92	178.31	58.55	28.39
212Ala	8.3	120.3	179.51	55.24	17.41
213Ile	8.27	118.48	177.52	66.59	38.27
214Leu	8.31	118.67	177.96	57.53	41.04
215Glu	8.82	120.21	176.3	57.18	29.5
216Ala	7.72	120.11	178.14	54.42	17.34
217Ile	8.18	117.62	177.64	66.73	38.47
218Arg	8.35	121.51	175.76	59.91	30.64
219Glu	8.46	119.36	179.11	55.43	29.09
220Gly	None	None	None	None	None
221Ile	None	None	None	None	None
222Val	8.62	121.58	173.86	59.83	31.29
223Ala	8.95	127.37	176.55	49.74	22.67
224Ile	8.87	111.03	176.82	58	41.78
225Asn	8	119.48	179.6	55.19	41.01
226Gln	None	None	176.69	58.47	27.82
227Glu	7.56	116.39	177.07	55.9	28.95
228Gly	8.44	107.02	173.58	45.1	None
229Thr	7.92	118.47	174.63	61.57	69.48
230Ile	8.32	124.32	176.77	62.56	37.26
231Thr	7.82	121.32	None	None	None
232Met	None	None	None	None	None
233Val	None	None	None	None	None
234Asn	None	None	None	None	None
235Gln	8.8	119.57	177.22	58.41	30.93
236Thr	7.87	115.37	176.67	66.4	68.04
237Ala	7.86	121.8	176.03	55.23	17.43
238Leu	8.48	117.44	177.95	57.59	40.55
239Lys	8.59	118.2	179.68	59.19	30.96
240Leu	8.35	118.81	178.52	55.43	40.16
241Leu	7.9	116.4	176.88	56.13	40.61
242Gly	8.36	106.73	172.75	45.08	None

Residue	H	N	C	Ca	Cb
243Tyr	7.6	120.37	176.58	58.09	40.66
244Asp	8.47	117.89	178.03	54.79	41.73
245Asn	7.65	115.66	178.9	55.74	38.72
246Glu	None	None	None	None	None
247Arg	None	None	None	None	None
248Asn	None	None	None	None	None
249Val	None	None	None	None	None
250Leu	7.48	120.7	178.03	57.08	40.67
251Gly	8.92	109.6	173.81	44.85	None
252Thr	7.83	118.64	176.41	62.24	None
253Pro	None	124.58	179.54	62.59	31.81
254Ile	8.99	127.21	175.92	63.63	34.17
255Leu	8.42	119.28	178.53	54.64	39.75
256Gln	7.57	114.76	176.44	57.43	28.38
257Leu	7.91	117.72	177.57	57.99	40.05
258Ile	8.39	117.27	179.16	57.66	38.17
259Pro	None	None	177.65	66.39	30.29
260His	8.05	118.78	177.61	55.31	27.83
261Ser	None	None	None	63.19	None
262Arg	7.76	120.63	178.57	58.53	28.84
263Leu	8.01	117.76	177.68	59.68	39.89
264Pro	None	None	178.83	65.49	30.2
265Glu	7.3	117.72	178.36	58.71	29.78
266Val	8.32	119.25	177.31	65.39	29.59
267Ile	8.73	117.69	176.99	62.7	38.8
268Arg	7.28	117.56	177.16	56.54	30.04
269Thr	8.56	107.04	177.27	62.21	71.54
270Gly	8.42	111.5	173.01	46.35	None
271Gln	8.04	119.15	174.36	53.62	29.6
272Ala	8.47	125.01	176.79	51.7	20.16
273Glu	8.78	119.34	174.62	59.6	30.76
274Tyr	8.57	119.76	177.52	56.16	40.85
275Asp	8.86	118.85	174.95	54.79	40.62
276Asp	8.06	120.54	None	54.88	None
277Glu	None	None	None	None	None
278Met	None	None	None	None	None
279Val	None	None	None	None	None
280Leu	None	None	178.66	55.48	None
281Gly	8.25	112.22	176.25	44.67	None
282Gly	7.73	107.65	170.82	45.36	None
283Glu	7.9	121.05	175.21	55.1	30.8
284Thr	8.01	118.96	176.85	61.46	68.82
285Val	7.47	121.37	176.07	58.95	35.65
286Ile	7.79	117.79	175.59	59.42	40.25
287Ala	9.26	130.53	176.6	49.97	21.73
288Asn	None	None	None	None	None
289Arg	None	None	None	None	None
290Ile	None	None	None	None	None
291Pro	None	None	174.9	62.78	30.69

Residue	H	N	C	Ca	Cb
292Ile	8.35	121.4	175.69	59.24	38.69
293Lys	8.83	125.52	175.95	53.87	35.8
294Asn	8.56	117.93	178.01	50.27	37.88
295Lys	8.32	117.53	177.77	58.5	27.88
296Gln	7.55	116.11	176.13	55.87	28.87
297Gly	8.17	107.52	173.55	45.19	None
298Arg	8.14	120.94	176.27	54.89	30.23
299Val	8.86	124.73	176.62	62.95	30.34
300Ile	8.86	120.02	175.55	60.18	38.52
301Gly	7.94	107.43	170.67	45.37	None
302Ala	8.56	119.68	173.93	51.76	21.81
303Val	8.92	118.9	None	58.83	None
304Ser	None	None	None	None	None
305Thr	None	None	None	None	None
306Phe	None	None	None	None	None
307Arg	None	None	None	None	None
308Asn	None	None	None	None	None
309Lys	None	None	None	None	None

Table B.3: Predicted torsion angles from chemical shift of TM II in the free state

```
# Phi/Psi Angles From 'Strong' TALOS-N Predictions:
#    error margins are set to conservative default values of double the
#    deviation observed in TALOS-N capped at a minimum of +/-20 degree.
   3   VAL  PHI    -151.3   -75.7
   3   VAL  PSI     111.5   158.4
   4   GLY  PHI    -171.1   -44.6
   4   GLY  PSI     152.6   198.8
   5   ALA  PHI     -81.7   -41.7
   5   ALA  PSI     -55.7   -15.7
   6   VAL  PHI     -83.5   -43.5
   6   VAL  PSI     -63.3   -23.3
   7   ALA  PHI     -84.8   -44.8
   7   ALA  PSI     -60.9   -20.9
   8   ILE  PHI     -85.9   -45.9
   8   ILE  PSI     -63.3   -23.3
   9   ALA  PHI     -82.7   -42.7
   9   ALA  PSI     -62.4   -22.4
   10   LYS  PHI     -83.5   -43.5
   10   LYS  PSI     -60.4   -20.4
   11   ALA  PHI     -86.4   -46.4
   11   ALA  PSI     -60.3   -20.3
   12   VAL  PHI     -85.3   -45.3
   12   VAL  PSI     -65.7   -25.7
   13   LYS  PHI     -82.4   -42.4
   13   LYS  PSI     -56.7   -16.7
   14   LYS  PHI     -83.0   -43.0
   14   LYS  PSI     -50.4   -10.4

# Phi/Psi Angles From 'Generous' TALOS-N Predictions:
#    error margins are set to default values of triple the standard
#    deviation observed in TALOS-N capped at a minimum of +/-30 degree.
```

Table B.4: Predicted torsion angles from chemical shift of TM II in the bound state

```
# Phi/Psi Angles From 'Strong' TALOS-N Predictions:
#    error margins are set to conservative default values of double the
#    deviation observed in TALOS-N capped at a minimum of +/-20 degree.
   1   GLY  PHI      58.7    98.7
   1   GLY  PSI      -8.1    40.6
   3   VAL  PHI     -86.4   -46.4
   3   VAL  PSI     -58.7   -18.7
   5   ALA  PHI     -84.4   -44.4
   5   ALA  PSI     -59.5   -19.5
   6   VAL  PHI     -85.3   -45.3
   6   VAL  PSI     -61.7   -21.7
   7   ALA  PHI     -83.4   -43.4
   7   ALA  PSI     -62.7   -22.7
   8   ILE  PHI     -85.0   -45.0
   8   ILE  PSI     -64.5   -24.5
   9   ALA  PHI     -81.3   -41.3
   9   ALA  PSI     -61.7   -21.7
   10   LYS  PHI     -86.9   -46.9
   10   LYS  PSI     -56.9   -16.9
   11   ALA  PHI     -87.6   -47.6
   11   ALA  PSI     -51.7   -11.7
   12   VAL  PHI    -120.4   -69.1
   12   VAL  PSI     -17.5    22.5

# Phi/Psi Angles From 'Generous' TALOS-N Predictions:
#    error margins are set to default values of triple the standard
#    deviation observed in TALOS-N capped at a minimum of +/-30 degree.
   2   ALA  PHI     -92.4   -32.4
   2   ALA  PSI     -67.7    -7.7
   4   GLY  PHI     -93.0   -33.0
   4   GLY  PSI     -70.0   -10.0
   13   LYS  PHI    -139.2    19.7
   13   LYS  PSI     -70.0    19.5
```

APPENDIX C

Appendix: Chapter 3

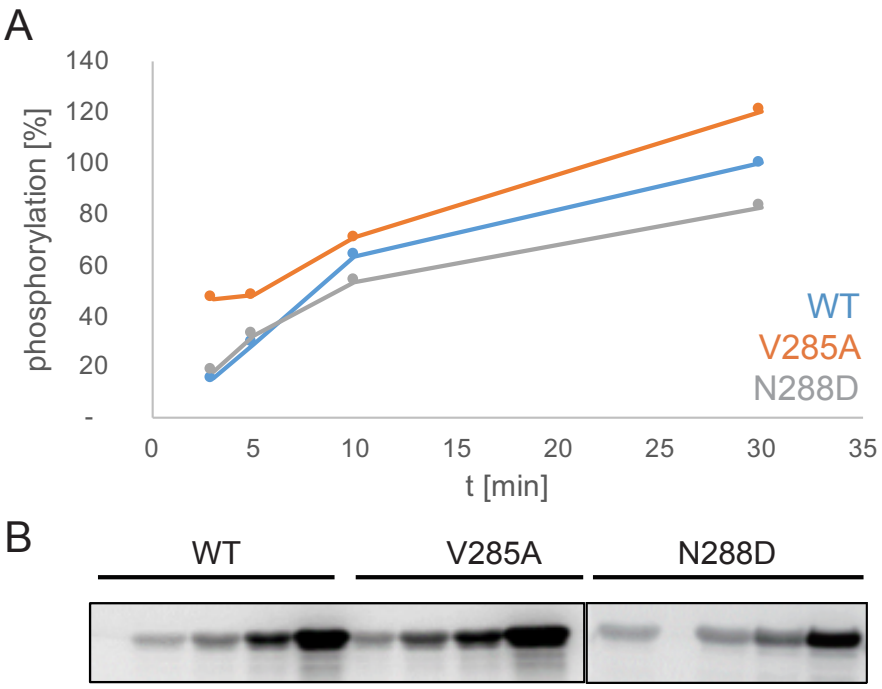

Figure C.1: Kinase activity of the WT, V285A and N288D PASc-kin constructs by SPA ^{33}P assay. The WT (blue) and V285A (orange) mutant display parallel dimer in crystal, which have elevated rate of phosphorylation compared with the antiparallel mutant N288D (grey) PASc attached kinase (A). Data are provided by M.Stopp

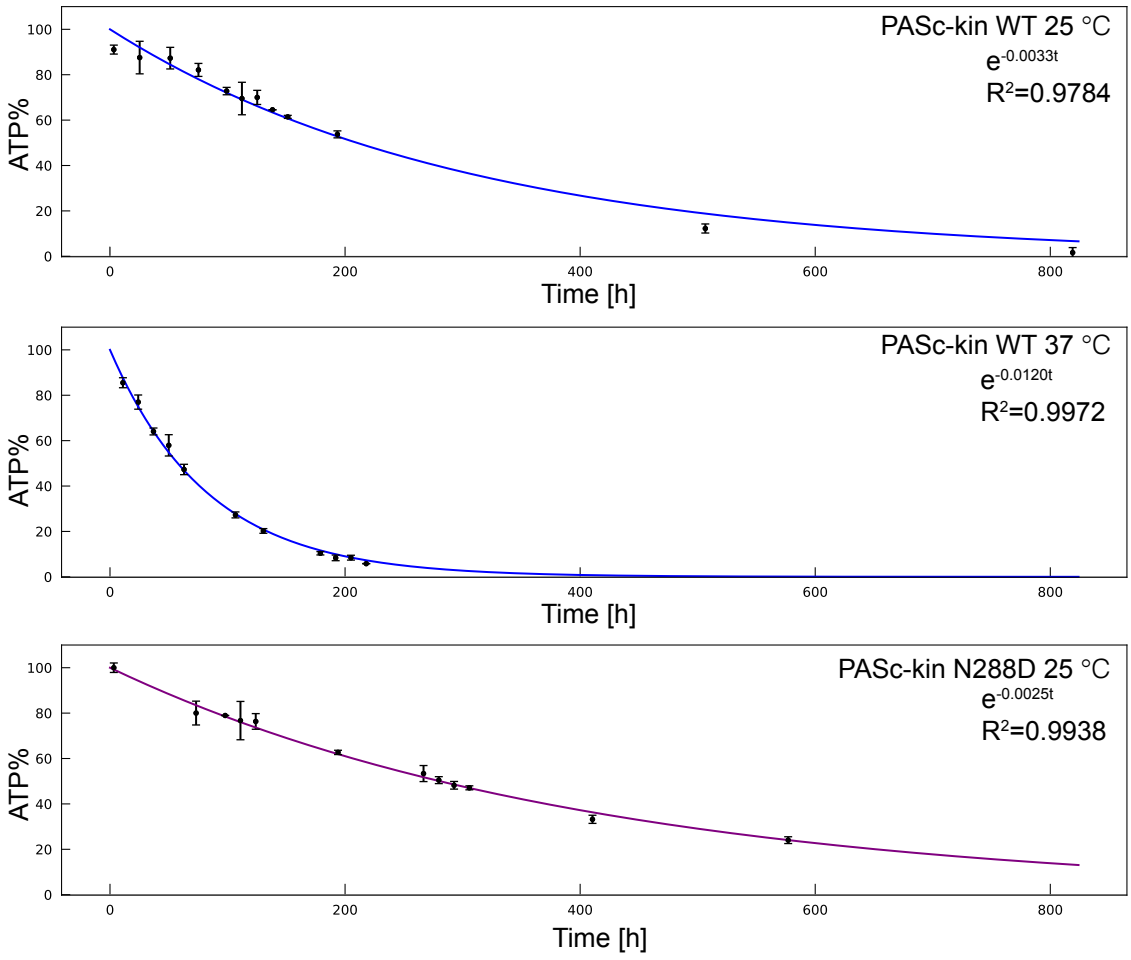

Figure C.2: Consumption of ATP from ^{31}P NMR activity assay measure to 800 h.

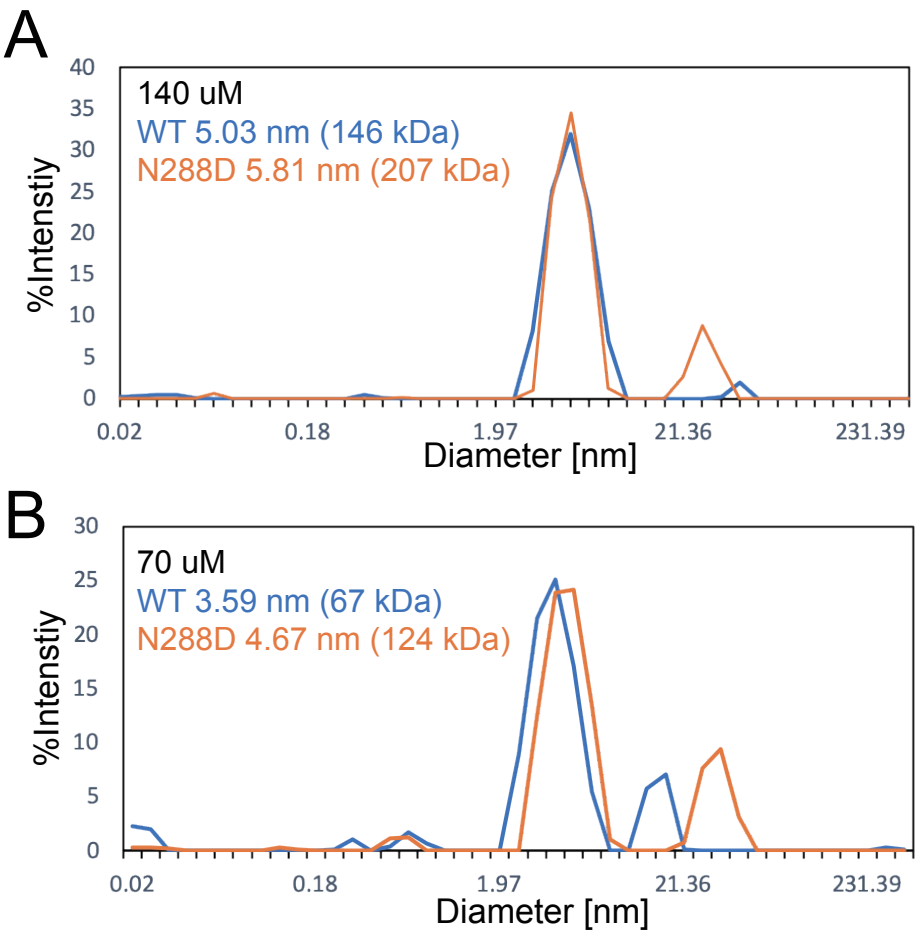

Figure C.3: Dynamic light scattering (DLS) measurement of the WT (blue) and N288D mutant (orange) PASc-kin at a concentration of 140 uM (A) and 70 uM (B). The data is provided by M. Han

C.1 Derivation of reaction kinetics of ATP hydrolysis

CitA kinase converts ATP into ADP and free phosphate, there is reaction

$$ATP + CitA \xrightarrow{k_1} CitA - Pi \xrightarrow{k_2} CitA + Pi \tag{C.1}$$

k_1 is the phosphorylation rate, while k_2 is the hydrolysis rate, both reactions are so far considered to be non-reversible.In the beginning since the ATP concentration is much larger than that of the CitA, it can be considered a constant. The change of CitA-Pi concentration is:

$$\Delta[CitA - Pi] = [CitA] \cdot k_1 - [CitA - Pi] \cdot k_2 \tag{C.2}$$

Change in ATP concentration

$$\Delta[ATP] = -[CitA] \cdot k_1 \tag{C.3}$$

Change in free phosphate concentration

$$\Delta[Pi] = [CitA - Pi] \cdot k_2 \tag{C.4}$$

Since the enzyme is not consumed, the total citA concentration remains unchanged at:

$$[CitA]_{total} = [CitA - Pi] + [CitA] \tag{C.5}$$

At steady state, the phophorylated CitA does not change,

$$\Delta[CitA - Pi] = 0 = [CitA] \cdot k_1 - [CitA - Pi] \cdot k_2 \tag{C.6}$$

with equation C.5,

$$[CitA] = \frac{k_2}{k_1 + k_2} \cdot [CitA]_{total} \tag{C.7}$$

$$[CitA - Pi] = \frac{k_1}{k_1 + k_2} \cdot [CitA]_{total} \tag{C.8}$$

With equation C.3 and C.4

$$\Delta[ATP] = -\frac{k_2 \cdot k_1}{k_1 + k_2} \cdot [CitA]_{total} \tag{C.9}$$

Change in free phosphate concentration

$$\Delta[Pi] = \frac{k_2 \cdot k_1}{k_1 + k_2} \cdot [CitA]_{total} \tag{C.10}$$

So in the beginning of the reaction, the consumption of ATP and the production of free phosphate follows a linear equation.

APPENDIX D

Appendix: Chapter 4

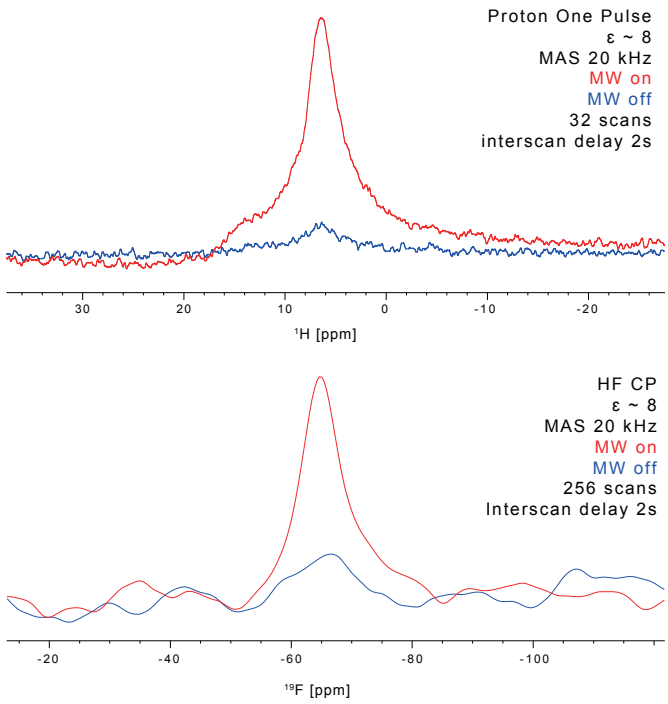

Figure D.1: DNP enhancement in CitA PASpc free sample is similar for proton one pulse (upper) and proton to fluorine CP (lower) experiment.

Table D.1: Intensity of the ^{19}F CODEX experiment of the CF3-N308C CitA PASpc in the free state and the intensities from their respective reference experiments.

Time [ms]	S	Error S	S0	Error S0	S/S0
250	3.52E+08	8.32E+06	4.11E+08	1.09E+07	0.86
300	5.40E+08	3.52E+07	3.38E+08	1.39E+07	1.60
500	3.11E+08	9.08E+06	6.27E+08	4.13E+07	0.50

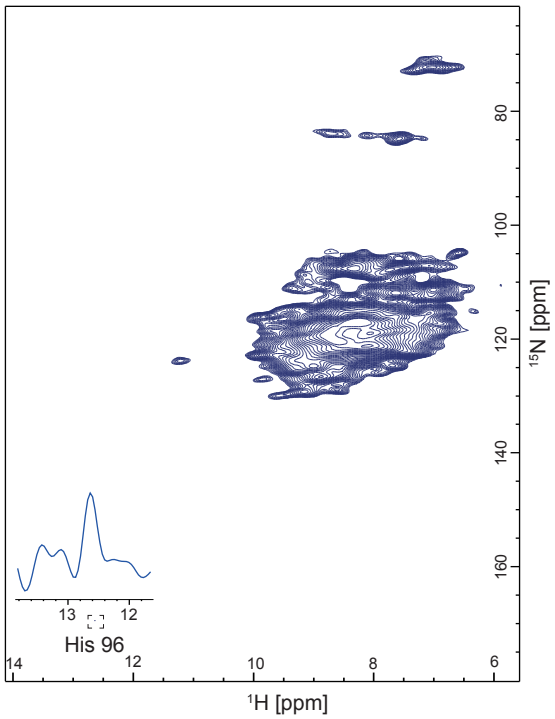

Figure D.2: (H)NH spectrum of CF3-N308C CitA PASpc liposome sample after incubation with citrate free buffer at 40 °C for one week. The intensity for the citrate indication His96 side-chain (black square) indicates that there is only a very small portion (1D trace) of the citrate bound sample left.

Table D.2: Intensity of the ^{19}F CODEX experiment of the CF3-N308C CitA PASpc in the citrate bound state and the intensities from their respective reference experiments.

Time [ms]	S	Error S	S0	Error S0	S/S0
20	3.94E+08	5.95E+06	4.19E+08	1.80E+07	0.94
50	5.70E+08	2.90E+07	5.54E+08	3.26E+07	1.03
100	3.10E+08	1.11E+07	3.42E+08	3.04E+07	0.91
250	2.70E+08	2.10E+07	4.50E+08	2.98E+07	0.60
275	3.93E+08	6.16E+07	5.85E+08	1.92E+07	0.67
300	4.25E+08	4.81E+07	5.85E+08	2.55E+07	0.73

APPENDIX E

Appendix: Chapter 5

E.1 Fitting of TREDOR curves

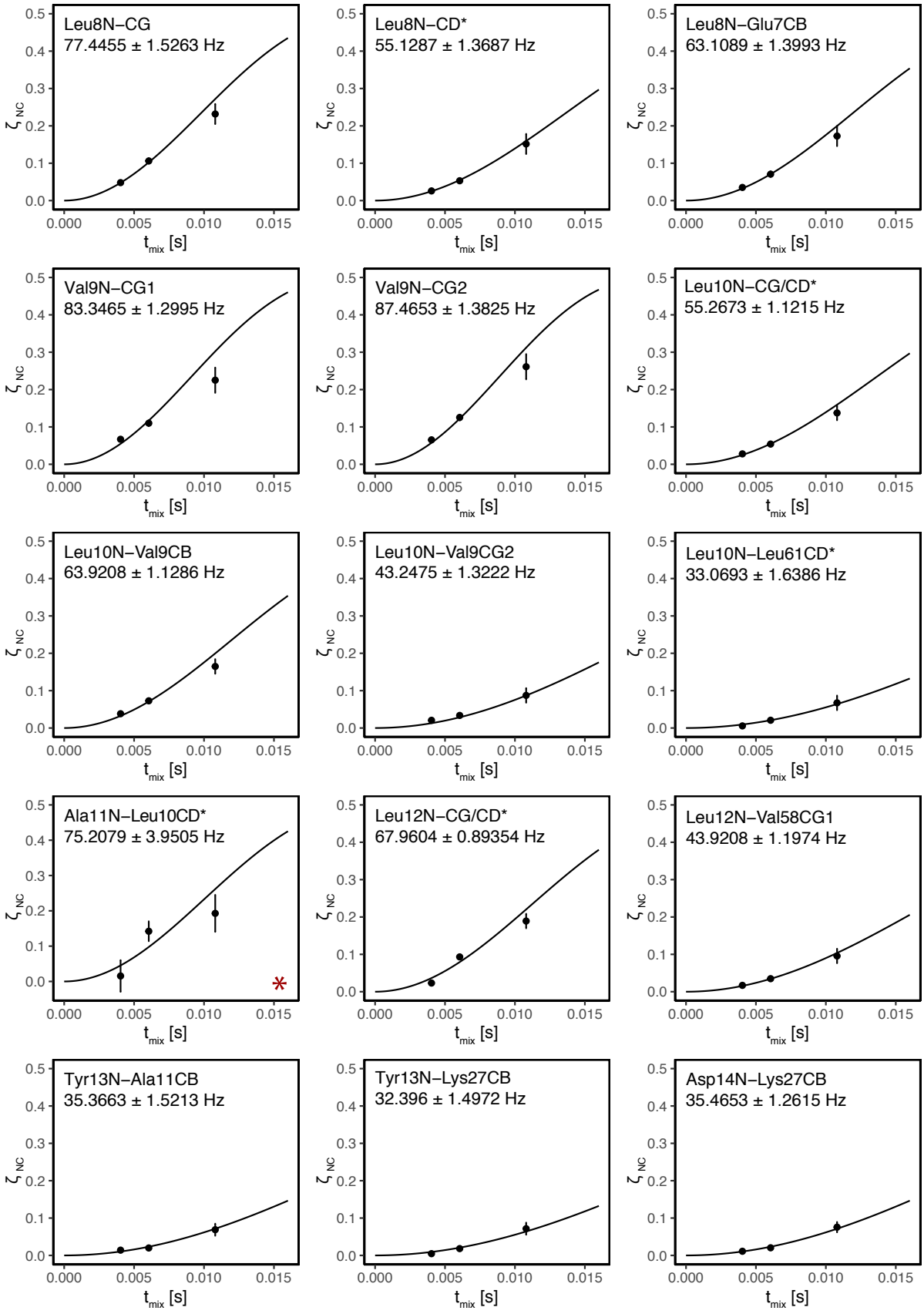
Leu8N–CG
77.4455 ± 1.5263 Hz
Leu8N–CD*
55.1287 ± 1.3687 Hz
Leu8N–Glu7CB
63.1089 ± 1.3993 Hz
Val9N–CG1
83.3465 ± 1.2995 Hz
Val9N–CG2
87.4653 ± 1.3825 Hz
Leu10N–CG/CD*
55.2673 ± 1.1215 Hz
Leu10N–Val9CB
63.9208 ± 1.1286 Hz
Leu10N–Val9CG2
43.2475 ± 1.3222 Hz
Leu10N–Leu61CD*
33.0693 ± 1.6386 Hz
Ala11N–Leu10CD*
75.2079 ± 3.9505 Hz
Leu12N–CG/CD*
67.9604 ± 0.89354 Hz
Leu12N–Val58CG1
43.9208 ± 1.1974 Hz
Tyr13N–Ala11CB
35.3663 ± 1.5213 Hz
Tyr13N–Lys27CB
32.396 ± 1.4972 Hz
Asp14N–Lys27CB
35.4653 ± 1.2615 Hz
ζ NC
t mix [s]
0.0
0.1
0.2
0.3
0.4
0.5
0.000
0.005
0.010
0.015

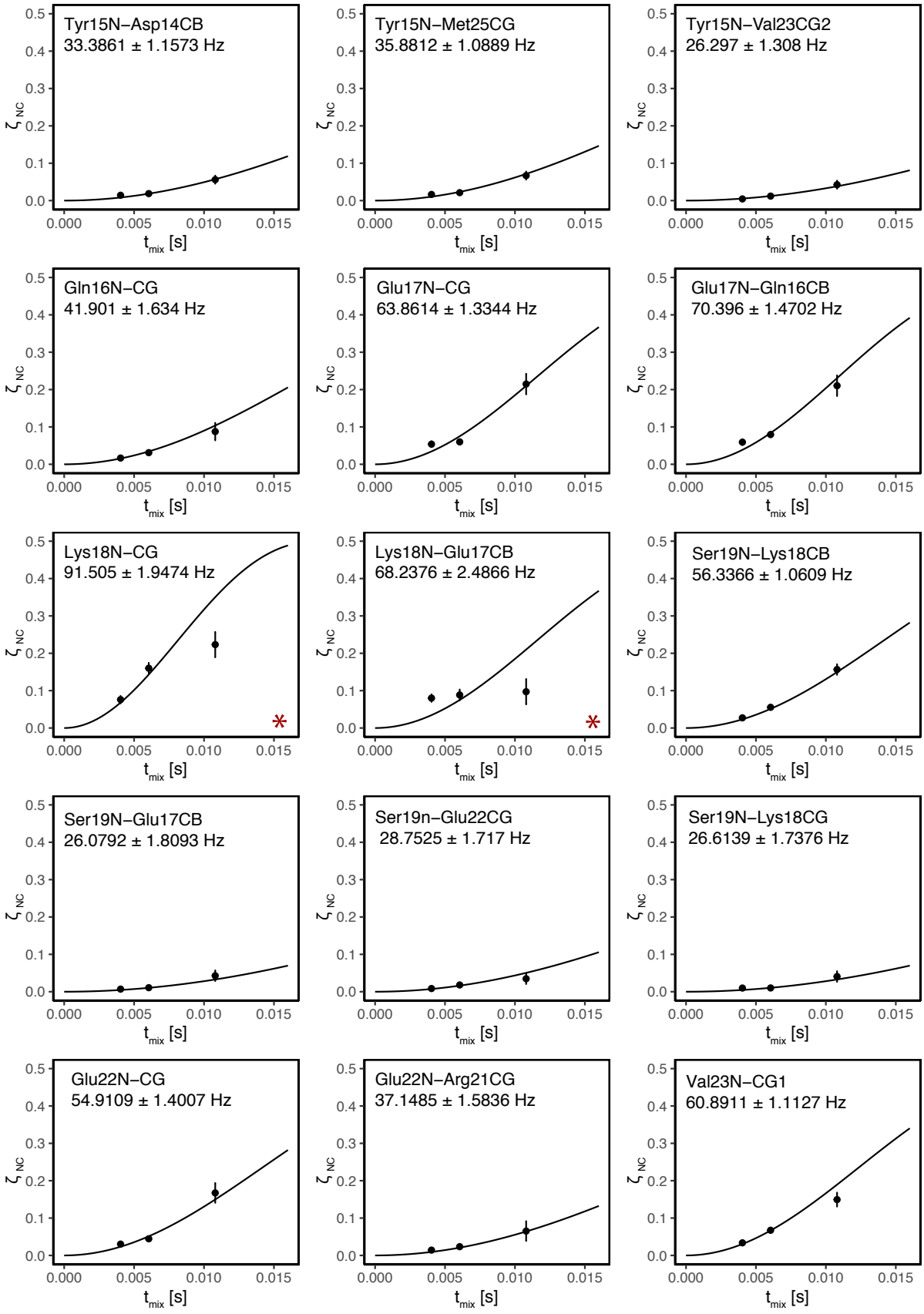
Tyr15N–Asp14CB
33.3861 ± 1.1573 Hz
Tyr15N–Met25CG
35.8812 ± 1.0889 Hz
Tyr15N–Val23CG2
26.297 ± 1.308 Hz
Gln16N–CG
41.901 ± 1.634 Hz
Glu17N–CG
63.8614 ± 1.3344 Hz
Glu17N–Gln16CB
70.396 ± 1.4702 Hz
Lys18N–CG
91.505 ± 1.9474 Hz
Lys18N–Glu17CB
68.2376 ± 2.4866 Hz
Ser19N–Lys18CB
56.3366 ± 1.0609 Hz
Ser19N–Glu17CB
26.0792 ± 1.8093 Hz
Ser19n–Glu22CG
28.7525 ± 1.717 Hz
Ser19N–Lys18CG
26.6139 ± 1.7376 Hz
Glu22N–CG
54.9109 ± 1.4007 Hz
Glu22N–Arg21CG
37.1485 ± 1.5836 Hz
Val23N–CG1
60.8911 ± 1.1127 Hz
ζ NC
t mix [s]
0.0
0.1
0.2
0.3
0.4
0.5
0.000
0.005
0.010
0.015

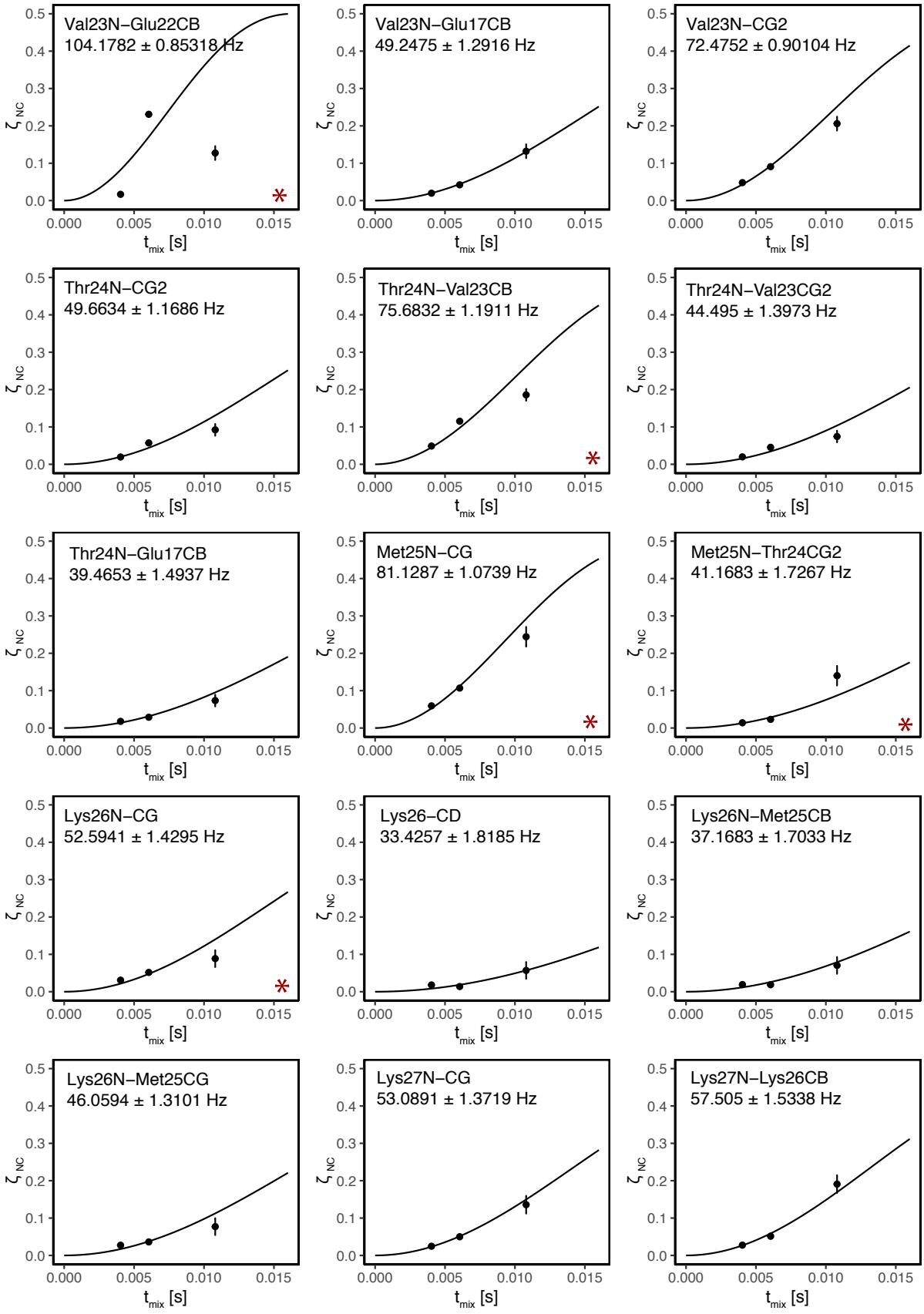
Val23N–Glu22CB
104.1782 ± 0.85318 Hz
Val23N–Glu17CB
49.2475 ± 1.2916 Hz
Val23N–CG2
72.4752 ± 0.90104 Hz
Thr24N–CG2
49.6634 ± 1.1686 Hz
Thr24N–Val23CB
75.6832 ± 1.1911 Hz
Thr24N–Val23CG2
44.495 ± 1.3973 Hz
Thr24N–Glu17CB
39.4653 ± 1.4937 Hz
Met25N–CG
81.1287 ± 1.0739 Hz
Met25N–Thr24CG2
41.1683 ± 1.7267 Hz
Lys26N–CG
52.5941 ± 1.4295 Hz
Lys26–CD
33.4257 ± 1.8185 Hz
Lys26N–Met25CB
37.1683 ± 1.7033 Hz
Lys26N–Met25CG
46.0594 ± 1.3101 Hz
Lys27N–CG
53.0891 ± 1.3719 Hz
Lys27N–Lys26CB
57.505 ± 1.5338 Hz
ζ NC
t mix [s]
0.0
0.1
0.2
0.3
0.4
0.5
0.000
0.005
0.010
0.015

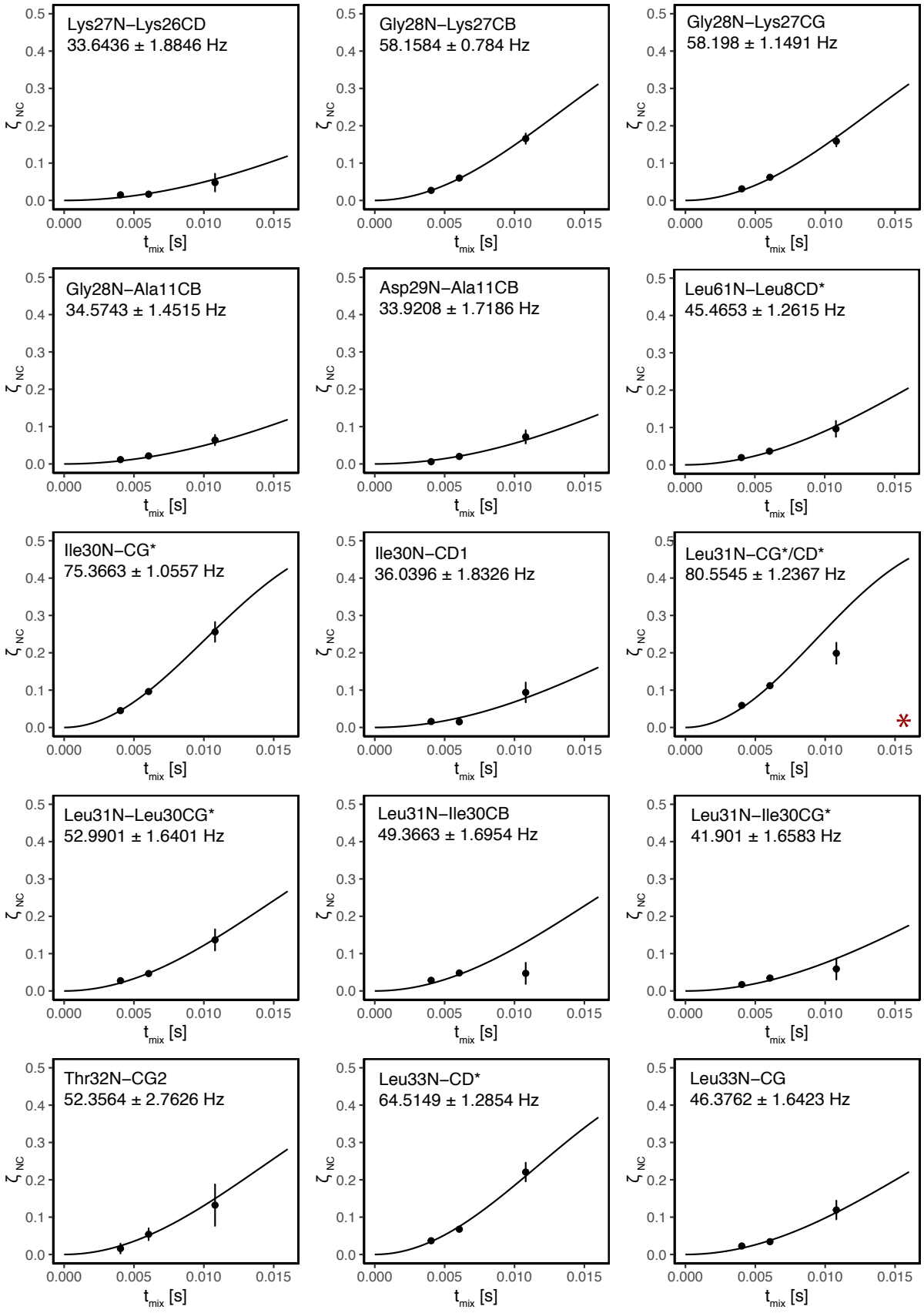
Lys27N–Lys26CD
33.6436 ± 1.8846 Hz
Gly28N–Lys27CB
58.1584 ± 0.784 Hz
Gly28N–Lys27CG
58.198 ± 1.1491 Hz
Gly28N–Ala11CB
34.5743 ± 1.4515 Hz
Asp29N–Ala11CB
33.9208 ± 1.7186 Hz
Leu61N–Leu8CD*
45.4653 ± 1.2615 Hz
Ile30N–CG*
75.3663 ± 1.0557 Hz
Ile30N–CD1
36.0396 ± 1.8326 Hz
Leu31N–CG*/CD*
80.5545 ± 1.2367 Hz
*
Leu31N–Leu30CG*
52.9901 ± 1.6401 Hz
Leu31N–Ile30CB
49.3663 ± 1.6954 Hz
Leu31N–Ile30CG*
41.901 ± 1.6583 Hz
Thr32N–CG2
52.3564 ± 2.7626 Hz
Leu33N–CD*
64.5149 ± 1.2854 Hz
Leu33N–CG
46.3762 ± 1.6423 Hz
ζ NC
t mix [s]
0.0
0.1
0.2
0.3
0.4
0.5
0.000
0.005
0.010
0.015

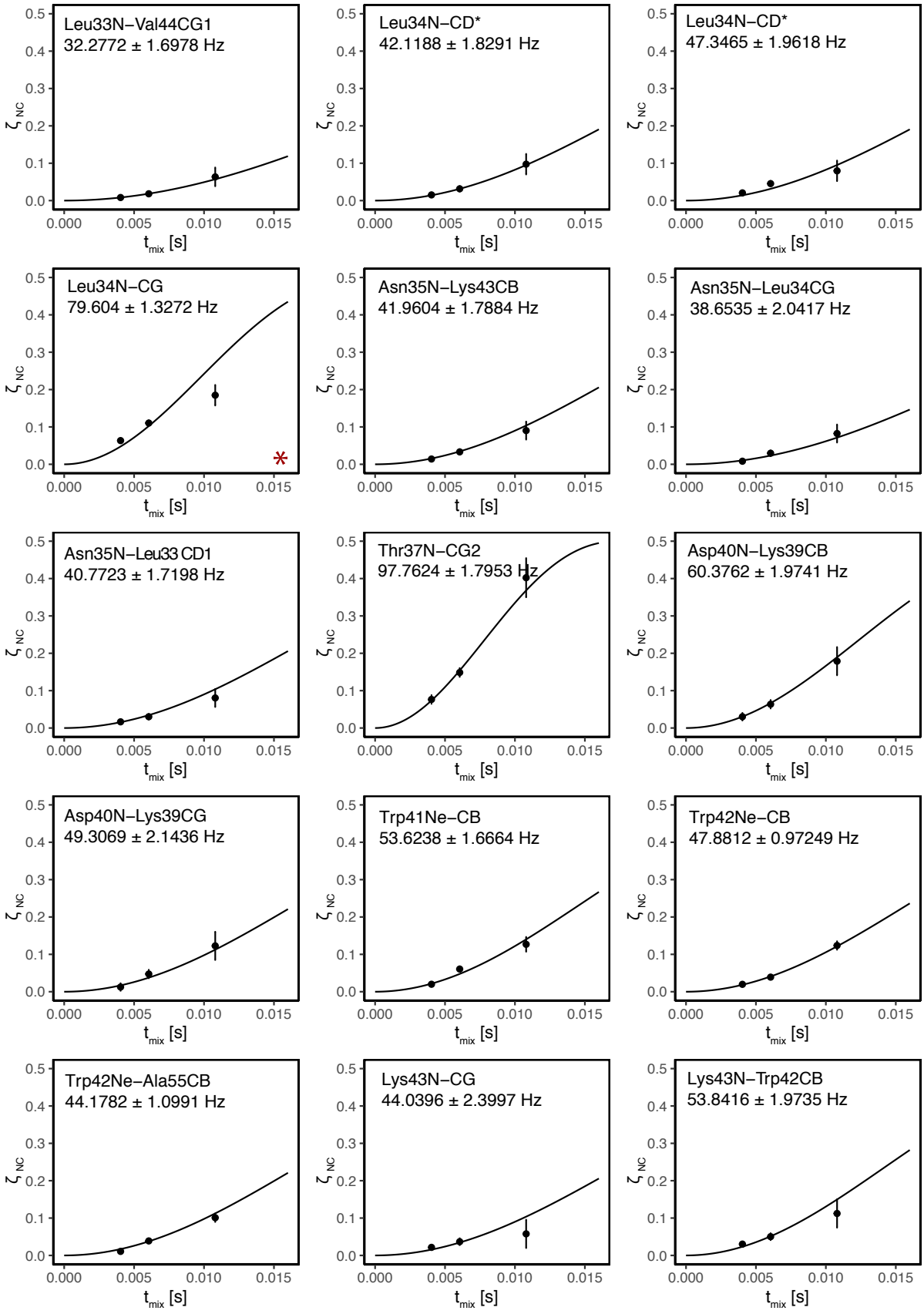
Leu33N–Val44CG1
32.2772 ± 1.6978 Hz
Leu34N–CD*
42.1188 ± 1.8291 Hz
Leu34N–CD*
47.3465 ± 1.9618 Hz
Leu34N–CG
79.604 ± 1.3272 Hz
*
Asn35N–Lys43CB
41.9604 ± 1.7884 Hz
Asn35N–Leu34CG
38.6535 ± 2.0417 Hz
Asn35N–Leu33 CD1
40.7723 ± 1.7198 Hz
Thr37N–CG2
97.7624 ± 1.7953 Hz
Asp40N–Lys39CB
60.3762 ± 1.9741 Hz
Asp40N–Lys39CG
49.3069 ± 2.1436 Hz
Trp41Ne–CB
53.6238 ± 1.6664 Hz
Trp42Ne–CB
47.8812 ± 0.97249 Hz
Trp42Ne–Ala55CB
44.1782 ± 1.0991 Hz
Lys43N–CG
44.0396 ± 2.3997 Hz
Lys43N–Trp42CB
53.8416 ± 1.9735 Hz
ζ NC
t mix [s]
0.0
0.1
0.2
0.3
0.4
0.5
0.000
0.005
0.010
0.015

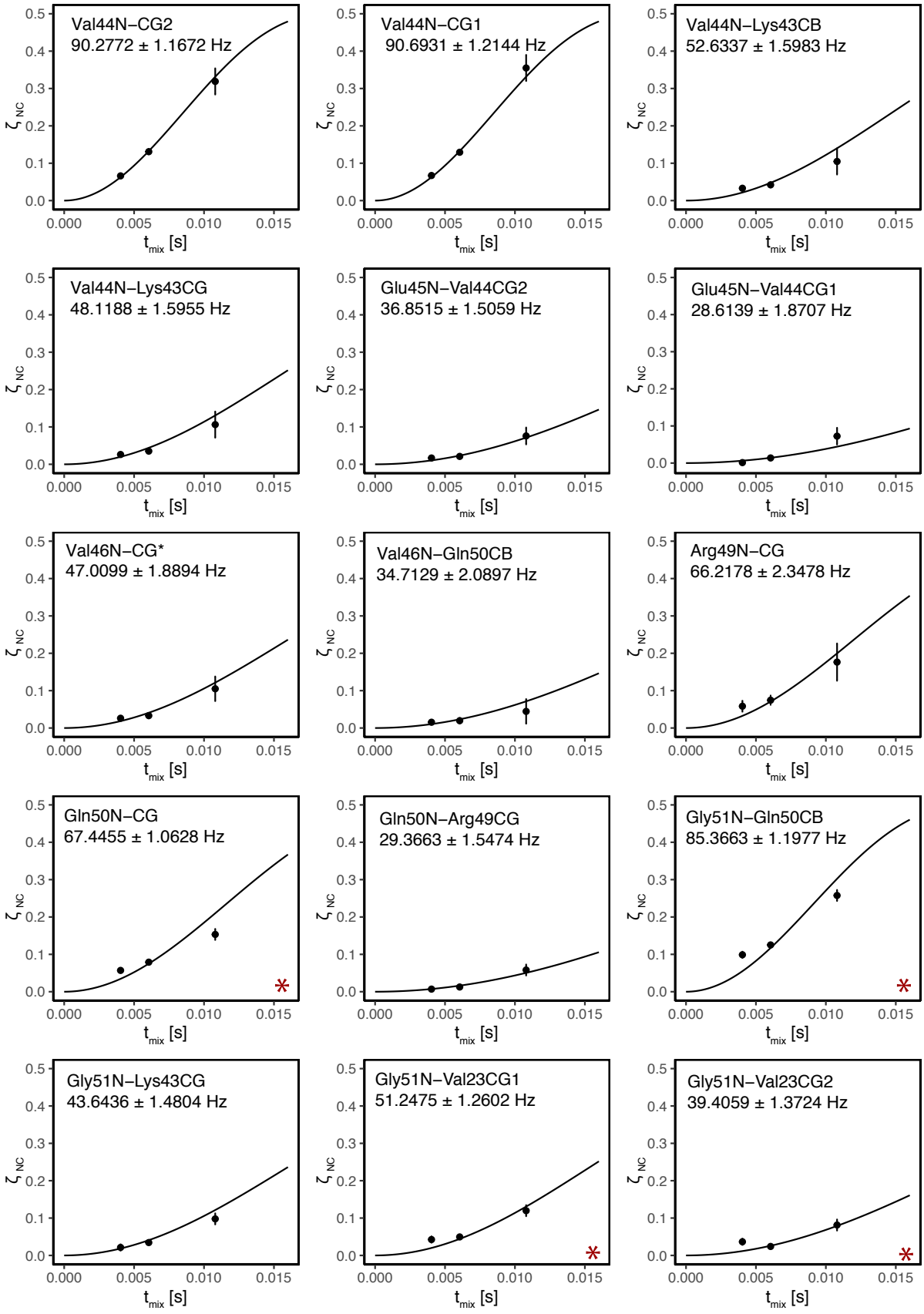
Val44N–CG2
90.2772 ± 1.1672 Hz
Val44N–CG1
90.6931 ± 1.2144 Hz
Val44N–Lys43CB
52.6337 ± 1.5983 Hz
Val44N–Lys43CG
48.1188 ± 1.5955 Hz
Glu45N–Val44CG2
36.8515 ± 1.5059 Hz
Glu45N–Val44CG1
28.6139 ± 1.8707 Hz
Val46N–CG*
47.0099 ± 1.8894 Hz
Val46N–Gln50CB
34.7129 ± 2.0897 Hz
Arg49N–CG
66.2178 ± 2.3478 Hz
Gln50N–CG
67.4455 ± 1.0628 Hz
Gln50N–Arg49CG
29.3663 ± 1.5474 Hz
Gly51N–Gln50CB
85.3663 ± 1.1977 Hz
Gly51N–Lys43CG
43.6436 ± 1.4804 Hz
Gly51N–Val23CG1
51.2475 ± 1.2602 Hz
Gly51N–Val23CG2
39.4059 ± 1.3724 Hz
ζ NC
t mix [s]
0.0
0.1
0.2
0.3
0.4
0.5
0.000
0.005
0.010
0.015

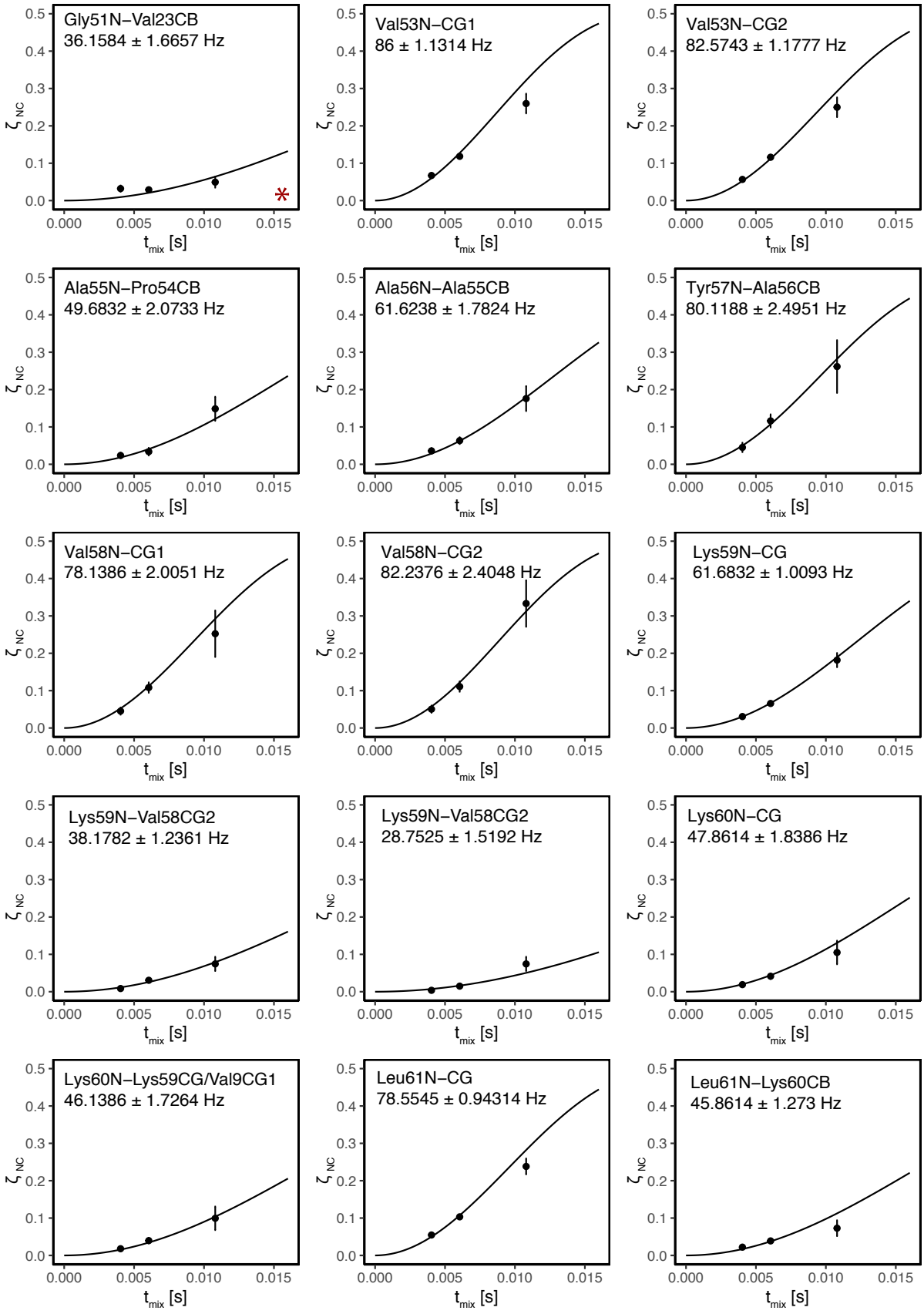
Gly51N–Val23CB
36.1584 ± 1.6657 Hz
Val53N–CG1
86 ± 1.1314 Hz
Val53N–CG2
82.5743 ± 1.1777 Hz
Ala55N–Pro54CB
49.6832 ± 2.0733 Hz
Ala56N–Ala55CB
61.6238 ± 1.7824 Hz
Tyr57N–Ala56CB
80.1188 ± 2.4951 Hz
Val58N–CG1
78.1386 ± 2.0051 Hz
Val58N–CG2
82.2376 ± 2.4048 Hz
Lys59N–CG
61.6832 ± 1.0093 Hz
Lys59N–Val58CG2
38.1782 ± 1.2361 Hz
Lys59N–Val58CG2
28.7525 ± 1.5192 Hz
Lys60N–CG
47.8614 ± 1.8386 Hz
Lys60N–Lys59CG/Val9CG1
46.1386 ± 1.7264 Hz
Leu61N–CG
78.5545 ± 0.94314 Hz
Leu61N–Lys60CB
45.8614 ± 1.273 Hz
ζ NC
t mix [s]
0.0
0.1
0.2
0.3
0.4
0.5
0.000
0.005
0.010
0.015

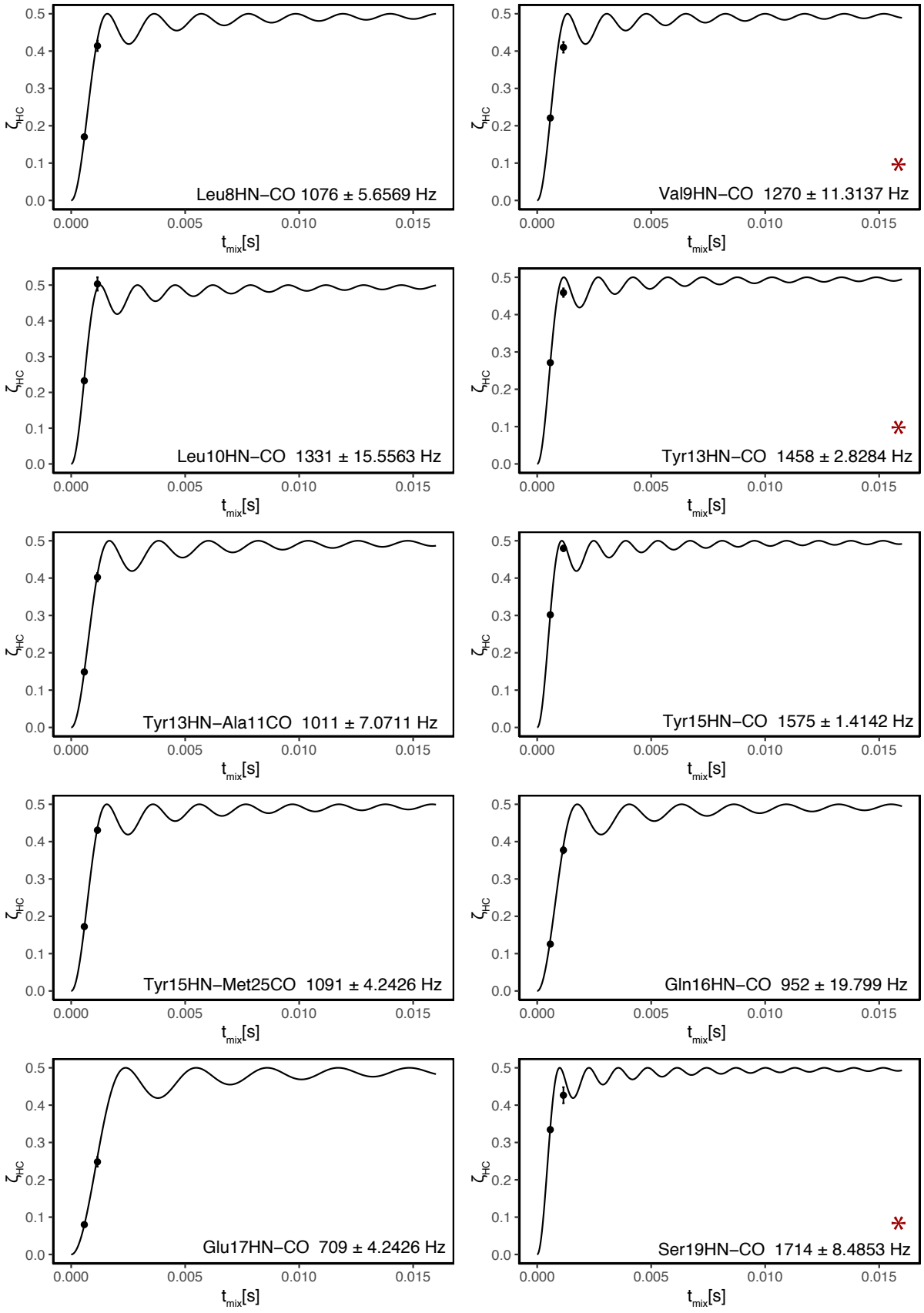
Leu8HN–CO 1076 ± 5.6569 Hz
Val9HN–CO 1270 ± 11.3137 Hz
Leu10HN–CO 1331 ± 15.5563 Hz
Tyr13HN–CO 1458 ± 2.8284 Hz
Tyr13HN–Ala11CO 1011 ± 7.0711 Hz
Tyr15HN–CO 1575 ± 1.4142 Hz
Tyr15HN–Met25CO 1091 ± 4.2426 Hz
Gln16HN–CO 952 ± 19.799 Hz
Glu17HN–CO 709 ± 4.2426 Hz
Ser19HN–CO 1714 ± 8.4853 Hz
ζHC
tmix[s]
0.0
0.1
0.2
0.3
0.4
0.5
0.000
0.005
0.010
0.015

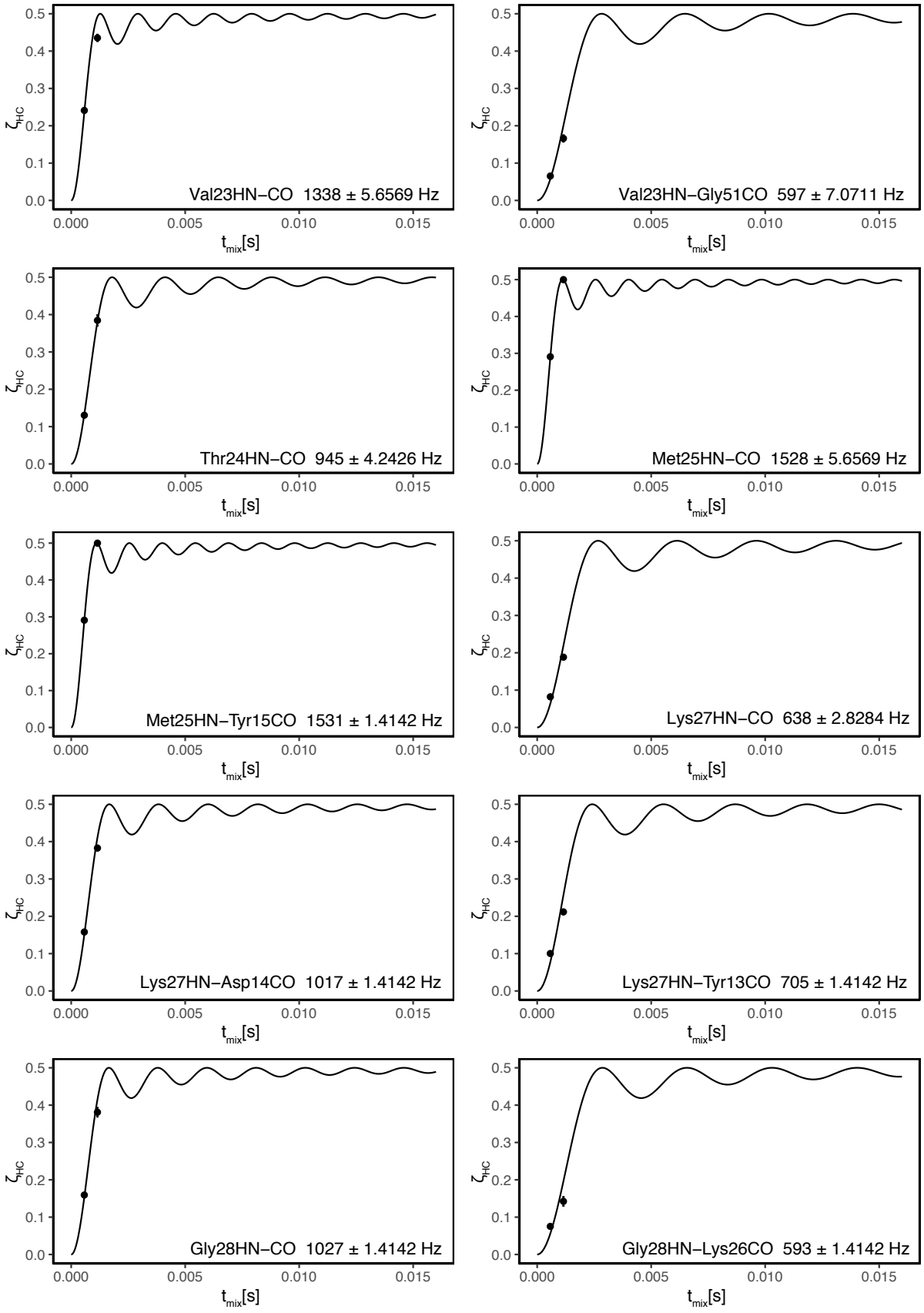
Val23HN–CO 1338 ± 5.6569 Hz
Val23HN–Gly51CO 597 ± 7.0711 Hz
Thr24HN–CO 945 ± 4.2426 Hz
Met25HN–CO 1528 ± 5.6569 Hz
Met25HN–Tyr15CO 1531 ± 1.4142 Hz
Lys27HN–CO 638 ± 2.8284 Hz
Lys27HN–Asp14CO 1017 ± 1.4142 Hz
Lys27HN–Tyr13CO 705 ± 1.4142 Hz
Gly28HN–CO 1027 ± 1.4142 Hz
Gly28HN–Lys26CO 593 ± 1.4142 Hz
ζ_{HC}
t_{mix}[s]
0.0
0.1
0.2
0.3
0.4
0.5
0.000
0.005
0.010
0.015

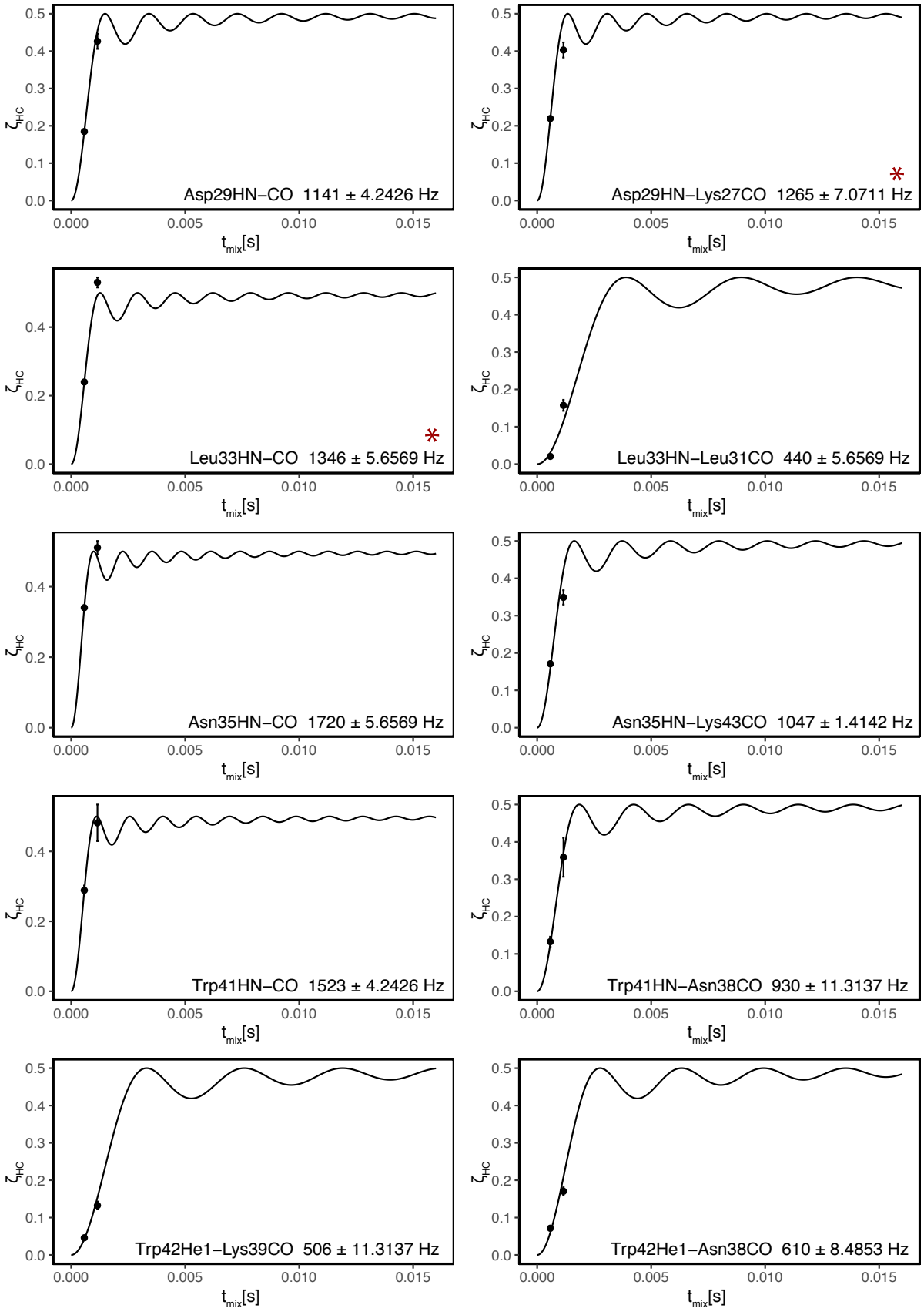
Asp29HN–CO 1141 ± 4.2426 Hz
Asp29HN–Lys27CO 1265 ± 7.0711 Hz *
Leu33HN–CO 1346 ± 5.6569 Hz *
Leu33HN–Leu31CO 440 ± 5.6569 Hz
Asn35HN–CO 1720 ± 5.6569 Hz
Asn35HN–Lys43CO 1047 ± 1.4142 Hz
Trp41HN–CO 1523 ± 4.2426 Hz
Trp41HN–Asn38CO 930 ± 11.3137 Hz
Trp42He1–Lys39CO 506 ± 11.3137 Hz
Trp42He1–Asn38CO 610 ± 8.4853 Hz
ζHC
tmix[s]
0.0
0.1
0.2
0.3
0.4
0.5
0.000
0.005
0.010
0.015

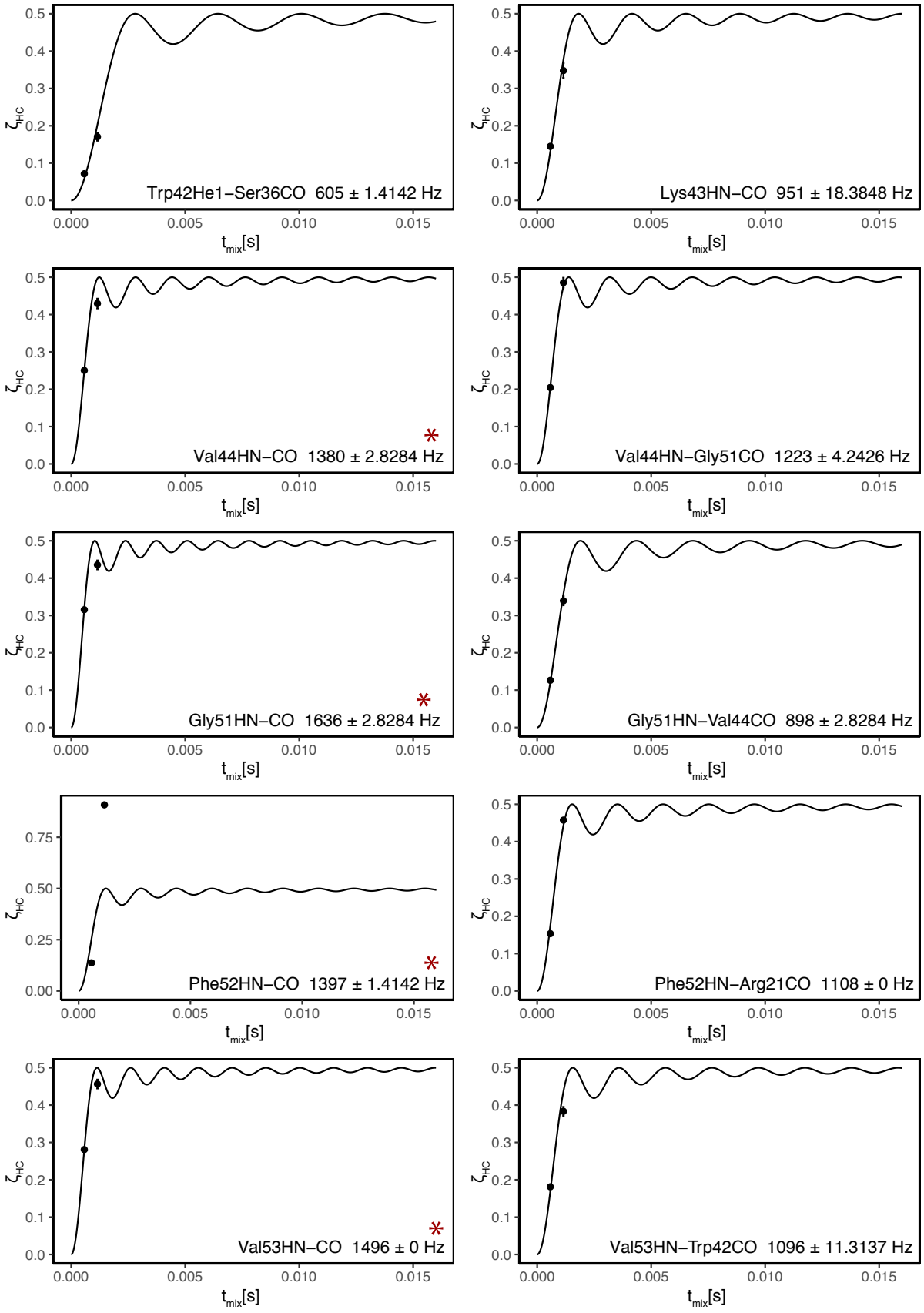
Trp42He1−Ser36CO 605 ± 1.4142 Hz
Lys43HN−CO 951 ± 18.3848 Hz
Val44HN−CO 1380 ± 2.8284 Hz
Val44HN−Gly51CO 1223 ± 4.2426 Hz
Gly51HN−CO 1636 ± 2.8284 Hz
Gly51HN−Val44CO 898 ± 2.8284 Hz
Phe52HN−CO 1397 ± 1.4142 Hz
Phe52HN−Arg21CO 1108 ± 0 Hz
Val53HN−CO 1496 ± 0 Hz
Val53HN−Trp42CO 1096 ± 11.3137 Hz
ζHC
tmix[s]

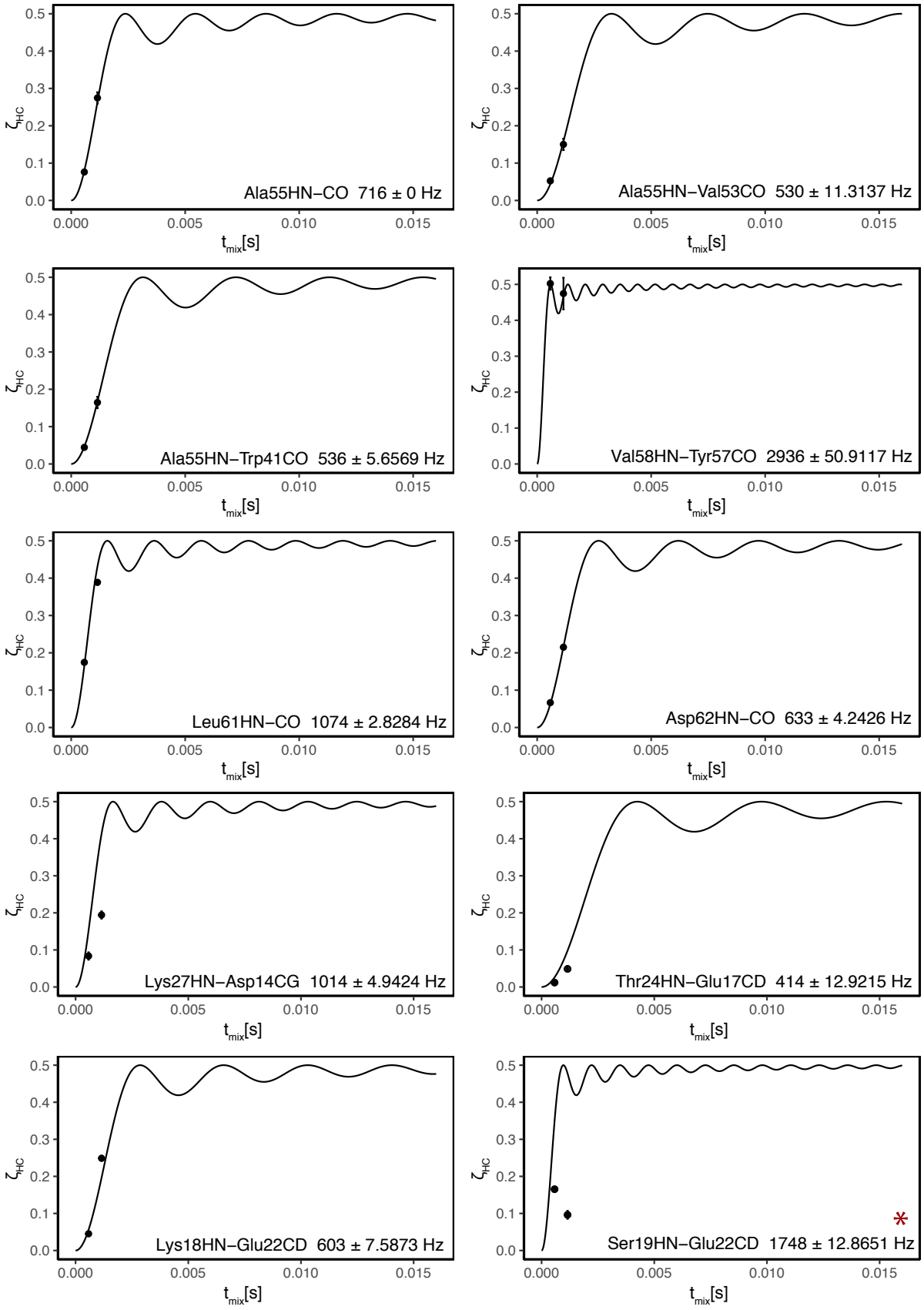
Ala55HN−CO 716 ± 0 Hz
Ala55HN−Val53CO 530 ± 11.3137 Hz
Ala55HN−Trp41CO 536 ± 5.6569 Hz
Val58HN−Tyr57CO 2936 ± 50.9117 Hz
Leu61HN−CO 1074 ± 2.8284 Hz
Asp62HN−CO 633 ± 4.2426 Hz
Lys27HN−Asp14CG 1014 ± 4.9424 Hz
Thr24HN−Glu17CD 414 ± 12.9215 Hz
Lys18HN−Glu22CD 603 ± 7.5873 Hz
Ser19HN−Glu22CD 1748 ± 12.8651 Hz
*
ζHC
tmix[s]
0.0
0.1
0.2
0.3
0.4
0.5
0.000
0.005
0.010
0.015

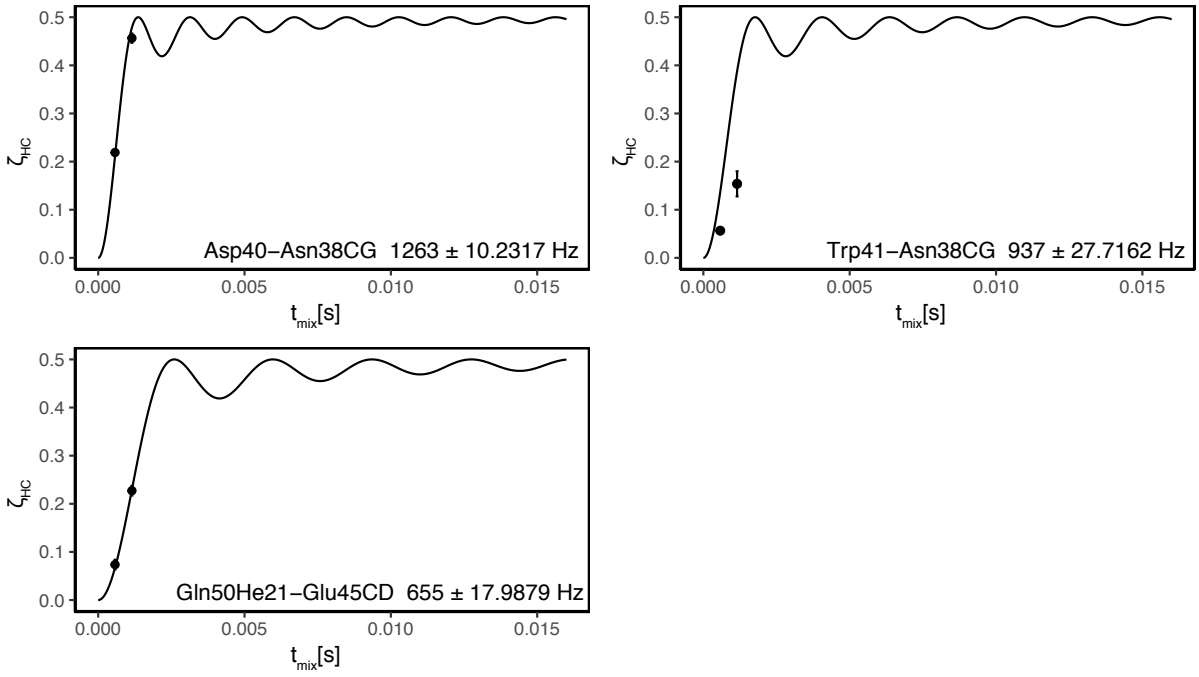

* indicates potentially compromised fit quality due to spectral overlap

Table E.1: Relaxation rate Nitrogen T2 from (H)NH vs. TREDOR relaxation rate

Residue	hNH t2 [ms]	TREDOR T2[ms]	Residue	hNH t2[ms]	TREDOR T2 [ms]
7GluN	19.55	3.87	34LeuN	64.94	4.34
8LeuN	68.45	4.51	35AsnN	56.15	4.02
9ValN	67.61	3.52	37ThrN	70.08	5.82
10LeuN	64.02	4.68	38AsnN	69.74	4.46
11AlaN	103.95	0.91	39LysN	92.85	4.16
12LeuN	78.37	3.98	40AspN	49.85	5.12
13TyrN	84.67	4.93	41TrpN	64.31	3.27
14AspN	109.89	4.79	41TrpNe1	53.30	4.73
15TyrN	74.18	5.17	42TrpN	72.10	9.68
16GlnN	136.61	5.30	42TrpNe1	162.07	5.81
17GluN	88.34	5.72	43LysN	86.43	4.08
18LysN	83.61	4.42	44ValN	76.05	3.05
19SerN	65.40	5.72	45GluN	79.11	5.30
22GluN	74.35	3.57	49ArgN	52.88	6.50
23ValN	101.01	4.03	50GlnN	75.24	5.29
24ThrN	118.62	4.86	51GlyN	69.54	9.48
25MetN	79.74	3.90	52PheN	104.60	4.98
26LysN	108.70	4.21	53ValN	77.04	3.50
27LysN	106.27	3.73	55AlaN	93.37	4.64
28GlyN	70.32	6.40	56AlaN	73.42	4.73
29AspN	75.13	5.23	57TyrN	85.84	3.94
30IleN	91.49	3.59	58ValN	86.13	3.35
31LeuN	70.18	3.87	59LysN	60.28	3.14
32ThrN	90.33	4.92	60LysN	119.19	3.64
33LeuN	98.91	4.46	61LeuN	85.76	3.88

Table E.2: Upper and lower distance restraints used in the SH3 structure calculation. Ambiguous restraints are given in the CYANA format as putting them with 0 Å

Contact		Upper limit [Å]	Lower limit [Å]
8 LEU N	8 LEU CG	3.44	2.82
8 LEU N	8 LEU CD1	3.91	3.2
8 LEU N	8 LEU CD2	0	0
8 LEU N	7 GLU CB	3.78	3.09
9 VAL N	9 VAL CG1	3.44	2.81
9 VAL N	9 VAL CG2	3.31	2.71
10 LEU N	10 LEU CG	3.92	3.21
10 LEU N	10 LEU CD1	0	0
10 LEU N	10 LEU CD2	0	0
10 LEU N	9 VAL CB	3.77	3.09
10 LEU N	9 VAL CG2	4.3	3.52
10 LEU N	61 LEU CD1	4.73	3.87
10 LEU N	61 LEU CD2	0	0
11 ALA N	10 LEU CD1	3.51	2.87
11 ALA N	10 LEU CD2	0	0
12 LEU N	12 LEU CG	3.6	2.94
12 LEU N	12 LEU CD1	0	0
12 LEU N	12 LEU CD2	0	0
12 LEU N	58 VAL CG1	4.28	3.51
13 TYR N	11 ALA CB	4.54	3.71
13 TYR N	27 LYS CB	4.77	3.9
14 ASP N	27 LYS CB	4.53	3.7
15 TYR N	14 ASP CB	4.77	3.24
15 TYR N	25 MET CG	4.45	3.64
15 TYR N	25 MET CE	5.05	4.01
16 GLN N	16 GLN CG	4.33	3.54
17 GLU N	17 GLU CG	3.76	3.08
17 GLU N	16 GLN CB	3.6	2.94
18 LYS N	18 LYS CG	3.3	2.7
18 LYS N	17 GLU CB	3.62	2.96
19 SER N	18 LYS CB	3.82	3.12
19 SER N	17 GLU CB	4.93	4.03
19 SER N	22 GLU CG	4.78	3.91
19 SER N	18 LYS CG	4.97	4.07
22 GLU N	22 GLU CG	3.91	3.2
22 GLU N	21 ARG CG	4.39	3.59
23 VAL N	23 VAL CG1	3.79	3.1
23 VAL N	22 GLU CB	3.18	2.6
23 VAL N	17 GLU CB	4.03	3.29
23 VAL N	23 VAL CG2	3.6	2.94
24 THR N	24 THR CG2	4.03	3.29
24 THR N	23 VAL CB	3.49	2.86
24 THR N	23 VAL CG2	4.23	3.46

24 THR N	17 GLU CB	4.34	3.55
25 MET N	25 MET CG	3.44	2.82
25 MET N	24 THR CG2	4.34	3.55
26 LYS N	26 LYS CG	4.02	3.29
26 LYS N	26 LYS CD	4.7	3.85
26 LYS N	25 MET CB	4.4	3.6
26 LYS N	25 MET CG	4.09	3.35
27 LYS N	27 LYS CG	4.02	3.29
27 LYS N	26 LYS CB	3.79	3.1
27 LYS N	26 LYS CD	4.69	3.83
28 GLY N	27 LYS CB	3.79	3.1
28 GLY N	27 LYS CG	3.79	3.1
28 GLY N	11 ALA CB	4.59	3.75
29 ASP N	11 ALA CB	4.7	3.85
30 ILE N	30 ILE CG1	3.49	2.86
30 ILE N	30 ILE CD1	4.5	3.68
31 LEU N	30 ILE CG1	4.03	3.29
31 LEU N	30 ILE CB	4.32	3.58
32 THR N	32 THR CG2	3.98	3.26
33 LEU N	33 LEU CD1	3.73	3.05
33 LEU N	33 LEU CD2	0	0
33 LEU N	33 LEU CG	4.07	3.33
33 LEU N	44 VAL CG1	4.75	3.88
34 LEU N	34 LEU CD1	4.31	3.52
34 LEU N	34 LEU CD2	0	0
34 LEU N	34 LEU CD1	4.06	3.32
34 LEU N	34 LEU CD2	0	0
34 LEU N	34 LEU CG	3.44	2.82
35 ASN N	43 LYS CB	4.32	3.53
35 ASN N	34 LEU CG	4.35	3.56
35 ASN N	33 LEU CD1	4.33	3.54
37 THR N	37 THR CG2	3.2	2.62
40 ASP N	39 LYS CB	3.78	3.1
40 ASP N	39 LYS CG	4.05	3.31
43 LYS N	43 LYS CG	4.2	3.44
43 LYS N	42 TRP CB	3.96	3.24
44 VAL N	44 VAL CG2	3.31	2.71
44 VAL N	44 VAL CG1	3.31	2.71
44 VAL N	43 LYS CB	4.02	3.29
44 VAL N	43 LYS CG	4.03	3.3
45 GLU N	44 VAL CG2	4.38	3.59
45 GLU N	44 VAL CG1	4.8	3.93
46 VAL N	46 VAL CG1	4.07	3.33
46 VAL N	50 GLN CB	4.56	3.73
49 ARG N	49 ARG CG	3.64	2.98
50 GLN N	50 GLN CG	3.6	2.95
50 GLN N	49 ARG CG	4.77	3.91

51 GLY N	50 GLN CB	3.36	2.75
51 GLY N	43 LYS CG	4.28	3.51
51 GLY N	23 VAL CG1	4.03	3.29
51 GLY N	23 VAL CG2	4.34	3.55
51 GLY N	23 VAL CB	4.46	3.65
53 VAL N	53 VAL CG1	3.33	2.73
53 VAL N	53 VAL CG2	3.44	2.81
55 ALA N	54 PRO CB	4.03	3.3
56 ALA N	55 ALA CB	3.79	3.1
57 TYR N	56 ALA CB	3.44	2.81
58 VAL N	58 VAL CG1	3.45	2.83
58 VAL N	58 VAL CG2	3.44	2.81
59 LYS N	59 LYS CG	3.79	3.1
59 LYS N	58 VAL CG2	4.34	3.55
59 LYS N	58 VAL CG1	4.78	3.91
60 LYS N	60 LYS CG	4.07	3.33
60 LYS N	59 LYS CG	4.11	3.36
60 LYS N	9 VAL CG1	4.11	3.36
61 LEU N	61 LEU CG	3.44	2.82
61 LEU N	60 LYS CB	4.09	3.34
61 LEU N	61 LEU CD1	4.16	3.4
61 LEU N	61 LEU CD2	0	0
41 TRP NE1	41 TRP CB	3.98	3.26
42 TRP NE1	42 TRP CB	4.03	3.29
42 TRP NE1	55 ALA CB	4.29	3.51
31 LEU N	31 LEU CD2	3.44	2.82
31 LEU N	31 LEU CG	4	3.27
31 LEU N	31 LEU CD1	0	0
31 LEU N	31 LEU CD2	0	0
8 LEU H	8 LEU C	3.1	2.54
9 VAL H	9 VAL C	2.95	2.41
10 LEU H	10 LEU C	2.89	2.37
13 TYR H	13 TYR C	2.81	2.3
13 TYR H	11 ALA C	3.17	2.59
15 TYR H	15 TYR C	2.73	2.23
15 TYR H	25 MET C	3.09	2.53
16 GLN H	16 GLN C	2.65	2.17
17 GLU H	17 GLU C	3.56	2.92
19 SER H	19 SER C	2.66	2.18
23 VAL H	23 VAL C	2.88	2.36
23 VAL H	51 GLY C	3.8	3.11
24 THR H	24 THR C	3.25	2.66
25 MET H	25 MET C	2.76	2.26
25 MET H	15 TYR C	2.76	2.26
27 LYS H	27 LYS C	3.69	3.02
27 LYS H	14 ASP C	3.17	3.17
27 LYS H	13 TYR C	3.56	2.92

28 GLY H	28 GLY C	3.15	2.57
28 GLY H	26 LYS C	3.78	3.1
29 ASP H	29 ASP C	3.04	2.48
29 ASP H	27 LYS C	2.95	2.41
33 LEU H	33 LEU C	2.88	2.36
33 LEU H	31 LEU C	4.2	3.44
35 ASN H	35 ASN C	2.65	2.17
35 ASN H	43 LYS C	3.14	2.57
41 TRP H	41 TRP C	2.75	2.25
41 TRP H	38 ASN C	3.25	2.66
42 TRP H	53 VAL C	3.05	2.49
42 TRP HE1	39 LYS C	4	3.28
42 TRP HE1	38 ASN C	3.76	3.08
42 TRP HE1	36 SER C	3.76	3.08
43 LYS H	43 LYS C	3.22	2.64
44 VAL H	44 VAL C	2.86	2.34
44 VAL H	51 GLY C	2.98	2.44
51 GLY H	51 GLY C	2.7	2.21
51 GLY H	44 VAL C	3.3	2.7
52 PHE H	52 PHE C	2.84	2.32
52 PHE H	21 ARG C	3.07	2.51
53 VAL H	53 VAL C	2.78	2.28
53 VAL H	42 TRP C	3.08	2.52
55 ALA H	55 ALA C	3.54	2.9
55 ALA H	53 VAL C	3.89	3.19
55 ALA H	41 TRP C	3.93	3.21
58 VAL H	58 VAL C	2.89	2.37
61 LEU H	61 LEU C	3.1	2.54
62 ASP H	62 ASP C	3.7	3.02
27 LYS H	14 ASP CG	3.17	2.59
24 THR H	17 GLU CD	4.27	3.49
18 LYS H	22 GLU CD	3.77	3.08
19 SER H	22 GLU CD	2.64	2.16
40 ASP H	38 ASN CG	2.94	2.41
41 TRP H	38 ASN CG	3.25	2.66
50 GLN HE21	45 GLU CD	3.45	2.82

Table E.3: TALOS-N angle restrains

Residue		Angle	Angle margin	
8	LEU	PHI	-155.7	-108
8	LEU	PSI	135.2	175.2
9	VAL	PHI	-148.2	-108.2
9	VAL	PSI	131.4	171.4
10	LEU	PHI	-145.1	-105.1
10	LEU	PSI	116.5	156.5
11	ALA	PHI	-94.3	-52.8
11	ALA	PSI	106.7	146.7
12	LEU	PHI	-103.9	-63.1
12	LEU	PSI	-60.8	-19.7
13	TYR	PHI	-182.5	-131.4
13	TYR	PSI	138	178
16	GLN	PHI	-149.5	-86.9
16	GLN	PSI	109.4	169.9
23	VAL	PHI	-175.6	-72.5
23	VAL	PSI	129.5	177.3
24	THR	PHI	-132.1	-83.3
24	THR	PSI	111.5	151.5
25	MET	PHI	-151.5	-89.7
25	MET	PSI	113.5	171.6
26	LYS	PHI	-118	-56.7
26	LYS	PSI	130.5	170.5
27	LYS	PHI	-76.5	-36.5
27	LYS	PSI	113.2	153.2
29	ASP	PHI	-84.6	-44.6
29	ASP	PSI	126.3	166.3
30	ILE	PHI	-129.2	-89.2
30	ILE	PSI	104.5	144.5
31	LEU	PHI	-130	-89.1
31	LEU	PSI	103.8	158.4
32	THR	PHI	-97.3	-52.6
32	THR	PSI	107.9	147.9
33	LEU	PHI	-117.8	-50.3
33	LEU	PSI	88.7	168.2
34	LEU	PHI	-79.4	-39.4
34	LEU	PSI	-51.9	-11.9
36	SER	PHI	-88.8	-48.8
36	SER	PSI	-55.9	-15.9
37	THR	PHI	-85.9	-45.9
37	THR	PSI	-59.5	-19.5
38	ASN	PHI	-81.9	-41.9
39	LYS	PSI	-38.9	1.1
40	ASP	PHI	-105.7	-65.7
40	ASP	PSI	-29.6	10.4
41	TRP	PHI	-123.6	-67.1
41	TRP	PSI	112.2	159.1

42	TRP	PHI	-144.3	-104.3
42	TRP	PSI	114.3	175.6
43	LYS	PHI	-138.7	-62.6
43	LYS	PSI	103.5	151
44	VAL	PHI	-146.1	-94.4
44	VAL	PSI	112.9	178.5
50	GLN	PHI	-162.6	-88.7
50	GLN	PSI	132.5	172.5
51	GLY	PHI	153.3	193.3
51	GLY	PSI	-192.9	-152.9
52	PHE	PHI	-119.7	-67
52	PHE	PSI	116.3	163.4
53	VAL	PHI	-157.6	-104
53	VAL	PSI	124.7	175.2
54	PRO	PSI	108.5	148.5
55	ALA	PHI	-82.5	-42.5
55	ALA	PSI	-51.7	-11.7
56	ALA	PHI	-87.5	-47.5
56	ALA	PSI	-39.1	3.8
59	LYS	PHI	-149.6	-94.6
59	LYS	PSI	107.6	172.9
60	LYS	PHI	-99.5	-50.9
60	LYS	PSI	108.3	148.3
61	LEU	PHI	-104	-50.2
61	LEU	PSI	115.2	155.2

E.2 Simultaneous multi-curve TREDOR fitting

starting with Equation E.1. This result can be extended [101] to a set of n_i equations, which is used to simultaneously fit the buildup curves of the individual carbon spins coupled to N_1.

$$n_i \begin{cases} V_{11}(t_m ix) = \Lambda_1(1 - [J_0(\sqrt{2}D_{11}t_{mix})]^2) \prod_{k=2}^{n_i}(1 + [J_0\sqrt{2}D_{1k}t_{mix}]^2) \\ V_{12}(t_m ix) = \Lambda_1(1 - [J_0(\sqrt{2}D_{12}t_{mix})]^2) \prod_{k=1\neq 2}^{n_i}(1 + [J_0\sqrt{2}D_{1k}t_{mix}]^2) \\ ... \\ V_{1i}(t_m ix) = \Lambda_1(1 - [J_0(\sqrt{2}D_{1i}t_{mix})]^2) \prod_{k=1\neq i}^{n_i}(1 + [J_0\sqrt{2}D_{1k}t_{mix}]^2) \end{cases} \tag{E.1}$$

Where Λ_1 is given as:

$$\Lambda_1 = \frac{1}{2^{n_i}} V_1(0)\lambda_1 exp(-\Gamma_1 t_{mix}) \tag{E.2}$$

The Γ_1 gives the coherence decay rate of spin coherence, which can be modeled as a single exponential. λ_1 is an amplitude scaling factor, which is typically fit freely since the starting signal is not recorded in a TEDOR measurement. So in a standard TEDOR fitting, to extract the dipolar couplings, one needs to fit the overall decay rate and an arbitrary scaling factor which are irrelevant to the parameter of concern. This consequently puts more demand on the data density, something that might be unachievable especially for samples with low sensitivity or short coherence times. In the pseudo-4D TREDOR experiment, we address this problem by recording the intensity of the untransferred part of the magnetization, so that the ratio $\zeta_{1i}(t_{mix})$ can be formed between transferred and total magnetization

$$\zeta_{1i}(t_{mix}) = \frac{V_{1i}(t_{mix})}{V_1(t_{mix}) + \sum_{k=1}^{n_i} V_{1k}(t_{mix})} \tag{E.3}$$

$$= \frac{V_{1i}(t_{mix})}{V_{total}(t_{mix})} \tag{E.4}$$

Where $V_1(t_{mix})$ is the intensity of the untransferred nitrogen signal, and the $V_{total}(t_{mix})$ is the total signal at a certain mixing time. The untransferred signal $V_1(t_{mix})$ appears with the same scaling and typically also the same decay parameter, and hence the total signal also follows a

single exponential decay of the original signal intensity.

$$V_{total}(t_{mix}) = V_1(0)exp(-\Gamma_1 t_{mix}) \tag{E.5}$$

Normalization by the total signal results in a coherence decay-free TEDOR curve, for which the parameters λ_1 and $V_1(0)$ no longer appear. Combining Equation E.1 and Equation E.3, it is straightforward to show that we can fit the simultaneous buildup curve of several ^{13}C spins coupled to the same N_1 as the following set of equations:

$$n_i \begin{cases} \zeta_{11}(t_{mix}) = \frac{1}{2^{n_i}}(1 - [J_0(\sqrt{2}D_{11}t_{mix})]^2) \prod_{k=2}^{n_i}(1 + [J_0\sqrt{2}D_{1k}t_{mix}]^2) \\ \zeta_{12}(t_{mix}) = \frac{1}{2^{n_i}}(1 - [J_0(\sqrt{2}D_{12}t_{mix})]^2) \prod_{k=1\neq 2}^{n_i}(1 + [J_0\sqrt{2}D_{1k}t_{mix}]^2) \\ ... \\ \zeta_{1i}(t_{mix}) = \frac{1}{2^{n_i}}(1 - [J_0(\sqrt{2}D_{1i}t_{mix})]^2) \prod_{k=1\neq i}^{n_i}(1 + [J_0\sqrt{2}D_{1k}t_{mix}]^2) \end{cases} \tag{E.6}$$

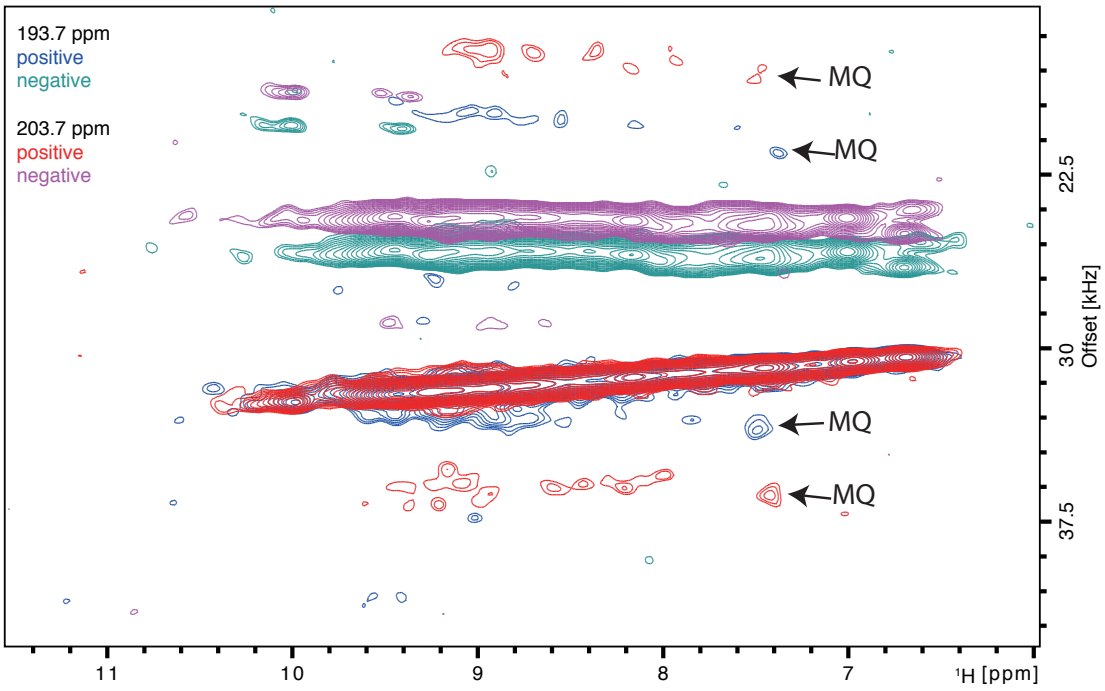

Figure E.1: Comparison of positions of multiple quantum artifacts in pseudo-3D H-CO TREDOR. With a shift of the offset from 193.7 ppm to 203.7 ppm, the artifacts changed chemical shifts on the H-CO dimension each by 20 ppm, confirming the major artifacts left are only the leftover double quantum terms but not zero quantum terms. When the offset is placed at 203.7 ppm, the artifacts are placed away from the signal of interest enough for quantitative analysis.

Table E.4: CO T2 rho in SH3 in ms with different hard pulse power in kHz and offsets in ppm

Power \ Offset	53 ppm	100 ppm
85 kHz	11.1 ms	64.7 ms
100 kHz	10.9 ms	60.4 ms

Table E.5: CA T2 rho in SH3 in ms with different hard pulse power in kHz and offsets in ppm

Power \ Offset	53 ppm	100 ppm
85 kHz	41.0 ms	41.1 ms
100 kHz	47.5 ms	48.5 ms

E.3 TREDOR pulse programs

E.3.1 hnCxNH TREDOR pulse program

```
;set F1 sweep width to 240 ppm and 13C offset to 60 ppm to place
;15N at correct freq.
; hnCANHtedor.mpibpc
;copy from 3D (H)CANH developed at CRMN in the group of G. Pintacuda

; Recent notes:
; this version does not require 13C axis inversion
; set inversion pulse bandwidth to 48 ppm

;Avance III version
;parameters:
;p1 : 1H 90 pulse duration
;p3 : 13C 90 pulse duration
;p7 : 15N 90 pulse duration
;p30 : water suppression time (30-200 ms)
;cnst21 : CO offset in Hz
;cnst22 : 60 ppm Carbon offset in Hz
;cnst23 : CA/CO offset in Hz
;d1 : recycle delay
;d5     : NOE mixing time
;d0     : 15N initial evolution time
;d10    : 1/2 of 13CO initial evolution time
;in0    : increment for 15N evolution
;in10   : 1/2 increment for 13CA evolution
;cpdprg1 : tppm (at pl13) or waltz (at pl13)
;cpdprg4 : cwY (at pl12)
;cpdprg5 : cwX (at pl12)
```

```
;pcpd1   : pulse length in decoupling sequence
;(2xtau_r for tppm, 25us for 10kHz waltz)
;pl1    : power level of 1H hard pulse
;pl12   : power level of decoupling (10-15 kHz)
;pl13   : power level for water suppression
;spnam1  : 1H shape for 1H->13CA CP (ramp 10-20%)
;spoal1  : N/A
;spoff1 : [ON/RES]
;sp1    : 1H power level during 1H->13CA CP
;spnam10 : 1H shape for 15N->1H(N) CP (ramp 10-20%)
;spoal10  : N/A
;spoff10 : [ON/RES]
;sp10    : 1H power level during 15N->1H CP
;cpdprg2 : 15N decoupling pattern during acq (waltz-16)
;p17     : contact time 15N->1H(N) CP (300-700 us)
;pcpd2   : pulse length in 15N decoupling sequence (25 us)
;pl7    : power level for 15N hard pulse
;pl16   : power level for 15N decoupling (corr. to 10 kHz)
;pl2    : power level for 15N hard pulse
;pl20   : 15N power level for 15N->1H CP
;spnam2  : 15N shape for 13CA->15N CP (tan-c100-w10pct)
;sp2    : 15N power level for 13CA->15N CP
;spoal2  : N/A
;spoff2 : [ON/RES]
;p15     : contact time 1H->15N CP (short, 300 - 700us)
;p14     : contact time for 15N->13CA CP (10ms)
;p16     : contact time 13CA->15N CP (10 ms)
;p18     : Reburp Cx pulse duration
;pcpd3   : pulse length in 13C decoupling sequence (25 us)
;cpdprg3 : 13CO/CA decoupling pattern during 15N evol (waltz-16)
```

```
;pl3    : power level of 13C hard pulse [REFERENCE]
;pl17   : power level for 13CO/CA decoupling (10 kHz)
;spnam9  : 13C shape for 13CA->15N CP (rectangle)
;sp9     : 13C power for 13CA->15N CP
;spoal9  : N/A
;spoff9 : [ON/RES CO]
;spnam18 : Reburp
;spoff18 : [ON/RES CO]
;spnam19 : 13CA selective pulse shape (Q3)
;spoal19  : N/A
;spoff19 : [ON/RES CA]
;spnam29 : 13C shape for 1H->13CO CP (rectangle)
;sp29   : 13C power level for 1H->13CO CP
;spoal29  : N/A
;spoff29 : [ON/RES CO]
;zgoptns : -Dfslg, -Dlacq, or blank

;l1 : to set mixing time
;l8 : z-filter time (number or rotor periods
;l9 : fraction of rotation rate for t1 increment, about 20 for 55 kHz
;d23 : indirect dim incrementation

;$COMMENT=Inverse Cp with INEPT CBCA mixing
;$CLASS=Solids
;$DIM=3D
;$TYPE=H detect
;$SUBTYPE=Heteronuclear
;$OWNER=CRMN

#include <Avancesolids.incl>
```

```
; Start evolutions from exactly 0
"d0=0.0"
"d10=0.0"
"d20=0.0"
;"tautotal=5.96*d10"

; 1H settings
"spoal1=0.5"   ; default value (irrelevant)
"spoff1=0.0"    ; on-resonance
"spoal10=0.5"  ; default value (irrelevant)
"spoff10=0.0"   ; on-resonance

; 15N settings
"pcpd2=25"                          ;does not work!
"plw2=plw7"
"plw16=plw2*(pow(p7/25,2))"     ; 15N waltz 10kHz decoupling power level
"spoal2=0.5"   ; default value (irrelevant)
"spoff2=0.0"     ; on-resonance

; 13C settings
"plw17=plw3*(pow(p3/25,2))"     ; 13C waltz 10kHz decoupling power level

"cnst20 = (sfo3-bf3)*1000000/bf3"  ; 40 ppm C frequency offset (ppm)

"cnst22 = cnst20-12"     ; 28 ppm, CB frequency offset (ppm)
"cnst23 = cnst20+(113.7-40)"    ; the offset half-way CO and CA (ppm)
"cnst21 = cnst20+(113.7)"     ; CO frequency offset (ppm)
```

```
"p18=5.81/(48.0*bf3/1000000)"    ; 5 to 53 ppm bandwidth (safe)
;"spw18=plw3*pow((0.5/(p18*0.1515))/(0.25/p3),2)" ;  Q3 power level
"spw18=plw3*pow((0.5/(p18*0.07981))/(0.25/p3),2)" ;  Reburp power level
"spoal18=0.5"                       ; default value (irrelevant)
"spoff18=bf3*((-12)/1000000)" ;on res with
CB, CG, etc

"p19=3.412/(105.0*bf3/1000000)"      ; 95 ppm bandwidth (safe)
"spw19=plw3*pow((0.5/(p19*0.1515))/(0.25/p3),2)" ;  Q3 power level
"spoal19=0.5"                           ; default value (irrelevant)
"spoff19=0.0"                       ; CA frequency

"spoal9=0.5"                        ; default value (irrelevant)
"spoff9=0.0"                        ; on-resonance

"spoal29=0.5"                       ; default value (irrelevant)
"spoff29=0.0"                       ; on-resonance CA

;"acqt0=1u*cnst11" ??

;"in0=inf1"
;"in10=inf2/2"



"d25=0.25s/cnst31-1u"
"d26=0.25s/cnst31-(p3)" ; one-quarter rotor cycle ...
"d27=0.25s/cnst31-larger((p7),(p3))"
;the 0.5u compensates for if statement in
```

```
;indirect acq. dim.
"d28=0.25s/cnst31-p7"
;"d29=0.25s/cnst31-p7"
"d23=1s*l9/cnst31"

"l21=p18/(2*(1s/cnst31))+0.25s/cnst31+1"
"d29=(l21+20)*1.0s/cnst31-p18/2-0.25/cnst31"
"d30=d29-p3*2"
;d29=0.75s/cnst31-(p3/2)" =p18/2+0.25rotor
;rounded up to even rotor period  -p18/2 -0.25rotor
"d31=1s/cnst31"
;define pulse tauz
;"tauz=l8*1s/cnst31-p3"

;"l10=1"
;"l11=l10 %l9"
define delay t1incr
"l22=((p18+p19+p18)/(1.0s/cnst31)+1)/2"
"d24=l22*2*1.0s/cnst31-p18-p19-p18"
;"d2=(l8+1)*1s/cnst31-p3-p7-d
"d2=1s/cnst31-p3-p7" ;d2
;if not using selective pulses for J dec in 13C evolution

"t1incr=(1s*l9)/(cnst31)"
"in0=t1incr"
"in10=(in0/2.48152)/2"

"inf1=in10*2"
"in20=inf2"
```

```
define delay mix
"mix=4*2*l1/cnst31"
  t1incr
  d23
  mix
1 ze

2 d1 do:f2
#include <p15_prot.incl>
#include <aq_prot.incl>

  1u fq= cnst22(bf ppm):f3

  (p1 pl1 ph4):f1

;  1u cpds2:f2 cpds3:f3
;  d20
;  (p1  pl1 ph0):f1 (1u do):f2  (1u do):f3

;3  d5
;   1u fq=cnst22(bf ppm):f3


;  (p1  pl1 ph4):f1  ;check phase

;HN cp
  (p15:sp0 ph17):f1 (p15 pl20 ph14):f2

;NCa
   1u cpds1:f1
```

```
   d25  pl7:f2 pl3:f3  ; tppm decoupling at pl12 if synchronized
   ;with TPPM use special decoupling sequence
5  d26  ; several F3 pulses ...
  (p3*2 ph8^):f3          ; ... at intervals of ...
   d26    ; ... one-half rotor cycle
   d26
  (p3*2 ph8^):f3         ; ... at intervals of ...
   d26                  ; F1 pulse
   d26  ; several F3 pulses ...
  (p3*2 ph8^):f3         ; ... at intervals of ...
   d26             ; ... at intervals of ...
   d26 ; ... one-half rotor cycle
  (p3*2 ph8^):f3         ; ... at intervals of ...
   d26              ; F1 pulse
lo to 5 times l1

  d29
  (center (p7*2 ph15):f2 (p18:sp18 ph15):f3)
  ;CO selective Pi to NOT REDOR
  (p3*2 pl3 ph18):f3
  d30          ; Hahn echo refocussing pulse on F1
6 d26  pl3:f3 ; several F3 pulses ...
  (p3*2 ph9^):f3         ; ... at intervals of ...
   d26               ; ... at intervals of ...
   d26 ; ... one-half rotor cycle
  (p3*2 ph9^):f3         ; ... at intervals of ...
   d26                 ;
   d26  ; several F3 pulses ...
  (p3*2 ph9^):f3         ; ... at intervals of ...
   d26              ; ... at intervals of ...
```

```
   d26 ; ... one-half rotor cycle
  (p3*2 ph9^):f3         ; ... at intervals of ...
   d26                 ; F1 pulse
lo to 6 times l1
   d27 fq= cnst20(bf ppm):f3
   (ralign (p7 ph12):f2   (p3 pl3 ph3):f3)  ; end of integer rotor period
   ;(tauz pl14 ph0):f1   ;Z-filter integer rotor period
   ; (p3 pl3 ph0):f3        ; begin rotor period at beginning of pulse

;;;;;; d0 cpds3:f2


; (rotor pi rotor d0):f2 (rotor pi rotor d10 d10 p3 pl3 ph0):f3

  ;if "d0==0" goto 7
;  0.5u
  ;(d0) (d10 d10 p3 pl3 ph0):f3
  ;(p7 pl7 ph0):f2
  ;if "d0>0" goto  8
;  INP,0.5u
   if  "d0 == 0"
   {
    (p7 pl7 ph20):f2 (p3 pl3 ph19):f3
   }
   if "d0 > 0"
   {
    (d0) (d10 d10 p3 pl3 ph19):f3
    (p7 pl7 ph20):f2
   }
```

```
;OLDDDDDDDDDDDDDDDDDDDDDDDDDDDDDDDDDDDDD
;  (d0) (d10 d10 p3 pl3 ph3):f3
;  (p7 pl7 ph0):f2  ; rotor period done at end of p1!
;OLDDDDDDDDDDDDDDDDDDDDDDDDDDDDDDDDDDDDD

; LAP, 0.5u
8 d28  pl7:f2  pl3:f3 ; tppm decoupling at pl12
9  d26 fq= cnst22(bf ppm):f3 ; several F3 pulses ...
  (p3*2 ph10^):f3        ; ... at intervals of ...
   d26            ; ... one-half rotor cycle
   d26
  (p3*2 ph10^):f3         ; ... at intervals of ...
   d26
   d26  ; several F3 pulses ...
  (p3*2 ph10^):f3         ; ... at intervals of ...
   d26             ; ... one-half rotor cycle
   d26
  (p3*2 ph10^):f3         ; ... at intervals of ...
   d26
lo to 9 times l1

  d29
  (center (p7*2 ph0):f2 (p18:sp18 ph0):f3)
  ; Hahn echo refocussing pulse
  (p3*2 pl3 ph18):f3
  d30
10 d26  pl3:f3 ; several F3 pulses ...
  (p3*2 ph11^):f3         ; ... at intervals of ...
   d26               ; ... one-half rotor cycle
   d26
```

```
  (p3*2 ph11^):f3         ; ... at intervals of ...
   d26
   d26  ; several F3 pulses ...
  (p3*2 ph11^):f3         ; ... at intervals of ...
   d26            ; ... one-half rotor cycle
   d26
  (p3*2 ph11^):f3         ; ... at intervals of ...
   d26
lo to 10 times l1
  d28   fq = cnst23(bf ppm):f3 ; Hahn echo occurs about now
  (p7 ph16):f2 (1u do):f1
 ; (tauz pl14 ph0):f1
  (p30*0.125 pl13 ph0):f1
  (p30*0.125 pl13 ph1):f1
  (p30*0.125 pl13 ph0):f1
  (p30*0.125 pl13 ph1):f1
  (p7 ph2):f2 (1u cpds1):f1 (1u cpds3):f3
 ; (p16:sp9 ph10):f3 (p16:sp2 ph2):f2

  d20 ;fq= 0 (bf ppm):f2
  ;0.5u fq= 75 (bf ppm):f2
;  1u do:f1 do:f3
  (p7 pl7 ph5):f2 (1u do):f1 (1u do):f3
 ;water suppression
  (p30*0.125 pl13 ph0):f1
  (p30*0.125 pl13 ph1):f1
  (p30*0.125 pl13 ph0):f1
  (p30*0.125 pl13 ph1):f1

;end water suppression
```

```
  (p7 pl7 ph6):f2
  (p17 pl20 ph7):f2 (p17:sp10 ph13):f1

  1u cpds2:f2
  go=2 ph31
  1m do:f2

  10m mc #0 to 2
  F1PH(calph(ph3, -90) & calph(ph12, -90) & calph(ph14, -90),
  caldel(d0, +in0) &caldel(d10, +in10))
  ;F1PH(calph(ph14, -90) & calph(ph12, -90), caldel(d0, +in0))
  F2PH(calph(ph2, +90), caldel(d20, +in20)) ;15N
  ;F3PH(calph(ph4, +90), caldel(d20, +in20)) ;1H


HaltAcqu, 1m   ;jump address for protection files
exit ;quit

ph0  = 0
ph1  = 1
ph3  = 2 2 0 0 ;was0   ;up after 13C evolution
ph4 = 2    ; proton flip down (FIRST PULSE)
; edge artifacts in 1H dimension without this phase cycle
ph2 =  0 0 2 2      ; down before 15N evolution
ph5 =  0
ph6 =  0 0 2 2
ph7  = 1
ph12 = 0 0 2 2;(float, 120.0) 0
ph14 = 0 0 2 2 ;(float, 120.0) 0
ph15 = 0 1
```

```
ph16 = 1 1 3 3
ph17 = 1 1 3 3 3 3 1 1

ph8= 0 1 0 1 1 0 1 0 2 3 2 3 3 2 3 2 ;xy16
ph9= 0 1 0 1 1 0 1 0 2 3 2 3 3 2 3 2
ph10= 0 1 0 1 1 0 1 0 2 3 2 3 3 2 3 2
ph11= 0 1 0 1 1 0 1 0 2 3 2 3 3 2 3 2

ph13 = 1
ph18 = 0 0 2 2 0 0 2 2
ph19 = 0 0 2 2 0 0 2 2  ; 13CA(all aliph) selective pulse
ph20 = 0 0 2 2
ph31 = 0 2 2 0 2 0 0 2  ; receiver phase for joint phase cycling
```

E.3.2 hNhCOH TREDOR pulse program

```
;reduced the extra time int he echo on 2020-12-4 land
;modification of hnCONHtedor_nozf.xifo.5 for H-C TREDOR
;TREDOR CO hNhCOHtredor.land
;alons lends version
;set F1 sweep width to 240 ppm and 13C offset to 60 ppm
;to place 15N at correct freq.
; hnCANHtedor.mpibpc
;copy from 3D (H)CANH developed at CRMN in the group of G. Pintacuda

; Recent notes:
; this version does not require 13C axis inversion
; set inversion pulse bandwidth to 48 ppm
```

```
;Avance III version
;parameters:
;p1 : 1H 90 pulse duration
;p3 : 13C 90 pulse duration
;p7 : 15N 90 pulse duration
;p30 : water suppression time (30-200 ms)
;cnst21 : CO offset in Hz
;cnst22 : 60 ppm Carbon offset in Hz
;cnst23 : CA/CO offset in Hz
;d1 : recycle delay
;d5     : NOE mixing time
;d0     : 15N initial evolution time
;d10    : 1/2 of 13CO initial evolution time
;in0    : increment for 15N evolution
;in10   : 1/2 increment for 13CA evolution
;cpdprg1 : tppm (at pl13) or waltz (at pl13)
;cpdprg4 : cwY (at pl12)
;cpdprg5 : cwX (at pl12)
;pcpd1   : pulse length in decoupling sequence
;(2xtau_r for tppm, 25us for 10kHz waltz)
;pl1    : power level of 1H hard pulse
;pl12   : power level of decoupling (10-15 kHz)
;pl13   : power level for water suppression
;spnam1  : 1H shape for 1H->13CA CP (ramp 10-20%)
;spoal1  : N/A
;spoff1 : [ON/RES]
;sp1    : 1H power level during 1H->13CA CP
;spnam10 : 1H shape for 15N->1H(N) CP (ramp 10-20%)
;spoal10  : N/A
;spoff10 : [ON/RES]
```

```
;sp10    : 1H power level during 15N->1H CP
;cpdprg2 : 15N decoupling pattern during acq (waltz-16)
;p17     : contact time 15N->1H(N) CP (300-700 us)
;pcpd2   : pulse length in 15N decoupling sequence (25 us)
;pl7    : power level for 15N hard pulse
;pl16   : power level for 15N decoupling (corr. to 10 kHz)
;pl2    : power level for 15N hard pulse
;pl20   : 15N power level for 15N->1H CP
;spnam2  : 15N shape for 13CA->15N CP (tan-c100-w10pct)
;sp2    : 15N power level for 13CA->15N CP
;spoal2  : N/A
;spoff2 : [ON/RES]
;p15     : contact time 1H->15N CP (short, 300 - 700us)
;p14     : contact time for 15N->13CA CP (10ms)
;p16     : contact time 13CA->15N CP (10 ms)
;p18     : Reburp Cx pulse duration
;pcpd3   : pulse length in 13C decoupling sequence (25 us)
;cpdprg3 : 13CO/CA decoupling pattern during 15N evol (waltz-16)
;pl3    : power level of 13C hard pulse [REFERENCE]
;pl17   : power level for 13CO/CA decoupling (10 kHz)
;spnam9  : 13C shape for 13CA->15N CP (rectangle)
;sp9     : 13C power for 13CA->15N CP
;spoal9  : N/A
;spoff9 : [ON/RES CO]
;spnam18 : Reburp
;spoff18 : [ON/RES CO]
;spnam19 : 13CA selective pulse shape (Q3)
;spoal19  : N/A
;spoff19 : [ON/RES CA]
;spnam29 : 13C shape for 1H->13CO CP (rectangle)
```

```
;sp29   : 13C power level for 1H->13CO CP
;spoal29  : N/A
;spoff29 : [ON/RES CO]
;zgoptns : -Dfslg, -Dlacq, or blank

;l1 : to set mixing time
;l8 : z-filter time (number or rotor periods
;l9 : fraction of rotation rate for t1 increment, about 4 for 55 kHz
;d23 : indirect dim incrementation

;$COMMENT=Inverse Cp with INEPT CBCA mixing
;$CLASS=Solids
;$DIM=3D
;$TYPE=H detect
;$SUBTYPE=Heteronuclear
;$OWNER=CRMN

#include <Avancesolids.incl>

; Start evolutions from exactly 0
"d0=0.0"
"d10=0.0"
"d20=0.0"
;"tautotal=5.96*d10"

; 1H settings
"spoal1=0.5"   ; default value (irrelevant)
"spoff1=0.0"    ; on-resonance
"spoal10=0.5"  ; default value (irrelevant)
"spoff10=0.0"   ; on-resonance
```

```
; 15N settings
"pcpd2=25"                          ;does not work!
"plw2=plw7"
"plw16=plw2*(pow(p7/25,2))"     ; 15N waltz 10kHz decoupling power level
"spoal2=0.5"   ; default value (irrelevant)
"spoff2=0.0"     ; on-resonance

; 13C settings
"plw17=plw3*(pow(p3/25,2))"     ; 13C waltz 10kHz decoupling power level

;"cnst20 = (sfo3-bf3)*1000000/bf3"  ; 40 ppm C frequency offset (ppm)
;"cnst22 = cnst20-12"     ; 28 ppm, CB frequency offset (ppm)
;"cnst23 = cnst20+(113.7-40)"    ; the offset half-way CO and CA (ppm)
;"cnst21 = cnst20+(113.7)"     ; CO frequency offset (ppm)

"cnst21 = (sfo3-bf3)*1000000/bf3-20"     ; CO frequency offset (ppm)
"cnst20 = (sfo3-bf3)*1000000/bf3"  ; 183.7 ppm C frequency offset (ppm)
"cnst23 = cnst20+(113.7-173.7)"    ; the offset half-way CO and CA (ppm)
"cnst22 = cnst20-12-133.7"     ; 28 ppm, CB frequency offset (ppm)

"p18=5.81/(100*bf3/1000000)"    ; 100 ppm bandwidth (safe)
;"spw18=plw3*pow((0.5/(p18*0.1515))/(0.25/p3),2)" ;  Q3 power level
"spw18=plw3*pow((0.5/(p18*0.07981))/(0.25/p3),2)" ;  Reburp power level
"spoal18=0.5"                       ; default value (irrelevant)
;"spoff18=bf3*((-30)/1000000)" ; on res bf3*((-10)/1000000)" ;on res with C
"spoff18=0.0"

;"p19=3.412/(105.0*bf3/1000000)"      ; 105 ppm bandwidth (safe)
;"spw19=plw3*pow((0.5/(p19*0.1515))/(0.25/p3),2)" ;  Q3 power level
```

```
;"spoal19=0.5"                          ; default value (irrelevant)
;"spoff19=0.0"                         ; CA frequency

"spoal9=0.5"                           ; default value (irrelevant)
"spoff9=0.0"                           ; on-resonance

"spoal29=0.5"                          ; default value (irrelevant)
"spoff29=0.0"                          ; on-resonance CA

;"acqt0=1u*cnst11" ??

;"in0=inf1"
;"in10=inf2/2"



"d25=0.25s/cnst31-1u"
"d26=0.25s/cnst31-(p3)" ; one-quarter rotor cycle ...
"d27=0.25s/cnst31-larger((p1),(p3))"  ;the 0.5u compensates for if statement
"d22=0.25s/cnst31-p1"
"d28=0.25s/cnst31-1u"
;"d29=0.25s/cnst31-p7"
"d23=1s*l9/cnst31"

"l21=p18/(2*(1s/cnst31))+0.25s/cnst31+1"
"d29=(l21+1)*1.0s/cnst31-p18/2-0.25/cnst31"
"d30=d29-p3*2"
;d29=0.75s/cnst31-(p3/2)" =p18/2+0.25rotor rounded up to even rotor period
"d31=1s/cnst31"
;define pulse tauz
```

```
;"tauz=l8*1s/cnst31-p3"

;"l10=1"
;"l11=l10 %l9"
define delay t1incr
"l22=((p18+p18)/(1.0s/cnst31)+1)/2"
"d24=l22*2*1.0s/cnst31-p18-p18"
;"d2=(l8+1)*1s/cnst31-p3-p7-d
"d2=1s/cnst31-p3-p7" ;d2 if not using selective pulses for J dec in 13C evo

"t1incr=(1s*l9)/(cnst31)"
"in0=t1incr"
;"in10=(in0/2.48152)/2"
;"in10=in0*3.976735/2"
"in10=in0/2"

"inf1=in10*2"
"in20=inf2"

define delay mix
"mix=4*2*l1/cnst31"
  t1incr
  d23
  mix
1 ze

2 d1 do:f2
#include <p15_prot.incl>
#include <aq_prot.incl>
```

```
  1u fq= cnst21(bf ppm):f3

  (p1 pl1 ph4):f1

;  1u cpds2:f2 cpds3:f3
;  d20
;  (p1  pl1 ph0):f1 (1u do):f2  (1u do):f3

;3  d5
;   1u fq=cnst22(bf ppm):f3


;  (p1  pl1 ph4):f1  ;check phase

;HN cp
  (p15:sp0 ph17):f1 (p15 pl20 ph14):f2

;NCa

;  (p7 ph16):f2 (1u do):f1
;  (p30*0.125 pl13 ph0):f1
;  (p30*0.125 pl13 ph1):f1
;  (p30*0.125 pl13 ph0):f1
;  (p30*0.125 pl13 ph1):f1
;  (p7 ph2):f2 (1u cpds1):f1 (1u cpds3):f3

  (0.5u cpds1):f1 (0.5u cpds3):f3
  d20
  ;fq= 0 (bf ppm):f2
  ;0.5u fq= 75 (bf ppm):f2
```

```
;  1u do:f1 do:f3
  (p7 pl7 ph5):f2 (1u do):f1 (1u do):f3
 ;water suppression
  (p30*0.25 pl13 ph0):f1
  (p30*0.25 pl13 ph1):f1
  (p30*0.25 pl13 ph0):f1
  (p30*0.25 pl13 ph1):f1

;end water suppression
  (p7 pl7 ph6):f2
  (p17 pl20 ph7):f2 (p17:sp10 ph13):f1

;past in, change channel for H-C TREDOR
   1u ;cpds1:f1
   d25  pl7:f2 pl3:f3
   ; tppm decoupling at pl12 if synchronized with TPPM use special
   ; decoupling sequence
5  d26  ; several F3 pulses ...
  (p3*2 ph8^):f3          ; ... at intervals of ...
   d26    ; ... one-half rotor cycle
   d26
  (p3*2 ph8^):f3         ; ... at intervals of ...
   d26                  ; F1 pulse
   d26  ; several F3 pulses ...
  (p3*2 ph8^):f3         ; ... at intervals of ...
   d26             ; ... at intervals of ...
   d26     ; ... one-half rotor cycle
  (p3*2 ph8^):f3         ; ... at intervals of ...
   d26              ; F1 pulse
lo to 5 times l1
```

```
  d29
  (center (p1*2 pl1 ph15):f1 (p18:sp18 ph15):f3)  ;; ... at intervals of ..
  (p3*2 pl3 ph18):f3
  d30          ; Hahn echo refocussing pulse on F1
6 d26  pl3:f3 ; several F3 pulses ...
  (p3*2 ph9^):f3         ; ... at intervals of ...
   d26                ; ... at intervals of ...
   d26 ; ... one-half rotor cycle
  (p3*2 ph9^):f3         ; ... at intervals of ...
   d26                  ;
   d26  ; several F3 pulses ...
  (p3*2 ph9^):f3         ; ... at intervals of ...
   d26               ; ... at intervals of ...
   d26 ; ... one-half rotor cycle
  (p3*2 ph9^):f3         ; ... at intervals of ...
   d26                 ; F1 pulse
lo to 6 times l1
   d27 fq= cnst20(bf ppm):f3
   (ralign (p1 ph12):f1   (p3 pl3 ph3):f3  (1u cpds2):f2)
   ; end of integer rotor period
   ;(tauz pl14 ph0):f1   ;(1u fq=cnst22(bf ppm)):f3
   ;Z-filter integer rotor period
   ; (p3 pl3 ph0):f3        ; begin rotor period at beginning of pulse



  d10 ;decouple CA?
  d10
  (p1 pl1 ph18):f1 (p3 pl3 ph19):f3 (1u do):f2
```

```
;   if  "d0 == 0"
;   {
;    (p1 pl1 ph18):f1 (p3 pl3 ph19):f3
;   }
;   if "d0 > 0"
;   {
;    (d0 p1 pl1 ph18):f1 (d10 d10)   ;switched which delay is shorter
;    (p3 pl3 ph19):f3
;   }

;OLDDDDDDDDDDDDDDDDDDDDDDDDDDDDDDDDDDDDD
;  (d0) (d10 d10 p3 pl3 ph3):f3
;  (p7 pl7 ph0):f2  ; rotor period done at end of p1!
;OLDDDDDDDDDDDDDDDDDDDDDDDDDDDDDDDDDDDDD

; LAP, 0.5u
8 d27  pl7:f2  pl3:f3 ; tppm decoupling at pl12
9  d26 fq= cnst21(bf ppm):f3 ; several F3 pulses ...
  (p3*2 ph10^):f3        ; ... at intervals of ...
   d26            ; ... one-half rotor cycle
   d26
  (p3*2 ph10^):f3         ; ... at intervals of ...
   d26
   d26  ; several F3 pulses ...
  (p3*2 ph10^):f3         ; ... at intervals of ...
   d26             ; ... one-half rotor cycle
   d26
  (p3*2 ph10^):f3         ; ... at intervals of ...
   d26
lo to 9 times l1
```

```
  d29
  (center (p1*2 pl1 ph0):f1 (p18:sp18 ph0):f3)
  ; Hahn echo refocussing pulse
  (p3*2 pl3 ph18):f3
  d30
10 d26  pl3:f3 ; several F3 pulses ...
  (p3*2 ph11^):f3         ; ... at intervals of ...
   d26                ; ... one-half rotor cycle
   d26
  (p3*2 ph11^):f3         ; ... at intervals of ...
   d26
   d26  ; several F3 pulses ...
  (p3*2 ph11^):f3         ; ... at intervals of ...
   d26            ; ... one-half rotor cycle
   d26
  (p3*2 ph11^):f3         ; ... at intervals of ...
   d26
lo to 10 times l1
  d28   fq = cnst21(bf ppm):f3 ; Hahn echo occurs about now
;  (p7 ph16):f2 (1u do):f1


  1u cpds2:f2
  go=2 ph31
  1m do:f2

  10m mc #0 to 2
  F1PH(calph(ph3, -90) & calph(ph12, -90) & calph(ph13, -90),
  caldel(d0, +in0) & caldel(d10, +in10))
```

```
  ;F1PH(calph(ph14, -90) & calph(ph12, -90), caldel(d0, +in0))
  F2PH(calph(ph14, +90), caldel(d20, +in20)) ;15N
  ;F3PH(calph(ph4, +90), caldel(d20, +in20)) ;1H


HaltAcqu, 1m   ;jump address for protection files
exit ;quit

ph0  = 0
ph1  = 1
ph3  = 2 2 0 0 ;was0   ;up after 13C evolution
ph4 = 2    ;edge artifacts in 1H dimension without this phase cycle
;ph2 =  0 0 2 2 ; down before 15N evolution
ph5 =  1
ph6 =  0 0 2 2    ;Remove this phase cycle?
ph7  = 1
ph12 = 0 0 2 2;(float, 120.0) 0
ph14 = 0 0 2 2 ;(float, 120.0) 0
ph15 = 0 1
;ph16 = 1 1 3 3
ph17 = 1 1 3 3 3 3 1 1   ;WHY THIS CYCLE? REMOVE?

ph8= 0 1 0 1 1 0 1 0 2 3 2 3 3 2 3 2 ;xy16
ph9= 0 1 0 1 1 0 1 0 2 3 2 3 3 2 3 2
ph10= 0 1 0 1 1 0 1 0 2 3 2 3 3 2 3 2
ph11= 0 1 0 1 1 0 1 0 2 3 2 3 3 2 3 2

ph13 = 2
ph18 = 0 0 2 2 0 0 2 2
ph19 = 0 0 2 2 0 0 2 2 ; 13CA(all aliph) selective pulse
```

```
ph31 = 0 2 2 0 2 0 0 2  ; receiver phase for joint phase cycling
```

E.4 TREDOR curve fitting script

```
    clear
res = 'leu12';
raw=readtable([res,'.txt']);
title = raw.Properties.VariableNames
timepts = raw{:,2}';
nitrogen = raw(:,3);
carbon1 = raw(:,4);
carbon2 = raw(:,5);
carbon3 = raw(:,7);
noise = raw{:,9}';
for i=1:height(nitrogen)
    V_total(i)=nitrogen{i,1}+carbon1{i,1};%+carbon2{i,1}+carbon3{i,1};
    curve1(i) = carbon1{i,1}/V_total(i);
    %curve2(i) = carbon2{i,1}/V_total(i);
    curve2(i) = 0
    %curve3(i) = carbon3{i,1}/V_total(i);
    curve3(i) = 0
end
jc1=0 ;% enter the j couplings here

lamsamp=[1];
%lamsamp=(1:10)/10;
%lamsamp=(1:3)/1; %for testing purposes
gamma2samp=(0)*30;%per second ~1/T2 to ~2/T2
%gamma2samp=0;
%gamma2samp=(3:5)*10; %for testing purposes
```

```
Dsamp=(0:30)*10;


montynumber=100; %number of monty carlo noise additions
%END DATA INPUT
%*******************************************************

jcoup1=(cos(3.14.*jc1.*timepts./2)).^2 ;%j coupling curve


c1noise=zeros(montynumber+1,length(noise));

for k=1:length(noise)
    c1noise(:,k)=[0; noise(k)*randn(montynumber,1)];
end
%the fit function value corresponding to the pH grid


chi2grid=zeros(length(Dsamp),length(gamma2samp),length(lamsamp),
         (montynumber+1));

%
%
%
%
for l=1:length(Dsamp)
    l
    [c1]=tedorcurve1full_scaled(Dsamp(l),timepts);
    c1j=c1.*jcoup1;
    for o=1:length(gamma2samp)
```

```
        tmp=exp(-gamma2samp(o).*timepts);
        c1g=tmp.*c1j;
        for p=1:length(lamsamp)
            c1glam=c1g.*lamsamp(p);
            for q=1:(montynumber+1)
                chi2grid(l,o,p,q)=sum(((c1glam-curve1+c1noise(q,:))./noise)

            end
        end
    end
end



fitD1s=zeros(montynumber+1,1);
fitgamma2s=zeros(montynumber+1,1);
fitlams=zeros(montynumber+1,1);

fitcurves1=zeros(montynumber+1,length(timepts));
for o=1:(montynumber+1)
    sqchi2grid=squeeze(chi2grid(:,:,:,o));
    [a,b,c]=ind2sub(size(sqchi2grid),find(sqchi2grid==min(sqchi2grid(:))));
    fitD1s(o)=Dsamp(a);
    fitgamma2s(o)=gamma2samp(b);
    fitlams(o)=lamsamp(c);



    [fitcurves1(o,:)]=tedorcurve1full_scaled(Dsamp(a),timepts);
```

```
end
fitD1s;
fitgamma2s;
fitlams;

fitr1s=(3061.41./fitD1s).^0.33333333;
timesmooth = (0:700)/50000;
[asmooth] = tedorcurve1full_scaled(Dsamp(a),timesmooth);
mean_D1 = mean(fitD1s)
erro_D1 = std(fitD1s)
```